



*Ministero dell'Istruzione,  
dell'Università e della Ricerca*



**DIPARTIMENTO DI INGEGNERIA CIVILE**

***Dottorato di Ricerca in Ingegneria delle Strutture e del  
Recupero Edilizio ed Urbano***

**XII Ciclo N.S. (2011-2013)**

**MECHANICAL BEHAVIOR OF WEB-FLANGE JUNCTIONS OF THIN-  
WALLED PULTRUDED FIBER-REINFORCED POLYMER PROFILES:  
AN EXPERIMENTAL AND NUMERICAL EVALUATION**

***Rosa Penna***

**Tutor**  
***Prof. Luciano Feo***

**Il Coordinatore**  
***Prof. Ciro Faella***

**Co-Tutors**  
***Prof. Francesco Ascione***

***Prof. Ayman S. Mosallam***



---

**CONTENTS**

<b>SUMMARY</b>	<b>I</b>
<b>CHAPTER 1 - STATE OF THE ART ON THE BEHAVIOR OF PULTRUDED COMPOSITES FRAME CONNECTIONS</b>	<b>1</b>
<b>1. INTRODUCTION</b>	<b>1</b>
<b>1.1. IMPACT OF CONNECTION DETAIL DESIGN ON THE OVERALL BEHAVIOR OF PULTRUDED COMPOSITES FRAME STRUCTURES</b>	<b>5</b>
<b>1.2. PFRP CONNECTIONS RELATED WORKS</b>	<b>6</b>
1.2.1. BANK & MOSALLAM (1990-1992)	7
1.2.2. MOSALLAM ET AL. (1993-2000)	23
1.2.2.1. QUASI-STATIC BEHAVIOR OF UC CONNECTIONS	25
1.2.2.3. QUASI-STATIC AND CYCLIC BEHAVIOR OF INTERIOR PFRP FRAME CONNECTIONS	34
1.2.3. MOTTRAM ET AL. (1994-1999)	36
1.2.4. SMITH ET AL. (1996-1999)	42
1.2.4.1. I-BEAM: STANDARD CONNECTION DETAIL	44
1.2.4.2. I-BEAM: THICK SEATS CONNECTION DETAIL	44
1.2.4.3. I-BEAM: STEEL CONNECTION DETAIL	46
1.2.4.4. BOX: STANDARD CONNECTION DETAIL	47
1.2.4.5. BOX: GUSSET CONNECTION DETAIL	48
1.2.4.6. BOX: CUFF CONNECTION DETAIL	51
1.2.4.7. BOX: STEEL CONNECTION DETAIL	54
1.2.5. BANK ET AL. (1996)	56
1.2.5.1. MULTICELL MOLDED CONNECTOR DETAIL	56
1.2.5.2. BACK-TO-BACK 6" (152.4 MM) PULTRUDED H-SECTION	58

1.2.5.3. 6"× ½" (152.4 MM × 12.7 MM) WRAPPED ANGLE CONNECTION	60
1.2.6. TURVEY (1998)	62
<b>1.3. WEB-FLANGE JUNCTION BEHAVIOR RELATED WORKS</b>	<b>66</b>
1.3.1. TURVEY AND ZHANG (2005-2006)	66
1.3.2. BOROWICZ AND BANK (2010)	74
<b>1.4. DESIGN CODES AND GUIDELINES</b>	<b>78</b>
<b>CHAPTER 2 – MECHANICS OF COMPOSITES MATERIALS</b>	<b>81</b>
<b>2. INTRODUCTION</b>	<b>81</b>
2.1. BASIC CONCEPTS AND TERMINOLOGY	84
2.2. GENERALIZED HOOKE'S LAW	86
2.2.1. MONOCLINIC MATERIALS	90
2.2.2. ORTHOTROPIC MATERIALS	93
2.2.3. TRANSVERSELY ISOTROPIC MATERIALS	95
2.2.4. ISOTROPIC MATERIAL	97
2.3. ENGINEERING MODULI OF ORTHOTROPIC MATERIALS	97
2.4. COORDINATE TRANSFORMATIONS	100
2.5. PLANE-STRESS CONDITIONS	105
2.6. FAILURE CRITERIA	113
2.7. MICROMECHANICAL CHARACTERIZATION OF A UNIDIRECTIONAL LAMINA	116
2.8. HYGROTHERMAL EFFECTS	118
<b>CHAPTER 3 – ON THE AXIAL BEHAVIOR OF WEB-FLANGE JUNCTIONS OF PFRP I-PROFILES</b>	<b>121</b>
<b>3. INTRODUCTION</b>	<b>121</b>
3.1. EXPERIMENTAL INVESTIGATION (@ UNISA)	123
3.1.1. PULL-OUT TEST SETUP AND INSTRUMENTATION	123

---

3.1.2. PFRP MATERIALS	127
<b>3.2. EXPERIMENTAL RESULTS</b>	<b>128</b>
3.2.1. FIRST GROUP: INFLUENCE OF PROFILE SIZE & PULL-OUT LOAD LOCATION	129
3.2.2. SECOND GROUP: INFLUENCE OF THE LOCATION OF PULL-OUT LOAD ON JUNCTIONS' STIFFNESS & STRENGTH	172
<b>3.3. FINITE ELEMENT ANALYSIS</b>	<b>186</b>
<b>3.4. RESULTS OF THE FIRST PHASE OF THE RESEARCH</b>	<b>198</b>
<b>CHAPTER 4 – ON THE AXIAL AND ROTATIONAL BEHAVIOR OF WEB-FLANGE JUNCTIONS OF PFRP H- AND L-PROFILES</b>	<b>201</b>
<b>4. INTRODUCTION</b>	<b>201</b>
<b>4.1. EXPERIMENTAL INVESTIGATION (@UCI)</b>	<b>203</b>
4.1.1. PULL-OUT TEST SETUP AND INSTRUMENTATION	203
4.1.2. RELATIVE ROTATION TEST SETUP AND INSTRUMENTATION	209
<b>4.2 EXPERIMENTAL RESULTS</b>	<b>213</b>
4.2.1. PULL-OUT TEST RESULTS	213
4.2.1.1. GROUP 1: MID-POINT LOADING TESTS RESULTS	217
4.2.1.2. GROUP 2: ECCENTRIC-POINT LOADING TESTS RESULT	224
4.2.2. RELATIVE ROTATION TEST RESULTS	230
<b>4.3 FINITE ELEMENT ANALYSIS</b>	<b>245</b>
<b>4.4 RESULTS</b>	<b>259</b>
<b>CHAPTER 5 – CONCLUSIONS</b>	<b>263</b>
<b>5. INTRODUCTION</b>	<b>263</b>
<b>5.1. EXPERIMENTAL RESULTS (@UNISA)</b>	<b>264</b>
<b>5.2. EXPERIMENTAL RESULTS (@UCI)</b>	<b>266</b>
<b>REFERENCES</b>	<b>271</b>



**ACKNOWLEDGEMENTS**

*I am grateful to my parents for their support, patience and for the sacrifices they have made so that I could pursue additional academic endeavors. A mere “thank you” is not enough.*

*Special thanks to my academic advisor and mentor, Professor Luciano Feo. His encouragement, guidance, and feedback throughout this process were invaluable. Whether it was a page or two of hand-written notes or a quick email pushing me forward, his words were always well-timed and inspiring. I look forward to collaborating with him on future research projects.*

*I would also like to express my gratitude to Professors Ayman S. Mosallam and Francesco Ascione whose advices, challenging questions and support during this investigation were instrumental to its success. I would welcome the opportunity to work with each of them again.*

## ACKNOWLEDGEMENTS

---

---

Mechanical behavior of web-flange junctions of thin-walled pultruded fiber-reinforced polymer profiles: an experimental and numerical evaluation.



## SUMMARY

Fibre-reinforced polymer (FRP) composites represent a class of advanced materials whose use has spread from the aeronautical, mechanical and naval industry to civil infrastructure, which has generated a new set of challenges.

Composites have unique features, such as high corrosion resistance, electromagnetic transparency, low maintenance costs and high strength-to-weight ratio. During the past few decades, pultruded fibre-reinforced polymer (PFRP) composites have been used in several successful applications related to corrosive environments such as cooling towers, mining and petrochemical facilities, water and wastewater treatment plants, as well as, off-shore structures. By mid-1990s, major applications of these materials were initiated in the field of seismic and corrosion repair and strengthening of existing reinforced concrete bridges and buildings.

Historically, off-the-shelf PFRP composites were developed and designed by the pultrusion industry and were intended for low-stress applications. Recently, composites have been introduced as primary structural members to replace or complement other conventional materials, such as steel, concrete and wood, in critical applications such as bridge decks, pedestrian bridges, and recently in highway bridges and other infrastructural systems [1, 2].

In order to make pultruded fibre-reinforced members appealing to the construction industry, most manufacturers produce profiles that imitate standard

structural steel members (*e.g.* I-, H-, C- and angles profiles); however, these steel-like profiles do not represent the optimum geometry for PFRP composites.

Unlike isotropic, time-independent structural materials, all PFRP pultruded materials are anisotropic and are characterized as viscoelastic materials [3-5]. Their stiffness and strength have values that depend on the orientation of the fibres. Consequently, these materials, under ambient environments, behave differently from those isotropic time-independent structural materials such as steel, under service, ultimate loads and dynamic excitations.

In order to ensure the structural reliability of load bearing pultruded composite members, the shape and fibre architecture of PFRP profiles must be optimized and designed properly.

Standard engineering guidelines, analytical and design tools developed for conventional materials are not applicable to FRP shapes. For this reason, several technical documents dealing with design equations and methods, material properties and safety factors for pultruded elements have been or being developed in recent years.

In particular, the EuroComp Design Code and Handbook [6], published in 1996, provided, for the first time, an independent, practical guidance on structural design of polymer composites.

In 2002, the EN 13706 standard [7] defined two different classes of materials, associated with minimum values of material properties, however, no design guidance was provided in this document.

In 2007, the Italian National Research Council (CNR) published the first Italian design guide (DT 205/2007) for the design and construction of structures made of FRP pultruded elements [8] which is not a binding regulations and is still rather incomplete.

Finally, in 2011, the Construction Institute of the American Society of Civil Engineers (ASCE) published the Manuals of Practice (MOP) #102 for the design of FRP composite connections [9]. This manual covers major issues related to the analysis and design of composite joints and frame connections manufactured from fibre-reinforced polymer composites in general and pultruded composites in particular. Currently, a joint effort between the Pultrusion Industry Council (PIC) and the ASCE Structure Institute for developing American Standards for PFRP structures is underway and will be published in the near future.

On the other hand, numerical simulation techniques such as finite element analysis (FEA), which could provide a more reliable prediction of the behavior of composite structures, may be difficult to use for typical office engineer, since these require specialized training. Therefore, in order to safely expand the use of pultruded composites in more structural applications, a comprehensive design protocol should be developed and should be accessible to practitioners in order to increase

their confidence level in such relatively new materials. At the same time, it became critical and essential to understand their short- and long-term mechanical behavior, as well as the behavior of their connections.

In recent years, relevant studies have been conducted and focused on the performance of PFRP frame structures and several research programs on optimizing pultruded composites have been initiated. For example Davalos et al. [10] presented an approach for flexural analysis and design of pultruded beams. This approach involved computational procedures for utilizing fibre volume fraction of the constituents, ply stiffness and panel laminate engineering constants. Over the past two decades or so, a number of studies focusing on the performance of PFRP connections and frame structures have also been reported. Some of the pioneering studies on PFRP frame structures were reported by Mosallam et al. [11-15] presenting the results of a comprehensive theoretical and experimental program to evaluate both the short-and long-term behavior of PFRP structures subjected to both quasi-static and sustained loading.

A highly complex and delicate mechanical aspect unique to steel-like unidirectional PFRP profiles is associated with the strength and stiffness of web-flange junctions (WFJ) of such profiles due to the insufficient fibre continuity.

In fact, the junction of web and flange of PFRP profile is an area that is relatively rich in resin and poor in fibers (matrix-dominated).

This insufficient fibre continuity will lead to progressive degradations of both axial and rotational stiffnesses and strengths affecting the buckling, post-buckling and the overall short- and long-term structural integrity of the PFRP profiles [16-19].

Some relevant studies related to this topic have highlighted the influence of the architecture of the web-flange junctions on the premature collapse of PFRP profiles. In fact, the mechanical properties of the WFJ are not the same as those of the web and the flanges due to the fact that this portion of the profile is resin-rich as compared to the web and flanges fibre-rich characteristics. Consequently, creep behavior of such zones may lead to a time-dependent failure. For example, Turvey and Zhang [20-22] have conducted an experimental investigation on web-flange junctions of 203 mm × 203 mm × 9.5 mm PFRP beams. Their study included junctions shear strength, rotational strength and stiffness, as well as the mechanism of tearing failure. The results of the study concluded that the collapse of the PFRP beams is a function of combined high shear stresses as well as bending stresses at the interfaces of different plies. Borowicz and Bank [23] have developed a design equation that governs the behavior of pultruded FRP beams subjected to concentrated loads in the plane of the web. The study also investigated the impacts of bearing plates on the ultimate capacity of these beams, and verifying experimental results through finite-element modeling.

This dissertation has been developed within the research activities of a multi-phase comprehensive joint research program between University of Salerno, Italy,

and the University of California, Irvine, USA, on investigating one of the major structural issues that defines the strength limit-state of pultruded fibre-reinforced polymer profiles. Specifically, the axial and rotational strength and stiffness of the web-flange junction (WFJ) of the majority of commercially-produced pultruded composite profiles.

As seen from the literature review, the failure mechanism of pultruded profiles web-flange junctions has yet to be fully understood and they often involve failure of the web-flange junctions. However, the local failure may have different modes due to the variability of materials properties of pultruded composites.

With this aim, the research activities have been developed in the following 4 phases:

- the first phase has been dedicated to the study of the mechanics of composites materials and their failure criteria (*Chapter 2*);
- the second phase consisted of an experimental investigation carried out at the Materials and Structural Testing Laboratory (LMS) of the Department of Civil Engineering (DICIV) of the University of Salerno in order to evaluate the axial strength and stiffness of WFJ of PFRP I-profiles [24-31] (*Chapter 3*);
- the third phase was an experimental study conducted at the Structural Engineering Testing Hall (SETH) of the University of California Irvine (UCI) to evaluate both the axial and the rotational strength and stiffnesses of WFJ of PFRP H- and L-profiles. From the results of the experimental investigations developed in

the previous two phases, load-displacement ( $P-\delta$ ) and moment-rotation ( $M-\theta$ ) relations were developed in order to accurate modeling and establishing the design limit-state of PFRP structures (*Chapter 4*);

- the last phase consisted of a finite element analysis (FEA) and a comparison of the numerical results with the experimental findings (*Chapter 5*).

#### **References of the Summary**

- [1] Mosallam A. S., Chapter on composites in construction. Materials selection handbook. John Wiley Publishing Co; 2002 [chapter 45].
- [2] Bank L. C., Composites for construction: Structural Design with FRP Materials. John Wiley & Sons; 2006.
- [3] Kollár L. P., Springer G. S., Mechanics of composites structures. Cambridge University Press; 2003.
- [4] Ascione L., Feo L., Mechanical behavior of composites for construction. In “Wiley Encyclopedia of Composites”, 2<sup>nd</sup> Edition, John Wiley & Sons, **2**, pp.1625-1649; 2012.
- [5] Barbero E. J., Introduction to composite material design. Taylor & Francis, Philadelphia; 1998.
- [6] Eurocomp Design Code and Handbook, Structural design of polymer composites. The European Structural Polymeric Composites Group; 1996. (ISBN 0419194509).
- [7] European Committee for Standardization (CEN). EN 13706: Reinforced plastics composites – Specifications for pultruded profiles. Part 1: Designation; Part 2: Methods of test and general requirements; Part 3: Specific requirements, Brussels: CEN; 2002.
- [8] Technical Document CNR-DT 205/2007. Guide for the design and construction of structures made of FRP pultruded elements. Italian National Research Council (CNR) Rome; 2008.

- [9] Mosallam A. S., Design guide for FRP composite connections. Manuals of Practice (MOP) 102. American Society of Civil Engineers (ASCE); 2011. ISBN9780784406120: 624.
- [10] Davalos J. F., Salim H. A., Qiao P., Lopez-Andio R., Analysis and design of pultruded FRP shapes under bending. *Composites Part B: Engineering*, 27B (3,4), pp. 295–305; 1996.
- [11] Mosallam A. S., Abdelhamid M. K., Conway J. H., Performance of pultruded FRP connection under static and dynamic loads. *Journal of Reinforced Plastic and Composites*, **13**, pp. 1052–1067; 1996.
- [12] Mosallam A. S., Abdelhamid M. K., Dynamic behavior of PFRP structural Sections. In Proc. of ASME (Energy Sources Tech. Conf. and Expo, Composite Material Tech.), **53**, pp. 37–44; 1993.
- [13] Mosallam A. S., Bank L. C., Short-term behavior of pultruded fiber reinforced plastic frame. *Journal of Structural Engineering (ASCE)*, **118(7)**, pp. 1037–1954; 1992.
- [14] Liu X., Mosallam A. S., Kreiner J., A numerical investigation on static behavior of pultruded composite (PFRP) portal frame structures. In Proceeding of the 43rd International SAMPE Symposium and Exhibition, Anaheim, California; 1998.
- [15] Mosallam A. S., Durability of pultruded fiber reinforced polymer (PFRP) composites in mining environments in Durability of fiber reinforced polymer (FRP) composites for construction. Edited by B. Benmokrane and H. Rahman, pp. 649-659; 1998.
- [16] Bank L. C., Nadipelli M., Gentry T.R., Local buckling and failure of pultruded fiber-reinforced plastic beams. *Journal of Engineering Materials and Technology*, **116**, pp. 223–237; 1994.
- [17] Bank L. C., Yin J., Failure of web-flange junction on postbuckled pultruded I-beams. *Journal of Composites for construction*, 177, pp.177-184; 1999.
- [18] Turvey G. J., Zhang Y., A computational and experimental analysis of the buckling , postbuckling and initial failure of pultruded GRP columns. *Composites & Structures*, 84, pp 1527-1537; 2006.
- [19] J. R. Correia, F. A. Branco, N. M. F. Silva, D. Camotim, N. Silvestre., First-order, buckling and post-buckling behaviour of GFRP pultruded beams. Part 1: Experimental study. *Computers and Structures*, 89, pp. 2052-2064; 2011.



- 
- [20] Turvey G. J., Zhang Y., Tearing failure of web-flange junctions in pultruded GRP profiles. *Composites Part A: applied science and manufacturing*, 36, pp. 309–317; 2005.
- [21] Turvey G. J., Zhang Y., Characterisation of the rotational stiffness and strength of web-flange junctions of pultruded GRP WF-sections via web bending tests. *Composites Part A: applied science and manufacturing*, 37, pp. 152–164; 2006.
- [22] Turvey G. J., Zhang Y., Shear failure strength of web-flange junctions in pultruded GRP WF profiles. *Construction and Building Materials*, 20, pp. 81–89; 2006.
- [23] Borowicz D. T., Bank L. C., Behavior of pultruded fiber-reinforced polymer beams subjected to concentrated loads in the plane of the web. *Journal of Composites for Construction*, 15, pp. 229–238; 2011.
- [24] Mosallam A. S., Elsadek A. A., Pul S., Semi-rigid behavior of web-flange junctions of open-web pultruded composites. In *Proceeding of the International Conference on FRP Composites*, San Francisco, California; 2009.
- [25] Feo L., Mosallam A. S., Penna R., Preliminary results of an experimental and computational analysis of the behavior of web-flange junctions of GFRP pultruded profiles subjected to concentrated loads. In *Proceeding of the 15<sup>th</sup> European Conference on Composites Materials (ECCM15)*, Venice; 2012.
- [26] Feo L., Mosallam A. S., Penna R., An Experimental Investigation on the Behavior of Web-Flange Junctions of GRP Pultruded Profiles in *Proceeding of the ICCE-20 (20<sup>th</sup> Annual International Conference on Composites/Nano Engineering)*, Beijing; 2012.
- [27] Feo L., Penna R., Analisi delle tensioni nei nodi “ala-anima” di profili pultrusi fibrorinforzati in *Proceeding of the Italian Association for Stress Analysis (AIAS) Conference*, Padova (Italy); 2012.
- [28] Feo L., Penna R., On the behavior of web-flange junctions of GRP pultruded profiles. In *Proceedings of Riga Technical University 53<sup>rd</sup> International Scientific Conference dedicated to the 150th anniversary and 1<sup>st</sup> Congress of World Engineers and Riga Polytechnical Institute / RTU Alumni*. Riga (Latvija); 2012.
- [29] Elsadek A., Mosallam A., Pul S., Feo L., Penna R., Experimental Evaluation of Axial Flexibility of Web-Flange Junctions of Thin-Walled Pultruded H-Profiles, *Composites Structures*, In press; 2012.

- [30] Feo L., Mosallam A. S., Penna R., Experimental and numerical results on the failure strength of web-flange junctions of thin walled pultruded composites profiles, in Proceeding of the Italian Association for Stress Analysis (AIAS) Conference, Salerno (Italy); 2013.
- [31] Feo L., Mosallam A. S., Penna R., Mechanical behavior of web-flange junctions of Thin-walled pultruded I-profiles: An experimental and numerical evaluation. Composites Part B: Engineering, Volume 48, Pages 18-39, May 2013.
- [32] Feo L., Mosallam A. S., Elsadek A., Pul S., Penna R., Structural evaluation of axial and rotational flexibility and strength of web-flange junctions of open-web pultruded. Composites Part B. (2014), Volume 66, Pages 311-327, October 2014.

**CHAPTER 1 – STATE OF THE ART ON THE BEHAVIOR OF PULTRUDED  
COMPOSITES FRAME CONNECTIONS**

**1. INTRODUCTION**

Understanding the behavior of frame connections for pultruded fiber reinforced polymer (PFRP) structures is an essential key to satisfying both the safety and efficiency requirement of such structures. This issue is particularly important when designing load-bearing pultruded composite structures such as bridges and building skeletons [Figs. 1.1-1.4].



**Figure 1.1.** The Fiberline All-Pultruded Composites Cable Stayed; Kolding, Denmark.



**Figure 1.2.** Aberfeldy All-Composites Cable Stay Bridge, UK.

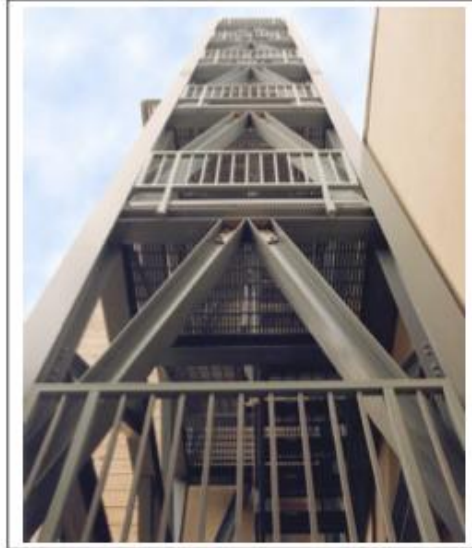


**Figure 1.3.** Pultruded composites frame structure.



**Figure 1.4.** The All-Composite “Eyecatcher” Building in Switzerland.

Despite their critical structural role, little attention has been given to PFRP frame connections. Regardless of the type of material used in any structural system, connections are needed to attach member ends to other structural members sufficiently to allow the loads to continue in an orderly flow to the foundation. The efficient connection design must produce a joint that is safe, economical and practical. For other construction materials such as steel, varieties of structurally sound connection details are available. Until recently, most available connection details were duplications of steel details. For this reason, and due to the absence of an authoritative unified design code, structural designers of most PFRP structures built in the last decade, or so, have utilized - and continue to utilize - the inadequate and in most cases unsafe steel-like connection details (Fig. 1.5).



**Figure 1.5.** An Example of "Steel-Like" frame connections [Photo by A. Mosallam].

In general, it is difficult to introduce a new structural material with no technical and scientific backup. For this reason, structural composites will have great difficulty in penetrating the construction industry without the development of strong design specifications. Some of the major obstacles limiting the use of pultruded structural composites in the construction industry are the following:

- lack of mechanical information on both short and long term performance;
- lack of design standards and acceptance by building codes;
- structural deficiency of some structural shapes amplified by a lack of communication and coordination between manufactures and the researches;
- limited sponsored-researches programs;
- lack of quality control of commercial products.

In this chapter, the state of the art as well as recommendations for repair and rehabilitation of steel-like PFRP connections are presented and discussed.

### **1.1. IMPACT OF CONNECTION DETAIL DESIGN ON THE OVERALL BEHAVIOR OF PULTRUDED COMPOSITES FRAME STRUCTURES**

The major impact of connection behavior on the overall performance of composite structures includes: (i) buckling and post-buckling capacity, (ii) premature localized-failure of open-web members, and (iii) the ultimate strength as well as the overall creep behavior of thin-walled FRP structures.

In order of pultruded composites to be considered as structural materials for civil engineering applications, these materials must be proven to have structural reliability and higher efficiency under different loading conditions (e.g., dead, live, wind, earthquake, etc.) during the expected useful-life of the structure.

The efficiency of a composite connection can be expressed as:

$$\eta = \frac{P_j}{P_m} [\%],$$

where:

$P_j$  = Load producing failure to connection;

$P_m$  = Load producing failure to member.

For this reason, reliable information on the behavior of pultruded composites under these loading regimes must be available to the structural engineers.

Several research studies have focused mainly on the static behavior of these FRP connections with little work on the dynamic and seismic behavior of these joints. Furthermore, due to the fact that composites are viscoelastic materials, structural engineers must include the long-term (creep) effects under ambient and other varying environmental conditions.

Other studies have been conducted in the area of characterizing the structural behavior of pultruded composite connections. The following is a summary of major studies in this area.

## **1.2. PFRP CONNECTIONS RELATED WORKS**

---

Mechanical behavior of web-flange junctions of thin-walled pultruded fiber-reinforced polymer profiles: an experimental and numerical evaluation.



### 1.2.1. Bank & Mosallam (1990-1992)

The first comprehensive, full-scale study was conducted by *Bank* and *Mosallam* in 1990 [1]. In this study, detailed theoretical and experimental investigations on the short and long-term behavior of PFRP frame structures were conducted.

In particular, two portal frame structures were constructed from off-the-shelf commercially produced pultruded sections and an analytical investigation was performed to predict their nonlinear response. The numerical model includes the effects of axial, shear and flexural deformation of the pultruded members; flexibility of the beam-to-column connections; and the post buckling of the frame girder. An expression for the nonlinear rotational stiffness of the pultruded beam-to-column connection was presented. The experimental data obtained from the full-size test [Fig. 1.6] correlated very well with the analytical model.

In 1992, *Bank & Mosallam* [2] presented results of an experimental and analytical investigation on the behavior of a pultruded composite portal frame subjected to short-term static loads.

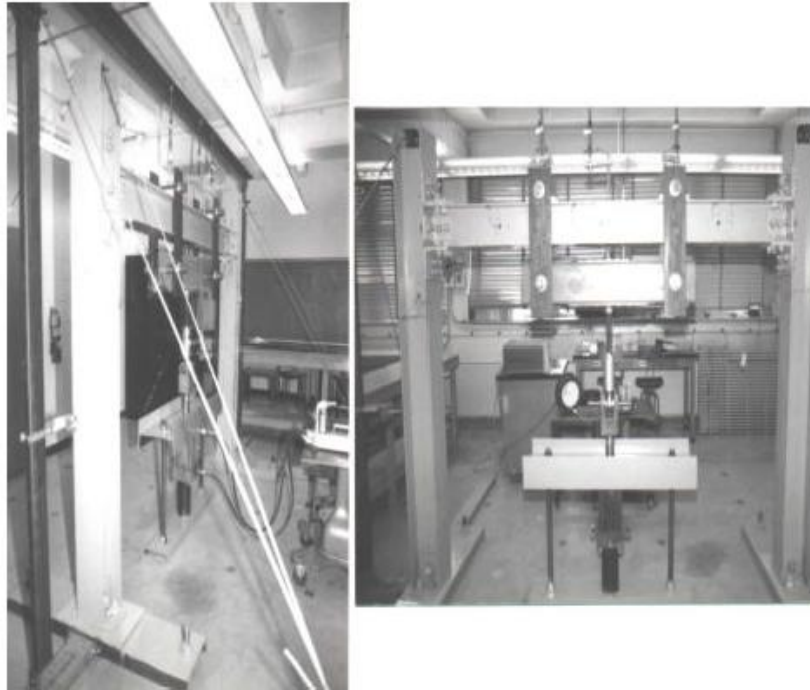


**Figure 1.6.** Study on PFRP portal frame with steel-like connection details.

The composite profiles used in this study were standard off-the-shelf H-profiles 8"×8"×3/8" (203.2 mm × 203.2 mm × 9.5 mm) glass/vinylester Pultex 1625 pultruded profiles (manufactured by Creative Pultrusions, U.S.A.).

These commercially produced pultruded composite sections consisted of E-glass roving and continuous strand mat (occupying approximately 45% by volume) in a vinylester resin. The beam-to-column and base-plate connections were detailed according to general recommendations of the majority of pultruders' design manuals [3-6].

From the experimental tests it was observed that the failure was not in the connection elements (angles, threaded rods, or nuts) but, rather, in the column section itself. The flange of the column separated from the web, behind the top row of bolts of the top angle, creating a hollow internal cavity in the pultruded section at the flange-web intersection (Figs. 1.7 -1.8).

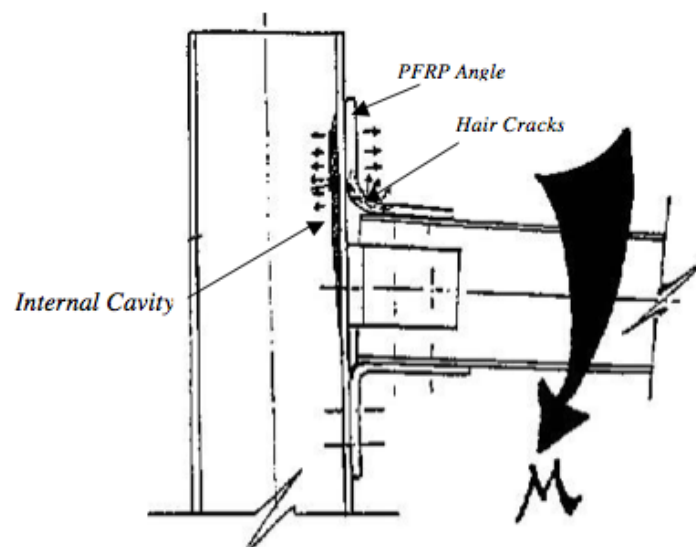


**Figure 1.7.** Premature failure of open-web unidirectional pultruded profiles and delamination of unidirectional PFRP angles.

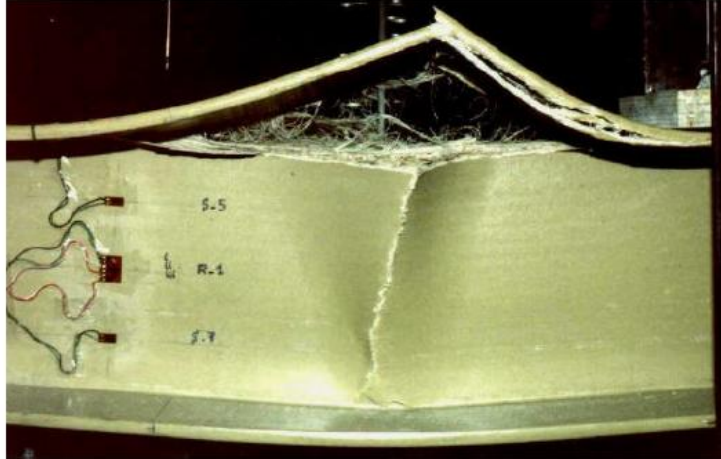


**Figure 1.8.** Premature failure of open-web unidirectional pultruded profiles [Mosallam 1990].

This transverse tension failure occurred perpendicular to the direction of longitudinal fiber reinforced in the pultruded section. The unidirectional pultruded equal-leg angles used in this test program had the major fiber reinforcements running in the *wrong* directions relative to the load path and applied stresses. For this reason, a premature failure initiated by hair cracks at the corners was unavoidable (Fig. 1.9).

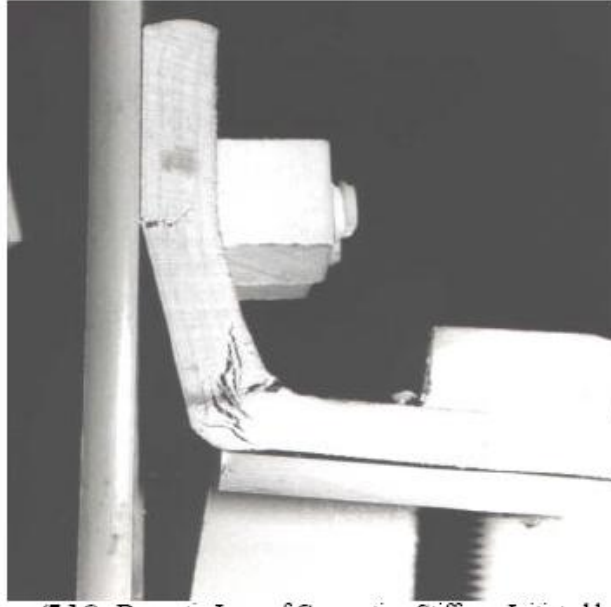


**Figure 1.9.** Dramatic loss of connection stiffness initiated by the development of hair cracks at the corners of the pfrp unidirectional angles.

Based on the findings of the experimental study conducted by *Bank* and *Mosallam* in 1990, the effect of connection details made of pultruded FRP composites, and their semi-rigid behavior, have been investigated by *Bank, Mosallam* and *Gonsior* in 1990 [7]. Figure 1.10 presents the four connection details evaluated in this study.

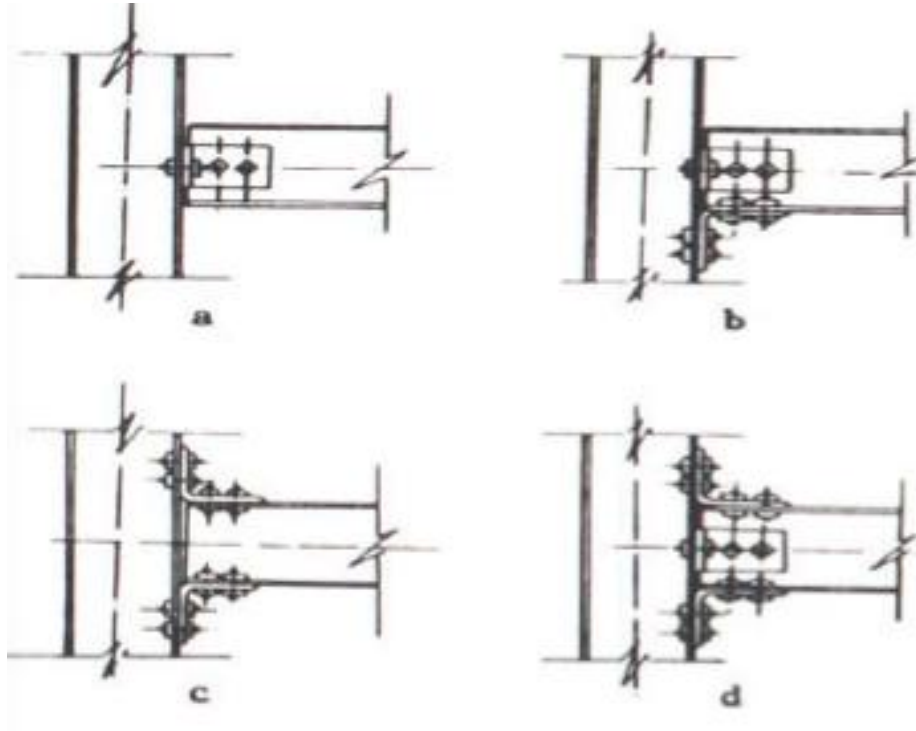


**Figure 1.10.** PFRP connection details evaluated.

This pilot investigation involved both experimental and analytical evaluation of several connection details for pultruded frame structures. All of the connections tested focused on exterior beam-to-column joints with flange attachment configuration.

Experimental results of three different PFRP connection details were presented.

The test setup used in this study is shown in Figure 1.11.

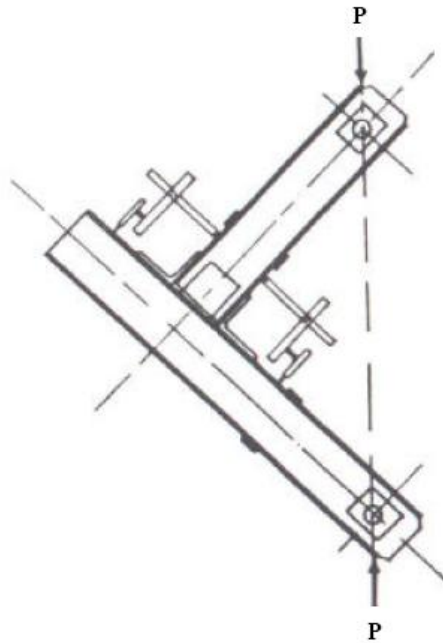


**Figure 1.11.** Exterior PFRP beam-to-column connection [Bank, Mosallam and Gonsior (1990)].

Figure 1.12 shows the typical moment-rotation ( $M-\theta$ ) curve for detail (d) of Figure 1.12, which was the same detail used in the PFRP portal frame investigated by Bank & Mosallam in 1990 and 1992 [1,2].

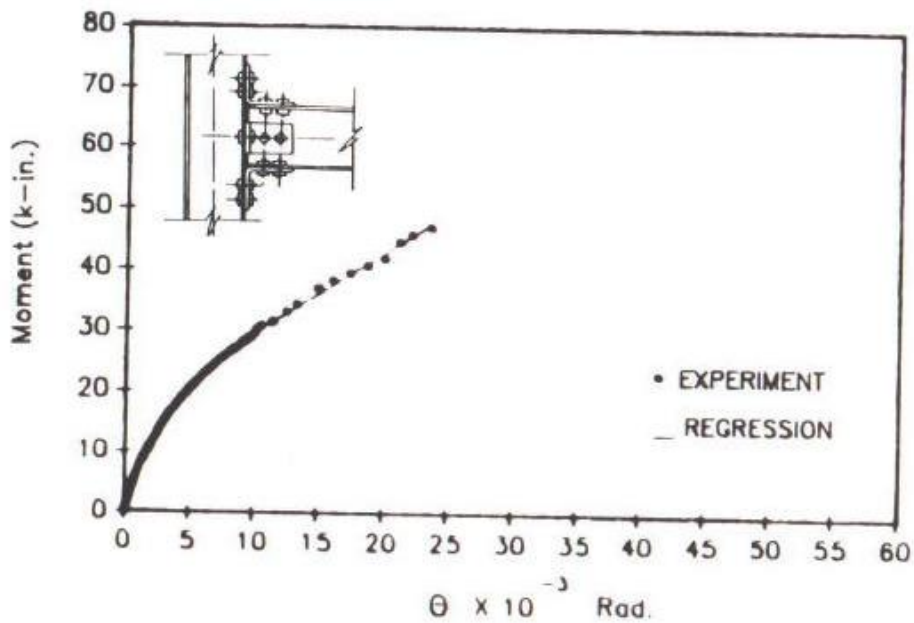


**Figure 1.12** Moment-rotation curve for exterior PFRP beam-to-column connection detail (d) described in figure 1.10 - Type i.

As reported by *Bank & Mosallam* [1,2], and illustrated in Figure 1.8, a premature failure in the form of a local separation of the column flange from the web was the major cause of the limited strength of this detail. For this reason, *Bank, Mosallam* and *Gonsior* [7] suggested a simple detail to avoid this premature failure by introducing a transfer member in the form of a unidirectional pultruded angle placed at the web/flange junction of the column at the connection zone as shown in Figure 1.13. As expected, the addition of this transfer member prevented, to a large extent, the formation of the cavity behind the connection and resulted in an increase in the strength up to 50%. In addition, the plastic relative rotation



increased of about 136% of the ultimate plastic deformation of the connection. However, no gain in stiffness was achieved up to the ultimate moment of the un-stiffened detail in Figures 1.12 and 1.13. As for the un-stiffened connection detail, a full regression analysis was performed.

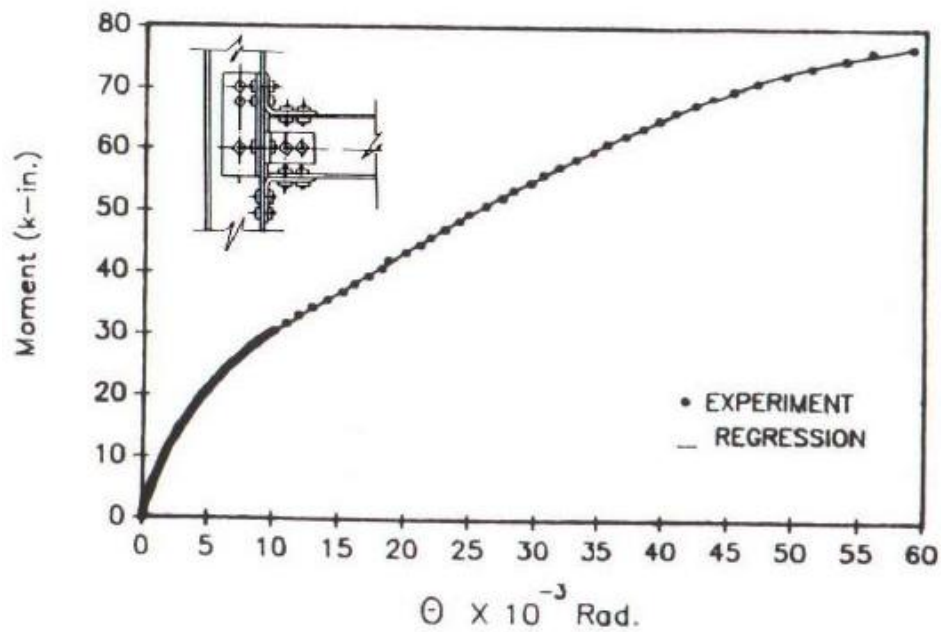


**Figure 1.13.** Moment-rotation curve for exterior PFRP beam-to-column connection detail (d) with transfer angle *Type ii* [Bank, Mosallam and Gonsior 1990].

Figures 1.14 and 1.15 show the ultimate failure mode of connection details *Type i* and *Type ii*, respectively.

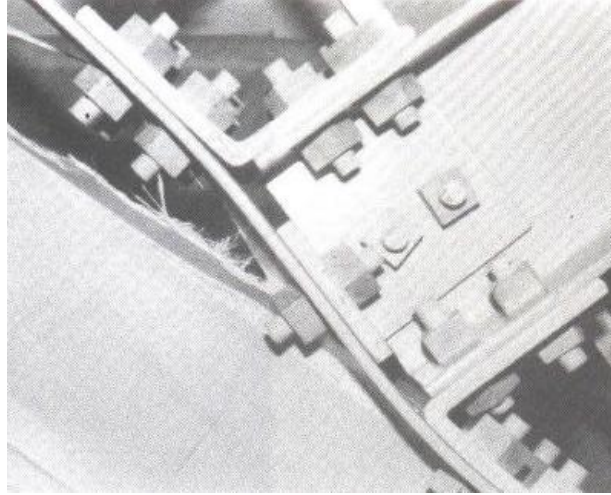


**Figure 1.14.** Ultimate failure mode of connection details *Type i*.

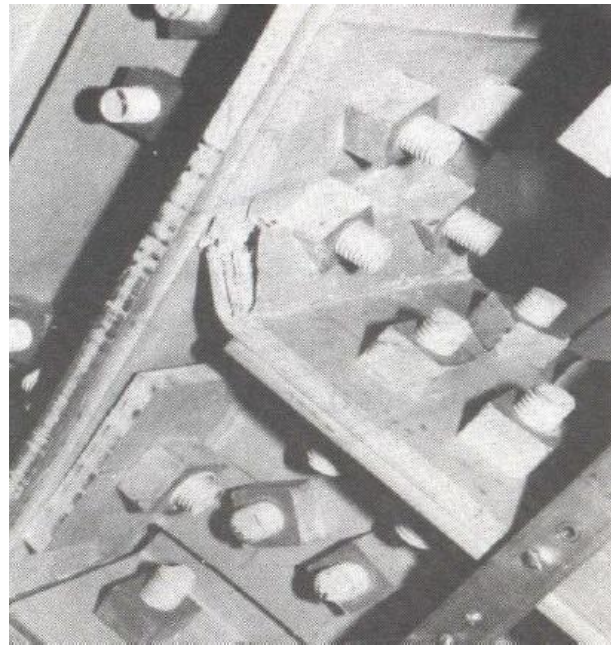


**Figure 1.15.** Ultimate failure mode of connection details *Type ii*.

As a continual effort in improving the structural behavior of steel-like connection details in 1991, *Bank and Mosallam* [8-10] proposed another PFRP beam-to-column connection detail using several off-the-shelf pultruded elements. This connection detail, referred to as *Type iii*, was similar to the *Type ii* detail, except for replacing the top pultruded angle by a miter connector consisting of two 228.6 mm long, 152.4 mm wide T- Flange elements bolted to the flanges of both the column and beam using 12.7 mm pultruded plates. The fiber orientation of the pultruded plate was aligned at a 45° with respect to the beam and column flanges as shown in Figure 1.16.

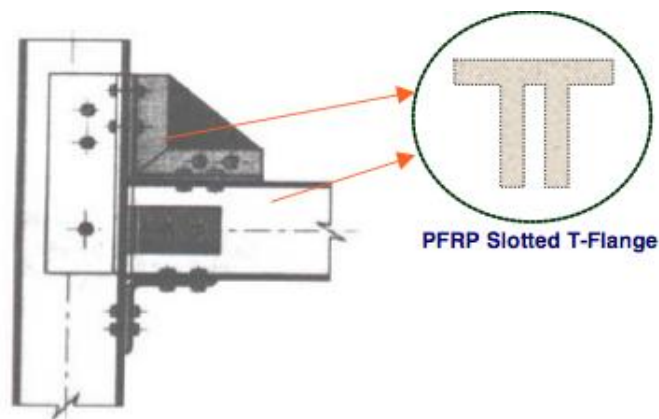


**Figure 1.16.** PFRP connection details *Type iii*.

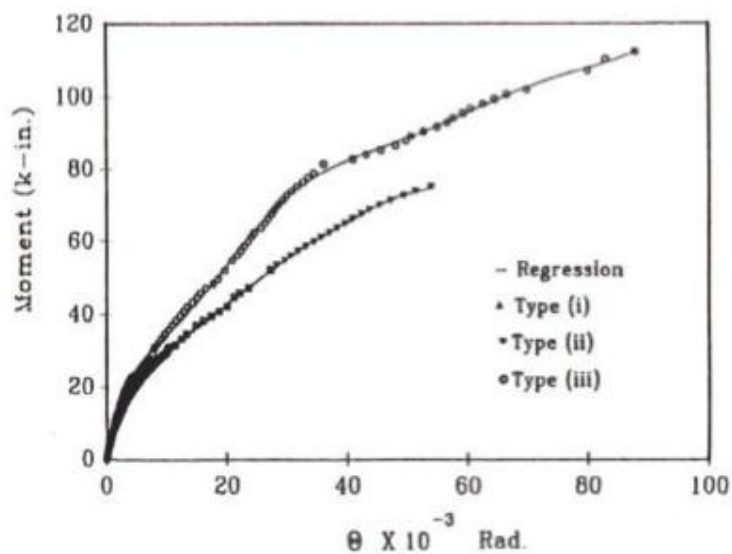
The PFRP plate was attached to the slotted section using PFRP threaded rods and FRP molded nuts.

The failure mode of *Type iii* connection specimen was initiated by a local transverse tension failure of the unidirectional pultruded elements. The *initial* failure occurred due to the development of high transverse tensile stresses at the unstiffened beam portion beneath the top T-flange miter joint. The second local damage was also caused by the high transverse tension stresses at the slotted section of the flange. This local failure was initiated first through the bolt holes connecting the T-flange and propagated to about half of the pultruded plate. The ultimate global failure was a combination of sudden splitting of the T-flange, shaving of the PFRP threads of the threaded rod connecting the shear PFRP angle, and a separation of the pultruded beam from the column [Fig. 1.17].



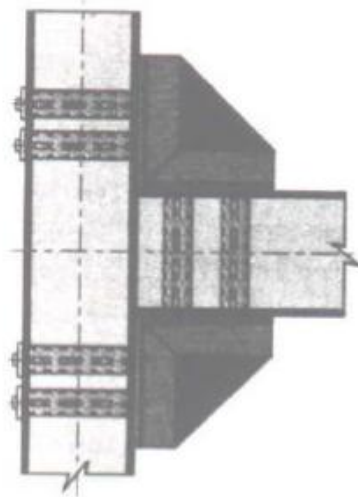
**Figure 1.17.** Ultimate Failure Mode of Connection Details *Type iii*.

Figure 1.18 shows a comparison between the three types of connection details *Type i*, *ii* and *iii*. As shown by this graph, it is hard to distinguish between the curves for *Type i* and *Type ii*, up to the failure moment of the *Type i* connection detail. However, this graph shows an appreciable increase in both the stiffness and the strength of the *Type iii* connection detail. The gain in the rotational stiffness of this detail was about 48% as compared to the rotational stiffness of connections *Type i* and *Type ii*. In addition, an appreciable strength gain of about 119%, and 50% was achieved, as compared to ultimate moment capacity of connections *Type i* and *Type ii*, respectively.



**Figure 1.18.** Moment-Rotation Curves of Connection Details Tested by *Bank and Mosallam 1991*.

In 1992, *Bank, Mosallam* and *McCoy* [11] presented a summary of different PFRP frame connections tested in previous studies conducted by *Bank and Mosallam* [1, 2] and *Bank, Mosallam and Gonsior* [7]. In addition, a new connection detail was proposed and was referred to as *Type iv*. Figure 1.19 shows the details connection *Type iv*. As seen in Figure 1.19, this connection detail was an improved version of the connection detail *Type iii*. However, in this detail, both the top and bottom PFRP seated angles were replaced with the T-Flange/Plate system described earlier for detail *Type iii*. The PFRP plate was attached to the slotted section using epoxy adhesives and no bolts were used.



**Figure 1.19.** PFRP Connection Details *Type iv*.

The ultimate failure of this connection was catastrophic due to failure of the adhesives (Fig. 1.20). The adhesive failure was attributed to lack of sufficient

surface pre-treatment of the adherends, especially in preparing the interior surfaces of the slot (or groove) of the T-Flange sections.

Figure 1.21 shows the experimental moment/rotation curves for the four connection details (*Types i, ii, iii, and iv*). As shown in this figure, a substantial improvement in both the strength and rotational stiffness was achieved using this connection detail. For example, the gains in the strength and rotational stiffness were about 196% and 272%, respectively, as compared to the strength and stiffness of connection detail *Type i* used in the portal frame study by *Bank and Mosallam* in 1990 [1].

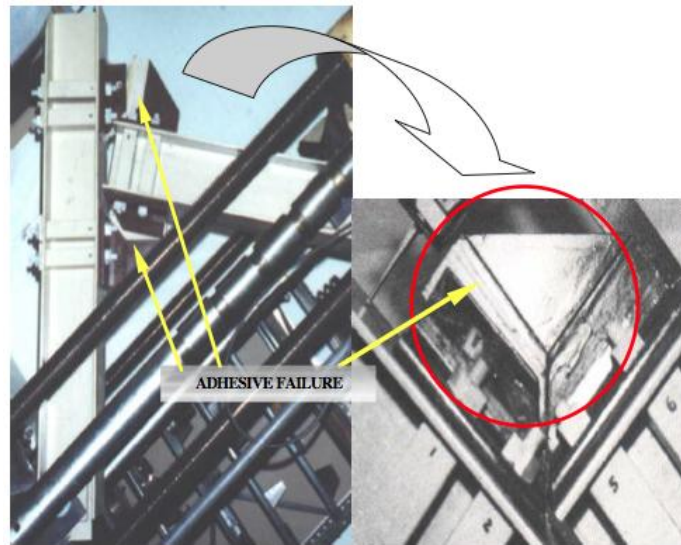


**Figure 1.20.** Adhesive failure of connection detail *Type iv*.

However, as shown in Figure 1.21 a tremendous loss in plastic rotational deformation (of connection *Type iv*) was observed (ultimate relative rotation of

*Type iv* is 0.02 rad vs. ultimate relative rotation of *Type iii* of 0.09 rad). This results reflected the lack of ductility of connection detail *Type iv*.

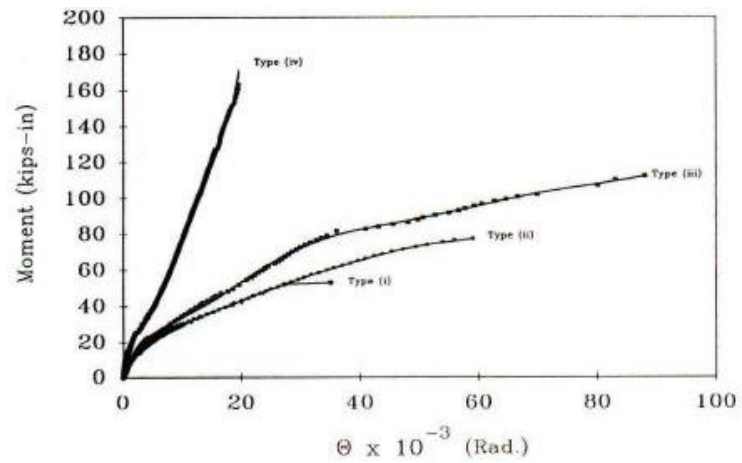


**Figure 1.21.** Moment-rotation curves of four connections details [Bank, Mosallam and McCoy (1992)].



### 1.2.2. Mosallam et al. (1993-2000)

Based on the past unsuccessful experience of utilizing “un-engineered” off-the-shelf pultruded products as connecting elements (e.g. *Bank & Mosallam* in 1990 [1], *Bank & Mosallam* in 1991 [8-10]), a different approach was adopted by *Mosallam* in 1993 [12] and *Mosallam et al.* [13] to develop customized connection details. In fact, in 1993 *Mosallam* [12] presented a novel approach to connecting PFRP framing elements using appropriate composite connectors. As said, the development of these connectors was the result of a combination of past experience, available research and design data, and knowledge of the anisotropic behavior of the composite materials.

The design criteria for what is called the *Universal Connector (UC)* included:

- *proper fiber orientation;*
- *ease of erection and duplication;*
- *geometrical flexibility and suitability for use in connecting a large variety of commercially available pultruded shapes;*
- *maximizing both the overall connection stiffness and ultimate capacity.*

The first *UC* prototype was modified and optimized using finite element (FE) techniques by *Mosallam et al.* in 1994 [13]. Figure 1.22 shows the dimensions and the geometry of the modified version of the *UC* connector. The FRP connector prototype was designed and fabricated from E-glass/vinylester composition.

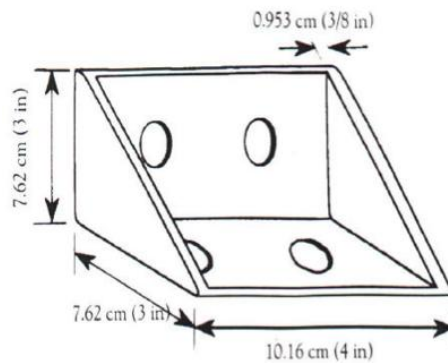


**Figure 1.22.** Dimensions and geometry of the modified *Universal Connector (UC)*.

The *UC* element was made in order to be used for the majority of PFRP connections for different shapes, e.g., exterior and interior beam-to-column connections, column-base connections, continuous beam connections, beam-to-girder connections, and others. In order to verify the performance of this *engineered* composite connector, a comprehensive experimental program to evaluate quasi-static, dynamic, creep and low fatigue cyclic behavior of connections constructed using the *UC* element(s) was conducted by *Mosallam et al.* between 1993-1999 [13-23].

This experimental program was composed of the following phases:

- i) quasi-static behavior of UC connections;
- ii) cyclic behavior of exterior UC PFRP connections;
- iii) UC PFRP connection response under sustained loads (creep test);
- iv) vibration and damping evaluation of UC PFRP frame connections;
- v) evaluation of mechanically fastened UC exterior flexible connections;
- vi) quasi-static and cyclic behavior of interior PFRP frame connections.

Details of the most important phases are presented in the following paragraphs.

#### 1.2.2.1. Quasi-Static Behavior of UC Connections

All beams and columns (Fig. 1.23) were constructed from "off-the-shelf" (101.6 mm × 101.6 mm × 6.35 mm) PFRP E-glass/vinylester H-profile manufactured by Bedford Reinforced Plastics Company (USA) [3]. The connecting elements used for these joints were, namely, a combination of the following: high-strength epoxy adhesive pultruded threaded rods and nuts, UC # 4, PFRP (76.2 mm × 76.2 mm × 9.53 mm), equal-leg unidirectional angles.

The objective of testing these connection details were to:

- i) determine, experimentally, both the rotational stiffness and the ultimate strength of each connection detail;
- ii) evaluate the performance of the newly designed and developed prototype of the universal connector;
- iii) identify the different failure mechanisms of each connection;
- iv) investigate the impact of using high-strength adhesive in both the strength and the stiffness of beam-to-column connections.

In order to characterize the rotational stiffness of PFRP connections, two measurements were obtained from the test. The first quantity was the applied moment at the connection, and the second quantity was the relative angle of rotation between the beam and the column. Details of these calculations can be found in *Bank, Mosallam and McCoy* [11].

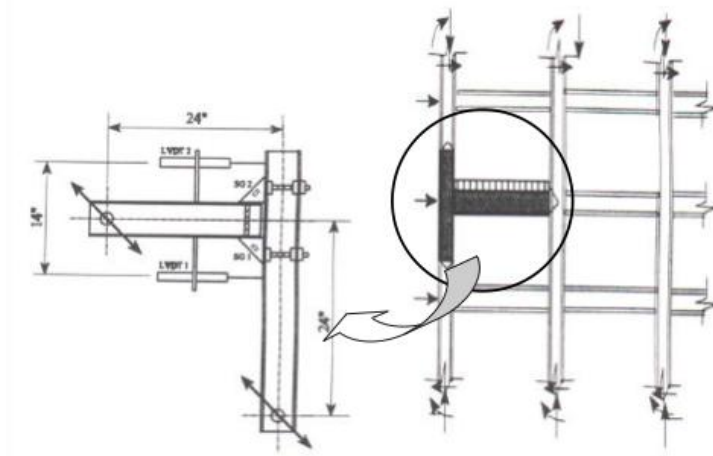


**Figure 1.23.** Typical geometry, dimensions and details of the PFRP exterior frame connection specimens.

Figure 1.24 shows details of the PFRP beam-to-column connection tested in this program. The same connection designation system used in 1992 by *Bank, Mosallam* and *McCoy* [11] was adopted by *Mosallam et al.* in 1993 [12] to assist the reader in relating and comparing the behavior of each connection and to add continuity to the research subject. Accordingly, the three PFRP connections developed in this study were designated as: *Types v, vi, and vii*. The design of these three connections included PFRP threaded rod stiffeners.

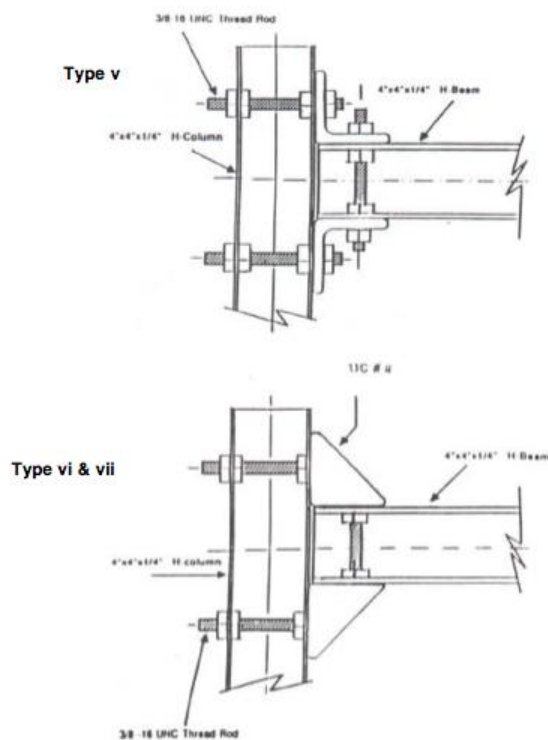


**Figure 1.24.** Details of the PFRP exterior frame connection: *Types v, vi and vii.*

As discussed earlier, the addition of these threaded rod stiffeners can be recommended in order to prevent the premature separation of the web and flanges of the PFRP H-sections (this recommendation applies to all open-web PFRP unidirectional profiles). Furthermore, this stiffening technique can ensure the integrity of the three composite plates (the flanges and the web) forming the H-shape. Consequently, an efficient utilization of the PFRP sections can be achieved by both enhancing the stiffness characteristics and increasing the ultimate strength of the connection. Based on past

experience, this stiffening detail could be strongly recommended at any high tensile stress concentration zones of PFRP open-web thin-walled structural shapes (e.g., H, I). The locations of high stress concentration are likely found near the connections (maximum shear and maximum negative moments), near the girder mid-span (maximum positive moments) and at the locations of concentrated loads (maximum shear). The need for this stiffening detail is especially important when minimum fiber reinforcement at the web-flange junction (WFJ) is provided. Unlike connection details (vi) and (vii), no UC element was employed in connection detail *Type v*. Instead, two PFRP unidirectional angles 3" × 3" × 3/8" (76.2 mm × 76.2 mm × 9.53 mm) were placed at both the top and the bottom of the beam. The connection was stiffened by PFRP threaded rods and FRP molded nuts. To investigate the effect of using adhesive in the overall performance of the joint, connection detail *Type vii* was designed.

This connection has the same details as connection *Type vi* except for the addition of thin films of high-strength epoxy adhesive (Magnobond 56 supplied by Bedford Reinforced Plastics, U.S.A.) between the contacting surfaces between the UC's and both the beam and the column. The experimental moment-rotation ( $M-\theta$ ) curves of the three connection details are shown in Figure 1.25. A linearized version of these curves is shown in Figure 1.26.

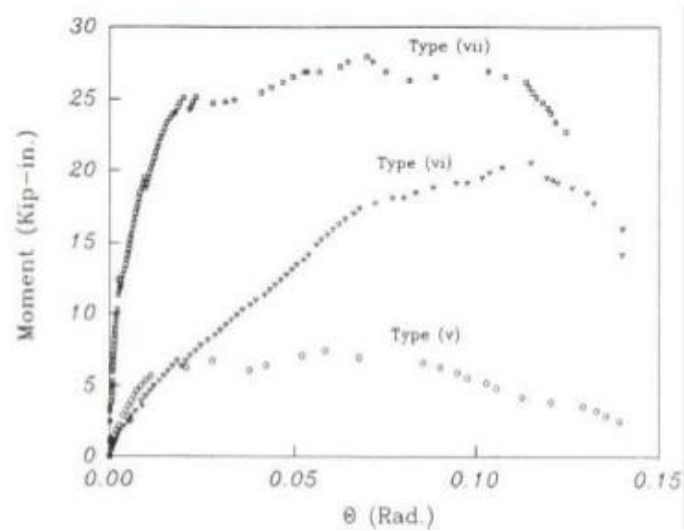


**Figure 1.25.** Experimental Moment-Rotation Curves for the Three PFRP Frame Connections: Types (v), (vi) and (vii).

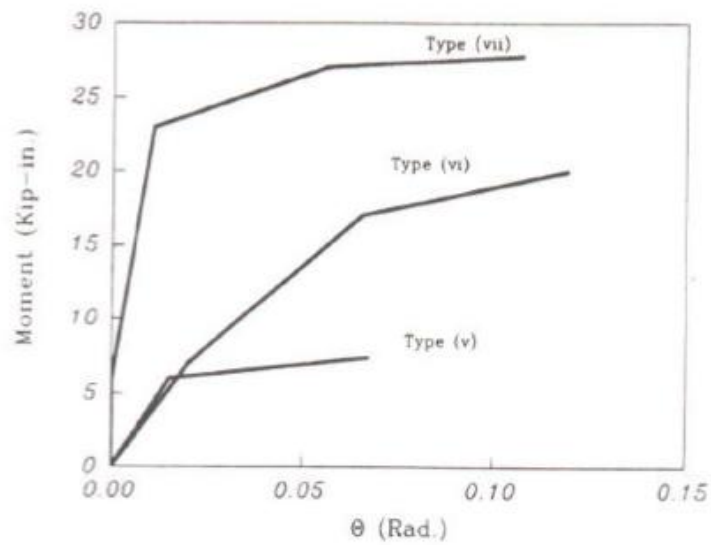


**Figure 1.26.** Linearized moment-rotation curves for the three PFRP frame connections: Types v, vi and vii.

Careful analysis of the three moment rotation curves shown in Figure 1.26 reveals the following facts: 1) the behavior of the three connections was "near-linear" up to about 80% of the ultimate moment capacity; 2) a premature failure of connection *Type v* was due to the duplicating metallic connection detail; 3) the use of the universal connector improved greatly both the overall stiffness and the ultimate flexural strength of the two *UC* connections (*Types vi* and *vii*); 4) a complete fixity was achieved in the initial loading history of connection *Type vii* by using a combination of bolts and high-strength epoxy adhesive

In addition, the following experimental information is important for the structural engineer in the design and the selection process of PFRP frame connection details including: a) the ultimate capacity of the connection; b) the service and the ultimate deformation of the connection. This rotational information can be obtained using both the average rotational stiffness ( $K_a$ ) and the ultimate angle of rotation ( $\theta_u$ ). For moderate loading conditions, an initial rotational stiffness ( $k_i$ ) can be used (*Gerstle* [24], *Bank & Mosallam* [1]).

#### 1.2.2.2. Evaluation of Mechanically Fastened UC Exterior Flexible Connections

As an extension of this program, a new flexible "seated" detail of a beam-to-column connection was evaluated in 1993 by *Zahr et al.* [25]. Details and test setup of this connection are shown in Figures 1.27 and 1.28, respectively.



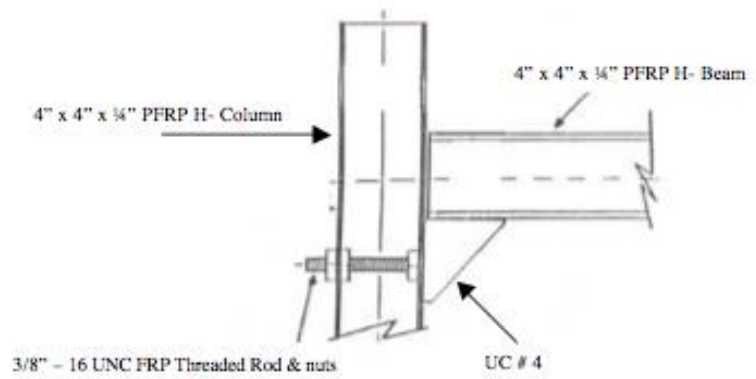


**Figure 1.27.** Details of the PFRP flexible connection (*Type viii*).



**Figure 1.28.** UC PFRP "Flexible" frame connection test setup [Zahr et al. (1993)].

The connection was tested under quasi-static loading regime. The failure was due to the large deformation on top side (tension) of the connection. As expected, and due to the flexible nature of this connection detail, as the load increased, a large horizontal relative rotation between the beam and the column flange was observed (*acting as a hinged support as intended*). The ultimate failure of the connection was due to a local failure of the web/flange junction at the top of the open-web H beam (high tensile stress concentration). This mode failure provides additional evidence of the importance of using reinforcing details such as threaded rod/nut system (*Mosallam* [14]) or transfer members such as angles at the junction with high stress concentration (*Bank and Mosallam* [8-10]). Figures 1.29 and 1.30 present the experimental and bi-linear representation of the moment-rotation behavior of this flexible detail.

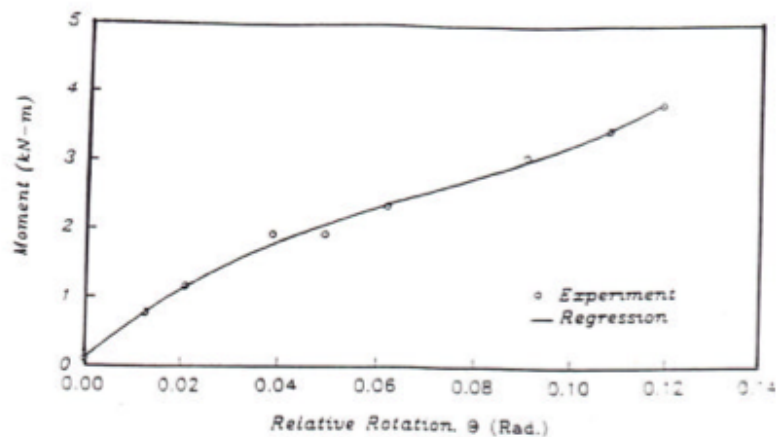


**Figure 1.29.** Experimental moment-rotation curve for UC PFRP flexible frame connection.

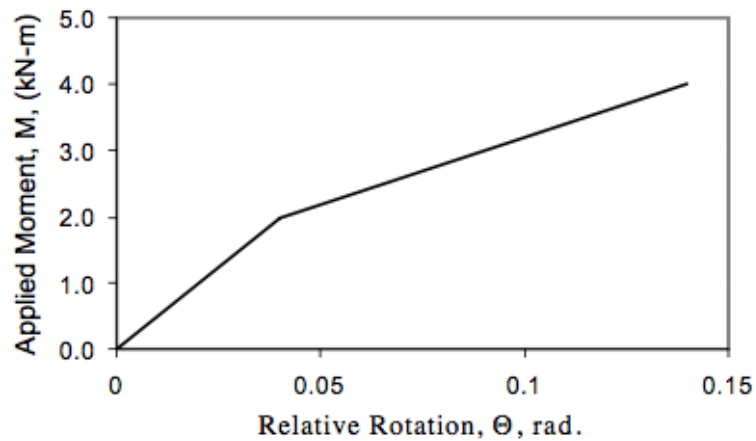


**Figure 1.30.** Bi-Linear representation of the experimental moment-rotation curve for UC PFRP flexible frame connection.

Comparing the stiffness and strength information presented with the results of connection details *Types vi* and *vii*, it can be seen the great difference in behavior. For example, the initial stiffness of this flexible detail is about 39% of the corresponding stiffness of connection *Type vi*, and about 1.2% of the initial stiffness of connection *Type vii* (fixed vs. hinged). This type of connection has negligible moment capacity of 0.45 kip-in (0.051 kNm) as compared to 20.50 kip-in (2.31 kNm) and 28 kip-in (3.36 kNm) of connections *Types vi* and *vii* discussed earlier. For this reason, this detail is the recommended shear type connection.

### 1.2.2.3. Quasi-Static and Cyclic Behavior of Interior PFRP Frame Connections

In 1999, a comprehensive program to evaluate the structural performance of different types of interior PFRP frame connections was conducted by *Mosallam* [23]. In this study, several full-scale cyclic tests were conducted on several pultruded-framing elements. This included box and H-beam profiles with different sizes. The emphasis of this study was on interior framing connections with both flange and web attachments. In addition to high-strength adhesives, both FRP and steel mechanical fasteners were studied. Bolted-only, adhesively-bonded-only and combined-joint details were evaluated using both metallic and non-metallic bolts. Strain, deflection, and load information were collected using a computerized data acquisition system. In particular,  $M-\theta$  and  $P-\delta$  hysteresis curves were developed and analyzed. For FRP mechanical fastener bolted-only connections, a common mode of failure was observed for all specimens. This was a combination of bolt thread shaving and flexural fatigue-type failure of pultruded threaded rods. Other local failures of the pultruded thin-walled beam sections were observed at the ultimate moment. Delamination cohesive failures were also observed for adhesively bonded connection details.

The connecting elements used in building the connection specimens included unidirectional pultruded angles, *Universal Connectors (UC)* and *Continuous Universal Connector (CUC)* as shown Figure 1.31.

Figures 1.32 and 1.33 show the typical test setup for interior and exterior connections, respectively.

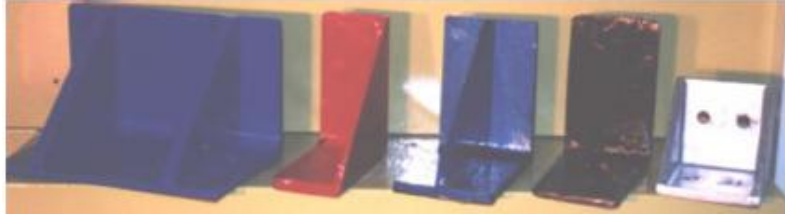


**Figure 1.31.** Continuous Universal Connector (*CUC*).

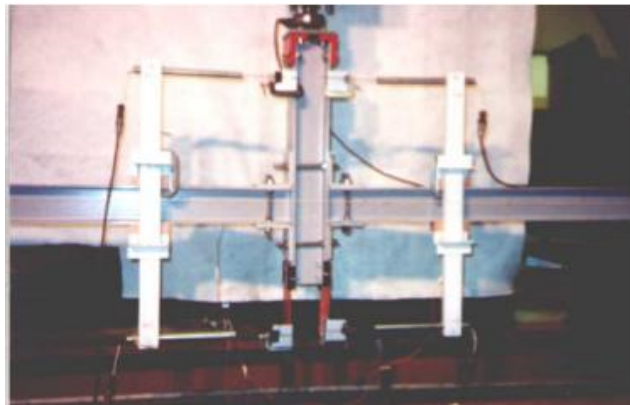


**Figure 1.32.** Test Setup for Interior Connections.



**Figure 1.33.** Test Setup for Exterior Connections.

### 1.2.3. Mottram et al. (1994-1999)

In 1994, *Bass and Mottram* [26] presented experimental results of five steel-like flange-crested sub-assemblies. Commercially produced pultruded profiles, similar to those tested by *Bank et al.*, were used. Figure 1.34 shows the different details tested in this program. Of the five full-scale interior connection tests, three major-axis (i.e., the beam connected to the column flanges) H-profile connection details were tested. Both steel mechanical fasteners and adhesives were used in building these connections.

In 1996, *Mottram and Zheng* [27] presented a comprehensive state-of-the-art review on connection design for pultruded structures. In this review, the researchers divided the test program into two connection groups similar to the classification adopted by the steel industry (AISC-LRFD). These two groups are: *Type I* - Pinned Connections and *Type II* - Semi-rigid Connections.

- ***Type I (Pinned) connection details:*** three types of connecting regimes were tested; namely, i) bolted- only, ii) bonded-only, and iii) combined bolted/bonded connection detail. All connection details were similar to those recommended by the Strongwell Design Manual [5] as shown in Figure 1.35.

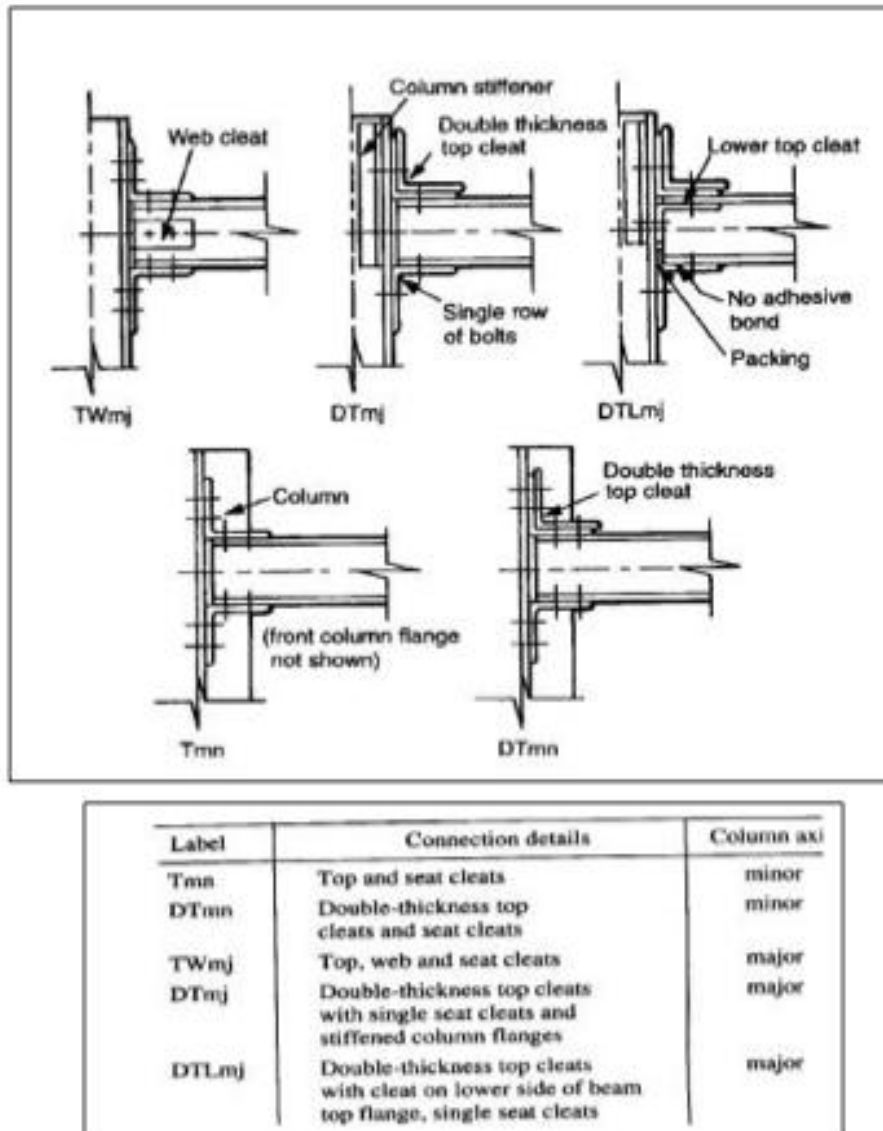
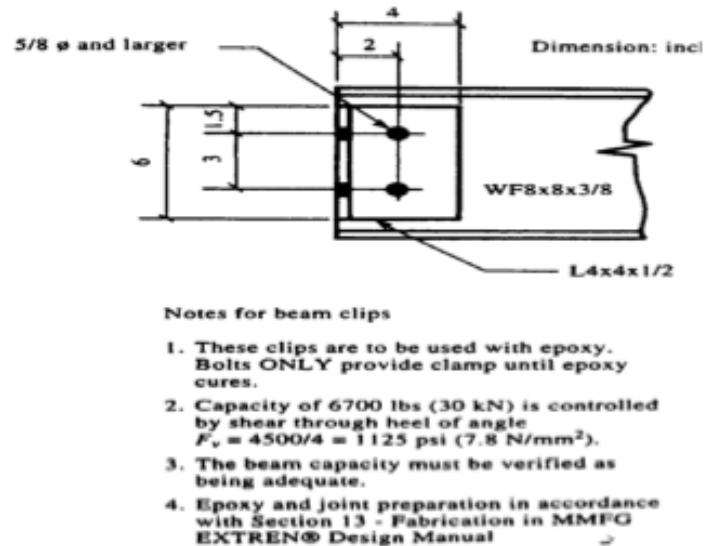


Figure 1.34. Interior Frame Connection Details.



**Figure 1.35.** Pre-1995 Strongwell Design Manual Connection Details Tested by Mottram & Zheng.

In general, the major function of these connections was to transmit the shear forces from beams to column. However, and as indicated from the experimental results, pinned connections had a limited capability to transmit bending moments to the column. A sudden adhesive failure was observed for bonded-only connection details at a relatively low load level.

Based on the experimental results, *Mottram & Zheng 1996* [27] recommended avoiding the use of adhesives as the sole connecting media. It was also concluded that when beams are connected to the column web (minor axis attachment), relative rotation would decrease due to the elimination of the deformation resulting from the prying action when connecting the beam to the column flanges. This is particularly significant for



commercially produced unidirectional open-web pultruded profiles where minimum fiber continuity exists between the web and flange reinforcements.

- **Type II (Semi-rigid) connection details:** the second group tested by *Mottram & Zheng* in 1996 was classified as *Type II* or “semi-rigid” connection details. A total of five full-scale connection specimens were tested. Both adhesives and metallic mechanical fasteners were used. In particular, the authors used double unidirectional cleat angles (Figure 1.36) to increase the flexural strength of these connections.

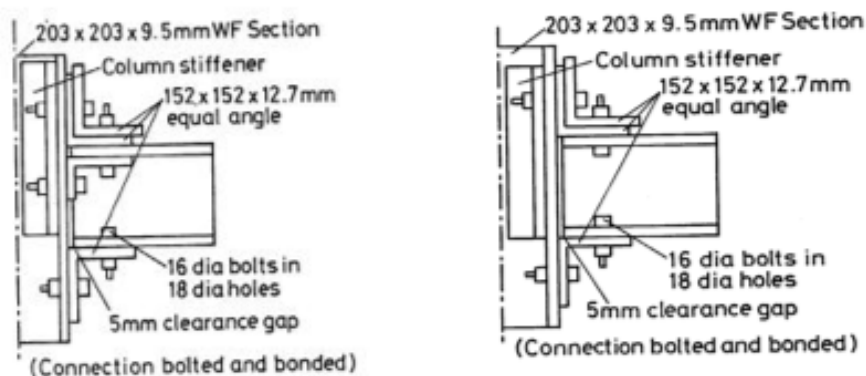


**Figure 1.36.** Mottram Double Cleat Angle Details.

Again, the fibers in both angles were running in the wrong direction, and the only addition was the increase of the matrix cross-section by doubling the thickness of the cleat angles (in their case Isophthalic polyester). For the same reason, the same expected delamination failure of the top cleat occurred. This common type of failure for steel-like connections was described in detail by *Mosallam* [14]. The same stiffening approach

was adopted by *Sanders et al.* [28] in their experimental study on the behavior of adhesively bonded "steel-like" pultruded connections.

As compared to other composite/composite connection details, this type of connection exhibited a relatively lower strength and rotational stiffness up to failure. The first observed localized failure was due to flexural rupture of the beam's top flange at the location of the single row of steel bolts. There are several disadvantages of using this hybrid connection detail (metallic/composite), including:

- limitation of usage in a corrosion or electromagnetic environments;
- mechanical properties mismatch (both short- and long-term) between steel and composites;
- thermo-mechanical properties mismatch including the coefficient of thermal expansions of metallic and non-metallic connection components.

*Mottram & Zheng*, in 1996, tested two other "steel-like" connection details [27]. The first connection detail was identical to that presented and tested by *Mosallam et al.* [12-15].

In this detail, in order to avoid the inherent premature local failure of the column section at the connection zone, these researchers adopted the recommendations given by *Mosallam* in the above mentioned studies concerning the use of prestressing double-nut threaded rods connecting the two flanges of the column at the connection zone.

In an effort to increase the rotational stiffness of the connections and to overcome the premature failure of the connecting elements, *Mottram & Zheng* [1996] used steel

angles and added a stiffening detail, which was proposed and validated by *Mosallam* in 1994. This steel/composite detail is shown in Figures 1.37-a and 1.38.

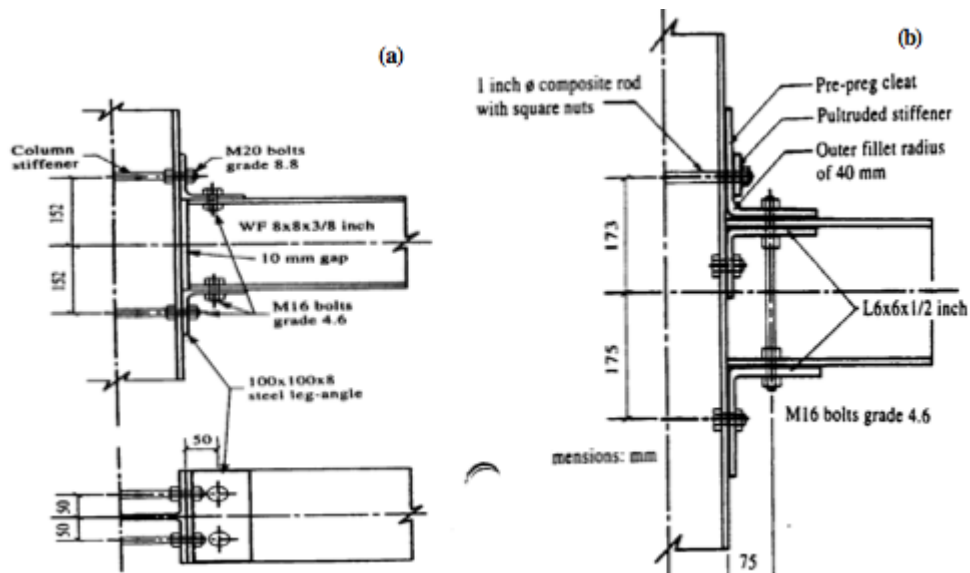


**Figure 1.37.** a) Steel/Composite Detail; b) Semi-rigid Composite Detail.

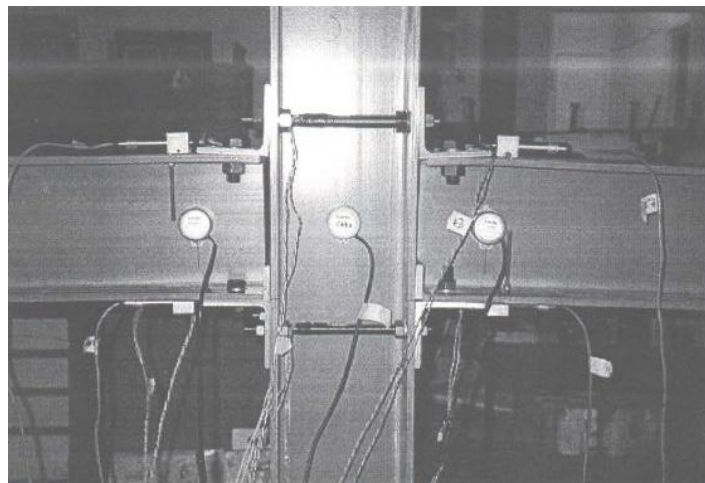


**Figure 1.38.** Composite/Steel Connection Detail STmj (Deformed Shape) [*Mottram (1999)*].

Mechanical behavior of web-flange junctions of thin-walled pultruded fiber-reinforced polymer profiles: an experimental and numerical evaluation.

Based on this study, the authors reached the following conclusions:

- (i) define standard definitions and design parameters for connection design of pultruded composite structures;
- (ii) develop standard test methods to determine connection properties under both short- and long-term loading conditions;
- (iii) consider new connection pieces and/or connection details, such as the *UC* developed by Mosallam that will ensure a connection with adequate strength and stiffness for primary pultruded load-bearing frame structures.

#### **1.2.4. Smith et al. (1996-1999)**

In 1996, *Smith et al.* [29] presented a study on the behavior of exterior beam-to-column connections using both pultruded rectangular tubes and I-profiles. The study focused on the static behavior of two full-scale connection details. The testing protocol followed that adopted by *Mosallam* in 1990 as shown in Figure 1.39. The two pultruded cross sections used in building the full-scale connection specimens are shown in Figure 1.40.

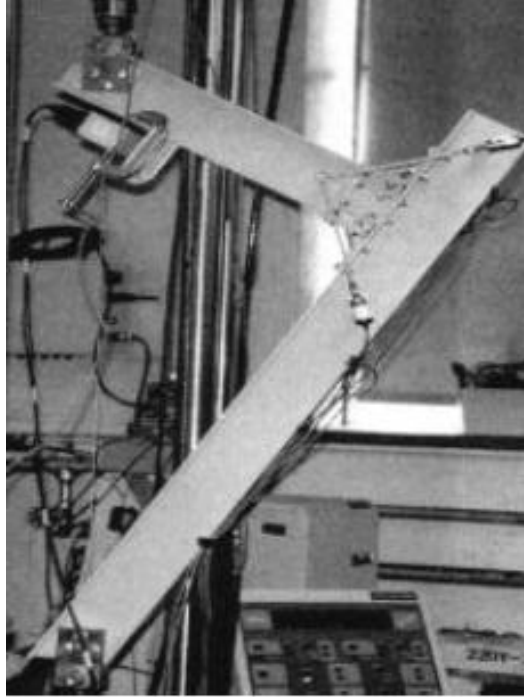


**Figure 1.39.** Smith et al. Test Setup (1996).

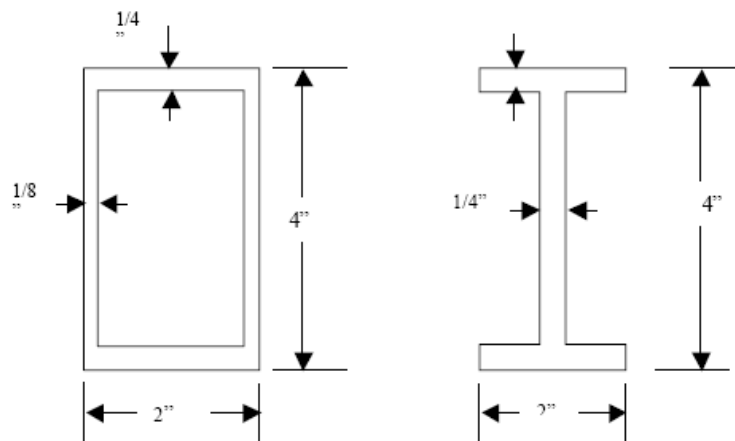


**Figure 1.40.** Geometry of the I-Beam and Box Pultruded Profiles [Smith et al. (1996, 1999)].

#### *1.2.4.1. I-Beam: Standard Connection Detail*

Two connection specimens were fabricated and tested. The failure modes of the two specimens were similar. The failure was initiated at the column face of the clip angles as the outer surfacing veil delaminated from the uniaxial reinforcement region. Immediately following this local failure, the unidirectional top angle failed resulting in collapse of the frame.

#### *1.2.4.2. I-Beam: Thick Seats Connection Detail*

This detail was similar to the standard connection detail reported earlier. The result of the first test indicated that the bottom seat pultruded angle contributed the overall stiffness of the connection. For this reason, a thicker pultruded angle was used in this detail. Again, the reader should be aware of the fact that the fibers are still running in the wrong direction and that the stiffness increase was gained by increasing the thickness of “unreinforced” plastic section. A slight increase in the ultimate moment capacity of the connection was also reported. However, this detail did not solve the problem associated with premature failure of the open web pultruded sections of both the column and the beam element due to the lack of adequate fiber continuity between the flanges and web elements of the commercially-produced I-profile as mentioned earlier. For this reason, extensive cracking along the column web-flange interface was observed. It should be noted that there was a direct relationship between the overall stiffness of the connection

and the individual stiffness of the connected member. The failure mode of this detail was sudden and ultimately occurred at the “thick” top angle as shown in Figure 1.41.

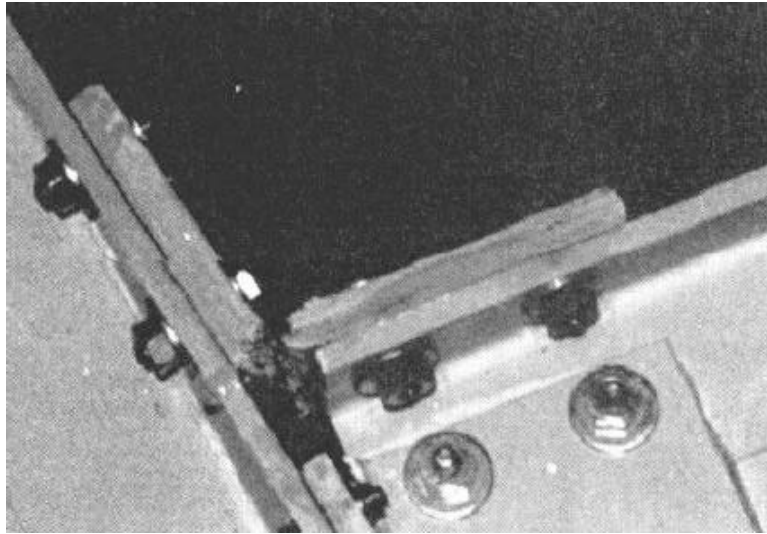


**Figure 1.41.** I-Beam: Thick Seats Connection Failure [Smith et al. (1999)].

It really does not matter how stiff the connecting element is as long as the individual members exhibit flexible behavior whether due to inherent low modulus or to faulty member fiber architecture design (as in the case of unidirectional (90°) pultruded angle connectors used in this detail). This will be clearly proven by observing the behavior of the next connection detail, where steel angles with higher stiffness were used. In addition, it should be noted that only a single connection test was conducted.

#### 1.2.4.3. I-Beam: Steel Connection Detail

In this test, two connection details were tested. The sections of both column and beam were pultruded I-profiles. The beam was connected to the column by two mild steel angles. As expected, the overall stiffness of the connection was increased due to the higher stiffness of the steel angles.

The ultimate moment capacity was also increased. The failure was in the form of separation of the column inner flange from the adjacent web interface. This failure mode should be avoided. In joint design for other materials such as steel and concrete, designers follow a concept called the “weak beam/strong column” concept. The idea is to ensure the occurrence of the ultimate failure away from the column and the joint region. Preventing this type of column failure, as reported in several papers by Mosallam, can be accomplished by introducing a prestressing threaded rod elements to avoid the inherent premature failure of web/flange junctions of the commercially produced open-web pultruded sections. Another important problem associated with this steel/composite hybrid connection was the mechanical and thermal properties mismatch ( $E_{\text{steel}} = 29 \times 10^6$  psi vs.  $E_{\text{FRP}} = 2$  to  $3 \times 10^6$  psi). This can result in both short- and long-term serviceability and strength problems.



#### 1.2.4.4. Box: Standard Connection Detail

This connection detail is composed of two 3" × 3" × ¼" (76.2 mm × 76.2 mm × 6.35 mm) equal-leg unidirectional pultruded angles placed at the top and bottom of the FRP box beam. Two connection specimens were tested in this program. A combination of adhesives and steel bolts was used. In addition, two side plate elements were attached to the sides of both beam and column as shown in Figure 1.42. The plates were commercially produced unidirectional plates with ¼" (6.35mm) thickness. Failure of this detail was sudden with no warning. The failure was initiated by a brittle fracture of one of the side plates at the bolt hole closest to the facing flange. This failure was propagated along the entire plate resulting in a complete failure of one of the side plates and then of the top unidirectional pultruded angle as shown in Figure 1.42.

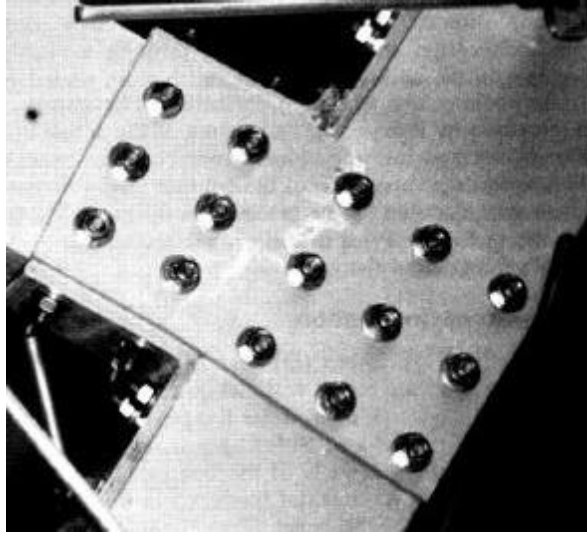


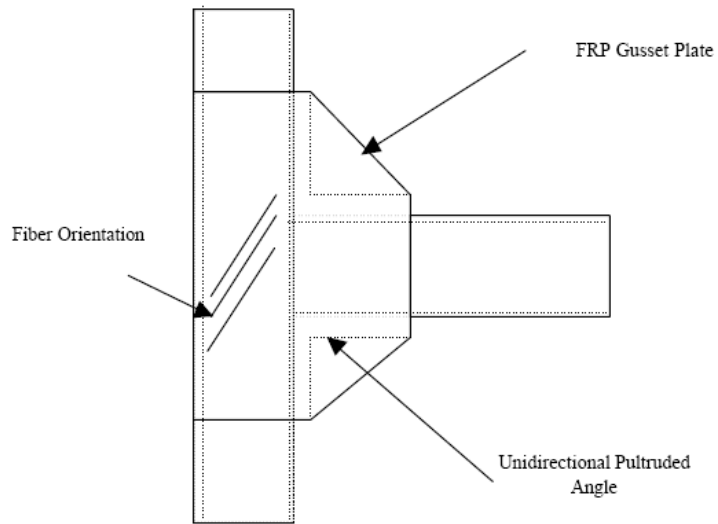
**Figure 1.42.** Standard Box Connection Detail [Smith et al. 1996, 1999].

The failure mode of the second specimen occurred at the beam side wall. The side wall separated completely from the rest of the beam member leading to immediate failure of the pultruded angle. The authors attributed this type of failure to a combination of a relatively thin side wall thickness of the tubular profile as well as to the inadequacy of the uniaxial reinforcement at this region.

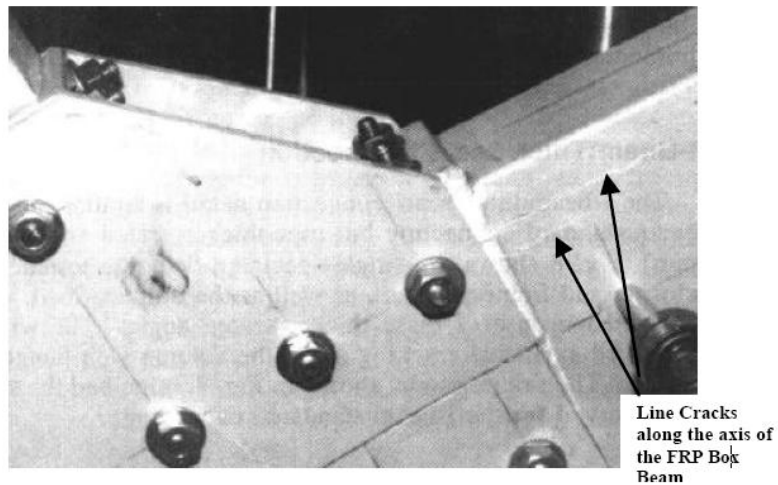
#### *1.2.4.5. Box: Gusset Connection Detail*

The detail of this connection is shown in Figure 1.43. In addition to the two top and bottom unidirectional angles, two side pultruded gusset plates were added. The plates were bolted via steel bolts to the sides of the box beam and column sections. The gusset plates were aligned so that the fibers are running at 45° relative to both

the pultruded box beam and column axes. Test results indicated that these plates contributed significantly to the connection stiffness (a 30% increase as compared to the standard box connection detail described earlier). In addition, the ultimate moment capacity of the connection was increased. The mode of failure was similar to the standard connections initiated by a tensile failure of the sides of the beam box section at the top of the beam side as shown in Figure 1.44. The longitudinal cracks propagated along the length of the beam section. This local failure was expected due to the unidirectional nature of the pultruded box beam and the mechanical property mismatch of the steel bolts and the pultruded composite materials. When compared to all other connection details tested by *Smith et al.* in 1999 [30], this connection detail achieved the highest opening stiffness of 3,100 kN-m/rad. The ultimate moment capacity was 5.80 kNm.



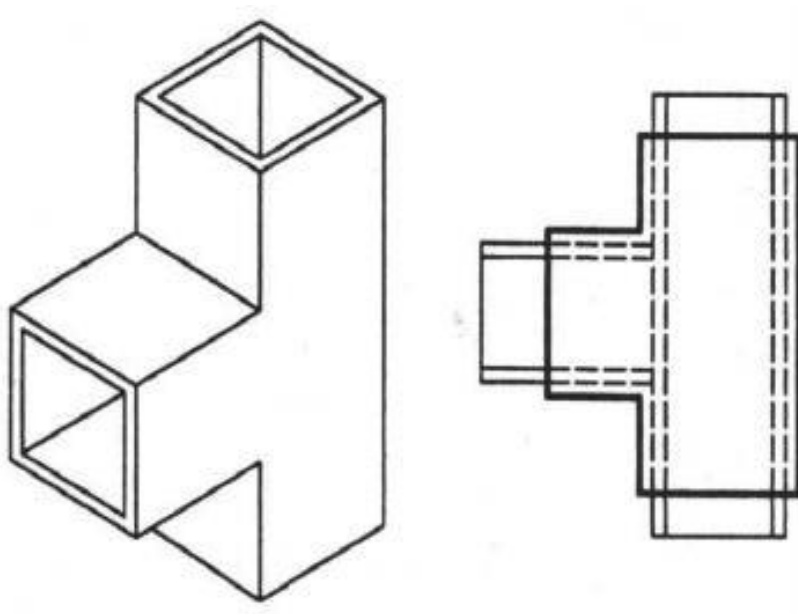
**Figure 1.43.** Details of the Gusset Connection Detail [Smith et al. 1999].



**Figure 1.44.** Local Failure of the FRP Gusset Plate Connection Detail [Smith et al. 1999].

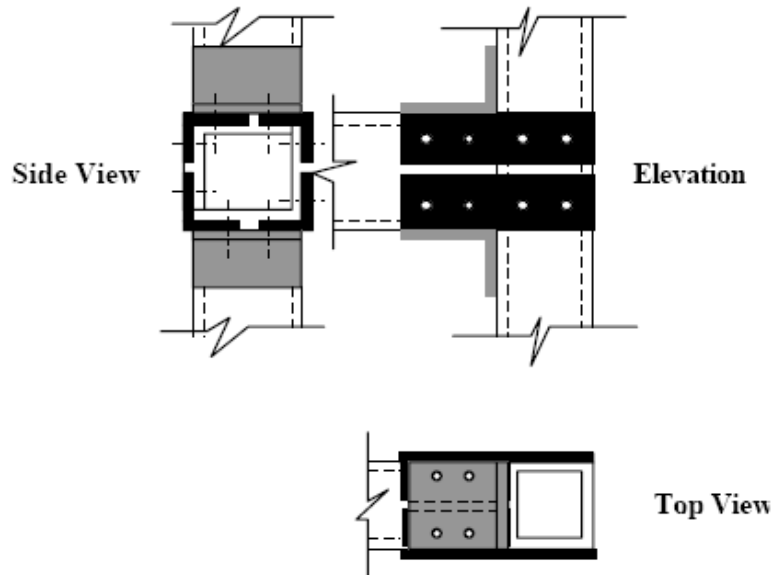
#### 1.2.4.6. Box: Cuff Connection Detail

Figure 1.45 shows a conceptual design of what is called a cuff connection. *Smith et al. 1999* suggested the use of this type of connection. They recommended this part to be fabricated as a single monolithic unit fully utilizing the entire column section. The primary fabrication difficulty of bolting closed section connections would be resolved by using the boltless nature of the proposed cuff connector. Ideally, using this connector, the beam and column can fit into the hollow section and then be bonded using epoxy adhesives without the need of mechanical fasteners. However, no prototype for this connection was reported by *Smith et al.* [30].



**Figure 1.45.** Idealized Cuff Connection. [*Smith et al. (1999)*].

Figure 1.46 shows the closest attempt to the proposed cuff design. A built-up cuff section was constructed by using four unidirectional pultruded angles. One leg of these angles was cut and cut portions were attached to the column side wall by means of two steel bolts at each side of the column. At the beam section, the complete two-leg angles wrapped the outer box beam side and top flange as shown in Figure 1.47. The legs attached to the top and the bottom flanges of the box section were connected to the column inner flange via bolted pultruded angles. The specimen was subjected to a quasistatic loading regime until failure. The opening stiffness of this connection was about 42% of the corresponding stiffness of the FRP gusset connection detail described earlier. However, this detail achieved the highest ultimate moment capacity among all connection details tested in this program with an ultimate value of 6.2 kNm (54.87 kip-in). The ultimate mode of failure was in the form of web-flange junction separation of the upper portion of the pultruded box column as shown in (Figure 1.47). As shown in this figure, one side wall separated from the facing flange and the other side wall also separated from the back flange. This typical mode of failure was reported earlier for open-web pultruded profiles such as H-sections due to the lack of fiber continuity between the webs and flanges (*Mosallam, 1994*). As discussed earlier, this premature failure could have been avoided by using *Mosallam's* recommendations for using a threaded rod prestressing rod extended through the box section at the connection zone.



**Figure 1.46.** Details of Built-Up Cuff Connection [Smith *et al.* (1999)].

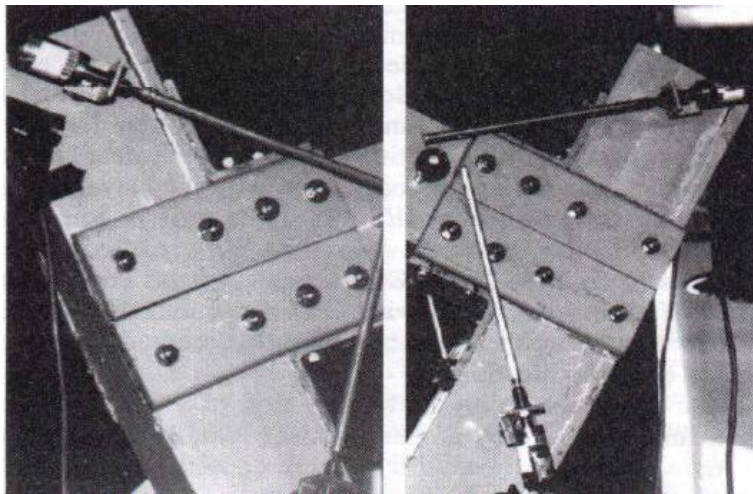


**Figure 1.47.** Ultimate Failure mode due to web/flange separation at the column section [Smith *et al.* (1999)].

#### 1.2.4.7. Box: Steel Connection Detail

This hybrid connection detail is identical to the standard box section details except that the PFRP plate was replaced with steel plate as shown in Figure 1.48. While the highest opening stiffness was achieved by the FRP gusset detail, this connection detail achieved the highest closing stiffness of 1.300 kN m/rad. However, for some reason, no value was reported for the opening stiffness of this connection detail, which is expected to be relatively higher as compared to other details due to the major increase in the stiffness resulted from the use of the steel plate. The failure mode was a combination of both localized beam failure and web/flange junction separation of the column-facing flange. Due to these premature local failures of the unidirectional pultruded composite profiles, the ultimate moment capacity was slightly lower than the ultimate moment value achieved by FRP plate detail. Based on the poor performance of this hybrid detail, it was concluded that, regardless of the added capacity of the individual connection elements, this detail did not succeed in overcoming the weakness of the local failure of the commercially produced unidirectional pultruded profiles. Unless the load path is modified or load is redistributed, the steel detail will have a limited strength contribution. However, an appreciable increase in the connection rotational stiffness can be achieved by using metal parts. As mentioned earlier, the use of metal parts is associated with several problems including lower resistance to corrosion environments as compared to FRP materials, and the mechanical incompatibility



due to both the mechanical and thermal properties mismatch.

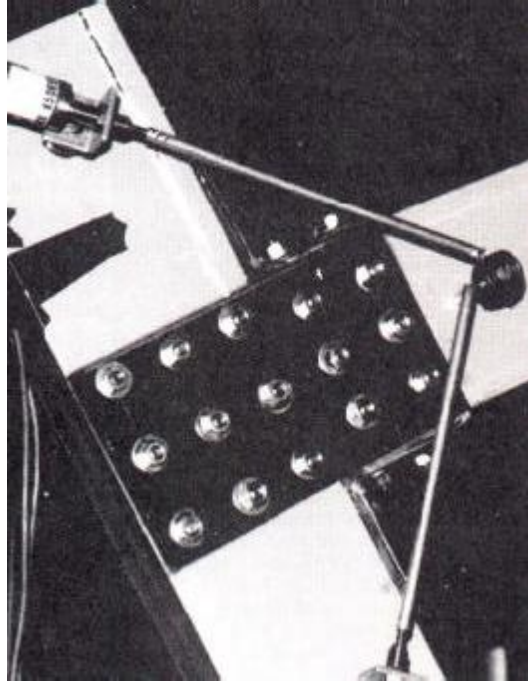


**Figure 1.48.** Box Steel Connection Detail (*Smith et al. 1999*).

### 1.2.5. Bank et al. (1996)

*Bank et al.* in 1996 extended the work initiated by *Bank & Mosallam* in 1990 [1]. In this program, three connection details were designed and developed. A total of five full-scale quasi-static tests were performed to evaluate the performance of each new design. All the connections tested were fabricated from  $8 \times 8 \times 3/8$ " (203.2 mm  $\times$  203.2 mm  $\times$  9.53 mm) commercially produced unidirectional E-glass/vinylester H-profiles manufactured by Creative Pultrusions Co., U.S.A.. The test setup followed the earlier work performed by *Bank & Mosallam* in 1990 [1] and *Bank et al.* in 1992-1994 [11,15].

#### 1.2.5.1. Multicell molded connector detail

A hand-fabricated, E-glass/polyester, connecting element was fabricated using hand lay-up. The connector is composed of three separate parts a square and two triangles. The three parts are then connected together to produce the *multicell connector*. The beam and the column pultruded members were connected together using two connectors placed at the top and at the bottom of the beam flanges. In addition, the epoxy is subjected to not only shear, but also tensile and compressive stresses. For these reasons, these details are not recommended. This connection detail is shown in Figure 1.49.

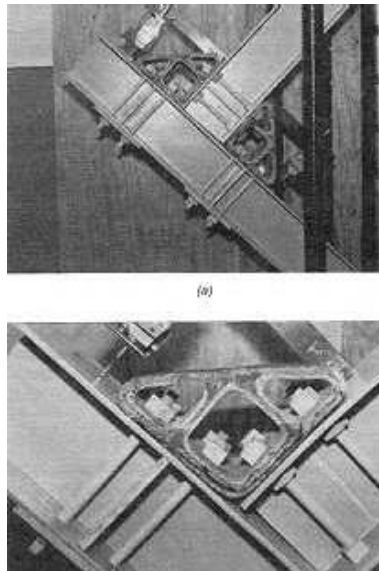


**Figure 1.49.** Photographs shown the *multicell molded connector* detail.

As described by the authors, this connection detail was “massive” as compared to three connection details reported earlier by *Bank et al.* [15]. During the test, no failure was observed to the multi-cell connectors. However, local failure was due to damages of the FRP threaded rods and nuts. The pultruded threaded rods failed by “threaded stripping or shaving” and by bending failure in the connection zone. This typical mode of premature failure of FRP pultruded threaded rods was observed during other research investigations [15-23]. Due to the use of the prestressing threaded rods/nuts system, no failure of the pultruded open-web beam or column was observed. Adhesive local failure to one of the bonded FRP plates occurred.

### 1.2.5.2. *Back-to-back 6" (152.4 mm) Pultruded H-section*

This connection detail was constructed using two pieces of 6" H-sections that were cut at 45° with respect to the beam axis (Figure 1.50).

The two pieces were then bonded back-to-back using EPON™828 epoxy adhesives (produced by Shell) to form a rightangle "brace" as shown in Figure 1.51. The two bonded pieces were attached to the 8" (203.2 mm) H-beam and column flanges using two ¾" (19 mm) FRP treaded rods and FRP molded square nuts at each side of the connection. As shown in this figure, the fiber orientation of these pieces is not optimum for the connection load path. The connection specimen was subjected to a similar loading regime. It is clear from Figure 1.50 that the lack of fiber continuity between the flange and the web of the right angle H-profile piece contributed to the development of this premature local failure. Test results indicated that this detail performed very poorly and the ultimate mode of failure was due to through-the-thickness tensile failure of the wide flange section used to construct the right brace as shown in Figure 1.51. The ultimate moment capacity of this connection was only about 14% (40 kip-in) as compared to the multi-cell connection detail described earlier.

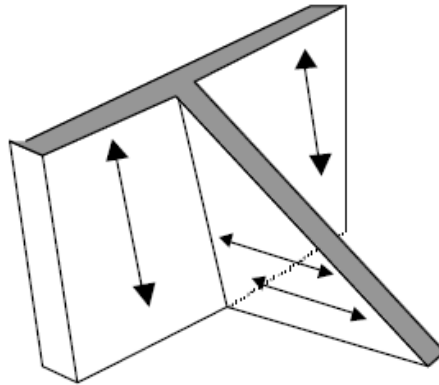


**Figure 1.50.** 6" H-sections Cut @ 45° With Respect to the Beam Axis.

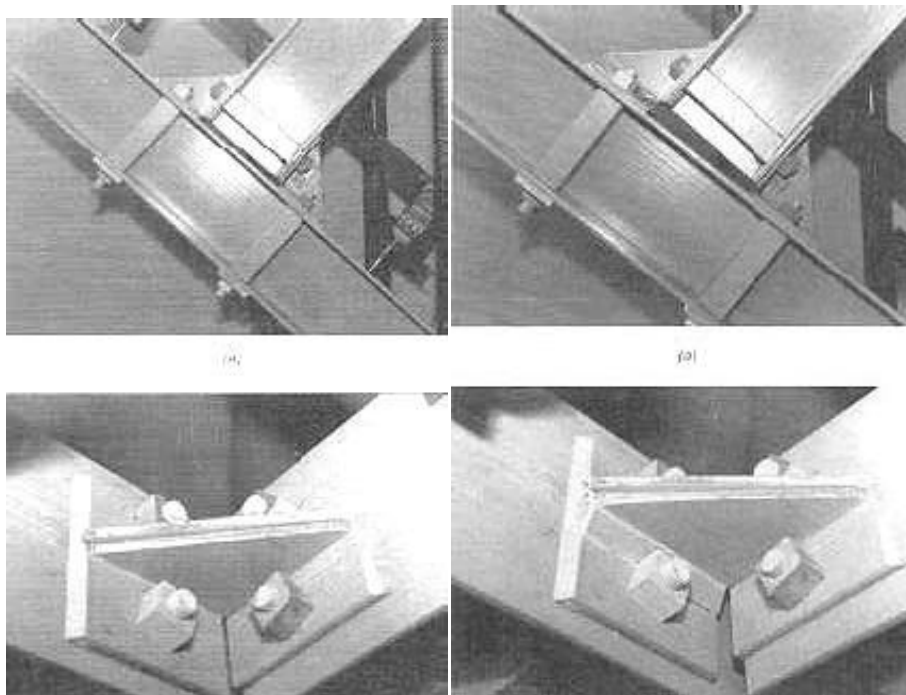


**Figure 1.51.** Back-to-back 6" brace connection detail.

### 1.2.5.3. 6" × ½" (152.4 mm × 12.7 mm) Wrapped Angle Connection

Figure 1.52 shows the details of this connection specimen. The connecting elements were constructed by wrapping a unidirectional E-glass/vinlyester pultruded 6" × ½" (152.4 mm × 12.7 mm) equal-leg angle with two layers of fabric mat (Fabmat™2415). In this case, the open-web pultruded angles were converted to a closed thin section with diagonal fibers following the load path. These closed section angles were connected to the flanges of the H-beam and column using ¾" (19 mm) pultruded threaded rods and molded square nuts at each side of the joint. The failure of this detail occurred in two interrelated stages. Initially, and under a relatively low load level, the diagonal membrane of the bottom (compression) wrapped angle buckled locally. This can be attributed to the stiffness mismatch between the "thicker" pultruded angle with fibers running in the wrong direction and the "thinner" membrane wrapped around the angle with fibers following the load path. In this regime, and as the load increased, excessive deformation occurred to the pultruded angle (closing mode) and axial forces developed at the ends of the thin-walled diagonal membrane causing it to buckle. It was expected that this initial mode of failure would be avoided by increasing the thickness of the wrap material and by ensuring complete adhesion between the wrapping materials and the pultruded angle skin. Also, due to the limited area for bolting, only two bolts were used which allowed for more flexibility to the seated wrapped member. In this case, combining both bolts and adhesives may delay the initial

local failure and improve the overall performance of this innovative and simple connection detail. As a result of the initial local buckling mode of failure, the top (tension) brace was activated and performed well reaching an ultimate load of 100 kip-in (11.3 kN-m) with a large plastic rotation. The ultimate failure was due to the failure of threaded rod connecting the top flange of the beam to the inner flange of the column as shown in Figure 1.53. As compared to connection detail *Type iii* tested by *Bank et al.* in 1994, the stiffness and the strength of the wrapped angle detail were slightly less. However, the *Type iii* connection detail was more complicated and composed of several parts.

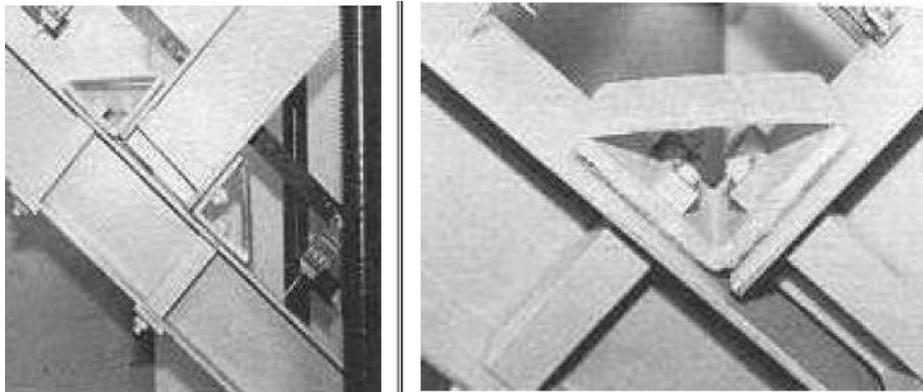


**Figure 1.52.** Wrapped angle detail.



**Figure 1.53.** Local failure of 6" x ½" wrapped angle connection detail.

#### **1.2.6. Turvey (1998)**

In 1998, in *Turvey's* program [31-32], tension, moment/rotation, and uplift full-scale tests were conducted on frame connections for commercially produced pultruded composite frame structures constructed from H-profiles. The test results were analyzed. This work is considered to be one of the comprehensive research programs in the area of pultruded moment frame connections under quasi-static loading conditions. Based on the 4-year test program results, some closed-form formulae were derived which can possibly be used in design of pultruded frame structure connections.

In particular, a total of 29 coupon specimens cut from the webs and flanges of EXTREN™ (product of Strongwell) pultruded profiles were tested under both



tension and compression. This part of the experimental program is always necessary to verify the data supplied by the pultruders on the mechanical properties of the sections. Results of this study showed that the pultruders' information was conservative.

In this program, two series of bolted *beam-to-column connection* tests were performed on different sizes of commercially produced unidirectional H-profiles specimens. Two types of connecting elements were used in these tests. The first connecting elements were comprised of pultruded unidirectional angles while the other tests were conducted on connections with a combination of pultruded angles, pultruded plates, and special resin injected composite elements.

Two test rigs were employed in this program. Figures 1.54 and 1.55 show the two test setups for evaluating the structural behavior of interior beam-to-column connections.

In this program, a total of 7 conventional beam-to-column pultruded connection specimens were evaluated. Three of which with small size H-profiles were used and the specimens were tested in a quasi-static mode as shown in Figure 1.54. Two of the connections tested were web cleat connections while the third was detailed to have both web and flange cleats. The mechanical fasteners used in this study were 10 mm (0.39") mild steel bolts in close tolerance holes. All bolts were torqued to 30 Nm (22.14 lb-ft). The large specimens were tested in the test rig shown in Figure 1.55. In addition, a total of six "unconventional" beam-to-column

details were also evaluated under quasi-static loading conditions. Figure 1.56 shows the cruciform beam-to-column detail. As shown in this figure, the pultruded plates were bolted to the column and beam webs using steel bolts. The plates were cut so that the major reinforcements (pultrusion axis) were at  $\pm 45^\circ$  with respect to beam and column centerlines. It was reported that fabricating this type of detail is cumbersome and that the initial *rotational stiffness* ( $ki$ ) of the connection was somewhat lower than the conventional cleat angle connection detail. In addition, two exterior beam-to-column connections were tested in this program. Figure 1.57 shows the test setup for the exterior PFRP connection evaluation.



**Figure 1.54.** Simply supported beam test rig .

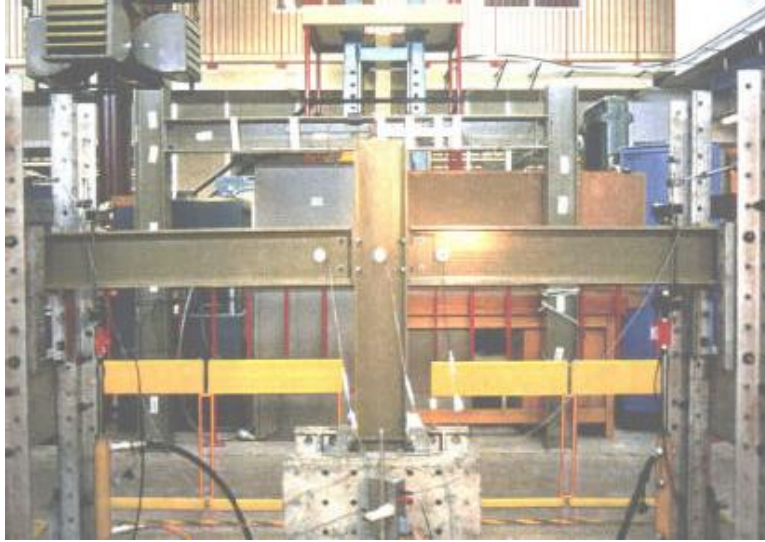


**Figure 1.55.** Sub-frame test rig (double cantilever mode).

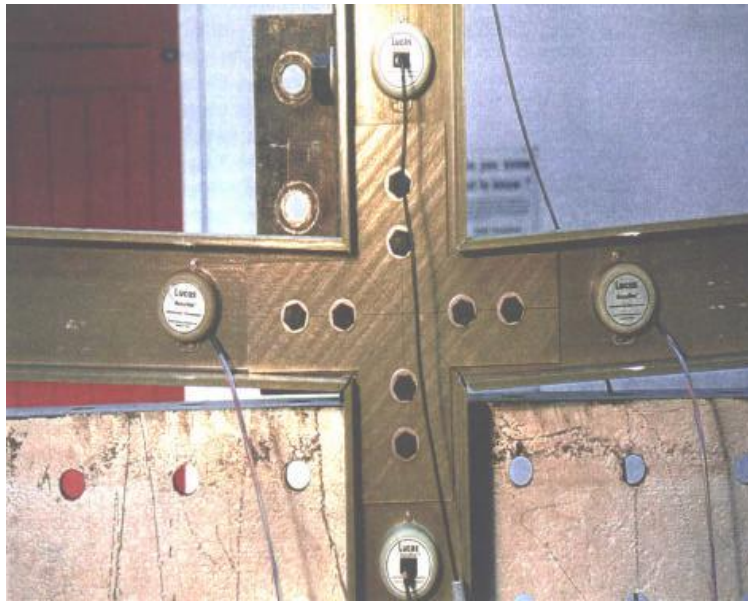


**Figure 1.56.** Cruciform beam-to-column detail.

---

Mechanical behavior of web-flange junctions of thin-walled pultruded fiber-reinforced polymer profiles: an experimental and numerical evaluation.



**Figure 1.57.** Sub-frame test rig for exterior connections (single cantilever mode).

### **1.3. WEB-FLANGE JUNCTION BEHAVIOR RELATED WORKS**

#### **1.3.1. Turvey and Zhang (2005-2006)**

Turvey and Zhang have conducted extensive research on the behavior of the web-flange junction of FRP beams. Their works include investigations into the mechanism of tearing failure [33], the shear strength [34] and the rotational strength and stiffness [35] for the web-flange junction.

In particular, in 2005, Turvey and Zhang [33] presented details of T-section specimens for determining the tensile tearing strengths of web-flange junctions of

two sizes of pultruded glass reinforced plastic GRP wide flange (WF) profiles. EXTRENw 500 series structural grade WF profiles, manufactured by Strongwell at their factory in Bristol, VA, USA, were selected for the tensile tearing strength tests. The size of the smaller profile was 102×102×6.4 mm (nominal dimensions) and the size of the larger profile was 203×203×9.5 mm. These specimens were referred to as I4 and I8 profiles, respectively (Fig.1.58).

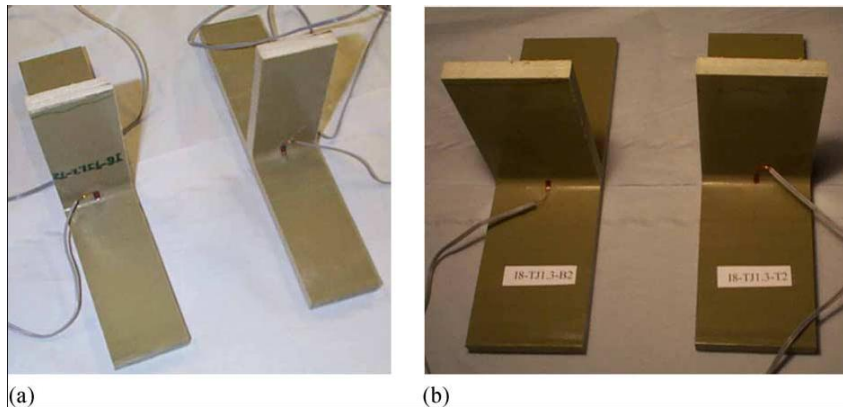


**Figure 1.58.** Pairs of web-flange junction specimens, with strain gauges bonded to the roots of the junctions, ready for testing: (a) I4 specimens and (b) I8 specimens.

Two simple test rigs, used to carry out the tension tests on the web-flange junctions, were described. A total of 43 tension tests were carried out on the web-flange junctions of two sizes of pultruded GRP WF profiles in order to quantify the tensile tearing strength of the junction. It was shown that the tearing strength reduces slightly with specimen length. Moreover, the tensile tearing strengths of the web-flange junctions of the smaller WF profiles were about one-quarter to

one-third greater than those of the larger WF profiles. Comparison of the tensile tearing strengths of web-flange junctions with the tensile strength of coupons cut transversely from the flanges and web of pultruded WF profiles demonstrated that the latter vary from about two to four and a half times the former strengths. It was also shown that failure of the web-flange junction under tension loading arises in a characteristic manner, i.e. as a small inverted 'v' shaped crack at the interface of the CFM and the upper vertex of the triangular core of rovings at the centre of the junction. As the load increased, the shape of the crack changed from an inverted 'v' to an inverted 'y' as a crack starts to extend up to the middle of the web (Fig. 1.59). It was noticed that further increase in the tension load caused the cracks to extend into and along the middle of the flange and up to the middle of the web until failure of the junction occurs.

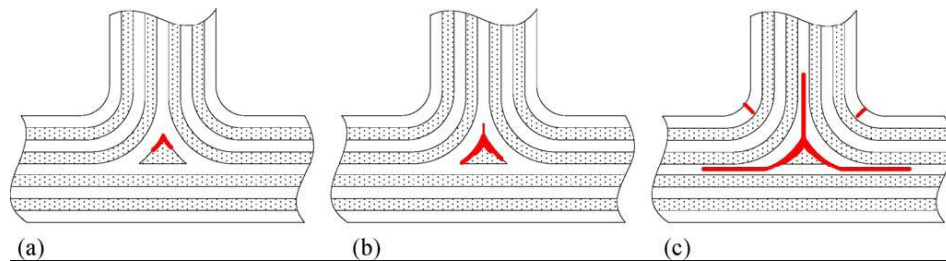


**Figure 1.59.** Sketch of crack initiation and development in the web-flange junction of a test specimen: (a) initial inverted 'v' shaped crack, (b) change to an inverted 'y' shaped crack as the tensile load increases and (c) crack shape at failure with flexural-tension cracks in the outer CFM layers.

It was also shown that the tearing strengths of the junctions of the smaller WF profile were larger than those of the larger WF profile and, moreover, that they

were only about one-quarter to one-third of the minimum transverse tensile strength of the material given the manufacturer's design manual.

In 2006, Turvey and Zhang [34] presented shear tests carried out on the web-flange junctions of two sizes of pultruded GRP WF-profile. Two types of specimen, i.e. un-notched and notched, were tested at three nominal lengths, 25, 40 and 60 mm. It was observed that failure tended to initiate in the roving-rich zone at the core of the web-flange junction.

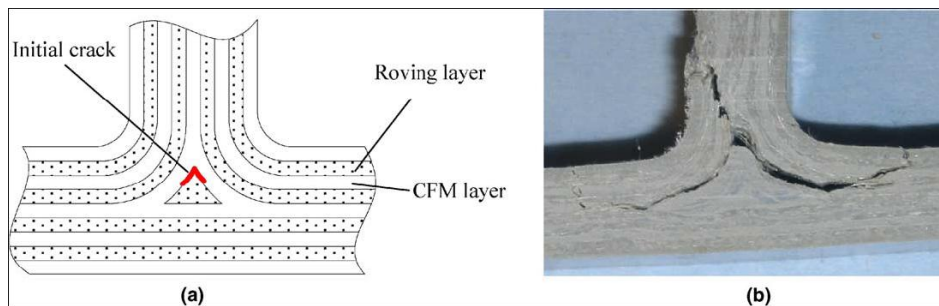


**Figure 1.60.** Sketch of the initial inverted vee crack and (b) typical failure mode observed in unnotched web-flange junction shear tests.

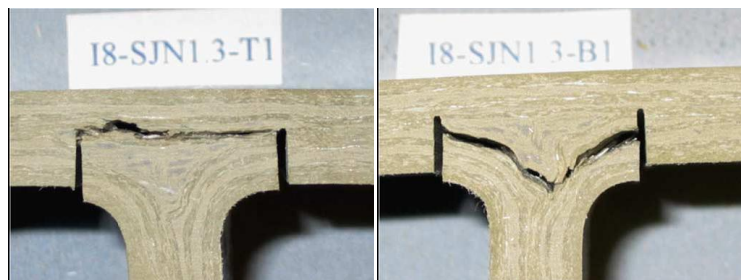


**Figure 1.61.** Shear failure modes of the upper and lower web-flange junctions of 203 × 203 × 9.5 mm pultruded GRP WF profiles observed in notched web-flange junction shear tests.

The shear strengths of the web-flange junctions were quantified and failure modes were identified from the tests. The test results show that the shear strengths of the web-flange junctions were much lower than those obtained from flat V-notched (Iosipescu) coupons. Because of the effect of the bending moment at the web-flange junction it was found that the shear strength increases as the specimen length increases for the tests on the un-notched web-flange junction specimens. The highest average strengths of notched web-flange junction specimens, however, were obtained with the 40 mm long specimens, which were 30% and 16% higher, respectively, than the strengths of the 25 and 60 mm long specimens. It was unclear as to whether or not this observation is significant. The more so, as the highest specimen strength was 24% greater than the lowest strength for the 25 mm long specimens and the corresponding figures for the 40 and 60 mm long specimens were 30% and 56%, respectively. Furthermore, as evident from Fig. 1.60 and similar images taken of other test specimens, there was considerable divergence between the idealised and the real fibre architecture in the web-flange junctions and that is likely to account for the variability in the measured shear strengths. The shear strengths of the web-flange junctions of the notched specimens were shown to be only about one-seventh of the shear strengths of the web or flange material, as measured in Iosipescu tests. Likewise, it was shown that the shear failure load per unit length of the notched specimens was about 50% of that of the un-notched specimens. Finally, it has been suggested that the notched



shear strengths may be potentially useful in design, since they are about 22% lower than the un-notched shear strengths when calculated on the same basis as the un-notched shear strengths.

Moreover, in [35] Turvey and Zhang presented the results of a series of three-point flexure tests on the webs of 12 pultruded GRP 203×203×9.5 mm WF specimens. The majority of the webs of the specimens were subjected to three low load tests under both simply supported and semi-rigid (clamped flange) end conditions.



**Fig. 1.62.** Photograph showing the dual knife-edges loosely clamped to the upper half-flange at each end of the WF specimen.



**Fig. 1.63.** Photograph of the test set up showing the web of a WF specimen with clamped flanges being tested in three-point flexure.

Using equations derived from simply and semirigidly supported beam analyses, the transverse elastic modulus of the webs, and the rotational stiffness per unit length and the rotational initial failure strength of the web-flange junctions were obtained. The tests not only served to quantify the initial failure loads of the web-flange junctions and the ultimate failure loads of the webs, but also the failure modes (Fig. 1.64) of the web-flange junctions and the webs. In the case of the WF specimens with clamped flanges some light was shed on the failure progression, i.e. delamination failure occurred first in the web-flange junctions, followed by

final failure due to flexural tension cracking in the outer CFM layer of the web at mid-span and delamination in the adjacent roving layer.

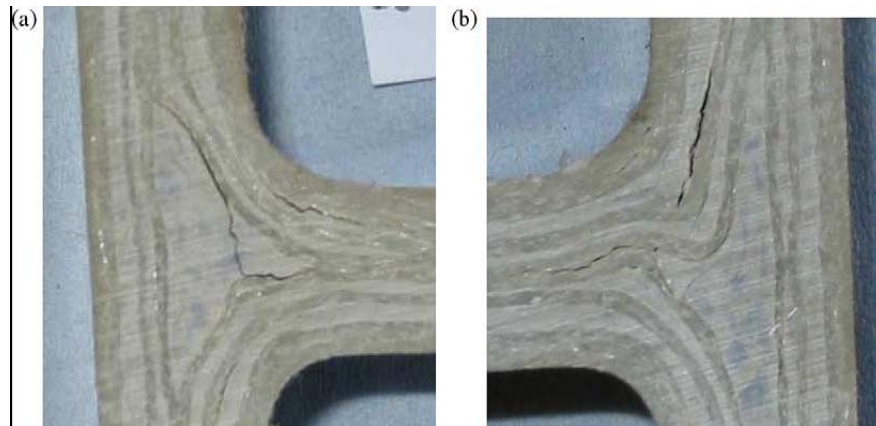


**Fig. 1.64.** Views of delamination cracks in the web-flange junctions of the WF specimen I8-BH1.1-1 with clamped flanges: (a) left hand junction and (b) right hand junction.

The values of rotational stiffness per unit length of the web flange junctions obtained from the tests on the two groups of specimens were not as consistent as the values of the transverse modulus. This relative lack of consistency was attributable to the fact that the fibre architecture in the web- flange junction region was much less ordered than in the central region of the web. The former influences the rotational stiffness per unit length and the latter the transverse modulus.

### **1.3.2. Borowicz and Bank (2010)**

In 2010, Borowicz and Bank [36] presented results of the behavior of pultruded fiber-reinforced polymer I-shaped beams subjected to concentrated loads in the plane of the web. Twenty beams with nominal depths from 152.4 to 304.8 mm were tested in three-point bending with a span-to-depth ratio of four. Load was applied to the top flange directly above the web, 12 without bearing plates and 8 with bearing plates of varying width and thickness. All test specimens failed with a wedgelike shear failure at the upper web-flange junction. In particular, eleven vinylester beams from U.S. manufacturers were tested in three-point bending without a bearing plate. The cylindrical steel load-head applied a “concentrated” load directly to the upper flange of the member. Each of these beams failed with minimal audible cracking (noticeable only just before failure) in a manner consistent with the postmortem photos in Fig. 1.65. A shallow wedge formed at the web-flange junction and thrust downward into the web (Fig. 1.65a). As a result, the web began to split and formed a vertical crack that extended downward into the web. Fig. 1.65b shows the extent of the longitudinal cracking along the beam at the web-flange junction.

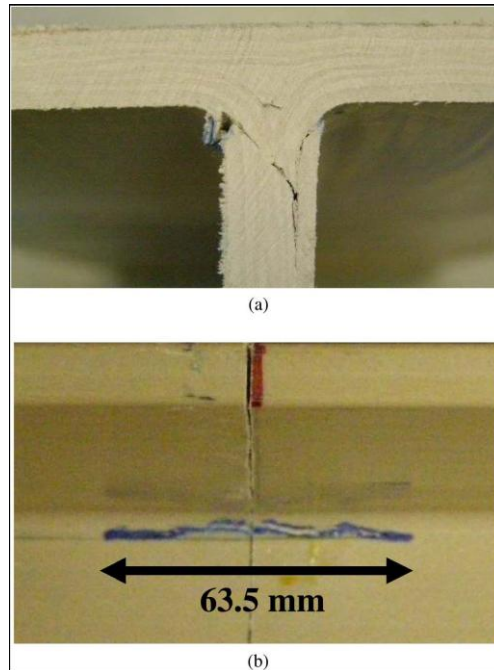


**Fig. 1.65.** SW-W8-VE-NP-4 specimen: (a) wedge failure; (b) longitudinal cracking.

For the beams with no bearing plates, the average length of cracking was 0.33 times the depth of the respective specimens.

A twelfth specimen, FL-I8-PE-NP-13, was tested without a bearing plate. The specimen was from Fiberline Composites, pultruded with a polyester resin, and did not contain continuous filament mats within the interior of the section to provide additional transverse strength and stiffness. FL-I8-PE-NP-13 developed a “wedge” at failure, but there was increased audible cracking before failure and greater longitudinal cracking (219 mm). Fig. 1.66 a shows the failed cross section and Fig.

1.66b shows the extended longitudinal cracking below the toe of the web fillet for specimen FL-I8-PE-NP-13.

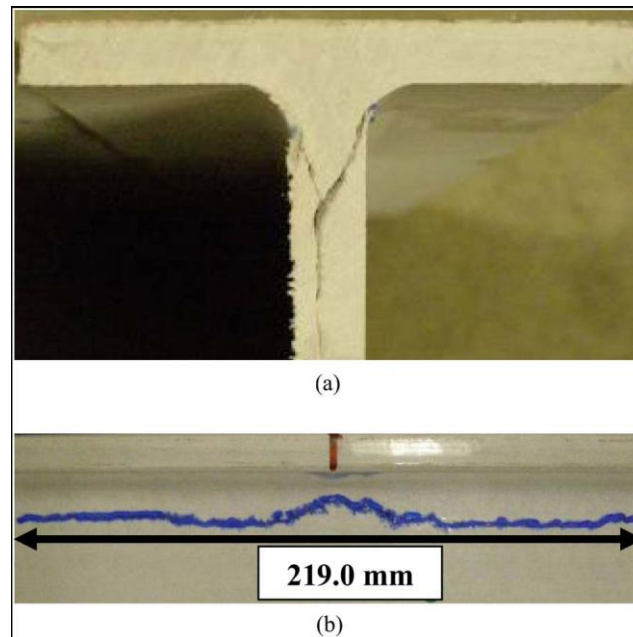


**Fig. 1.66.** FL-I8-PE-NP-13: (a) wedge failure; (b) longitudinal cracking.

Results of these tests showed that the introduction of bearing plates to mitigate the effects of concentrated loads increased the capacity of the beams by 35% or more. Despite this increase in ultimate capacity, the application of concentrated loads to the top flange of an FRP beam (with and without bearing plates) caused failure at average shear stresses 0.20–0.46 the accepted value of in-plane shear strength (69 MPa). The interlaminar shear strength (ILSS) of pultruded materials used in beams was typically 27.6–34.5 MPa (4,000–5,000 psi) and was generally lower than the

ILSS of composite materials made by other processes because of the fiber layup of alternative layers of rovings and mats and the rather high void fraction in these parts (2–3% by volume, typically). Tests also demonstrated that the ultimate capacity of the beams that utilized bearing plates was a function of both bearing plate width and bearing plate thickness. Results of these tests facilitated the development of a design equation to predict the capacity of an FRP beam subjected to concentrated loads in the plane of the web as a function of interlaminar shear strength. Key geometric parameters include the web thickness, length of stiff bearing, member depth, distance from top of flange to the toe of the web fillet, and bearing plate width and thickness. The predicted capacities were 12% conservative on average and minimally dispersed. The equation considers a materials failure at the web-flange junction and is valid for beams up to 304.8 mm in depth.

#### **1.4. DESIGN CODES AND GUIDELINES**

As it is well known, standard engineering guidelines, analytical and design tools developed for conventional materials are not applicable to FRP shapes. For this reason, several technical documents dealing with design equations and methods, material properties and safety factors for pultruded elements have been or being developed in recent years. In particular, the EuroComp Design Code and Handbook [37], published in 1996, provided, for the first time, an independent, practical guidance on structural design of polymer composites.

In 2002, the EN 13706 standard [38] defined two different classes of materials, associated with minimum values of material properties, however, no design guidance was provided in this document.

In 2007, the Italian National Research Council (CNR) published the first Italian design guide (DT 205/2007) for the design and construction of structures made of FRP pultruded elements [39] which is not a binding regulations and is still rather incomplete.

In 2011, the Construction Institute of the American Society of Civil Engineers (ASCE) published the Manuals of Practice (MOP) #102 for the design of FRP composite connections [40]. This manual covers major issues related to the analysis and design of composite joints and frame connections manufactured from



fibre-reinforced polymer composites in general and pultruded composites in particular. Currently, a joint effort between the Pultrusion Industry Council (PIC) and the ASCE Structure Institute for developing American Standards for PFRP structures is underway and will be published in the near future.

Finally, the experience so far gained through the realization of full composite structures in many European countries, as well as the theoretical and experimental knowledge gained in this field, has made possible the recent publication of a new guideline shared by the countries of EC [41]: the “CEN/TC 250/2014 FIBRE REINFORCED POLYMER STRUCTURES: Scientific and Technical Report”, drawn up by the Working Group No. 4 (WG4). This guideline collects a body of rules to be applied to the design and execution of full composite structures, being an expression of the considerable scientific and technological progress achieved by member countries in this field.

The drawing up of this Guideline will facilitate the free movement within the European Community of materials and contractors in the field of composite materials. This field offers all guarantees for a progressive expansion, with interesting consequences of economic nature, favoured by the existence of a body shared rules able to ensure a uniform level of safety.

The CEN-TC 250/2014 report includes all the predictive rules which, being based on the most current worldwide scientific literature, can be considered as the most advanced and reliable for the design and execution of full composite structures.

Some relevant examples of civil engineering structures, realized in Europe with the use of FRPs, are given in the document as a measure of the large spread of this kind of structures and the big interest toward them.

## CHAPTER 2 – MECHANICS OF COMPOSITES MATERIALS

### 2. INTRODUCTION

The term *composites* is generally used to refer to materials formed by combining two or more constituent materials (also known as phases), with the aim of giving the final product properties (physical, chemical, mechanical, etc.) greater than those of the individual phases.

Typical examples of composite materials used in construction are masonry and concrete strengthened with steel bars.

This chapter deals with the mechanical behavior of composites composed of long continuous fibers embedded in a polymeric matrix, known as ***fiber-reinforced polymers (FRP)***. This special class of composite materials offers numerous advantages over conventional structural materials such as high strength and stiffness, low weight as well as good corrosion resistance.

Fibers have a much greater resistance than the bulk material that constitutes them due to the preferential orientation of the molecules along the fiber direction as well as the reduced number of defects present in a fiber in contrast to the bulk material. The most common fibers in composites are ***carbon (CFRP)***, ***glass (GFRP)*** and ***aramid (AFRP)*** with the most widespread polymeric matrices being ***epoxy***, ***vinyl ester*** and ***phenolic resins***. The creep properties of a composite material can be principally attributed to the polymeric matrix. Thus, composites with short fibers or particles exhibit high creep deformations even at room temperature. This explains the preferential use of long continuous fibers for structural applications.

The typical values of both the main physical and mechanical properties of the most common fibers and polymeric matrix used in relation to steel are summarized in Table 2.1. Since their first appearance in 1930 for aeronautical, mechanical and naval engineering applications, the use of FRPs has gradually been extended to the field of civil engineering, which includes the structural restoration as well as construction of new structures, or part of them, especially bridges and viaducts.

Consequently, the demand in the market for FRPs has steadily increased and, with it, the interest of the international scientific and technical communities working in civil engineering field.

This chapter, while dealing with general issues, is focused on these types of application and, therefore, briefly discusses the static behavior of structural elements for civil engineering applications including FRP laminates and pultruded beams. For further details, refer to [42-54].

**Table 2.1**

Typical values of the physical and mechanical properties of fibers and polymeric matrix in relation to steel.

	Young's modulus	Tensile strength	Strain at failure	Coefficient of thermal expansion	Density
	$E$	$\sigma_r$	$\epsilon_r$	$\alpha$	$\rho$
	[GPa]	[MPa]	[%]	[ $10^{-6} \text{ } ^\circ\text{C}^{-1}$ ]	[ $\text{g}/\text{cm}^3$ ]
E-glass	70 – 80	2000 – 3500	3.5 – 4.5	5.0 – 5.4	2.5 – 2.6
S-glass	85 – 90	3500 – 4800	4.5 – 5.5	1.6 – 2.9	2.46 – 2.49
Carbon (high modulus)	390 – 760	2400 – 3400	0.5 – 0.8	-1.45	1.85 – 1.90
Carbon (high strength)	240 – 280	4100 – 5100	1.6 – 1.73	-0.6 – -0.9	1.75
Aramid	62 – 180	3600 – 3800	1.9 – 5.5	-2.0	1.44 – 1.47
Polymeric matrix	2.7 – 3.6	40 – 82	1.4 – 5.2	30 – 54	1.10 – 1.25
Steel	206	250 – 400 (yield) 350 – 600 (failure)	20 – 30	10.4	7.8

Mechanical behavior of web-flange junctions of thin-walled pultruded fiber-reinforced polymer profiles: an experimental and numerical evaluation.

## 2.1. BASIC CONCEPTS AND TERMINOLOGY

This section describes several basic concepts as well as introduces some of the most common definitions used in the present chapter.

Composites are frequently made of thin sheets, known as *laminae*, *layers* or *plies*, bonded together to form a laminate. A lamina may have either *unidirectional* or *bidirectional* fibers embedded in a matrix. A lamina containing woven or braided fibers is referred to as *fabric* (see Fig. 2.1).

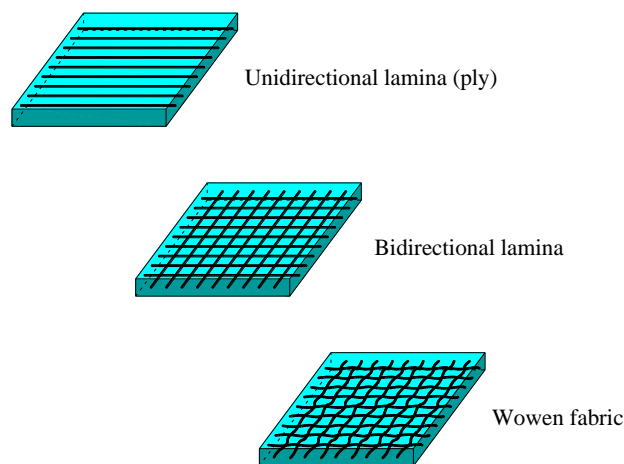


**Figure 2.1.** Composite material systems.

The mechanical behavior of a laminate depends on the properties of the fibers, the matrix as well as the amount and orientations of the fibers. Adjacent laminae

realized with the same fibers and having the same orientation are referred to as a **ply group** which can be treated as one layer.

An  $x, y$  and  $z$  orthogonal system is used to analyze laminates with the  $z$ -axis being perpendicular to the plane of the laminate (see Fig. 2.2).

The orientation of continuous, unidirectional layers are specified by the angle  $\theta$  (in degrees) with respect to the  $x$ -axis. The angle  $\theta$  is positive in the counterclockwise direction. The number of plies within a ply group is specified by a numerical subscript (laminate code or laminate description).

For example, the code  $[30_3/45_4/60_2/90]$  refers to a laminate composed of four ply groups, the first containing three plies of the same thickness in the 30-degree direction, the second containing four plies in the 45-degree direction, the third containing two plies in the 60-degree direction, the fourth containing one ply in the 90-degree direction. A laminate is **balanced** if, for every ply in the  $+\theta$  direction, there is an identical ply in the  $-\theta$  direction. A laminate is **symmetric** if layers of the same material, thickness, and orientation are symmetrically located with respect to its middle surface. For example, the laminate  $[30_3/45_2/45_2/30_3]$  is symmetric, but not balanced, and the annotation  $[30_3/45_2]_S$  can be used.

In a **cross-ply** laminate, fibers are only in the 0- and 90-degree directions. Cross ply laminates are balanced and can be both symmetric as well as unsymmetric.

An **angle-ply** laminate consists of plies in the  $+\theta$  and  $-\theta$  directions. Angle ply laminates may be symmetric and unsymmetric, balanced or unbalanced.

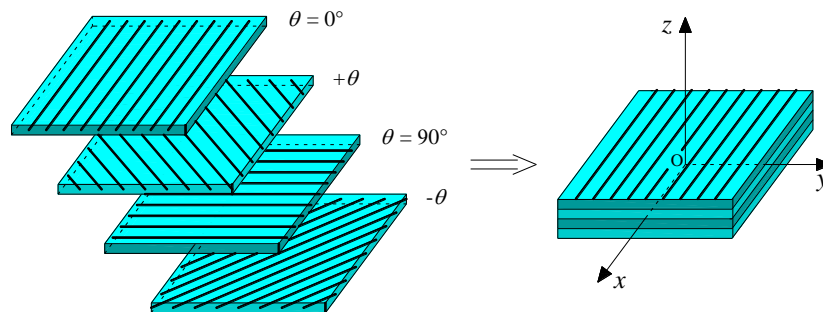


Figure 2.2. Laminated composite.

## 2.2. GENERALIZED HOOKE'S LAW

Due to their intrinsic constitution, from a microscopic point of view, FRPs are anisotropic and inhomogeneous materials. However, from a macroscopic point of view, it is possible to consider them both as *linear elastic orthotropic* materials up to failure and elastically homogeneous.

Consequently, their constitutive law can be expressed through the relation:

$$\underline{\underline{\mathbf{T}}} = \underline{\underline{\mathcal{C}}} \left[ \underline{\underline{\mathbf{E}}} \right], \quad (2.1a)$$

where  $\underline{\underline{\mathbf{T}}}$  and  $\underline{\underline{\mathbf{E}}}$  are the second-order stress tensor (or *Cauchy tensor*), and the second-order *infinitesimal strain* tensor, respectively;  $\underline{\underline{\mathcal{C}}}$  is the fourth-order tensor of the *elastic stiffness (stiffness tensor)*.



In terms of components, with respect to a Cartesian orthogonal reference system (Cartesian components), the generalized Hooke's law (Eq. 2.1a) can be expressed as:

$$T_{ij} = \mathcal{E}_{ijkl} E_{kl}, \quad (2.1b)$$

where the indices  $i, j, k, l \in \{1, 2, 3\}$  and the summation convention has been adopted.

The inverse of tensor  $\mathcal{E}$  is known as *compliance tensor*  $\mathcal{D}$ :

$$\underline{\mathbf{E}} = \underline{\mathcal{D}}[\underline{\mathbf{T}}], \quad (2.2a)$$

$$E_{ij} = \mathcal{D}_{ijkl} T_{kl}. \quad (2.2b)$$

Under the hypothesis of homogeneity of the elastic properties, the two fourth-order tensors  $\mathcal{E}$  and  $\mathcal{D}$  are independent from the position. The Cartesian components of these tensors are therefore also called *elastic constants* of the composite material.

For the symmetry of the two second-order tensors  $\underline{\mathbf{T}}$  and  $\underline{\mathbf{E}}$  (with the possibility of exchanging between them, in Eqs. (2.1b) and (2.2b), the indices  $i$  and  $j$ , as well as the indices  $k$  and  $l$ ) the  $3^4=81$  elastic constants are reduced to 36. Moreover,

assuming the hypothesis of *hyperelasticity* (existence of an elastic potential), the elastic constants are further reduced to 21: in this last case, the fourth-order tensors  $\underline{\mathcal{E}}$  and  $\underline{\mathcal{D}}$  are symmetric, with the pairs of indices  $ij$  and  $kl$  being interchangeable in Eqs. (2.1b) and (2.2b).

For technical purposes, it is preferable to adopt the Voigt-Kelvin notation (contracted notation), which transforms the matrices of the components of the two second-order tensors  $\underline{\mathbf{T}}$  and  $\underline{\mathbf{E}}$  (square matrices with order  $6 \times 6$ ) into column vectors with six components (matrices of order  $6 \times 1$ )  $\boldsymbol{\sigma}$  and  $\boldsymbol{\varepsilon}$ , respectively (contracted vectors). Similarly, the matrices of the components of the two fourth-order tensors  $\underline{\mathcal{E}}$  and  $\underline{\mathcal{D}}$  in square matrices (with order  $6 \times 6$ ):  $\mathbf{C}$  (**stiffness matrix**) and  $\mathbf{S}$  (**compliance matrix**), respectively.

These transformations are defined below:

$$\mathbf{T} = [T_{ij}] \Rightarrow \boldsymbol{\sigma} = \begin{bmatrix} \sigma_1 = T_{11} \\ \sigma_2 = T_{22} \\ \sigma_3 = T_{33} \\ \sigma_4 = T_{23} = \tau_{23} \\ \sigma_5 = T_{13} = \tau_{13} \\ \sigma_6 = T_{12} = \tau_{12} \end{bmatrix}, \quad (2.3a)$$

$$\mathbf{E} = [E_{ij}] \Rightarrow \boldsymbol{\varepsilon} = \begin{bmatrix} \varepsilon_1 = E_{11} \\ \varepsilon_2 = E_{22} \\ \varepsilon_3 = E_{33} \\ \varepsilon_4 = 2E_{23} = \gamma_{23} \\ \varepsilon_5 = 2E_{13} = \gamma_{13} \\ \varepsilon_6 = 2E_{12} = \gamma_{12} \end{bmatrix}, \quad (2.3b)$$

$$\tilde{\mathbf{T}} = \tilde{\mathcal{C}}[\tilde{\mathbf{E}}] \Rightarrow \boldsymbol{\sigma} = \mathbf{C}\boldsymbol{\varepsilon}, \quad (\sigma_i = C_{ij}\varepsilon_j), \quad (2.4a)$$

$$\tilde{\mathbf{E}} = \tilde{\mathcal{D}}[\tilde{\mathbf{T}}] \Rightarrow \boldsymbol{\varepsilon} = \mathbf{S}\boldsymbol{\sigma}, \quad (\varepsilon_i = S_{ij}\sigma_j). \quad (2.4b)$$

The products  $\mathbf{C}\boldsymbol{\varepsilon}$  and  $\mathbf{S}\boldsymbol{\sigma}$  have to be considered as “rows per columns”. The number of independent elastic contracted constants,  $C_{ij}$  and  $S_{ij}$ , is equal to 36. In the case of hyperelasticity, assumed here, the stiffness matrix  $\mathbf{C}$  and the compliance matrix  $\mathbf{S}$  are symmetric ( $C_{ij} = C_{ji}$ ;  $S_{ij} = S_{ji}$ ,  $\forall i, j \in \{1, 2, 3\}$ ,  $i \neq j$ ) and only 21 of the 36 elements are independent.

It is worth noting that, due to the original tensorial nature of the quantities  $\tilde{\mathbf{T}}$ ,  $\tilde{\mathbf{E}}$ ,  $\tilde{\mathcal{C}}$  and  $\tilde{\mathcal{D}}$ , the contracted vectors  $\boldsymbol{\sigma}$  and  $\boldsymbol{\varepsilon}$ , as well as  $\mathbf{C}$  and  $\mathbf{S}$ , do not change according to the specific rules of the numerical vectors and matrices when passing

from one reference system to another (*engineering vectors* and *engineering matrices*).

Particular symmetry properties of the material may introduce further simplifications of the constitutive law, resulting in substantial reductions in the number of independent elastic constants.

The most significant cases of symmetry are discussed below.

### 2.2.1. Monoclinic materials

A *monoclinic* material has a plane of orthogonal symmetry in every point.

Consequently, its elastic constants do not change if they refer to any pair of systems of Cartesian axes that are one the mirror image of the other with respect to the symmetry plane.

Assuming that, with respect to the reference system  $\{\xi_1, \xi_2, \xi_3\}$ , the plane of symmetry is the plane  $(\xi_1, \xi_2)$  of equation  $\xi_3 = 0$  (see Fig. 2.3).

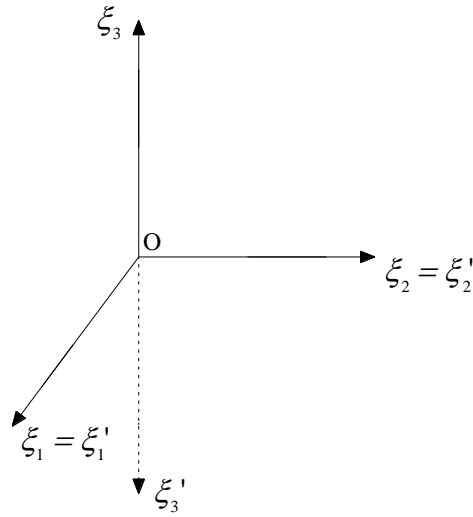


**Figure 2.3.** Monoclinic material.

The transformation matrix from the reference system  $\{\xi_1, \xi_2, \xi_3\}$  to the system  $\{\xi'_1, \xi'_2, \xi'_3\}$  is the following orthogonal matrix:

$$\mathbf{P} = [P_{ij}] = \begin{bmatrix} 1 & 0 & 0 \\ 0 & 1 & 0 \\ 0 & 0 & -1 \end{bmatrix}. \quad (2.5)$$

The matrices of the components of the two tensors  $\underline{\mathbf{T}}$  and  $\underline{\mathbf{E}}$ , in relation to the transformed system  $\{\xi'_1, \xi'_2, \xi'_3\}$ ,  $\mathbf{T}'$  and  $\mathbf{E}'$  respectively, can be obtained from the well-known relations:

$$\mathbf{T}' = \mathbf{P}^T \mathbf{T} \mathbf{P}, \quad (2.6a)$$

$$\mathbf{E}' = \mathbf{P}^T \mathbf{E} \mathbf{P}, \quad (2.6b)$$

where  $(\cdot)^T$  is the transposition symbol and the products between the matrices at the second member of Eqs. (2.6) have to be intended as “rows per columns”.

Consequently, the new components of the contracted vectors,  $\boldsymbol{\sigma}'$  and  $\boldsymbol{\varepsilon}'$ , are:

$$\boldsymbol{\sigma}' = \begin{bmatrix} \sigma_1 \\ \sigma_2 \\ \sigma_3 \\ -\sigma_4 \\ -\sigma_5 \\ -\sigma_6 \end{bmatrix}, \quad \boldsymbol{\varepsilon}' = \begin{bmatrix} \varepsilon_1 \\ \varepsilon_2 \\ \varepsilon_3 \\ -\varepsilon_4 \\ -\varepsilon_5 \\ -\varepsilon_6 \end{bmatrix}. \quad (2.7a,b)$$

The hypothesis of orthogonal symmetry with respect to the plane  $(\xi_1, \xi_2)$  makes it possible to recognize that:

$$\sigma_i = C_{ij} \varepsilon_j \Rightarrow \sigma'_i = C_{ij} \varepsilon'_j. \quad (2.8a,b)$$

It follows that, necessarily, some of the elastic constants must be zero. More specifically, it is:

$$\mathbf{C} = [C_{ij}] = \begin{bmatrix} C_{11} & C_{12} & C_{13} & 0 & 0 & C_{16} \\ C_{12} & C_{22} & C_{23} & 0 & 0 & C_{26} \\ C_{13} & C_{23} & C_{33} & 0 & 0 & C_{36} \\ 0 & 0 & 0 & C_{44} & C_{45} & 0 \\ 0 & 0 & 0 & C_{45} & C_{55} & 0 \\ C_{16} & C_{26} & C_{36} & 0 & 0 & C_{66} \end{bmatrix}. \quad (2.9)$$

Finally, for a monoclinic (and hyperelastic) material only 13 of the elastic constants are independent.

### 2.2.2. Orthotropic materials

An *orthotropic* material has three mutually perpendicular planes of symmetry in every point.

With reference to Fig. 2.3, assume that the three planes of orthogonal symmetry are  $(\xi_1, \xi_2)$ ,  $(\xi_1, \xi_3)$  and  $(\xi_2, \xi_3)$ . Repeating what was discussed in the previous section, and extending it to the plane of equation  $\xi_2 = 0$ , it results in further elastic constants being zero so that the elastic stiffness matrix becomes:

$$\mathbf{C} = [C_{ij}] = \begin{bmatrix} C_{11} & C_{12} & C_{13} & 0 & 0 & 0 \\ C_{12} & C_{22} & C_{23} & 0 & 0 & 0 \\ C_{13} & C_{23} & C_{33} & 0 & 0 & 0 \\ 0 & 0 & 0 & C_{44} & 0 & 0 \\ 0 & 0 & 0 & 0 & C_{55} & 0 \\ 0 & 0 & 0 & 0 & 0 & C_{66} \end{bmatrix}. \quad (2.10)$$

It is also possible to verify that the existence of an additional plane of symmetry,  $\xi_1 = 0$ , does not lead to further reductions in the number of elastic constants. Consequently, for an orthotropic (and hyperelastic) material only 9 elements are independent.

The axes  $\xi_1$ ,  $\xi_2$  and  $\xi_3$  of the intersection of the three mutually perpendicular planes of symmetry are known as *principal axes* or *natural axes*.



### 2.2.3. Transversely isotropic materials

A **transversely isotropic** material has three planes of symmetry and, as such, is orthotropic: in one of the planes of symmetry (plane of **transverse isotropy**) the material is treated as isotropic. Transversely isotropic materials are particularly important in the study of FRPs.

Referring to Fig. 2.4, and assuming that the plane of transverse isotropy coincides with the plane of equation  $\xi_3 = 0$ , the transformation matrix corresponding to the change of the reference system  $\{\xi_1, \xi_2, \xi_3\}$  as a consequence of a rotation  $\theta$  of the axes  $\xi_1$  and  $\xi_2$ , around the natural axis  $\xi_3$  is the following orthogonal matrix:

$$\mathbf{P} = [P_{ij}] = \begin{bmatrix} \cos\theta & \sin\theta & 0 \\ -\sin\theta & \cos\theta & 0 \\ 0 & 0 & 1 \end{bmatrix}. \quad (2.11)$$

Through considerations similar to the previous ones, it is possible to obtain the following expression of the elastic stiffness matrix (contracted) for a transversely isotropic material:

$$\mathbf{C} = [C_{ij}] = \begin{bmatrix} C_{11} & C_{12} & C_{13} & 0 & 0 & 0 \\ C_{12} & C_{11} & C_{13} & 0 & 0 & 0 \\ C_{13} & C_{13} & C_{33} & 0 & 0 & 0 \\ 0 & 0 & 0 & C_{44} & 0 & 0 \\ 0 & 0 & 0 & 0 & C_{44} & 0 \\ 0 & 0 & 0 & 0 & 0 & C_{66} \end{bmatrix}, \quad (2.12)$$

with  $C_{66} = \frac{1}{2}(C_{11} - C_{12})$ .

Consequently, of the 12 nonzero elements only 5 are independent.

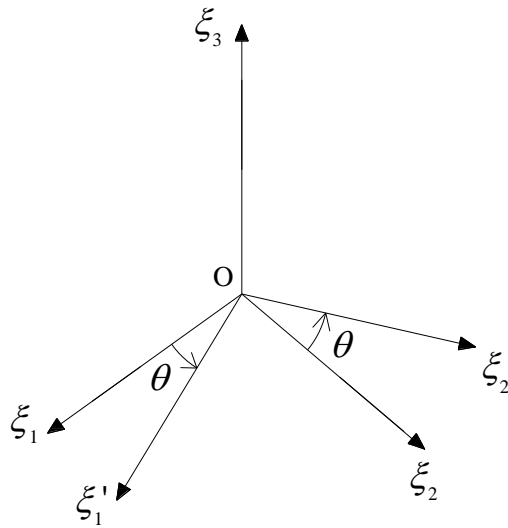


**Figure 2.4.** Transversely isotropic material.

#### 2.2.4. Isotropic material

A material is *isotropic* if at all its points there are no preferred directions and every plane is a plane of symmetry.

The elements of the stiffness matrix, with respect to any reference system

$\{\xi_1, \xi_2, \xi_3\}$  are:

$$\mathbf{C} = [C_{ij}] = \begin{bmatrix} C_{11} & C_{12} & C_{12} & 0 & 0 & 0 \\ C_{12} & C_{11} & C_{12} & 0 & 0 & 0 \\ C_{12} & C_{12} & C_{11} & 0 & 0 & 0 \\ 0 & 0 & 0 & C_{44} & 0 & 0 \\ 0 & 0 & 0 & 0 & C_{44} & 0 \\ 0 & 0 & 0 & 0 & 0 & C_{44} \end{bmatrix}, \quad (2.13)$$

$$\text{with } C_{44} = \frac{1}{2}(C_{11} - C_{12}).$$

It follows that of the 12 nonzero elements only 2 are independent. It is also possible to demonstrate that an isotropic material is necessarily hyperelastic, in other words, that it has an elastic potential.

### 2.3. ENGINEERING MODULI OF ORTHOTROPIC MATERIALS

Fiber-reinforced polymer materials are generally orthotropic or even transversely isotropic such as, for example, in the case of pultruded beams. The principal axes are naturally defined by the directions of the reinforcing fibers.

In the technical field, it is customary to express the elastic constants as a function of the Young moduli,  $E_i$ , the shear moduli,  $G_{ij}$ , as well as the Poisson ratios  $\nu_{ij}$ , ( $i, j \in \{1, 2, 3\}, i \neq j$ ), also called *engineering moduli*.

As a function of these parameters, the compliance matrix  $\mathbf{S}$ , can be expressed as:

$$\mathbf{S} = [S_{ij}] = \begin{bmatrix} \frac{1}{E_1} & -\frac{\nu_{21}}{E_2} & -\frac{\nu_{31}}{E_3} & 0 & 0 & 0 \\ -\frac{\nu_{12}}{E_1} & \frac{1}{E_2} & -\frac{\nu_{32}}{E_3} & 0 & 0 & 0 \\ -\frac{\nu_{13}}{E_1} & -\frac{\nu_{23}}{E_2} & \frac{1}{E_3} & 0 & 0 & 0 \\ 0 & 0 & 0 & \frac{1}{G_{23}} & 0 & 0 \\ 0 & 0 & 0 & 0 & \frac{1}{G_{13}} & 0 \\ 0 & 0 & 0 & 0 & 0 & \frac{1}{G_{12}} \end{bmatrix}. \quad (2.14)$$

The compliance matrix is the inverse of the stiffness matrix,  $\mathbf{C}$ , and is also symmetric.

Due to the symmetry of the compliance matrix, it results:

$$\frac{\nu_{ij}}{E_i} = \frac{\nu_{ji}}{E_j} \quad (i, j \in \{1, 2, 3\}, i \neq j), \quad (2.15)$$

so that, as mentioned before in §2.2.2, only 9 elastic parameters are independent.

The elements of the elastic stiffness matrix are obtained by inverting the compliance matrix.

It follows:

$$C_{11} = \frac{1 - \nu_{23}\nu_{32}}{E_2 E_3 \Delta}, \quad (2.16a)$$

$$C_{12} = \frac{\nu_{21} + \nu_{31}\nu_{13}}{E_2 E_3 \Delta} = \frac{\nu_{12} + \nu_{32}\nu_{23}}{E_1 E_3 \Delta}, \quad (2.16b)$$

$$C_{13} = \frac{\nu_{31} + \nu_{21}\nu_{32}}{E_2 E_3 \Delta} = \frac{\nu_{13} + \nu_{12}\nu_{23}}{E_1 E_2 \Delta}, \quad (2.16c)$$

$$C_{22} = \frac{1 - \nu_{13}\nu_{31}}{E_1 E_3 \Delta}, \quad (2.16d)$$

$$C_{23} = \frac{\nu_{32} + \nu_{12}\nu_{31}}{E_1 E_3 \Delta} = \frac{\nu_{23} + \nu_{21}\nu_{13}}{E_1 E_2 \Delta}, \quad (2.16e)$$

$$C_{33} = \frac{1 - \nu_{12}\nu_{21}}{E_1 E_2 \Delta}, \quad (2.16f)$$

$$C_{44} = G_{23}, \quad (2.16g)$$

$$C_{55} = G_{13}, \quad (2.16h)$$

$$C_{66} = G_{12}, \quad (2.16i)$$

being:

$$\Delta = \frac{1 - \nu_{12}\nu_{21} - \nu_{23}\nu_{32} - \nu_{31}\nu_{13} - 2\nu_{21}\nu_{32}\nu_{13}}{E_1 E_2 E_3}. \quad (2.17)$$

Finally, simple considerations on the physical plausibility of the constitutive law (see Eq. 2.14) imply that the following restrictions have to be applied “*a priori*” to the engineering moduli:

$$E_1, E_2, E_3, G_{32}, G_{13}, G_{12} > 0. \quad (2.18)$$

#### 2.4. COORDINATE TRANSFORMATIONS

In the previous sections, the structures of the stiffness and compliance matrices of an orthotropic material were analyzed with respect to the natural reference system.

The following section shows how these matrices are transformed when referring to a different reference system which can be chosen on the basis of convenience of calculation as well as the fact that its axes usually have preferential directions. For example, they may coincide with the sides of a rectangular laminate; further on, two of them can coincide with the central axes of inertia of the cross-section of a beam and the third one with the centroidal axis of the latter.

The same problem is not relevant in the case of a linear elastic isotropic material being that the components of the stiffness and compliance matrices are independent of the choice of the reference system.

It is possible to denote the axes of the natural system as  $\xi_1$ ,  $\xi_2$  and  $\xi_3$  and their unit vectors as  $e_1$ ,  $e_2$  and  $e_3$ , respectively; the axes of the structural reference frame as  $x_1 = x$ ,  $x_2 = y$  and  $x_3 = z$ , and their unit vectors as  $i_1 = i_x$ ,  $i_2 = i_y$  and  $i_3 = i_z$ , respectively.

The case in which the axes  $\xi_3$  and  $x_3$  coincide, while the axes  $\xi_1$  and  $\xi_2$  are obtained from the axes  $x_1$  and  $x_2$  through a rotation  $\theta$  around the axis common to both reference systems is of particular interest to the study of FRP laminates. The rotation  $\theta$  is assumed positive when counter-clockwise with respect to  $\xi_3 = x_3$  (see Fig. 2.5).

Upon examining this specific case, let  $\underline{\mathbf{P}}$  be the tensor that transforms  $i_1$  into  $e_1$ ,  $i_2$  into  $e_2$ , and  $i_3$  into  $e_3$ . It is orthogonal and its components matrix,  $\mathbf{P}$ , with respect to the base  $\{i_1, i_2, i_3\}$ , is called the **transformation matrix** from the structural reference to the natural one.

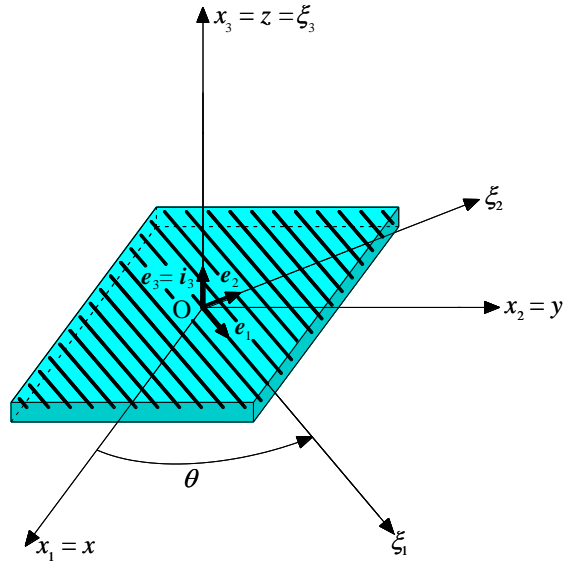


**Figure 2.5.** Structural reference system and natural reference system.

It results:

$$\mathbf{P} = [P_{ij}] = \begin{bmatrix} \cos\theta & -\sin\theta & 0 \\ \sin\theta & \cos\theta & 0 \\ 0 & 0 & 1 \end{bmatrix}. \quad (2.19)$$

The transformation formulae of the Cartesian coordinates and the components of the tensors  $\underline{\mathbf{T}}$  and  $\underline{\mathbf{E}}$  from the structural reference system,  $\bar{T}_{ij}$  and  $\bar{E}_{ij}$ , to the natural one and vice-versa, are:



$$\boldsymbol{\zeta} = \begin{bmatrix} \zeta_1 \\ \zeta_2 \\ \zeta_3 \end{bmatrix} = \mathbf{P}^T \mathbf{x} = \mathbf{P}^T \begin{bmatrix} x_1 \\ x_2 \\ x_3 \end{bmatrix}, \quad (2.20a)$$

$$\mathbf{x} = \mathbf{P} \boldsymbol{\zeta}, \quad (2.20b)$$

$$\mathbf{T} = \mathbf{P}^T \bar{\mathbf{T}} \mathbf{P}, \bar{\mathbf{T}} = \mathbf{P} \mathbf{T} \mathbf{P}^T, \quad (2.21a,b)$$

$$\mathbf{E} = \mathbf{P}^T \bar{\mathbf{E}} \mathbf{P}, \bar{\mathbf{E}} = \mathbf{P} \mathbf{E} \mathbf{P}^T, \quad (2.22a,b)$$

where, obviously,  $\bar{\mathbf{T}} = [\bar{T}_{ij}]$  and  $\bar{\mathbf{E}} = [\bar{E}_{ij}]$ , and where, as already seen, the product between the matrices have to be considered as “rows per columns”.

In terms of contracted notations, denoting the vectors of the stress and strain components in the structural reference with  $\bar{\boldsymbol{\sigma}} = [\bar{\sigma}_1, \bar{\sigma}_2, \dots, \bar{\sigma}_6]^T = [\bar{\sigma}_x, \bar{\sigma}_y, \dots, \bar{\tau}_{xy}]^T$  and  $\bar{\boldsymbol{\varepsilon}} = [\bar{\varepsilon}_1, \bar{\varepsilon}_2, \dots, \bar{\varepsilon}_6]^T = [\bar{\varepsilon}_x, \bar{\varepsilon}_y, \dots, \bar{\gamma}_{xy}]^T$ , respectively, it is possible to obtain, through Eqs. (2.21) and (2.22), the following relations:

$$\bar{\boldsymbol{\sigma}} = \mathcal{J} \boldsymbol{\sigma}, \boldsymbol{\sigma} = \mathcal{R} \bar{\boldsymbol{\sigma}}, \quad (2.23a,b)$$

$$\bar{\boldsymbol{\varepsilon}} = \mathcal{R}^T \boldsymbol{\varepsilon}, \boldsymbol{\varepsilon} = \mathcal{J}^T \bar{\boldsymbol{\varepsilon}}, \quad (2.24a,b)$$

being  $\mathcal{J}$  and  $\mathcal{R}$  two appropriate square matrices with order  $6 \times 6$ , whose components are a function of the angle  $\theta$ . For brevity, their expressions are not given here. Their characterization to the case of plane-stress conditions will be discussed in the following paragraph.

More details about the mathematical derivation of Eqs. (2.23) and (2.24) can be found in [53].

Using Eqs. (2.23) and (2.24), it is possible to correlate the elastic constants in the natural and structural reference systems. The stiffness and compliance matrices, with respect to the structural reference systems, are denoted with  $\bar{\mathbf{C}}$  and  $\bar{\mathbf{S}}$ , respectively. It follows:

$$\bar{\boldsymbol{\sigma}} = \mathcal{J} \boldsymbol{\sigma} = \mathcal{J} \mathbf{C} \boldsymbol{\varepsilon} = \mathcal{J} \mathbf{C} \mathcal{J}^T \bar{\boldsymbol{\varepsilon}} \Rightarrow \bar{\mathbf{C}} = \mathcal{J} \mathbf{C} \mathcal{J}^T, \quad (2.25a)$$

$$\bar{\boldsymbol{\varepsilon}} = \mathcal{R}^T \boldsymbol{\varepsilon} = \mathcal{R}^T \mathbf{S} \boldsymbol{\sigma} = \mathcal{R}^T \mathbf{S} \mathcal{R} \bar{\boldsymbol{\sigma}} \Rightarrow \bar{\mathbf{S}} = \mathcal{R}^T \mathbf{S} \mathcal{R}. \quad (2.25b)$$

It is possible to verify that, in the case of an orthotropic material, the matrices  $\bar{\mathbf{C}}$  and  $\bar{\mathbf{S}}$ , have the same structure as the corresponding matrices of a monoclinic material (see Eq. 1.9).

## 2.5. PLANE-STRESS CONDITIONS

When plane-stress conditions exist, the relationship between stresses and strains (see Eq. 2.14) can be considerably simplified. With reference to Fig. 2.5, the plane of stress is supposed to coincide with the plane  $\xi_3 = 0$ . Consequently, Eq. (2.14) can be rewritten as follows:

$$\begin{bmatrix} \varepsilon_1 \\ \varepsilon_2 \\ \varepsilon_6 \end{bmatrix} = \begin{bmatrix} S_{11} & S_{12} & 0 \\ S_{12} & S_{22} & 0 \\ 0 & 0 & S_{66} \end{bmatrix} \begin{bmatrix} \sigma_1 \\ \sigma_2 \\ \sigma_6 \end{bmatrix} = \begin{bmatrix} \frac{1}{E_1} & -\frac{\nu_{21}}{E_2} & 0 \\ -\frac{\nu_{21}}{E_1} & \frac{1}{E_2} & 0 \\ 0 & 0 & \frac{1}{G_{12}} \end{bmatrix} \begin{bmatrix} \sigma_1 \\ \sigma_2 \\ \sigma_6 \end{bmatrix}. \quad (2.26)$$

On the other hand, the inverse of Eq. (2.26) can be put in the form:

$$\begin{bmatrix} \sigma_1 \\ \sigma_2 \\ \sigma_6 \end{bmatrix} = \begin{bmatrix} Q_{11} & Q_{12} & 0 \\ Q_{12} & Q_{11} & 0 \\ 0 & 0 & Q_{66} \end{bmatrix} \begin{bmatrix} \varepsilon_1 \\ \varepsilon_2 \\ \varepsilon_6 \end{bmatrix}. \quad (2.27)$$

where the quantities  $Q_{ij}$  are known as ***stiffness reduced for stress-plane conditions***.

Their expressions, as a function of the engineering moduli, are the following:

$$Q_{11} = \frac{E_1}{1 - \nu_{12}\nu_{21}}, \quad (2.28a)$$

$$Q_{12} = \frac{\nu_{12}E_2}{1-\nu_{12}\nu_{21}} = \frac{\nu_{21}E_1}{1-\nu_{12}\nu_{21}}, \quad (2.28b)$$

$$Q_{22} = \frac{E_2}{1-\nu_{12}\nu_{21}}, \quad (2.28c)$$

$$Q_{66} = G_{12}. \quad (2.28d)$$

Under plane-stress conditions, the expressions of the components of the matrices

$\mathcal{R}$ ,  $\mathcal{I}$ ,  $\bar{\mathcal{C}}$  and  $\bar{\mathcal{S}}$ , introduced in the previous paragraph, become:

$$\begin{bmatrix} \sigma_1 \\ \sigma_2 \\ \sigma_6 \end{bmatrix} = \begin{bmatrix} \cos^2 \theta & \sin^2 \theta & \sin 2\theta \\ \sin^2 \theta & \cos^2 \theta & -\sin 2\theta \\ -\sin \theta \cdot \cos \theta & \sin \theta \cdot \cos \theta & \cos 2\theta \end{bmatrix} \begin{bmatrix} \bar{\sigma}_1 = \sigma_x \\ \bar{\sigma}_2 = \sigma_y \\ \bar{\sigma}_6 = \tau_{xy} \end{bmatrix}, \quad (2.29a)$$

$$\begin{bmatrix} \varepsilon_1 \\ \varepsilon_2 \\ \varepsilon_6 \end{bmatrix} = \begin{bmatrix} \cos^2 \theta & \sin^2 \theta & \sin \theta \cdot \cos \theta \\ \sin^2 \theta & \cos^2 \theta & -\sin \theta \cdot \cos \theta \\ -\sin 2\theta & \sin 2\theta & \cos 2\theta \end{bmatrix} \begin{bmatrix} \bar{\varepsilon}_1 = \varepsilon_x \\ \bar{\varepsilon}_2 = \varepsilon_y \\ \bar{\varepsilon}_6 = \gamma_{xy} \end{bmatrix}. \quad (2.29b)$$

It can be observed that the squared matrix on the right of Eq. (2.29a) is the reduced expression of  $\mathcal{R}$ , while the squared matrix (Eq. 2.29b) is the reduced expression of  $\mathcal{I}^T$ .

In addition, adopting for both the components of stress and strain the notation with the subscripts  $x$ ,  $y$  and  $z$ , instead of 1, 2 and 3, the reduced stiffness matrix, with respect to the structural reference system, assumes the following expression:

$$\begin{bmatrix} \sigma_x \\ \sigma_y \\ \tau_{xy} \end{bmatrix} = \begin{bmatrix} \bar{Q}_{11} & \bar{Q}_{12} & \bar{Q}_{16} \\ \bar{Q}_{12} & \bar{Q}_{22} & \bar{Q}_{26} \\ \bar{Q}_{16} & \bar{Q}_{26} & \bar{Q}_{66} \end{bmatrix} \begin{bmatrix} \varepsilon_x \\ \varepsilon_y \\ \gamma_{xy} \end{bmatrix}. \quad (2.30)$$

The expressions of quantities  $\bar{Q}_{ij}$  are the following:

$$\bar{Q}_{11} = Q_{11} \cos^4 \theta + 2(Q_{12} + 2Q_{66}) \sin^2 \theta \cdot \cos^2 \theta + Q_{22} \sin^4 \theta, \quad (2.31a)$$

$$\bar{Q}_{12} = (Q_{11} + Q_{22} - 4Q_{66}) \sin^2 \theta \cdot \cos^2 \theta + Q_{12} (\sin^4 \theta + \cos^4 \theta), \quad (2.31b)$$

$$\bar{Q}_{16} = (Q_{11} - Q_{12} - 2Q_{66}) \sin \theta \cdot \cos^3 \theta + (Q_{12} - Q_{22} + 2Q_{66}) \sin^3 \theta \cdot \cos \theta, \quad (2.31c)$$

$$\bar{Q}_{26} = (Q_{11} - Q_{12} - 2Q_{66}) \sin^3 \theta \cdot \cos \theta + (Q_{12} - Q_{22} + 2Q_{66}) \sin \theta \cdot \cos^3 \theta, \quad (2.31d)$$

$$\bar{Q}_{22} = Q_{11} \sin^4 \theta + 2(Q_{12} + 2Q_{66}) \sin^2 \theta \cdot \cos^2 \theta + Q_{22} \cos^4 \theta, \quad (2.31e)$$

$$\bar{Q}_{66} = (Q_{11} + Q_{22} - 2Q_{12} - 2Q_{66}) \sin^2 \theta \cdot \cos^2 \theta + Q_{66} (\sin^4 \theta + \cos^4 \theta). \quad (2.31f)$$

The quantities  $\bar{Q}_{ij}$  are also called the **apparent stiffness** of the orthotropic material. In some problems, the stress state in a lamina cannot be considered as plane, because, even if the normal stress acting on its plane is negligible, the shear stresses acting in the transverse direction of the plane are not. Due to the principle

of symmetry of the shear stresses, such stresses also act at the interface between two adjacent layers in the case of laminates. Consequently, they are also called ***interlaminar stresses***.

Where necessary, Eq. (2.27) is supported by:

$$\begin{bmatrix} \sigma_4 \\ \sigma_5 \end{bmatrix} = \begin{bmatrix} Q_{44} & 0 \\ 0 & Q_{55} \end{bmatrix} \begin{bmatrix} \varepsilon_4 \\ \varepsilon_5 \end{bmatrix}, \quad (2.32)$$

where  $Q_{44} = C_{44} = G_{23}$  and  $Q_{55} = C_{55} = G_{13}$ .

Similarly, the following relation supports (see Eq. 1.30):

$$\begin{bmatrix} \tau_{yz} \\ \tau_{xy} \end{bmatrix} = \begin{bmatrix} \bar{Q}_{44} & \bar{Q}_{45} \\ \bar{Q}_{45} & \bar{Q}_{55} \end{bmatrix} \begin{bmatrix} \gamma_{yz} \\ \gamma_{xz} \end{bmatrix}. \quad (2.33)$$

The expressions of quantities  $\bar{Q}_{ij}$  are the following:

$$\bar{Q}_{44} = Q_{44} \cos^2 \theta + Q_{55} \sin^2 \theta, \quad (2.34a)$$

$$\bar{Q}_{55} = Q_{55} \cos^2 \theta + Q_{44} \sin^2 \theta, \quad (2.34b)$$

$$\bar{Q}_{45} = (Q_{55} - Q_{44}) \cos \theta \cdot \sin \theta. \quad (2.34c)$$

By inverting Eq. (2.30), it is possible to obtain the following expression of the elastic compliance matrix with respect to the structural reference system:

$$\bar{\mathbf{S}} = \begin{bmatrix} \frac{1}{E_x} & -\frac{\nu_{yx}}{E_y} & \frac{\eta_{xy,x}}{E_x} \\ -\frac{\nu_{xy}}{E_x} & \frac{1}{E_y} & \frac{\eta_{xy,y}}{E_y} \\ \frac{\eta_{x,xy}}{G_{xy}} & \frac{\eta_{y,xy}}{G_{xy}} & \frac{1}{G_{xy}} \end{bmatrix}. \quad (2.35)$$

In Eq. (2.35), *Lekhniski coefficients* have been introduced:

$$\eta_{i,j,i} = \frac{\varepsilon_i}{\gamma_{ij}}, \quad (2.36a)$$

$$\eta_{i,ij} = \frac{\gamma_{ij}}{\varepsilon_i}, \quad (2.36b)$$

being  $\eta_{i,j,i}$  and  $\eta_{i,ij}$ , respectively, the *specific dilatations* in the i-direction caused by shear stress,  $\tau_{ij}$ , and the shear strains between the axes i and j caused by normal stress,  $\sigma_i$ .

It is worth noting that the matrix  $\bar{\mathbf{S}}$  is a full matrix unlike  $\mathbf{S}$ . However, the independent elastic constants are only 4:  $E_1$ ,  $E_2$ ,  $\nu_{12}$  and  $G_{12}$ .

The components of the matrix  $\bar{\mathbf{S}}$  are also called the *apparent compliances* of the orthotropic material.

In Figs 2.6 and 2.7, the values of both the Young modulus,  $E_x$ , and shear modulus,  $G_{xy}$ , are plotted as a function of the angle  $\theta$  between fibers and applied load, for different values of the modulus  $E_1$ .

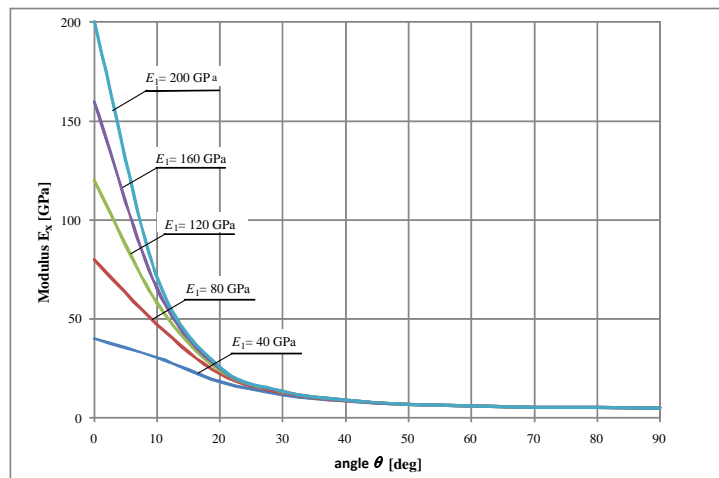


**Figure 2.6.** Young modulus of elasticity  $E_x$  as a function of  $\theta$  for fiber-reinforced composites and for several values of the Young modulus of elasticity,  $E_1$  ( $E_2 = 5$  GPa ;  $G_{12} = 3$  GPa ;  $\nu_{12} = 0.35$ ).



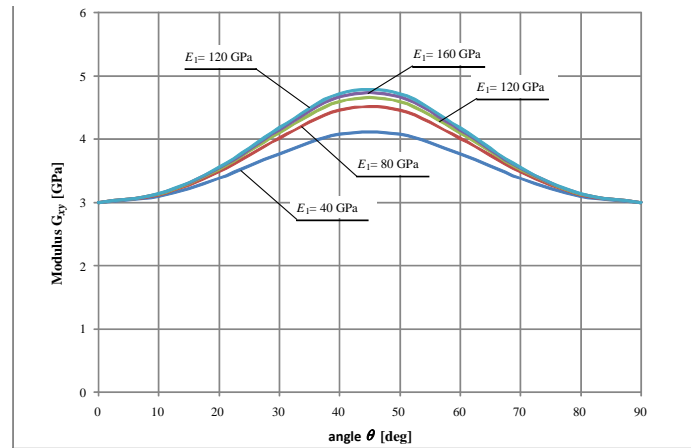


**Figure 2.7.** Shear modulus  $G_{xy}$  as a function of  $\theta$  for fiber-reinforced composites and for several values of the Young modulus of elasticity,  $E_1$  ( $E_2 = 5 \text{ GPa}$ ;  $G_{12} = 3 \text{ GPa}$ ;  $\nu_{12} = 0.35$ ).

The significant variations of the moduli  $E_x$  and  $G_{xy}$  with the angle  $\theta$  are apparent. In the case of fabrics, fibers are distributed along two or more directions (multi-axial fabrics). If the crimping due to the weaving of fibers is neglected and assuming that the fabric is made out of two separated unidirectional layers of fibers running at 0- and 90-degree directions, the modulus of elasticity,  $E_x$ , can be evaluated through simplified methods by neglecting the slip between the layers. In the particular case of fabric having the same percentage of fibers in the two considered directions (balanced fabric), Fig. 2.8 plots the relationship between  $E_x$  and  $\theta$ .

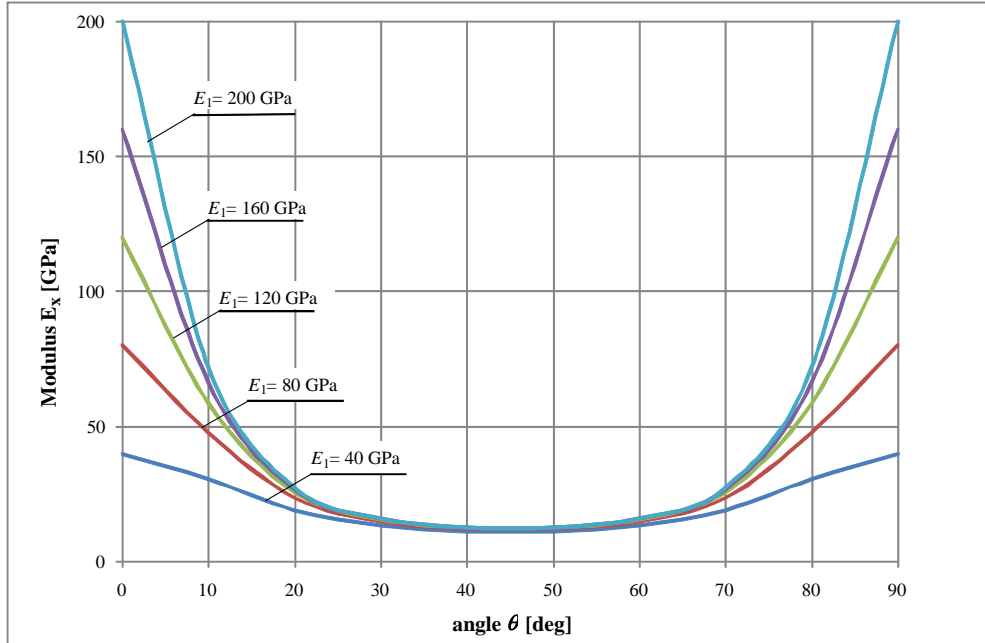


**Figure 2.8.** Modulus of elasticity,  $E_x$ , as a function of  $\theta$  for balanced fabric depending upon the modulus of elasticity,  $E_1$ .

## 2.6. FAILURE CRITERIA

The micro-mechanic collapse mechanism of fiber-reinforced materials is a complex phenomenon that depends on a multitude of parameters including loading type as well as type of fiber and resin. For this reason, the failure criteria for composites usually refer to the macro-mechanical level assuming that the composite itself can be regarded as a homogeneous material exhibiting a linear elastic behavior up to collapse. In the case of laminates subjected to planar stresses, one of the simplest failure criteria is that of the *maximum stress*.

If  $\sigma_{1u,t}$  ( $\sigma_{1u,c}$ ) and  $\sigma_{2u,t}$  ( $\sigma_{2u,c}$ ) represent the tensile (compressive) failure stress in the principal directions, and  $\tau_{12u}$  is the corresponding shear stress at failure, this criterion can be represented as follows:

$$\sigma_1 \begin{cases} \leq \sigma_{1u,t} , & \text{if } \sigma_1 > 0 , \\ \geq \sigma_{1u,c} , & \text{if } \sigma_1 < 0 , \end{cases}$$

$$\sigma_2 \begin{cases} \leq \sigma_{2u,t} , & \text{if } \sigma_2 > 0 , \\ \geq \sigma_{2u,c} , & \text{if } \sigma_2 < 0 , \end{cases} \quad (2.37)$$

$$|\tau_{12}| \leq \tau_{12u}.$$

The maximum stress criterion does not depend on the sign of the shear stress nor does it consider the interactions between the different failure modes. Different failure modes can occur irrespectively one from another. The maximum stress that the laminate can withstand is given by the lowest among the following values:

$$\begin{aligned}\sigma_{xu} &< \frac{\sigma_{1u}}{\cos^2 \theta}, \\ \sigma_{xu} &< \frac{\sigma_{2u}}{\sin^2 \theta}, \\ \sigma_{xu} &< \frac{\tau_{12u}}{\sin \theta \cdot \cos \theta}.\end{aligned}\tag{2.38}$$

The variation of  $\sigma_{xu}$  as a function of  $\theta$  is plotted in Fig. 2.9.

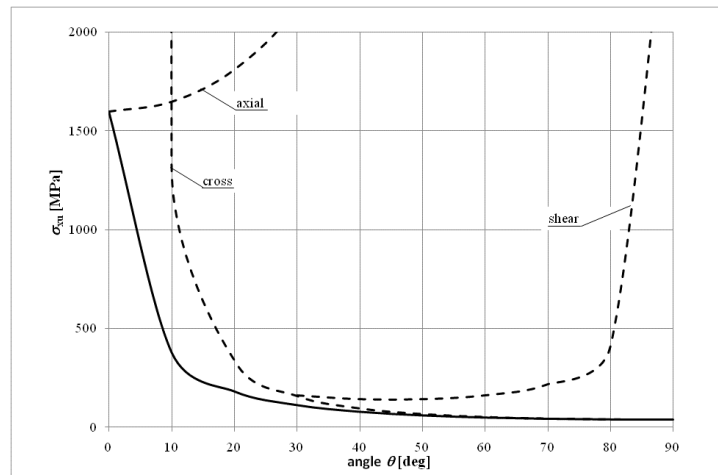


**Figure 2.9.** Criterion of maximum stress: Tensile failure stress as a function of  $\theta$  for unidirectional laminates ( $\sigma_{1u} = 1600$  MPa,  $\sigma_{2u} = 40$  MPa,  $\tau_{12u} = 70$  MPa).

The criterion of the maximum stress is usually only in good agreement with the experimental data for tensile tests with  $\theta$  smaller than  $15^\circ$  and larger than  $45^\circ$ . Otherwise, the measured values for compression are quite higher. Another widely used criterion to estimate the failure of a laminate is *Tsai-Hill*, which may be expressed as follows:

$$\left(\frac{\sigma_1}{\sigma_{1u}}\right)^2 + \left(\frac{\sigma_2}{\sigma_{2u}}\right)^2 - \frac{\sigma_1 \cdot \sigma_2}{\sigma_{1u}^2} + \left(\frac{\tau_{12}}{\tau_{12u}}\right)^2 \leq 1. \quad (2.39)$$

The stress at failure as a function of  $\theta$  can be written as follows:

$$\sigma_{xu} = \left[ \frac{\cos^4 \theta}{\sigma_{1u}^2} + \left( \frac{1}{\tau_{12u}^2} - \frac{1}{\sigma_{1u}^2} \right) \cos^2 \theta \cdot \sin^2 \theta + \frac{\sin^4 \theta}{\sigma_{2u}^2} \right]^{-1/2}, \quad (2.40)$$

and is plotted in Fig. 2.10.

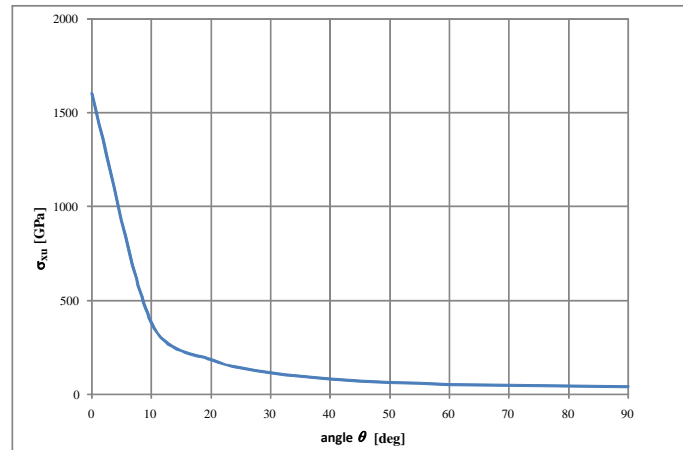


**Figure 2.10.** Tsai-Hill criterion: tensile failure stress as a function of  $\theta$  for unidirectional

laminates ( $\sigma_{1u} = 1600$  MPa ,  $\sigma_{2u} = 40$  MPa ,  $\tau_{12u} = 70$  MPa ).

## 2.7. MICROMECHANICAL CHARACTERIZATION OF A UNIDIRECTIONAL LAMINA

For design purposes, the elastic constants of a lamina have to be experimentally determined through accurate laboratory tests. However, in the case of unidirectional laminae and as a first approximation, it is possible to use a micromechanical theoretical approach based on the following assumptions:

- i. perfect bond between matrix and fibers,
- ii. fibers arranged parallel to each other in a uniform manner,
- iii. absence of initial defects,
- iv. linear elastic behavior up to failure.

The engineering moduli of the composite material can be deduced from those of the matrix and fibers. For this purpose, the following are:

- $E_f$  : Young's modulus of the fibers,
- $E_m$  : Young's modulus of the matrix,
- $\nu_f$  : Poisson ratio of the fibers,

- $\nu_m$  : Poisson ratio of the matrix,
- $V_f$  : volume fraction of the fibers,
- $V_m$  : volume fraction of the matrix.

Assuming the natural reference system axis  $\xi_1$  to be parallel to the fibers, the axis  $\xi_2$  orthogonal to it and the axis  $\xi_3$  perpendicular to the lamina (see Fig. 2.5), through simple considerations of equilibrium and compatibility, it is possible to demonstrate that:

$$E_1 = V_f E_f + V_m E_m, \quad (2.41a)$$

$$\nu_{12} = V_f \nu_f + V_m \nu_m, \quad (2.41b)$$

$$\frac{1}{E_2} = \frac{V_f}{E_f} + \frac{V_m}{E_m}, \quad (2.42a)$$

$$\frac{1}{G_{12}} = \frac{V_f}{G_f} + \frac{V_m}{G_m}. \quad (2.42b)$$

It is worth noting that:

$$G_f = \frac{E_f}{2(1 + \nu_f)}, \quad (2.43a)$$

$$G_m = \frac{E_m}{2(1+\nu_m)}. \quad (2.43b)$$

Generally speaking, it is possible to claim that  $E_1$  and  $\nu_{12}$  adhere to the **rule of mixtures**;  $E_2$  and  $G_{12}$  to the **inverse rule of mixtures**.

## 2.8. HYGROTHERMAL EFFECTS

Hygrothermal strains may occur in a FRP laminate in the presence of temperature variations and/or moisture concentration, both of which may vary across the thickness of the laminate. The moisture concentration is mainly absorbed by the polymer matrix rather than the fibers. Aramid fibers are the exception, due to them being polymeric.

Once absorbed, the moisture produces a swelling of the matrix resulting in hygrothermal deformations.

Owing to these hygrothermal and mechanical loads, the strains at a point of an orthotropic lamina, with respect to the natural reference system, can be expressed as:

$$\begin{bmatrix} \varepsilon_1 \\ \varepsilon_2 \\ \varepsilon_6 \end{bmatrix} = \begin{bmatrix} S_{11} & S_{12} & 0 \\ S_{12} & S_{22} & 0 \\ 0 & 0 & S_{66} \end{bmatrix} \begin{bmatrix} \sigma_1 \\ \sigma_2 \\ \sigma_6 \end{bmatrix} + \Delta T \begin{bmatrix} \alpha_1 \\ \alpha_2 \\ 0 \end{bmatrix} + \Delta m \begin{bmatrix} \beta_1 \\ \beta_2 \\ 0 \end{bmatrix}, \quad (2.44)$$



where  $\alpha_1$ ,  $\alpha_2$ ,  $\beta_1$  and  $\beta_2$  are the *thermal* and *hygrothermal expansions coefficients* in both the principal directions  $\xi_1$  and  $\xi_2$  of the lamina;  $\Delta T$  and  $\Delta m$  are the variations of the temperature ( $T$ ) and moisture ( $m$ ) concentration from a reference state,  $\Delta T = T - T_0$  and  $\Delta m = m - m_0$ , respectively. It is worth noting that the latter is defined as the ratio between the moisture weight and dry weight of the FRP.

In the most common engineering applications, both  $\Delta T$  as well as  $\Delta m$  can be considered as data of the problem and, therefore, the corresponding deformations as distortions.

In the structural reference system, the last two addends on the right of Eq. (2.44) are transformed in accordance to Eq. (2.29b).

It is therefore:

$$\begin{bmatrix} \varepsilon_x \\ \varepsilon_y \\ \gamma_{xy} \end{bmatrix} = \begin{bmatrix} \bar{S}_{11} & \bar{S}_{12} & \bar{S}_{16} \\ \bar{S}_{12} & \bar{S}_{22} & \bar{S}_{26} \\ \bar{S}_{16} & \bar{S}_{26} & \bar{S}_{66} \end{bmatrix} \begin{bmatrix} \sigma_x \\ \sigma_y \\ \tau_{xy} \end{bmatrix} + \Delta T \begin{bmatrix} \alpha_x \\ \alpha_y \\ \alpha_{xy} \end{bmatrix} + \Delta m \begin{bmatrix} \beta_x \\ \beta_y \\ \beta_{xy} \end{bmatrix}. \quad (2.45)$$

In Eq. (1.45), there is:

$$\begin{bmatrix} (\cdot)_x \\ (\cdot)_y \\ (\cdot)_{xy} \end{bmatrix} = \begin{bmatrix} \cos^2 \theta & \sin^2 \theta & \sin \theta \cdot \cos \theta \\ \sin^2 \theta & \cos^2 \theta & -\sin \theta \cdot \cos \theta \\ -\sin 2\theta & \sin 2\theta & \cos 2\theta \end{bmatrix}^{-1} \begin{bmatrix} (\cdot)_1 \\ (\cdot)_2 \\ 0 \end{bmatrix}, \quad (2.46)$$

being denoted by the symbol  $(\cdot)$ , the quantities  $\alpha$  and  $\beta$ .

However, wanting to calculate the stresses starting from the strains, from Eq. (2.45), the following is obtained:

$$\begin{bmatrix} \sigma_x \\ \sigma_y \\ \tau_{xy} \end{bmatrix} = \begin{bmatrix} \bar{Q}_{11} & \bar{Q}_{12} & \bar{Q}_{16} \\ \bar{Q}_{12} & \bar{Q}_{22} & \bar{Q}_{26} \\ \bar{Q}_{16} & \bar{Q}_{26} & \bar{Q}_{66} \end{bmatrix} \left( \begin{bmatrix} \varepsilon_x \\ \varepsilon_y \\ \gamma_{xy} \end{bmatrix} - \Delta T \begin{bmatrix} \alpha_x \\ \alpha_y \\ \alpha_{xy} \end{bmatrix} - \Delta m \begin{bmatrix} \beta_x \\ \beta_y \\ \beta_{xy} \end{bmatrix} \right). \quad (2.47)$$

It is well-known that hygrothermal effects can cause stresses in statically indeterminate structures. This can occur in a laminate even in the case of isostatic structures when the layers mutually exert a constraining action against the displacements associated with the hygrothermal changes on one another. For instance, this may occur if the values of the coefficients  $\alpha$  and  $\beta$  of adjacent laminae are different.

## **CHAPTER 3 - ON THE AXIAL BEHAVIOR OF WEB-FLANGE JUNCTIONS OF PFRP I-PROFILES**

### **3. INTRODUCTION**

In past few decades, the interest in using pultruded fiber reinforced polymeric (PFRP) composites in construction applications has grown rapidly. Several research studies were conducted and focused on the performance of PFRP beams, columns and frame structures. The results of the majority of previous studies highlighted a major problem associated with the deficiency of the off-the-shelf, unidirectional open-web pultruded profiles. In this regards, a common conclusion

was drawn by many researchers; that is: the inherent structural deficiency of commercially produced unidirectional PFRP profiles, especially at the flange/web(s) junction(s) that lacks fiber continuity. The lack of fiber continuity creates a “resin-rich” zones at the junctions that were shown to be responsible for rapid degradation of both axial and rotational stiffness as well as the strength of the majority of PFRP profiles. Another related problem is the use of incorrect framing connection details, currently being used by industry. Such connection details mimic those associated with steel structures. This approach ignores both the anisotropic and the viscoelastic nature of composites as well as the aforementioned inherent junction deficiency that, in most cases, lead to a greater risk with regard to the safety, reliability and economic aspects of such structures. This dissertation presents a summary of an experimental study aimed at evaluating both axial and rotational stiffnesses and strengths of web-flange junctions (WFJ), which may affect stiffness, buckling, post-buckling, torsional and overall strength of PFRP structures. In particular, web-flange junctions of commercially-produced unidirectional pultruded I-, H- and L-profiles were evaluated under both service and ultimate loads. Using full-scale experimental data,  $P-\delta$  and  $M-\theta$  relations and idealized expressions for each pultruded profile were developed that can be used for accurate modeling and for establishing design limit-states for PFRP structures. In addition, two special test fixtures were designed, fabricated and validated that can be adopted by ASTM/ISO standards for

characterizing such critical mechanical properties that are essential for reliable design of pultruded composite structures.

In particular, this chapter presents the results of the first phase of the research program on the web-flange junction characterization of pultruded I-profiles giving details of the pullout full-scale experiments. The test program was conducted at the Materials and Structural Testing Laboratory (LMS) of the Department of Civil Engineering (DICIV) of the University of Salerno.

### **3.1. EXPERIMENTAL INVESTIGATION (@ UNISA)**

#### **3.1.1. Pull-out test setup and instrumentation**

In the pullout tests, web-flange junctions are subjected to a uniform pull load applied on the bottom flange of the specimens.

Specifically, two different test setups were considered: in the first, the pull force was eccentrically applied at the end-point of the specimens (Fig. 3.1) while, in the second, the pull force was applied at their mid-point (Fig. 3.2) simulating the two typical types of junction failure modes observed in several earlier studies [57-63].

For all the specimens, the pull axial load was performed using a calibrated Shenck Hydropuls servo-hydraulic testing machine, updated with a *Zwick Roell* test control electronic and a testing software testXpert® II. Two rigid steel angles were used

in order to provide fixity to the upper flange and web of the specimens (Fig. 3.3). In order to measure the local deformations of the web/flange junction of the specimens, three rectangular self-temperature-compensated strain gages (*Vishay MM C2A-06-125LW-120*) were placed as shown in Figs. 3.4a,b.



**Figure 3.1.** End Point Pull-Out Test Setup.



**Figure 3.2.** Mid Point Pull-Out Test Setup.

In all tests, a force-controlled loading protocol was adopted and both the incremental applied load as well as the associated relative web/flange displacement were continuously recorded and monitored via a calibrated data acquisition system (*System 5100 Vishay MM*). The data obtained during tests were subsequently elaborated using the *StrainSmart* software.

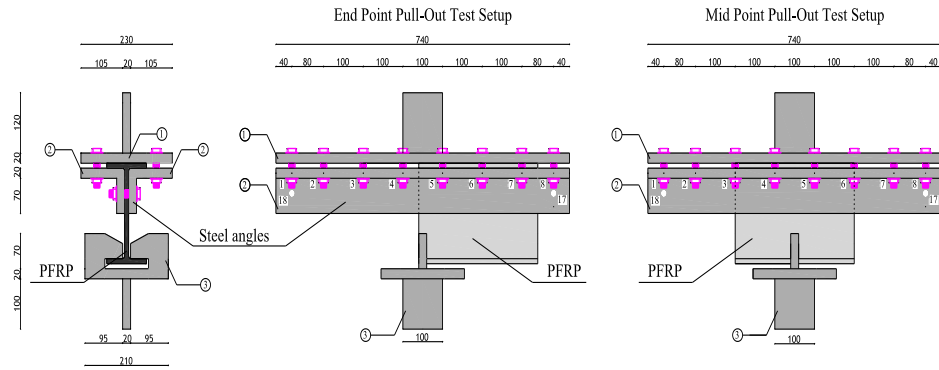
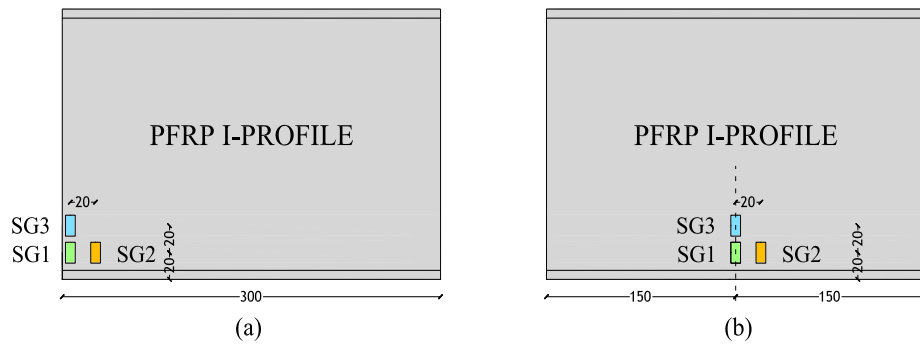


**Figure 3.3.** Schematic Setup of Web-Flange Junction Pull-Out Test (dimension in mm).



**Figures 3.4a,b.** Typical strain gages locations for (a) End Point Pull-Out, and (b) Mid-Point Pull-Out Test (*dimensions in mm*).



### 3.1.2. PFRP materials

Two sizes of commercially-produced structural pultruded I-profiles, i.e., 160 (H) x 80 (B) x 8 ( $T_f=T_w$ ) mm and 200 (H) x 100 (B) x 10 mm ( $T_f=T_w$ ), denoted as  $I_{160}$  and  $I_{200}$ , respectively, were evaluated in this investigation. The geometrical characteristics of the PFRP profiles discussed in this paper are reported in Table 3.1.

**Table 3.1.** Geometry of the pultruded profiles.

Profile	H	B	$T_f$	$T_w$	A	$\gamma$	$I_{xx}$
	[mm]	[mm]	[mm]	[mm]	$\times 10^3$ [mm <sup>2</sup> ]	[g/m]	$\times 10^6$ [mm <sup>4</sup> ]
$I_{160}$	160	80	8	8	2.49	4.480	9.66
$I_{200}$	200	100	10	10	3.89	6.990	23.60

The mechanical properties of the commercially-produced PFRP materials depend on the fibre/matrix volume fraction, which, for E-glass/polyester pultruded members, are commonly between 40% to 60%, assuming zero voids ratio.

It is well-known [42-56] that PFRP members can be simulated as a laminated configuration with the internal layer constituted of unidirectional fibres (*roving*) parallel to the longitudinal axis ( $z$ ) and the external layers composed of multi-directional fibres (*mat*) which completely wind around the pultruded element. Consequently, the material exhibits a transversely-isotropic behavior; anisotropic in the  $z$ -direction and isotropic in the  $x$  and  $y$  directions. In the aforementioned coordinate system ( $x$ ,  $y$  and  $z$ ), the engineering constants are related as follow:  $E_x =$

$E_y$ ;  $\nu_{zx} = \nu_{zy}$  and  $G_{zx} = G_{zy}$ . The nominal values of the main mechanical properties of the pultruded profiles were supplied by the manufactures (Table 3.2).

**Table 3.2.** Mechanical properties of GFRP structural profiles (Nominal values).

Property	Measurement Unit	Value
Longitudinal elastic modulus, $E_z$	MPa	23,000
Transversal elastic moduli, $E_x = E_y$	MPa	8,500
Transversal shear modulus, $G_{xy}$	MPa	3,000
Shear Moduli, $G_{zx} = G_{zy}$	MPa	3,455
Longitudinal Poisson's ratio, $\nu_{xy}$		0.23
Transversal Poisson's ratios, $\nu_{zx} = \nu_{zy}$		0.09
Material density ( $\gamma$ )	kg/m <sup>3</sup>	1,600-1,800

### 3.2. EXPERIMENTAL RESULTS

A total of 28 specimens were cut transversely from I-profile pultruded beams of two different sizes; H=160 mm (*L<sub>160</sub>*) and H=200 mm (*L<sub>200</sub>*). All specimens were subjected to tensile loading both at the *End-Point (EP)* and at the *Mid-Point (MP)* of the specimens at a constant rate of 0.001 N/sec.

In this study, two groups of tests were carried out. The first group of 15 specimens, having the same length of 300 mm, was subdivided into four series in order to investigate the influence of the profile size and of the pull force location on the mechanical behavior of the web-flange junctions. The second group of 13 specimens, obtained from the same pultruded beam (*L<sub>160</sub>*) with different lengths (*200 mm, 300 mm, 600 mm and 1200 mm*), were tested with the aim to evaluate the

influence of the location of the pull-out load on the stiffness and strength of the junctions.

### 3.2.1. First Group: Influence of profile size & pull-out load location

The detailed results obtained from the experimental investigation of the first group of 15 specimens are presented in Tables 3.3-3.6. In the last two columns of these tables, two proposed values for junction's linear stiffness are presented. Namely, the *linear axial stiffness*  $K_{jl}^A$ , and the *average linear axial stiffness*  $\bar{K}_{jl}^A$ .

The proposed average stiffness is extracted from the experimental  $P$ - $\delta$  curve by connecting the origin (O) by the midpoint,  $P^* = (P_m, \delta_m)$ , between the end of the linear range ( $P_l$ ) and the peak load ( $P_f$ ). Figure 3.5 shows the definition of the two proposed junction stiffness values. Figures 3.6a,b and 3.7a,b present the load versus displacement curves for the  $L_{160}$  and  $L_{200}$  specimens, respectively.

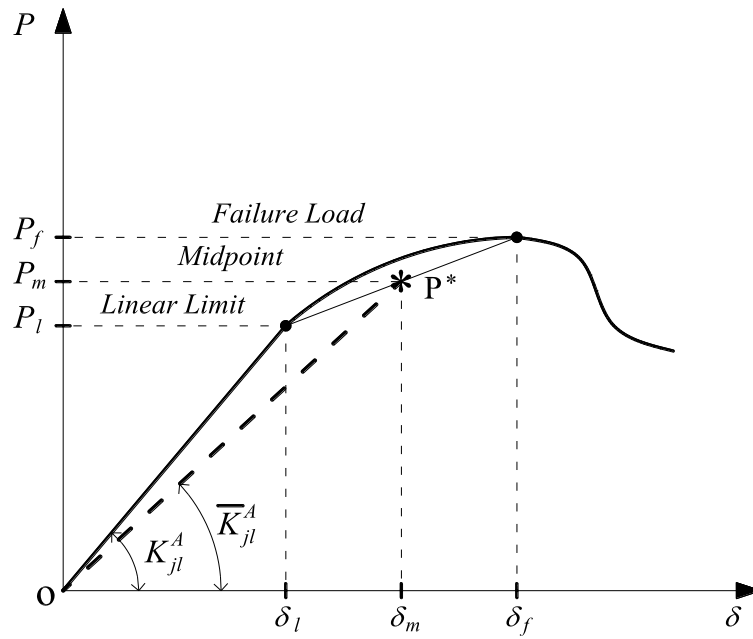


**Figure 3.5.** Linear axial stiffness,  $K_{jl}^A$ , and average linear axial stiffness,  $\bar{K}_{jl}^A$ .

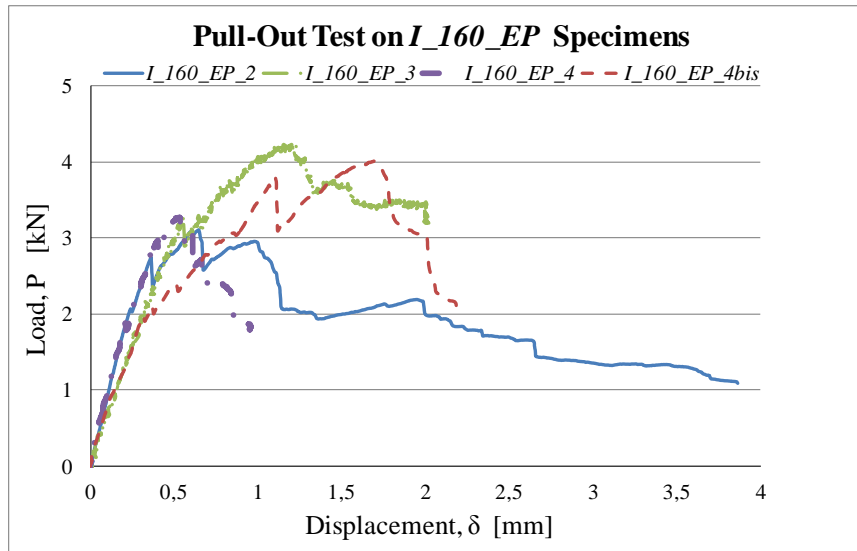


**Figure 3.6a.** Load ( $P$ ) versus displacement ( $\delta$ ) curve for  $I_{160\_EP}$  specimens (first group).

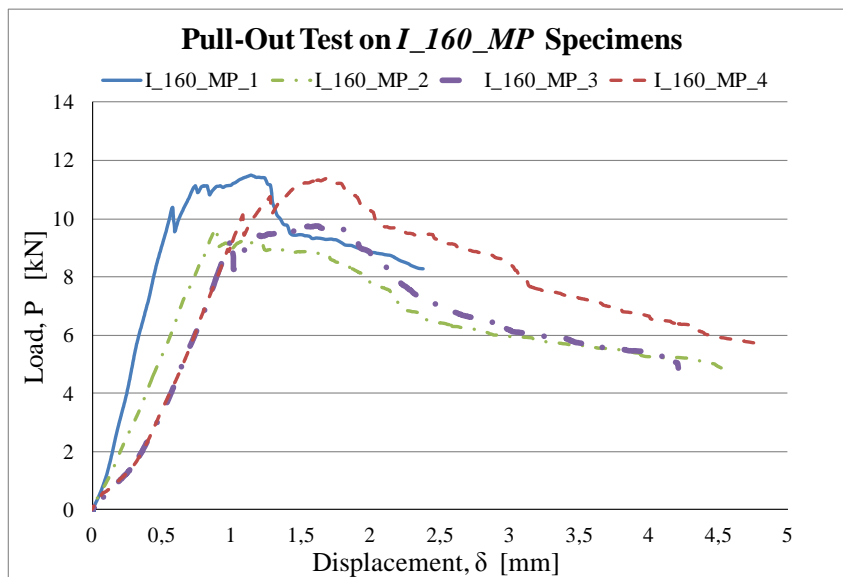


**Figure 3.6b.** Load ( $P$ ) versus displacement ( $\delta$ ) curve for  $I_{160\_MP}$  specimens (first group).

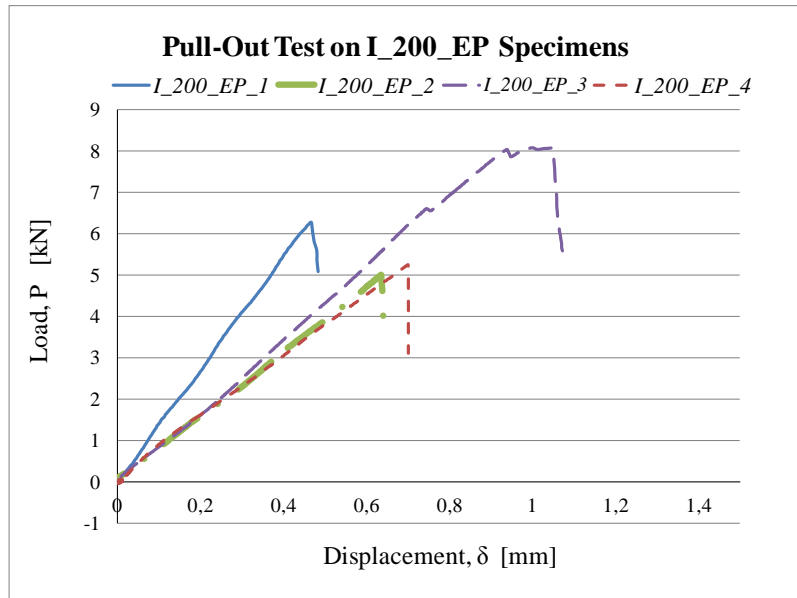


**Figure 3.7a.** Load ( $P$ ) versus displacement ( $\delta$ ) curve for  $I_{200\_EP}$  specimens (first group).

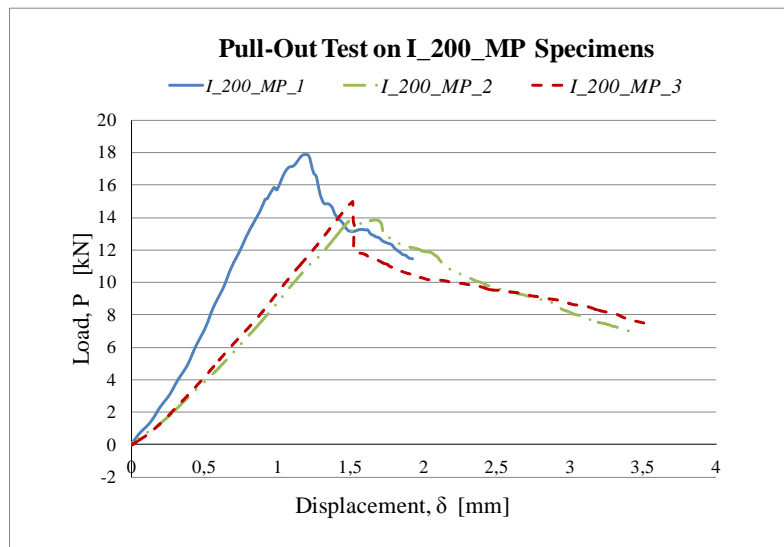


**Figure 3.7b.** Load ( $P$ ) versus displacement ( $\delta$ ) curve for  $I_{200\_MP}$  specimens (first group).

**Table 3.3.** Failure loads, displacements and linear axial stiffnesses obtained from the experimental tests on *I\_160\_EP* specimens (first group).

#	Specimens	Length	Load (linear limit) ( $P_l$ )	$\delta_l$	Failure Load ( $P_f$ )	$\delta_f$	Linear Axial stiffness $K_{jl}^A$	Average Lin. Axial stiffness $\bar{K}_{jl}^A$
		[mm]	[kN]	[mm]	[kN]	[mm]	[kN/mm]	[kN/mm]
1	<i>I_160_EP_2</i>	300	2.6751	0.3652	3.1160	0.6484	8.3650	6.6361
2	<i>I_160_EP_3</i>	300	3.0551	0.5860	4.1860	1.1598	6.0995	4.5014
3	<i>I_160_EP_4</i>	300	2.9440	0.4326	3.2489	0.5367	7.7959	6.8830
4	<i>I_160_EP_4_bis</i>	300	1.9829	0.3146	3.7942	1.1049	6.1310	3.0988

**Table 3.4.** Failure loads, displacements and linear axial stiffnesses obtained from the experimental tests on *I\_160\_MP* specimens (first group).

#	Specimens	Length	Load (linear limit) ( $P_l$ )	$\delta_l$	Failure Load ( $P_f$ )	$\delta_f$	Linear Axial stiffness $K_{jl}^A$	Average Lin. Axial stiffness $\bar{K}_{jl}^A$
		[mm]	[kN]	[mm]	[kN]	[mm]	[kN/mm]	[kN/mm]
5	<i>I_160_MP_1</i>	300	10.3826	0.5776	11.4842	1.1462	17.6730	15.0060
6	<i>I_160_MP_2</i>	300	9.2705	1.0952	9.2705	1.0952	10.7060	10.7060
7	<i>I_160_MP_3</i>	300	9.1769	0.9977	9.7393	1.6221	8.0646	7.4815
8	<i>I_160_MP_4</i>	300	10.1197	1.0858	11.2126	1.5285	8.3770	7.9222

**Table 3.5.** Failure loads, displacements and linear axial stiffnesses obtained from the experimental tests on *I\_200\_EP* specimens (first group).

#	Specimens	Length	Load (linear limit) ( $P_l$ )	$\delta_l$	Failure Load ( $P_f$ )	$\delta_f$	Linear Axial stiffness $K_{jl}^A$	Average Lin. Axial stiffness $\bar{K}_{jl}^A$
		[mm]	[kN]	[mm]	[kN]	[mm]	[kN/mm]	[kN/mm]
9	<i>I_200_EP_1</i>	300	6.2900	0.4600	6.2900	0.4600	13.5810	13.5810
10	<i>I_200_EP_2</i>	300	5.0063	0.6363	5.0063	0.6363	7.7522	7.7522
11	<i>I_200_EP_3</i>	300	8.0428	0.9373	8.0428	0.9373	8.6550	8.6550
12	<i>I_200_EP_4</i>	300	5.2407	0.7011	5.2407	0.7011	7.7454	7.7454

**Table 3.6.** Failure loads, displacements and linear axial stiffnesses obtained from the experimental tests on *I\_200\_MP* specimens (first group).

#	Specimens	Length	Load (linear limit) ( $P_l$ )	$\delta_l$	Failure Load ( $P_f$ )	$\delta_f$	Linear Axial stiffness $K_{jl}^A$	Average Lin. Axial stiffness $\bar{K}_{jl}^A$
		[mm]	[kN]	[mm]	[kN]	[mm]	[kN/mm]	[kN/mm]
13	<i>I_200_MP_1</i>	300	17.9000	1.1800	17.9000	1.1800	15.6300	15.6300
14	<i>I_200_MP_2</i>	300	13.7920	1.4838	13.7920	1.4838	8.8450	8.8450
15	<i>I_200_MP_3</i>	300	15.0095	1.5137	15.0095	1.5137	9.4982	9.4982

Mechanical behavior of web-flange junctions of thin-walled pultruded fiber-reinforced polymer profiles: an experimental and numerical evaluation.

In the following paragraphs, load-displacement curves at loading-point and the corresponding equivalent linearized relations  $P$ - $\delta$  for all the specimens of the first group are presented.

- *Specimen #1: I\_160\_EP\_2*

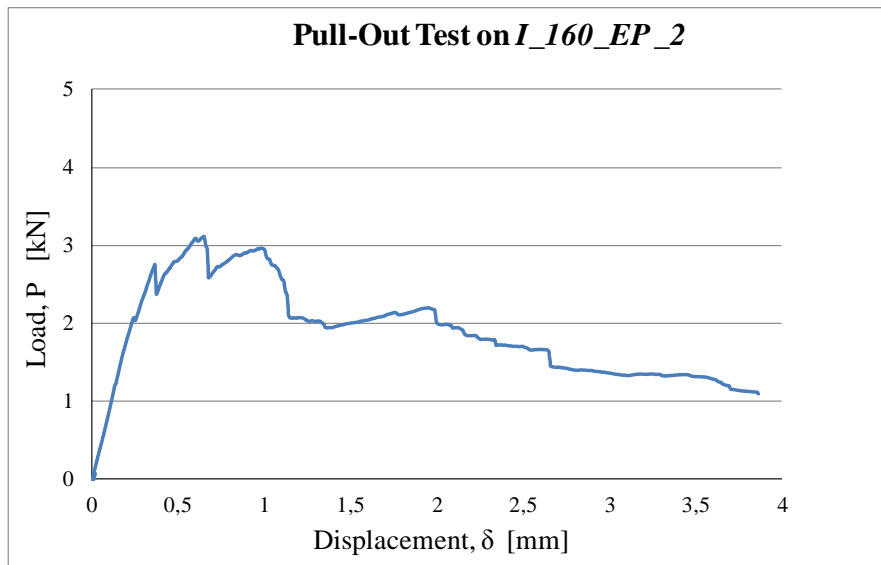
For the *I\_160\_EP\_2* specimen, the displacement increased linearly as the load increased up to an axial displacement of 0.3652 mm that occurred at a load level of 2.6751 kN. After which, a stiffness degradation was observed and the load-displacement ( $P$ - $\delta$ ) curve followed a non-linear behavior until a 0.6484 mm displacement level that corresponds to a 3.1160 kN axial load. Beyond this level, signs of local junction failure started to appear. This localized failure progressed rapidly leading to a ultimate failure in the form of separation between the flange and web as shown in Figure 3.8.

Figure 3.9a shows the load-displacement curve for this specimen at the loading-point. The equivalent linearized load-displacement relation measured at the specimen's loading-point is shown in Figure 3.9b (where  $P = y$  and  $\delta = x$ ). Figure 9c shows the proposed average stiffness of this specimen.





**Figure 3.8.** Web/Flange Junction Failure of *I\_160\_EP\_2* specimen.



**Figure 3.9a.** Load-Displacement Curve for *I\_160\_EP\_2* specimen at loading-point.

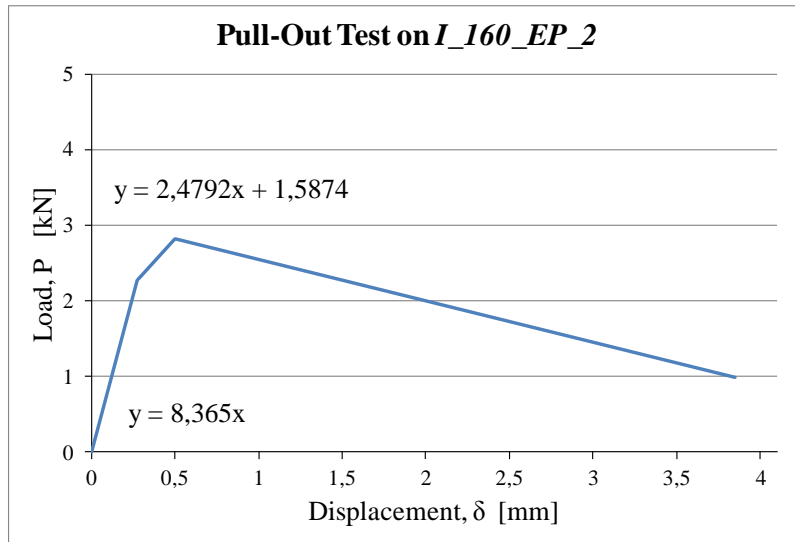


**Figure 3.9b.** Linearized Load-Displacement Curve for *I\_160\_EP\_2* specimen at loading-point.

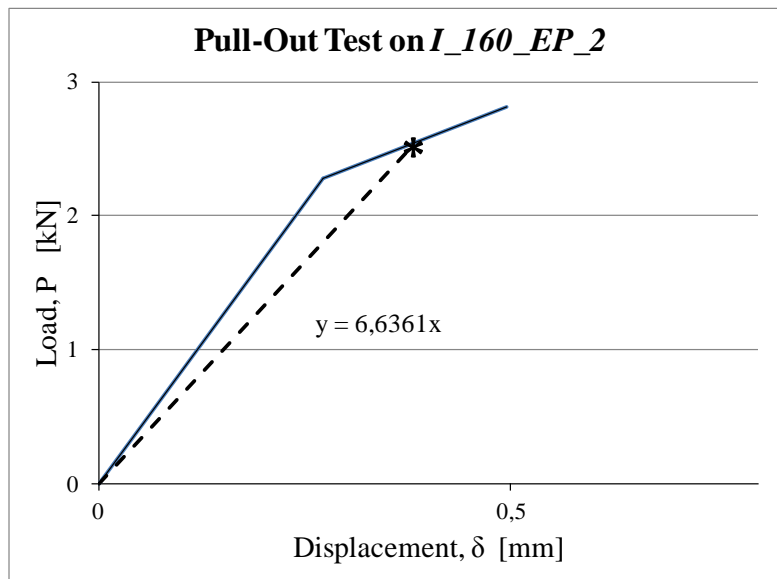


**Figure 9c.** Proposed Load-Displacement Curve for *I\_160\_EP\_2* specimen.

- Specimen #2: *L\_160\_EP\_3*

For specimen *L\_160\_EP\_3*, a similar  $P-\delta$  behavior was observed where linearity continued up to a displacement of 0.5860 mm that corresponds to a pull load of 3.0551 kN. Beyond this load level, stiffness degradation was observed and the load-displacement ( $P-\delta$ ) curve behaved nonlinearly until an axial junction displacement of 1.1598 mm at a load of 4.1860 kN. Following this displacement level, signs of local junction failure were observed at the resin-rich zone. The failure progressed rapidly resulting in a similar ultimate mode of failure that was observed for specimen *L\_160\_EP\_2* in the form of a total separation between the flange and the web as indicated in Figure 3.10.

Figure 11a shows the experimental load–displacement curve for this specimen. The equivalent linearized relation at loading-point of this specimen is presented in Figure 3.11b. Figure 3.11c shows the proposed average stiffness of this specimen.



**Figure 3.10.** Web/Flange Junction Failure of *I\_160\_EP\_3* specimen.

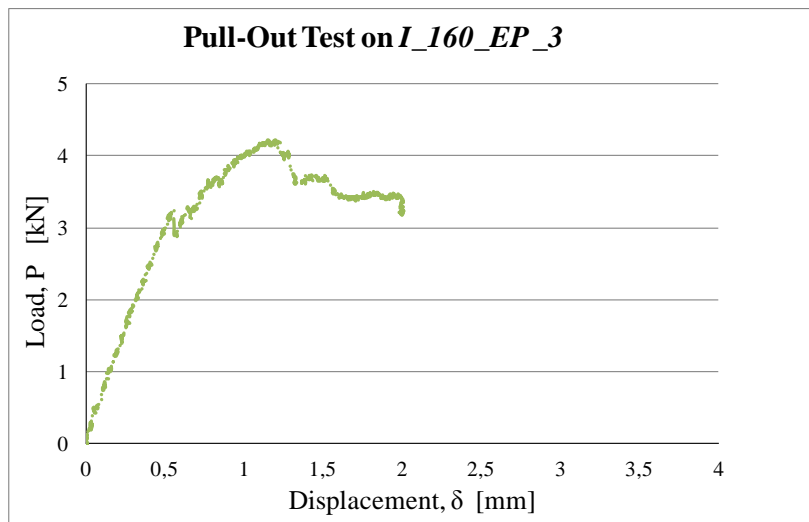


**Figure 3.11a.** Load-Displacement Curve for *I\_160\_EP\_3* specimen at loading-point.

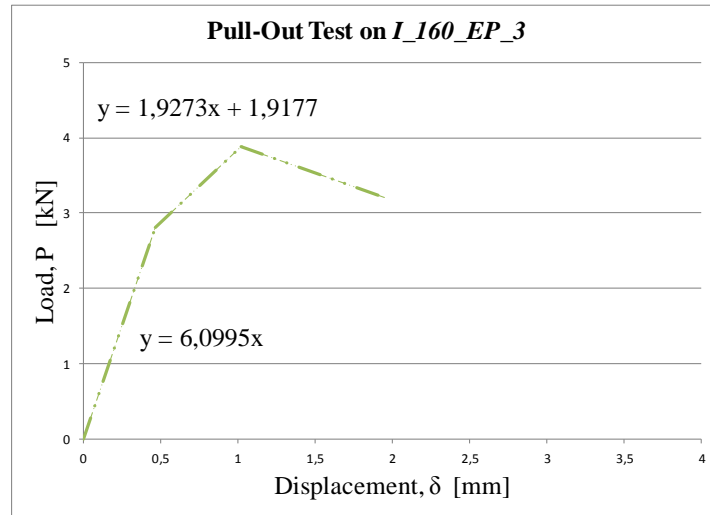


**Figure 3.11b.** Linearized Load-Displacement Curve for *I\_160\_EP\_3* specimen at loading-point.

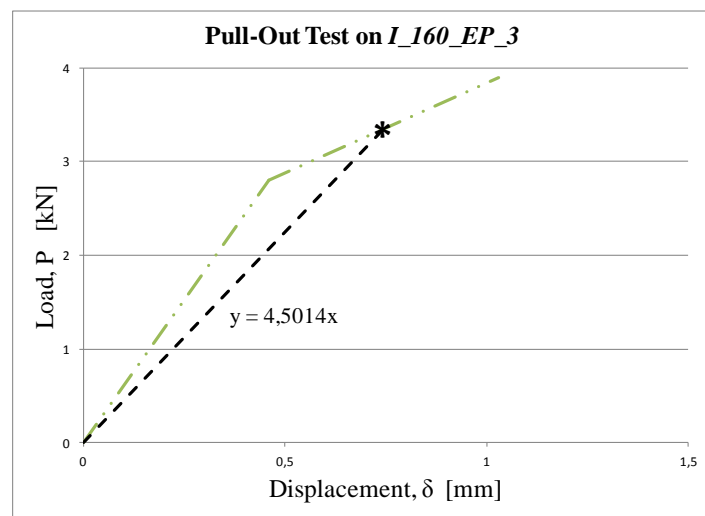


**Figure 3.11c.** Proposed Load-Displacement Curve for *I\_160\_EP\_3* specimen.

- *Specimen #3: I\_160\_EP\_4*

The general behavior of this specimen was similar to the two specimens reported earlier. For this specimen, the displacement increased linearly with an increasing load until an axial displacement of 0.4326 mm was reached that corresponds to a load level of 2.9440 kN. Following this point, the stiffness started to decrease while the relation between load and displacement remained linear up to a displacement of 0.5367 mm that corresponds to an axial load of 3.2489 kN. Beyond this point, local junction failure was initiated leading to a separation between the flanges from the web as shown in Figure 3.12. The load-displacement curve at the loading-point for this specimen is shown in Figure 13a and the corresponding equivalent linearized relation is shown in Figure 3.13b. Figure 3.13c shows the proposed average stiffness of this specimen.

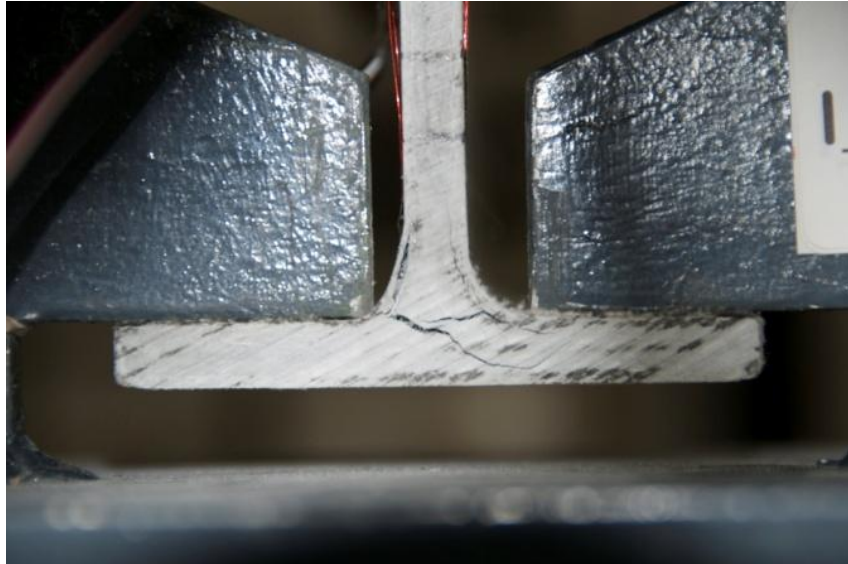


**Figure 3.12.** Web/Flange Junction Failure of *I\_160\_EP\_4* specimen.

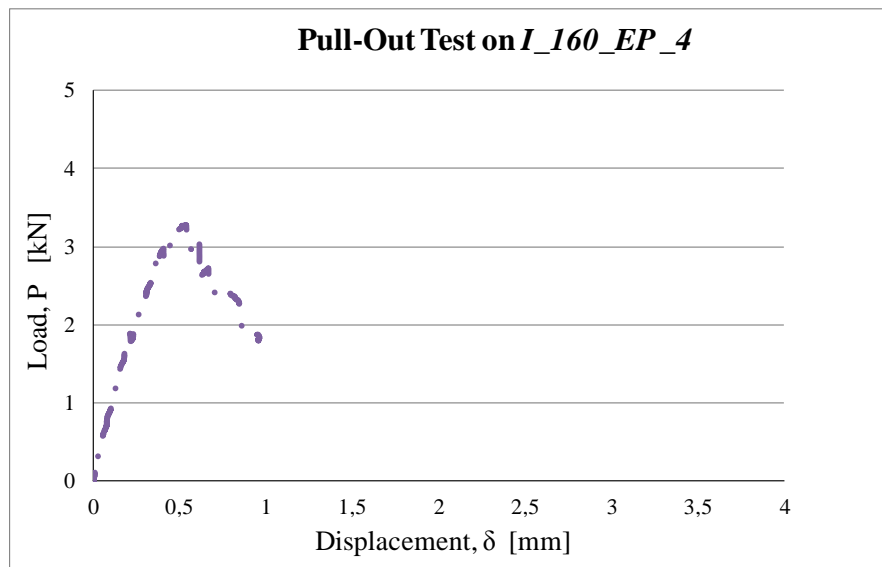


**Figure 3.13a.** Load-Displacement Curve for *I\_160\_EP\_4* specimen at loading-point.

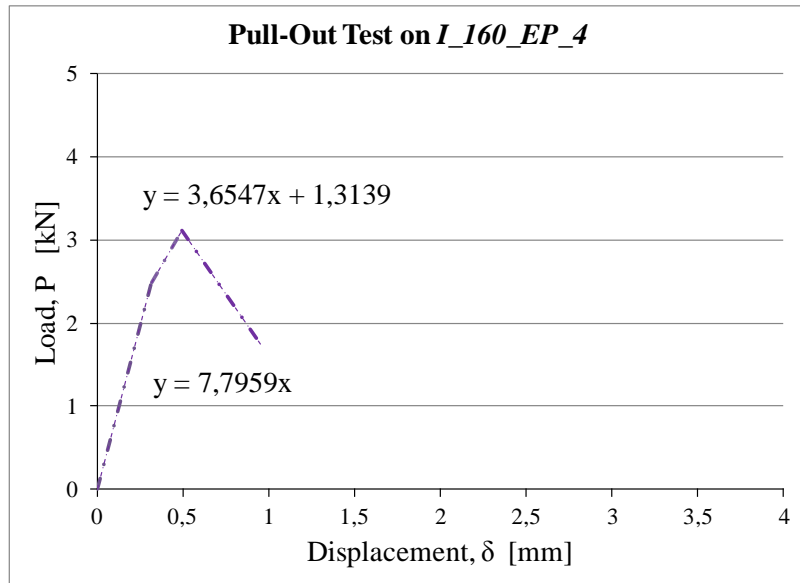


**Figure 3.13b.** Linearized Load-Displacement Curve for *I\_160\_EP\_4* specimen at loading-point.

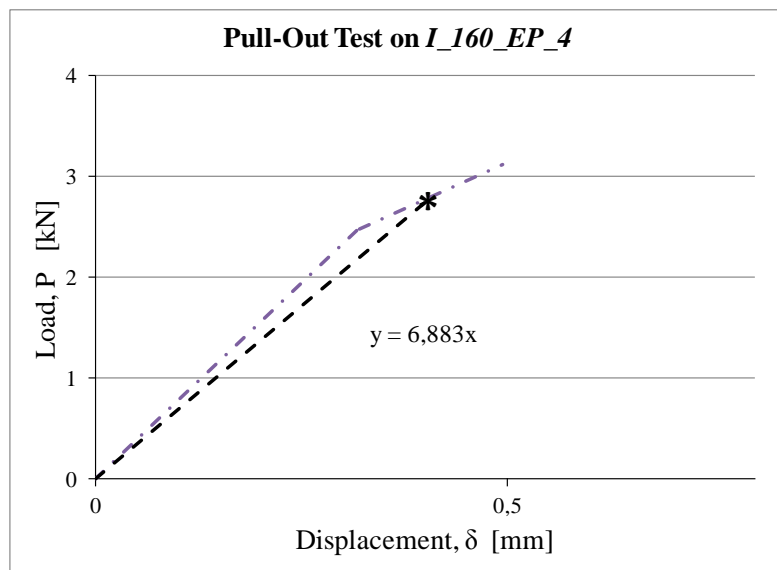


**Figure 3.13c.** Proposed Load-Displacement Curve for *I\_160\_EP\_4* specimen.



- *Specimen #4: I\_160\_EP\_4bis*

For the *I\_160\_EP\_4bis* specimen, the  $P$ - $\delta$  behavior was similar to *I\_160\_EP\_4* specimen where linearity was observed up to an axial displacement level of 0.3146 mm, corresponding to a load level of 1.9829 kN. Beyond this point, the stiffness decreased while the relation between the load and displacement remained linear up to 1.1049 mm displacement and 3.7942 kN load. After which, the initiation of local junction failure were observed leading to a separation between the flange from the web as show in Figure 3.14. Figures 3.15a,b show the load-displacement curve and the equivalent linearized relation at loading-point, respectively. Figure 3.15c shows the proposed average stiffness of this specimen.

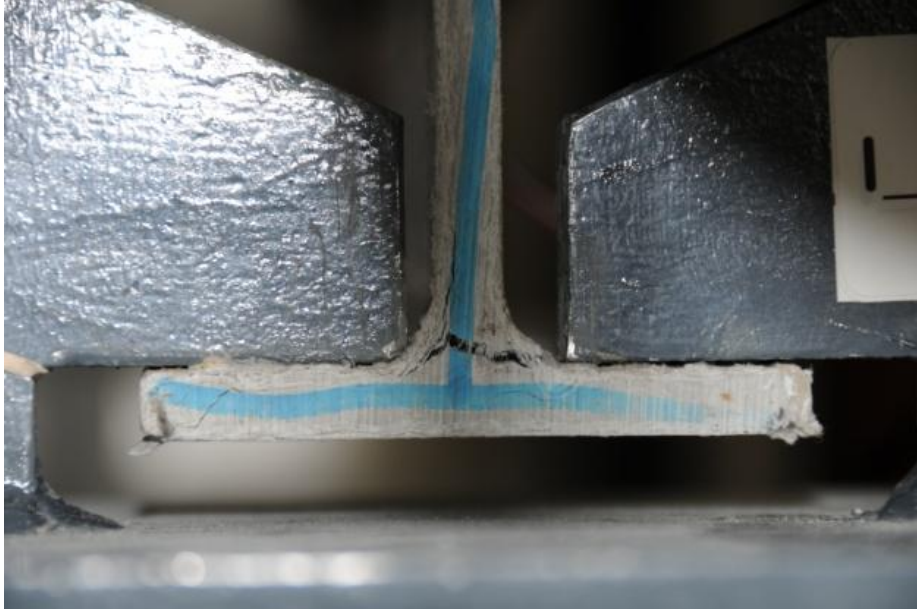


**Figure 3.14.** Web/Flange Junction Failure of *I\_160\_EP\_4bis* specimen.

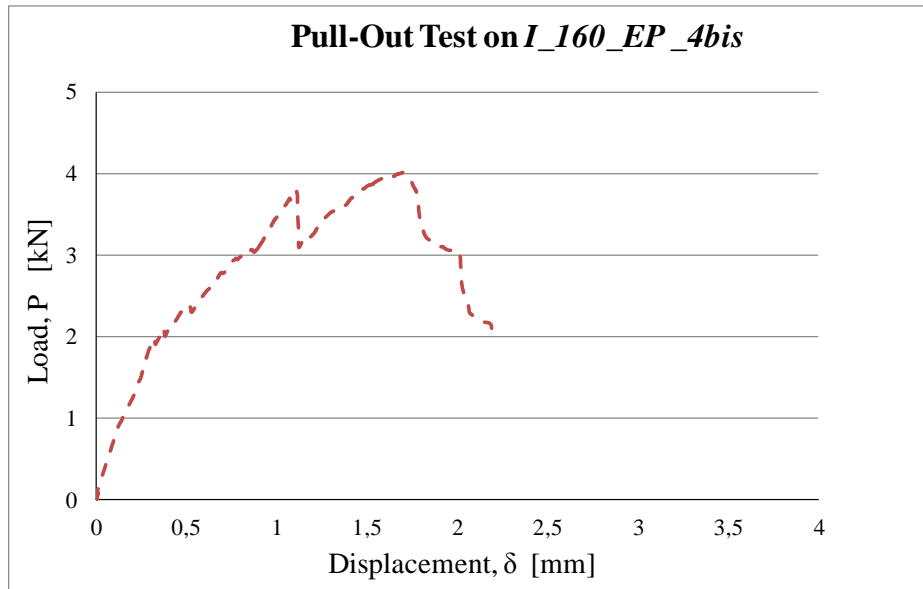


**Figure 3.15a.** Load-Displacement Curve for *I\_160\_EP\_4bis* specimen at loading-point.

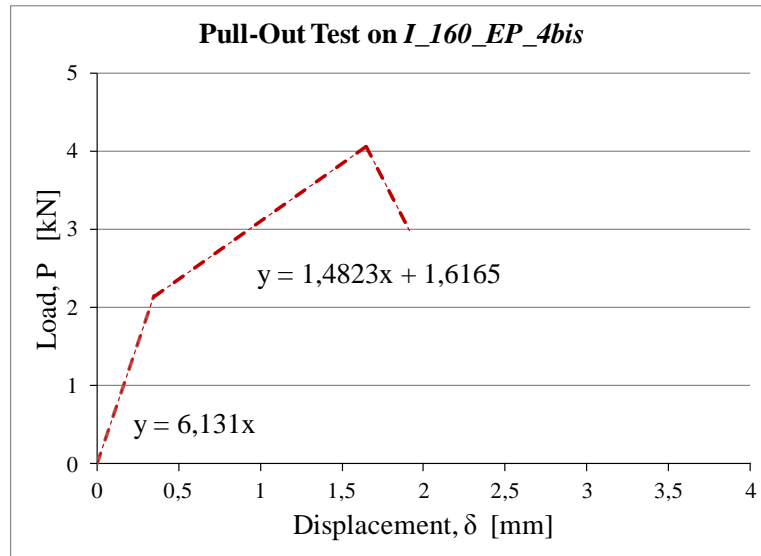


**Figure 3.15b.** Linearized Load-Displacement Curve for *I\_160\_EP\_4bis* specimen at loading-point.

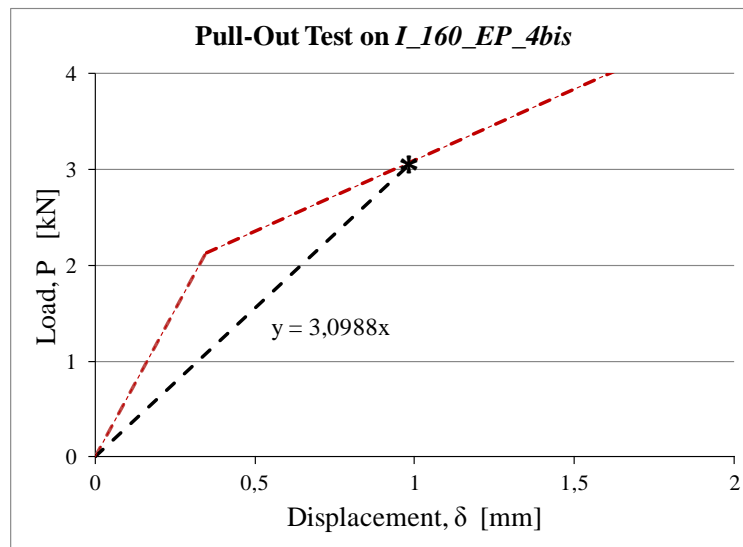


**Figure 3.15c.** Proposed Load-Displacement Curve for *I\_160\_EP\_4bis* specimen.

- *Specimen #5: L\_160\_MP\_1*

For the specimen *L\_160\_MP\_1* the axial junction displacement increased proportionally with load level until reaching a displacement equal to 0.5776 mm and load equal to 10.3826 kN. Beyond this point, local failure started to occur leading to a complete separation of the flange from the web that was initiated at the location of the pull load line and propagated along the rest of the junction length as shown in Figure 3.16. Figure 3.17a shows the load-displacement curve at mid-point for the junction of this specimen. The equivalent linearized load-displacement relation measured at the specimen's mid-point is shown in Figure 3.17b. Figure 3.17c shows the proposed average axial junction stiffness for this specimen.



**Figure 3.16.** Web/Flange Junction Failure of *I\_160\_MP\_1* specimen.

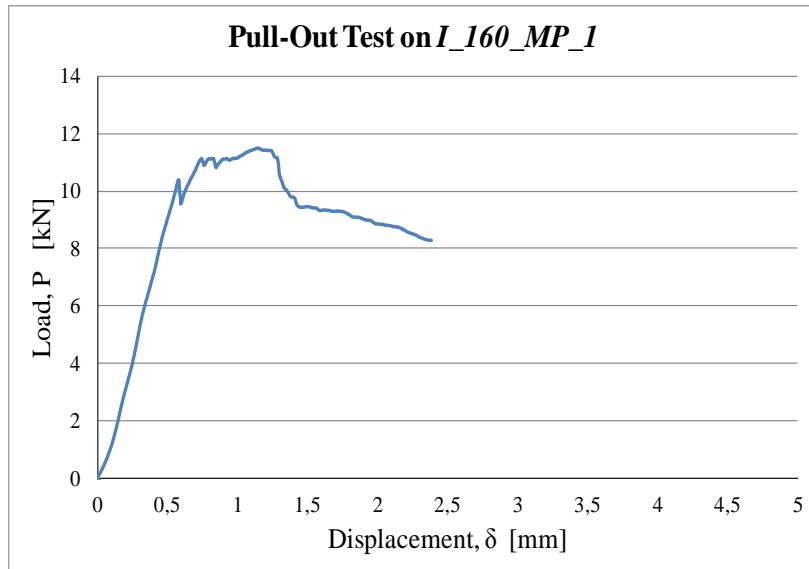


**Figure 3.17a.** Load-Displacement Curve for *I\_160\_MP\_1* specimen at mid-point.

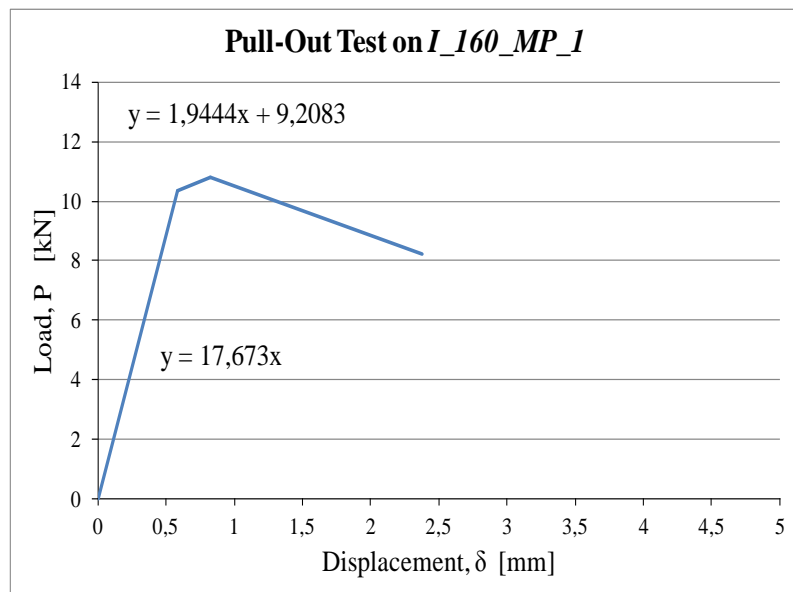


**Figure 3.17b.** Linearized Load-Displacement Curve for *I\_160\_MP\_1* specimen at mid-point.

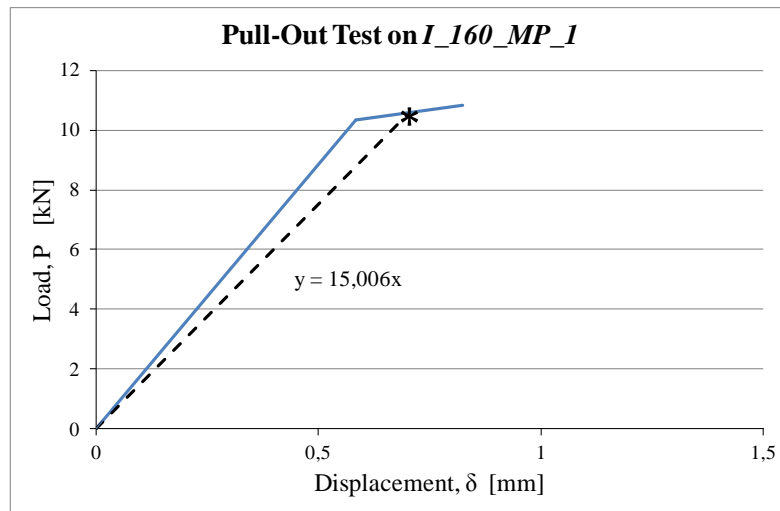
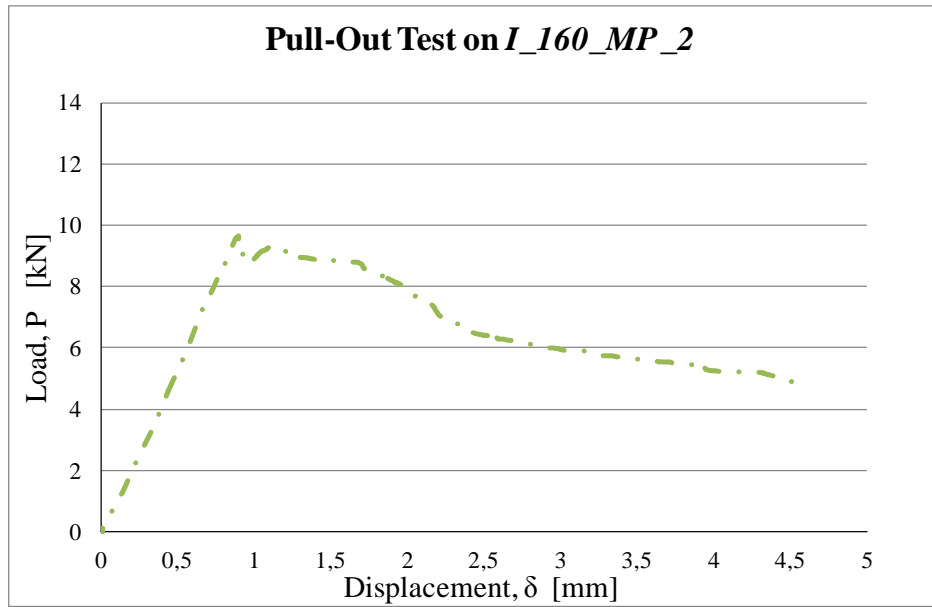


Figure 3.17c. Proposed Load-Displacement Curve for *I\_160\_MP\_1* specimen.

- Specimen #6: *I\_160\_MP\_2*

For the *I\_160\_MP\_2* specimen, a similar  $P$ - $\delta$  behavior was obtained where linearity continued up to a displacement of 1.0952 mm corresponding to a failure load level of 9.2705 kN. The failure of the web-flange junction was similar to that observed for *I\_160\_MP\_1* specimen. The load-displacement curve at the specimen's midpoint is shown in Figure 3.18a and the corresponding linearized curve is shown in Figure 3.18b. It should be noted that the average and initial linear stiffness values are identical for this specimen.



**Figure 3.18a.** Load-Displacement Curve for *I\_160\_MP\_2* specimen at mid-point.



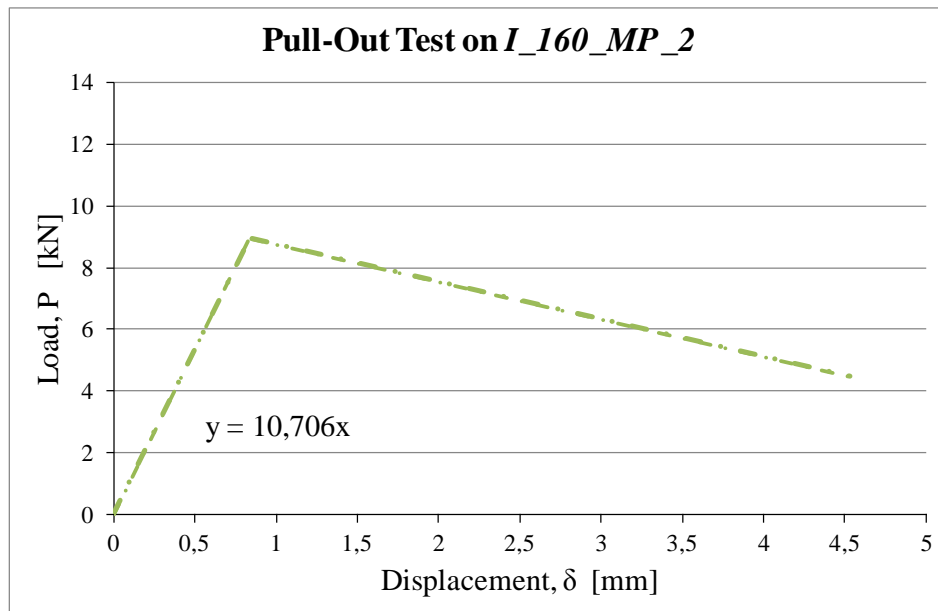


**Figure 3.18b.** Linearized Load-Displacement Curve for *I\_160\_MP\_2* specimen at mid-point.

- Specimen #7: *I\_160\_MP\_3*

For the *I\_160\_MP\_3* specimen, as the load was applied, axial displacement increased linearly 0.998 mm that was reached at a load of 9.177 kN. After which, a stiffness degradation was observed and the load-displacement ( $P-\delta$ ) curve followed a non-linear behavior until a 1.622 mm displacement level was reached, corresponding to a 9.74 kN axial load. Beyond this level, signs of failure started leading to a complete separation between the flange and web as already observed for *I\_160\_MP\_1* and *I\_160\_MP\_2* specimens.

Figure 3.19a shows the load-displacement curve at mid-point. The equivalent linearized load-displacement relation measured at specimen's mid-point is shown in Figure 3.19b. Figure 3.19c shows the proposed average axial junction stiffness for this specimen.

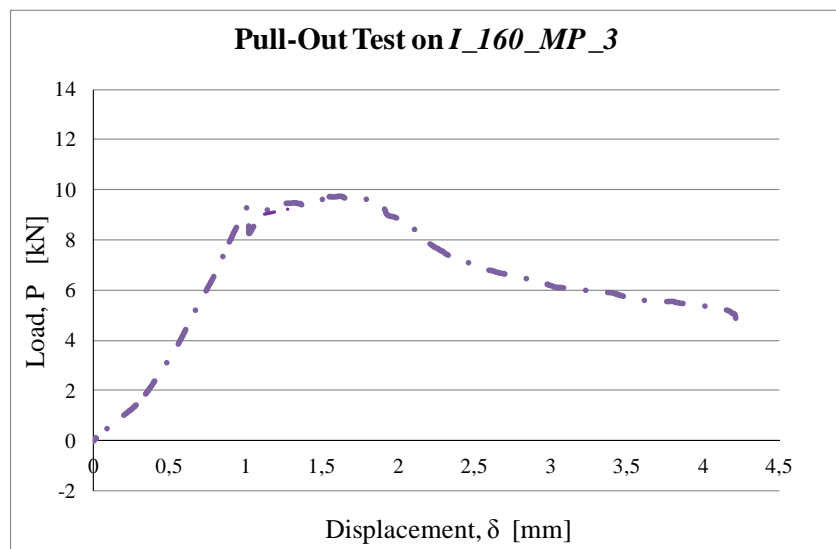


**Figure 19a.** Load-Displacement Curve for *I\_160\_MP\_3* specimen at mid-point.

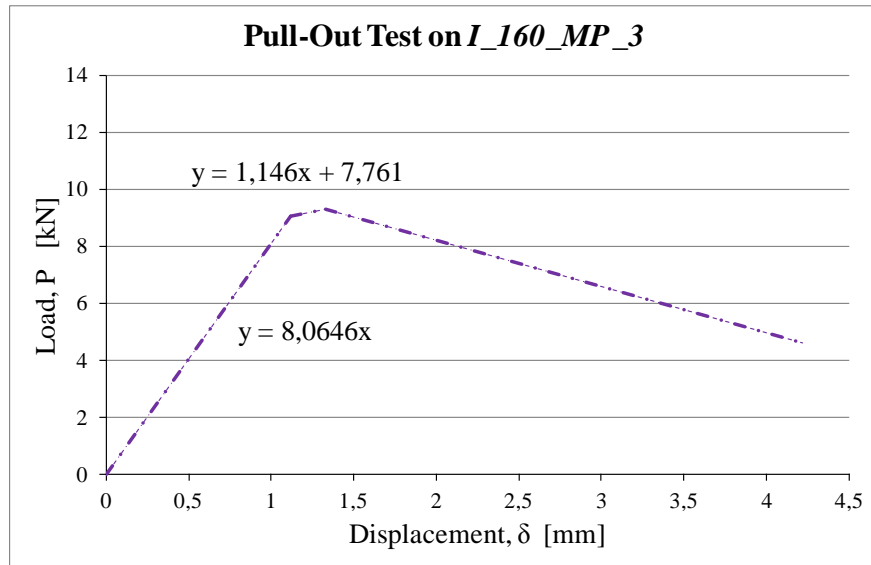


**Figure 19b.** Linearized Load-Displacement Curve for  $I_{160\_MP\_3}$  specimen at mid-point.

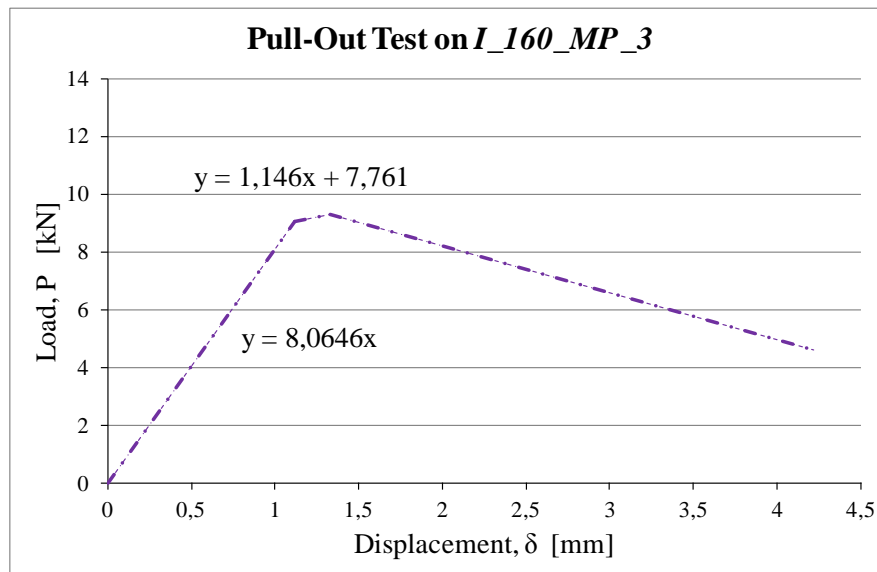


**Figure 19c.** Proposed Load-Displacement Curve for  $I_{160\_MP\_3}$  specimen.

- Specimen #8: *I\_160\_MP\_4*

As shown in Figure 20a, for the *I\_160\_MP\_4* specimen, the  $P$ - $\delta$  behavior was similar to the *I\_160\_MP\_3* specimen where linearity was observed up to an axial displacement level of 1.086 mm, corresponding to a load equal to 10.12 kN. After which, a stiffness degradation was observed and the load-displacement curve followed a non-linear behavior until a 1.53 mm displacement level was reached, corresponding to an axial load of 11.21 kN. After this load level, failure started to occur as described for the previous specimens. Figure 3.20b shows the linearized load-displacement relation measured at the specimen's mid-point. Figure 3.20c shows the proposed average axial junction stiffness for this specimen.

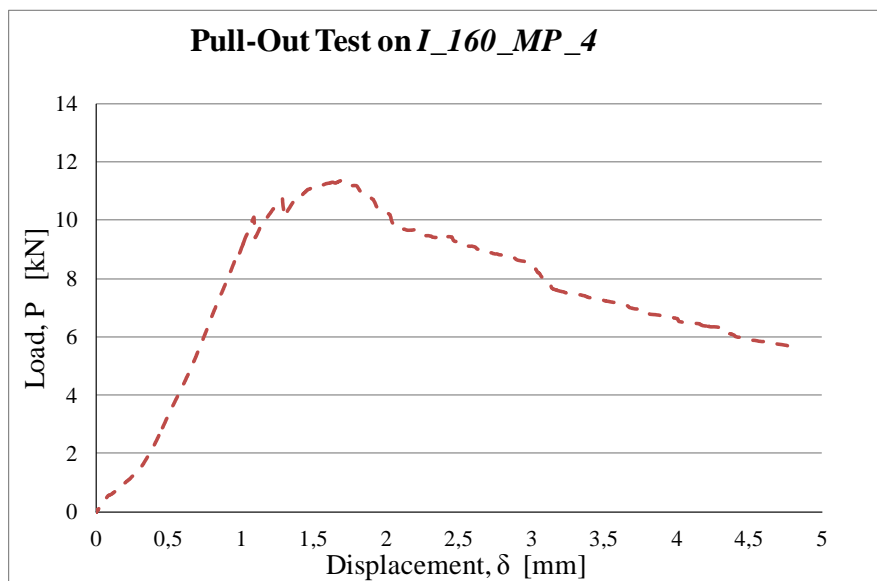


**Figure 3.20a.** Load-Displacement Curve for *I\_160\_MP\_4* specimen at mid-point.

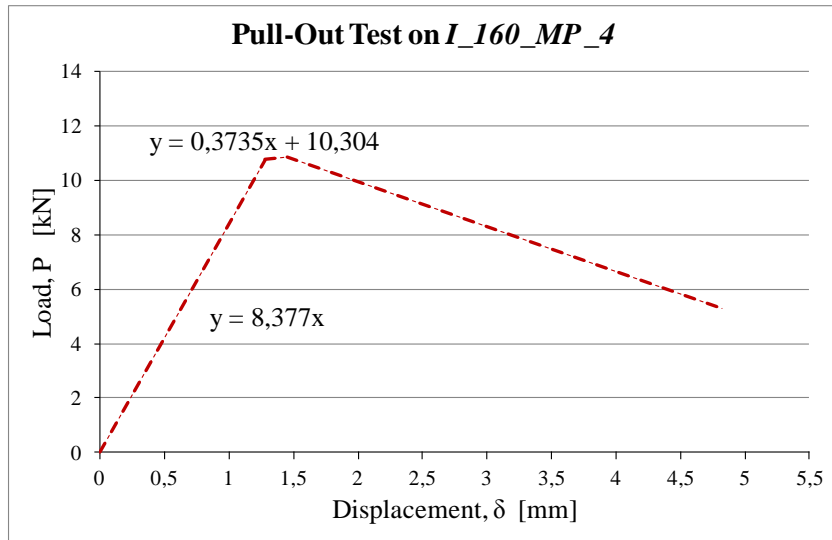


**Figure 3.20b.** Linearized Load-Displacement Curve for  $I_{160\_MP\_4}$  specimen at mid-point.

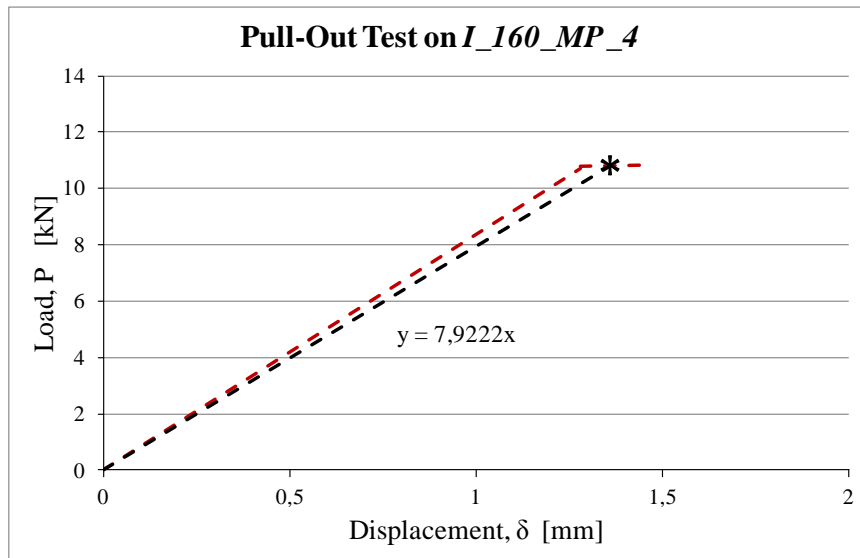


**Figure 3.20c.** Proposed Load-Displacement Curve for  $I_{160\_MP\_4}$  specimen.

- *Specimen #9: I\_200\_EP\_1*

For the *I\_200\_EP\_1* specimen, the displacement was observed increasing linearly with load until achieving a displacement equal to 0.46 mm and load equal to 6.29 kN. After this load level, failure started to occur, as shown in Figure 3.21. It should be noted that the failure mode of this specimen was different than those reported earlier for *I\_160\_EP* specimens where the failure did not occur at the junction (*resin-rich zone*) rather, it occurred at the fiber-rich web zone. Based on this fact, a higher strength value was recorded due to the presence of the fibres in the web. Figure 3.22a shows the load–displacement curve at loading-point while the equivalent linearized load-displacement curve is shown in Figure 3.22b. It should be noted that the average and initial linear stiffness values are identical for this specimen.

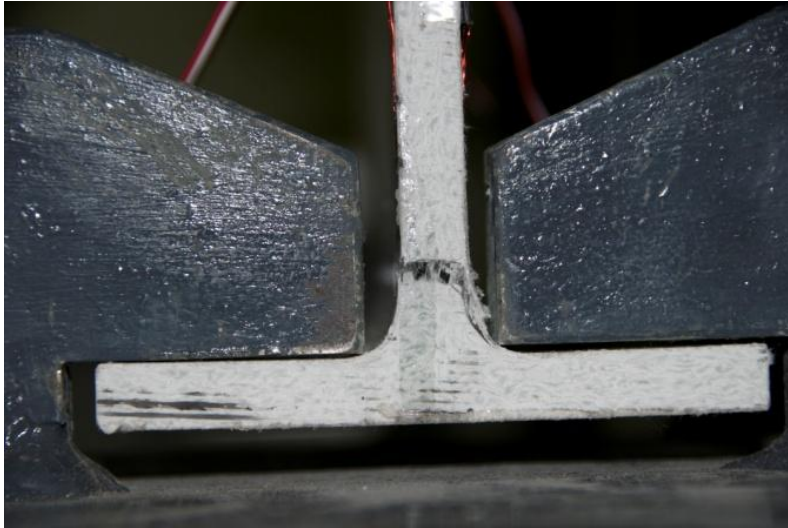


Figure 3.21. Web/Flange Junction Failure of *I\_200\_EP\_1* specimen.

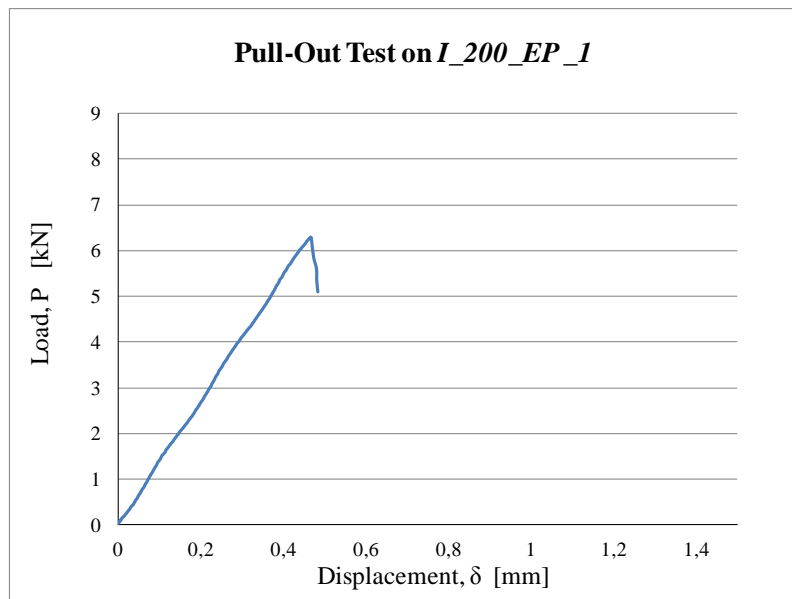
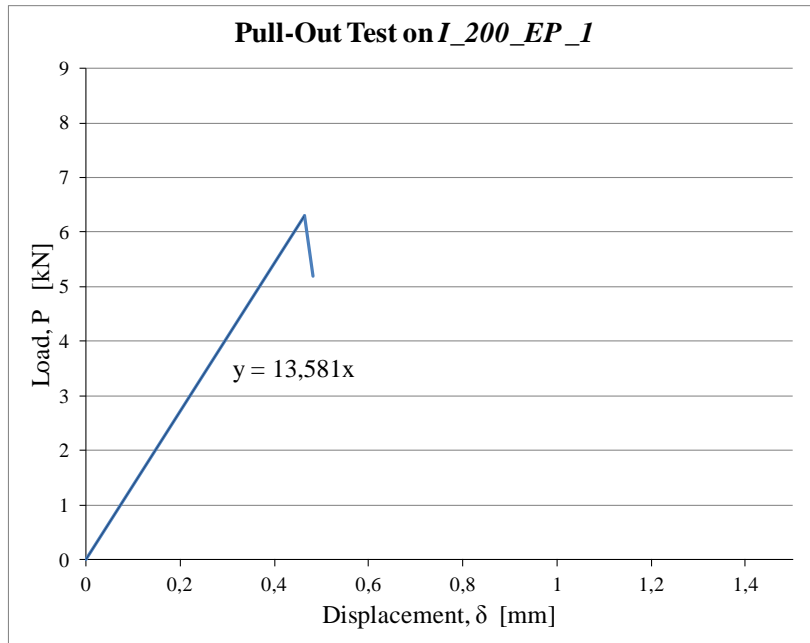


Figure 3.22a. Load-Displacement Curve for *I\_200\_EP\_1* specimen at loading-point.



**Figure 3.22b.** Linearized Load-Displacement Curve for *I\_200\_EP\_1* specimen at loading-point.

- Specimen #10: *I\_200\_EP\_2*

For the specimen *I\_200\_EP\_2*, the displacement and load were linearly proportional up to a displacement equal to 0.636 mm and a load equal to 5.006 kN. Beyond this point, failure started to occur (Fig. 3.23). Again, the failure occurred at the lower portion of the web as for *I\_200\_EP\_1* specimen. Figure 3.24a shows the load-displacement curve at loading-point. The equivalent linearized load-displacement relation measured at the specimen's loading-point is shown in Figure



3.24b. It should be noted that the average and initial linear stiffness values are identical for this specimen.



**Figure 3.23.** Web/Flange Junction Failure of *I\_200\_EP\_2* specimen.

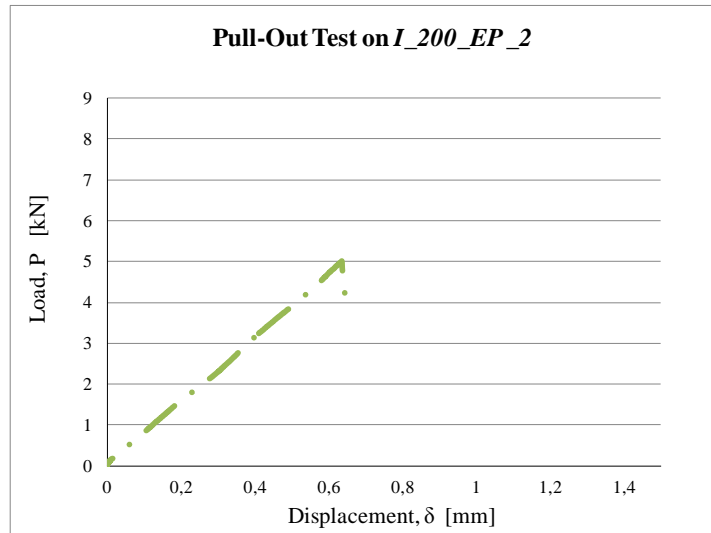


**Figure 3.24a.** Load-Displacement Curve for *I\_200\_EP\_2* specimen at loading-point.

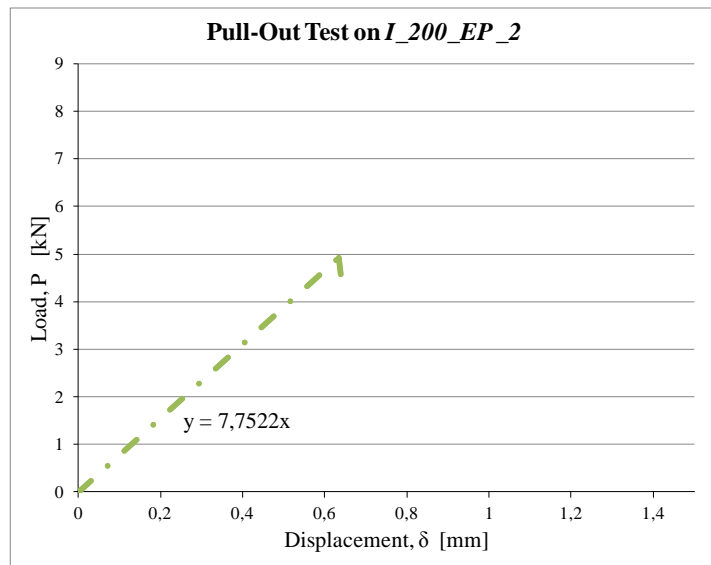


**Figure 3.24b.** Linearized Load-Displacement Curve for *I\_200\_EP\_2* specimen at loading-point.

- Specimen #11: *I\_200\_EP\_3*

As shown in Figure 3.25a, for the *I\_200\_EP\_3* specimen, the  $P$ - $\delta$  behavior was similar to the two previous specimens where linearity was observed up to a displacement level of 0.94mm, corresponding to a load equal to 8.04 kN. The linearized load-displacement relation measured at the specimen's loading-point is shown in Figure 3.25b. It should be noted that the average and initial linear stiffness values are identical for this specimen. The failure of the specimen is shown in Figure 3.26.

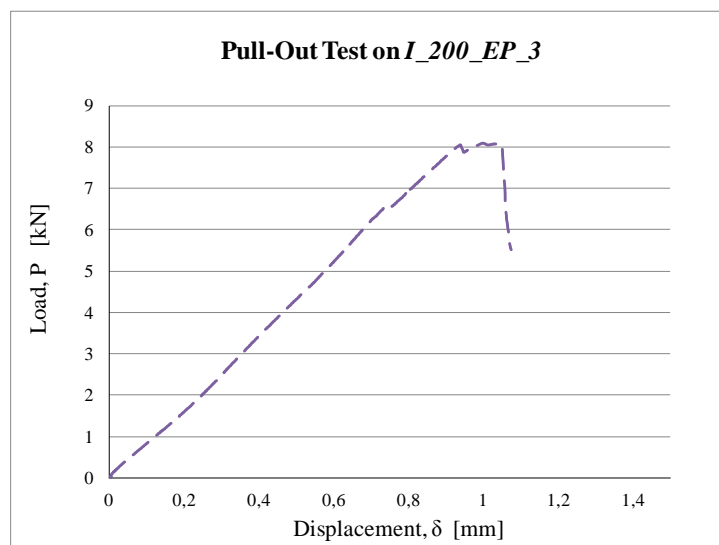


**Figure 3.25a.** Load-Displacement Curve for *I\_200\_EP\_3* specimen at loading-point.

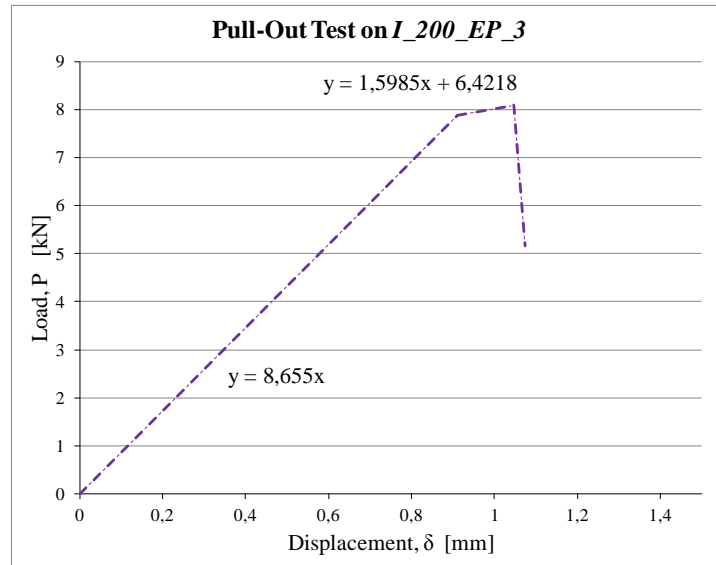


**Figure 3.25b.** Linearized Load-Displacement Curve for *I\_200\_EP\_3* specimen at loading-point.



**Figure 3.26.** Web/Flange Junction Failure of *I\_200\_EP\_3* specimen.

- Specimen #12: *L\_200\_EP\_4*

For the *L\_200\_EP\_4* specimen, the displacement increased linearly with an increasing load up to an axial displacement of 0.701 mm, corresponding to a load level of 5.24 kN. After which, signs of localized failure started to appear. This failure increases rapidly and determines the separation between the flange and web as shown in Figure 3.27. Figure 3.28a shows the load-displacement curve at loading-point. The equivalent linearized load-displacement relation measured at the specimen's loading-point is shown in Figure 3.28b. It should be noted that the average and initial linear stiffness values are identical for this specimen.



**Figure 3.27.** Web/Flange Junction Failure of *L\_200\_EP\_4* specimen.

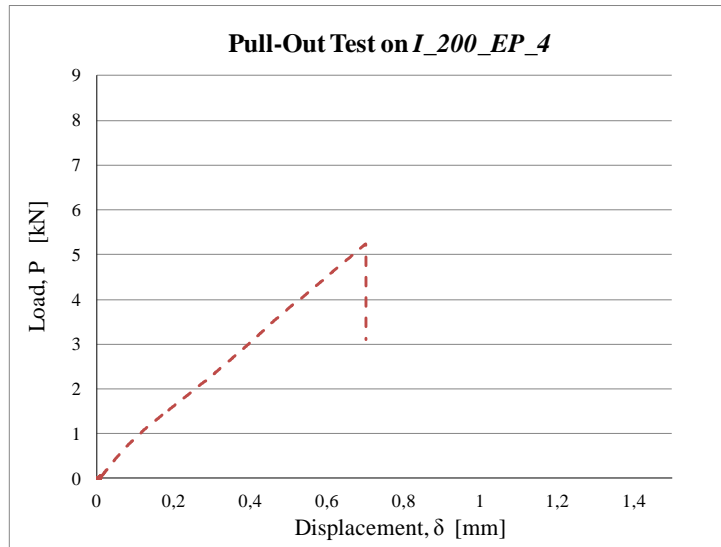


Figure 3.28a. Load-Displacement Curve for *I\_200\_EP\_4* specimen at loading-point.

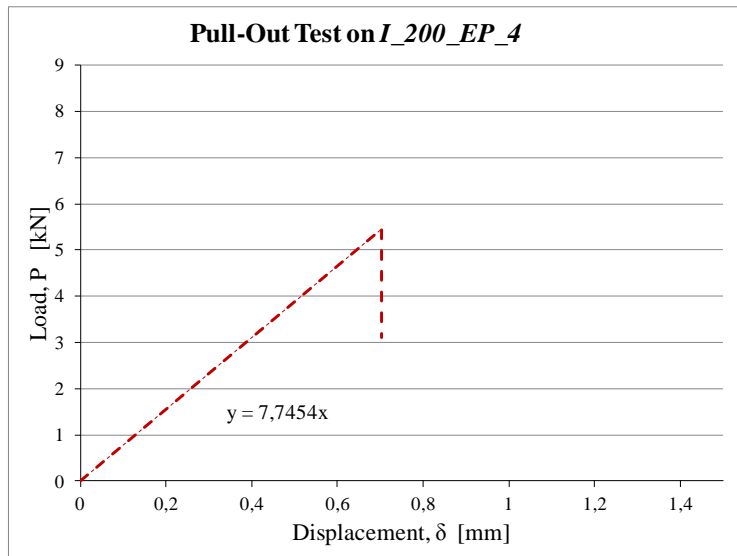
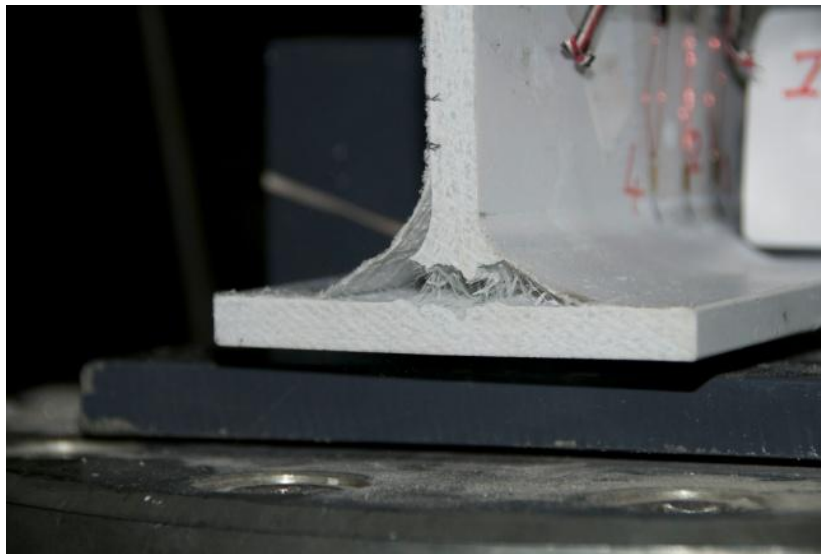


Figure 3.28b. Linearized Load-Displacement Curve for *I\_200\_EP\_4* specimen at loading-point.

- Specimen #13: *I\_200\_MP\_1*

For the specimen *I\_200\_MP\_1*, the displacement was observed increasing linearly with load until achieving a displacement equal to 1.18 mm and load equal to 17.90 kN. Beyond this level, failure started to occur. This failure increases rapidly and determines a large region of separation between the flange and web as shown in Fig. 3.29. Figure 3.30a shows the load–displacement curve at mid-point while Figure 3.30b shows the equivalent linearized load-displacement. It should be noted that the average and initial linear stiffness values are identical for this specimen.



**Figure 3.29.** Web/Flange Junction Failure of *I\_200\_MP\_1* specimen.

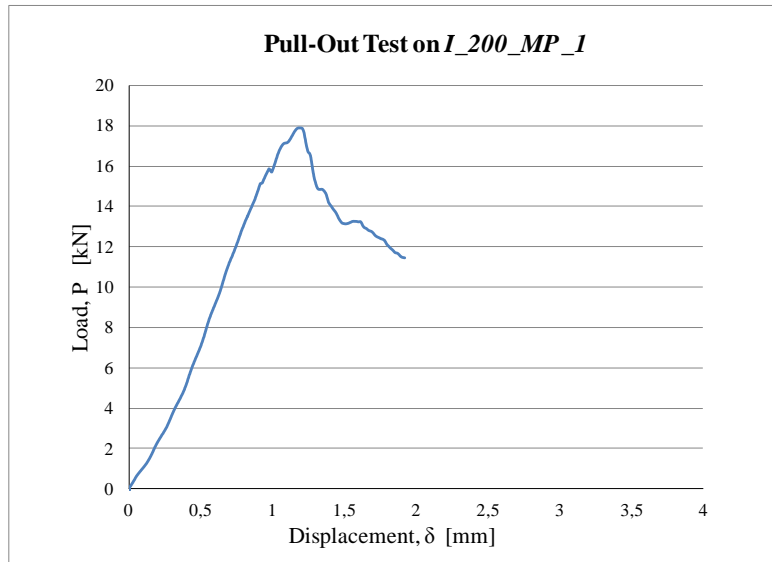


**Figure 3.30a.** Load-Displacement Curve for *L200\_MP\_1* specimen at loading-point.

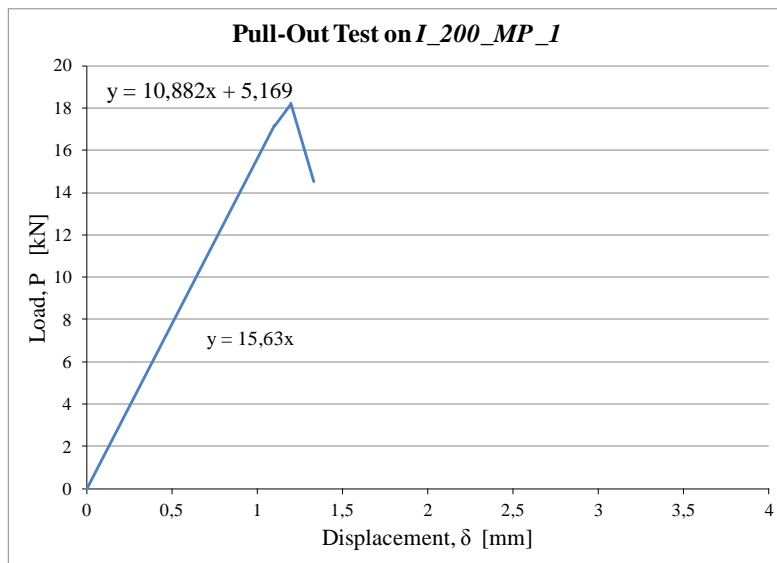


**Figure 3.30b.** Linearized Load-Displacement Curve for *L200\_MP\_1* specimen at loading-point.



- Specimen #14: *I\_200\_MP\_2*

For the *I\_200\_MP\_2* specimen, the displacement and load were linearly proportional up to a displacement equal to 1.48 mm and a load equal to 13.79 kN. After this point, failure started to occur as observed for the *I\_200\_MP\_1* specimen. Figure 3.31a shows the load-displacement curve at the mid-point while Figure 3.31b shows the equivalent linearized load-displacement at the loading-point. Similar to the previous mid-point junction specimens, the average and initial linear stiffness values are identical for this specimen.

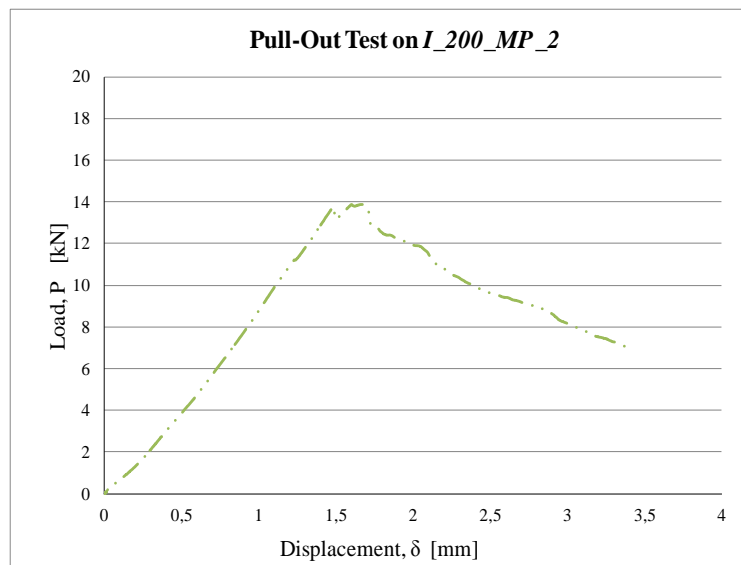


**Figure 3.31a.** Load-Displacement Curve for *I\_200\_MP\_2* specimen at loading-point.

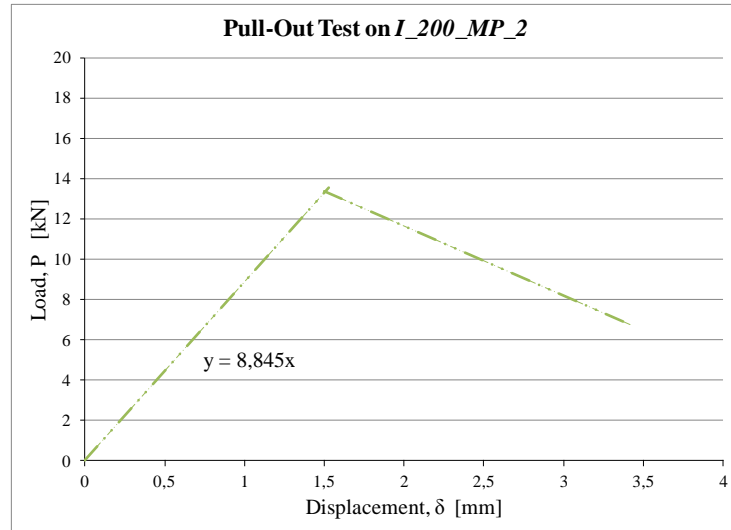


**Figure 3.31b.** Linearized Load-Displacement Curve for *I\_200\_MP\_2* specimen at loading-point.

- Specimen #15: *I\_200\_MP\_3*

As shown in Figure 3.32a, for the *I\_200\_MP\_3* specimen, the  $P$ - $\delta$  behavior was similar to the two previous specimens where linearity was observed up to a displacement level of 1.52 mm, corresponding to a load equal to 15.01 kN, after which, a failure mode occurred that is similar to those observed for the two previous specimens. Figure 3.32b shows the equivalent linearized load-displacement relation measured at the specimen's mid-point, respectively. It should be noted that the average and initial linear stiffness values are identical for this specimen.

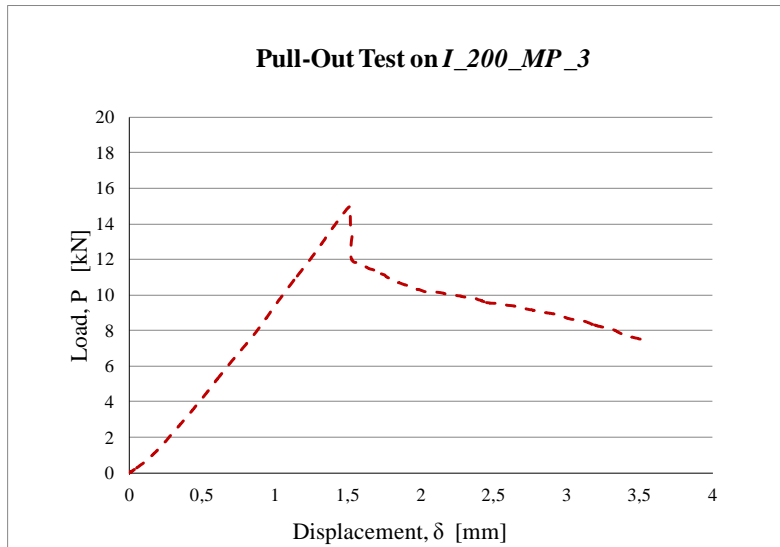


**Figure 3.32a.** Load-Displacement Curve for *I\_200\_MP\_3* specimen at loading-point.

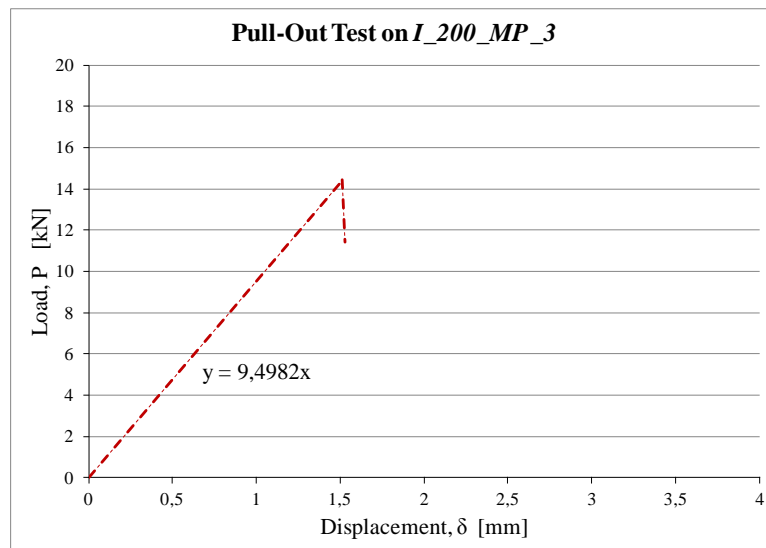


**Figure 3.32b.** Linearized Load-Displacement Curve for *I\_200\_MP\_3* specimen at loading-point.

Finally, Figures 3.33a-d show the experimental load-strain curves ( $P$ - $\epsilon_{yy}$ ) recorded at points SG1, SG2 and SG3 (Figures 4a,b) for specimens  $I_{160\_EP\_4}$ ,  $I_{160\_MP\_4}$ ,  $I_{200\_EP\_2}$  and  $I_{200\_MP\_1}$ , respectively.

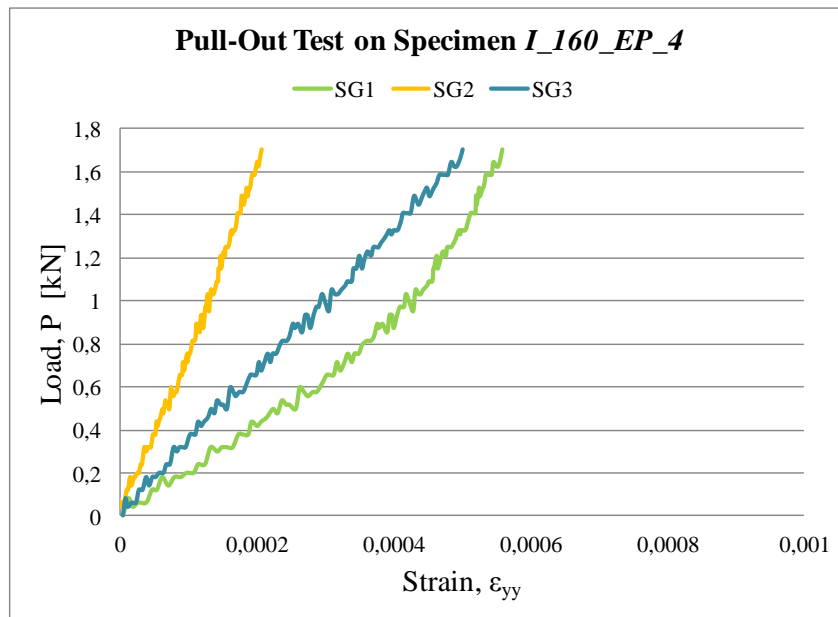


**Figure 3.33a.** Load ( $P$ ) versus experimental strain ( $\epsilon_{yy}$ ) of  $I_{160\_EP\_4}$  specimen.

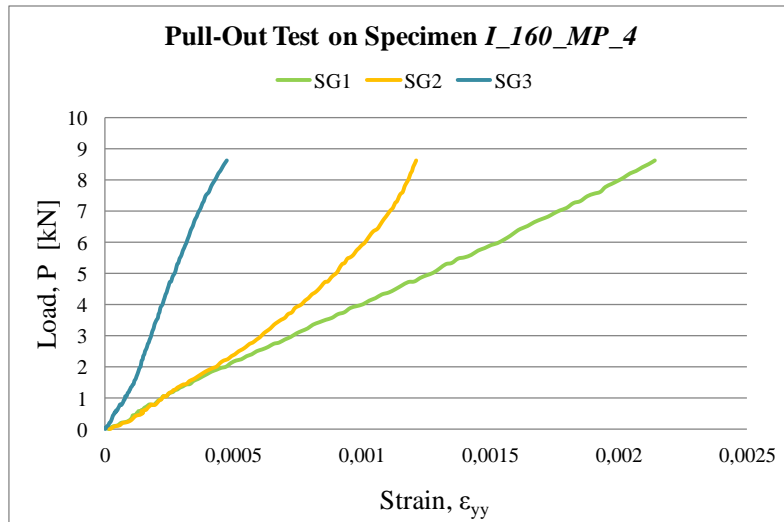


**Figure 3.33b.** Load ( $P$ ) versus experimental strain ( $\epsilon_{yy}$ ) of *I\_160\_MP\_4* specimen.

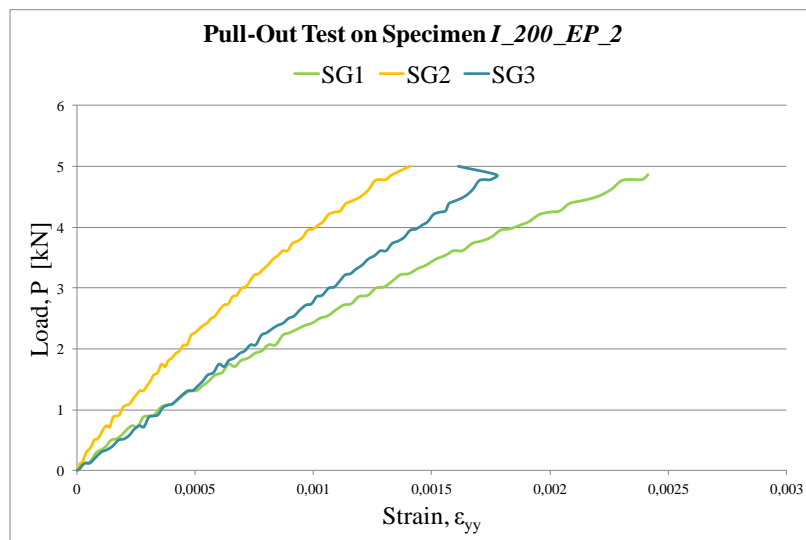


**Figure 3.33c.** Load ( $P$ ) versus experimental strain ( $\epsilon_{yy}$ ) of *I\_200\_EP*.

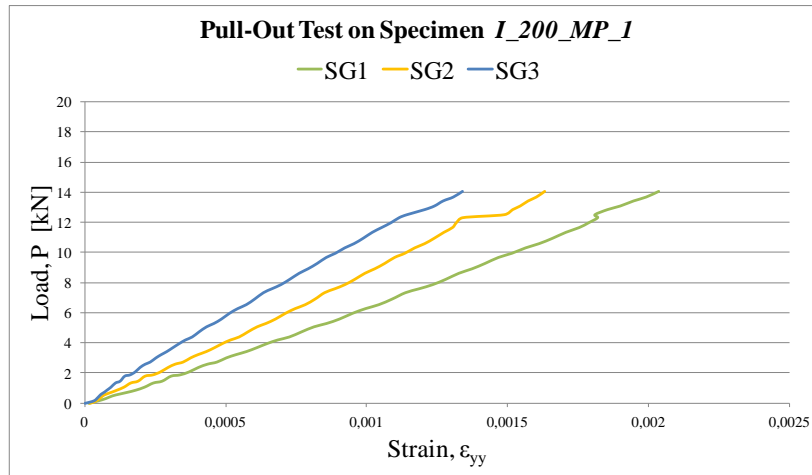


**Figure 3.33d.** Load (P) versus experimental strain ( $\epsilon_{yy}$ ) of I\_200\_MP\_1 specimen.

### 3.2.2. Second Group: Influence of the Location of Pull-Out Load on Junctions' Stiffness & Strength

Table 3.7 presents a summary of the stiffness and strength experimental values, including the two proposed stiffnesses ( $K_{jl}^A$  and  $\bar{K}_{jl}^A$ ) for the thirteen specimens evaluated in the second group. Figures 3.34a-d show the corresponding load-displacement curves. For completeness, the experimental results of specimens *I\_160\_EP* and *I\_160\_MP* of 300 mm length, belonging to the first group of the specimens, are also reported. Moreover, Figures 3.35a-d show the failure modes that were observed for specimens *I\_160\_MP\_20* (200 mm), *I\_160\_MP\_6* (300 mm), *I\_160\_MP\_7* (600 mm) and *I\_160\_EP\_12* (1200 mm), respectively. The linearized

load-displacement relations measured at the mid-point of the thirteen specimens evaluated in the second group are shown in Figures 3.36a-o. In the same figures the proposed average axial junction stiffness for these specimens are reported. Figure 3.37 shows the influence of the pull-out load location ( $d$ ) on the stiffness and strength of the junctions. As one can see, the mean value of the failure load of the junction of specimen  $I_{160}$  notably increases in the interval between  $d=0$  mm ( $I_{160\_EP\_L300}$ ) and  $d=150$  mm ( $I_{160\_MP\_L300}$ ), varying from 2.66 kN to 9.91 kN. As this distance increases, a slight decrease in the strength is observed. This could be related to the fact that as the length decreases, shear deformation becomes the predominant straining action subjecting a shorter area of the resin-rich junction to high stress concentrated that leads to premature failure of the junction. However, as the length increases, the junction stressed area increases resulting in a lower stress concentration. From the experimental observations, it is found that once the length became larger than the profile depth, its influence will have less effect and only a decrease in strength is observed. From the figure, one can notice that the highest strength is obtained at a distance  $d$  equal to about the depth of the PFRP I-profile. Based on this observation, one can define the *influence zone* to be extended to a distance equals to the depth of the PFRP member cross-section at which maximum junction strength is obtained. Table 3.8 summarizes the mean values of load, displacement and linear and average axial stiffness for all the specimens tested in this study. As expected, the  $I_{200}$  specimens present higher values of the

strength as compared to those obtained from  $L_{160}$  specimens, however, similar values of the axial stiffnesses are observed.

**Table 3.7.** Failure loads, displacements and linear axial stiffnesses obtained from experimental tests on  $L_{160\_MP}$  specimens (second group).

#	Specimens	Length	Load ( $P_l$ ) (linear limit)	$\delta_l$	Failure Load ( $P_f$ )	$\delta_f$	Linear Axial stiffness $K_{jl}^A$	Average Lin. Axial stiffness $\bar{K}_{jl}^A$
		[mm]	[kN]	[mm]	[kN]	[mm]	[kN/mm]	[kN/mm]
1	$L_{160\_EP\_2}$	300	2.6751	0.3652	3.1160	0.6484	8.3650	6.6361
2	$L_{160\_EP\_3}$	300	3.0551	0.5860	4.1860	1.1598	6.0995	4.5014
3	$L_{160\_EP\_4}$	300	2.9440	0.4326	3.2489	0.5367	7.7959	6.8830
4	$L_{160\_EP\_4\_bis}$	300	1.9829	0.3146	3.7942	1.1049	6.1310	3.0988
16	$L_{160\_MP\_9}$	200	8.1510	0.7470	8.1510	0.7470	11.0990	11.0990
17	$L_{160\_MP\_20}$	200	8.4315	0.9682	11.1010	1.5622	9.2123	7.8529
18	$L_{160\_MP\_16}$	200	8.0079	0.6581	9.7641	0.9344	12.6210	11.3270
5	$L_{160\_MP\_1}$	300	10.3826	0.5776	11.4842	1.1462	17.6730	15.0060
6	$L_{160\_MP\_2}$	300	9.2705	1.0952	9.2705	1.0952	10.7060	10.7060
7	$L_{160\_MP\_3}$	300	9.1769	0.9977	9.7393	1.6221	8.0646	7.4815
8	$L_{160\_MP\_4}$	300	10.1197	1.0858	11.2126	1.5285	8.3770	7.9222
19	$L_{160\_MP\_6}$	300	11.4778	0.9039	11.4778	0.9039	12.4980	12.4980
20	$L_{160\_MP\_13}$	300	9.0160	0.9247	10.2351	1.5017	12.8100	8.9726
21	$L_{160\_MP\_7}$	600	7.6560	0.8327	7.6560	0.8327	9.4464	9.4464
22	$L_{160\_MP\_10}$	600	10.2236	0.9196	10.7205	1.9937	12.1640	7.3172
23	$L_{160\_MP\_14}$	600	9.4137	0.9538	10.0458	1.1364	10.0680	10.0680
24	$L_{160\_MP\_17}$	600	10.0028	0.9786	12.1516	1.6323	10.0270	8.5880
25	$L_{160\_MP\_8}$	1200	8.2094	0.7658	8.2094	0.7658	11.1830	11.1830
26	$L_{160\_MP\_12}$	1200	8.0165	0.6968	8.8544	1.2362	11.7630	11.7630
27	$L_{160\_MP\_15}$	1200	7.9414	0.6263	7.9414	0.6263	13.2700	13.2700
28	$L_{160\_MP\_19}$	1200	10.0552	1.0085	12.5607	11.7937	9.1158	7.9788



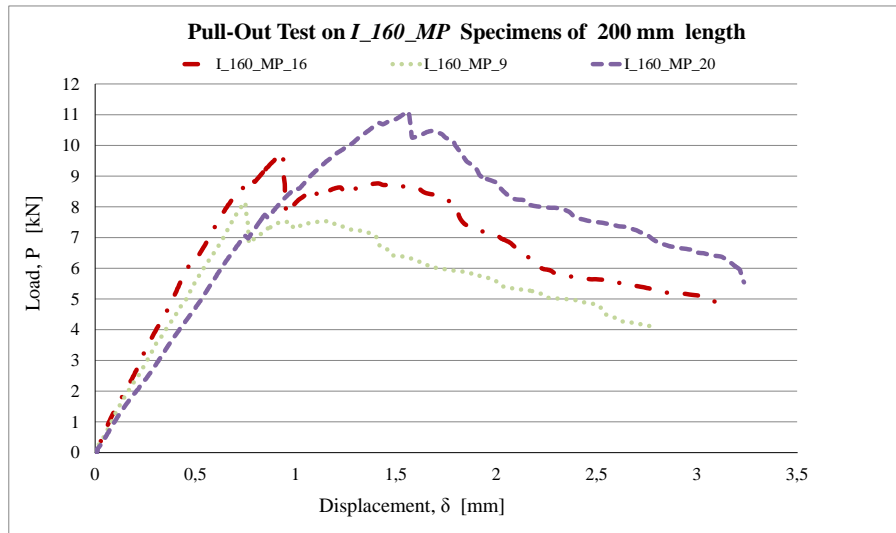


**Figure 3.34a.** Load ( $P$ ) versus displacement ( $\delta$ ) curve for  $I_{160\_MP}$  specimens of 200 mm length.

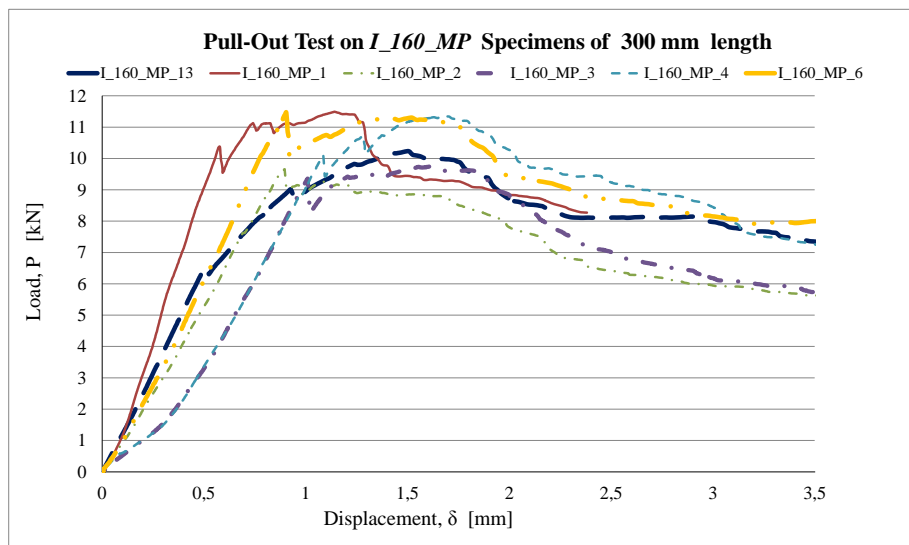


**Figure 3.34b.** Load ( $P$ ) versus displacement ( $\delta$ ) curve for  $I_{160\_MP}$  specimens of 300 mm length.

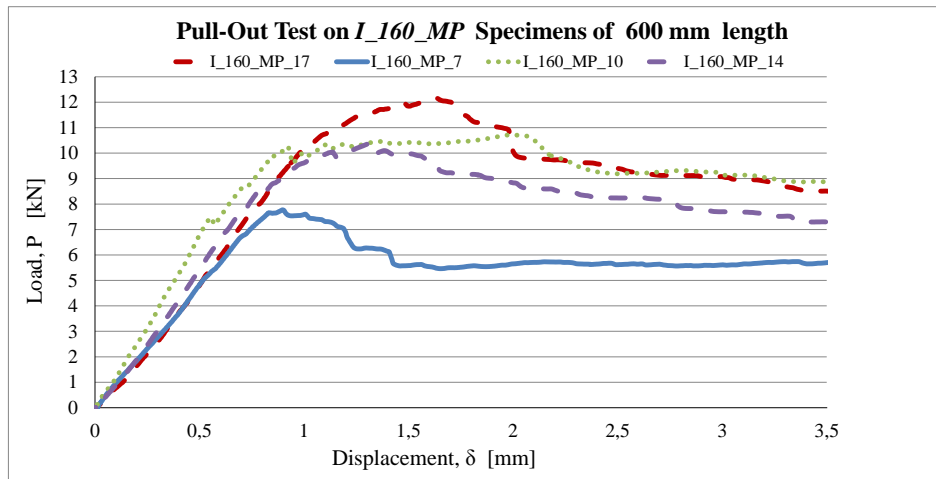


**Figure 3.34c.** Load ( $P$ ) versus displacement ( $\delta$ ) curve for  $I_{160\_MP}$  specimens of 600 mm length.

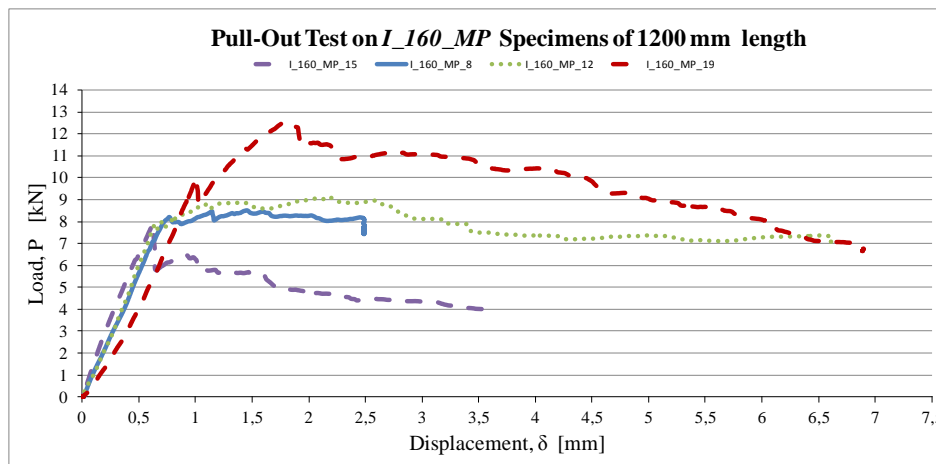


**Figure 3.34d.** Load ( $P$ ) versus displacement ( $\delta$ ) curve for  $I_{160\_MP}$  specimens of 1200 mm length.



**Figure 3.35a.** Failure mode of *I\_160\_MP\_20* specimen of 200 mm length.



**Figure 3.35b.** Failure mode of *I\_160\_MP\_6* specimen of 300 mm length.



**Figure 3.35c.** Failure mode of *I\_160\_MP\_7* specimen of 600 mm length.



**Figure 3.35d.** Failure mode of *I\_160\_MP\_12* specimen of 1200 mm length.

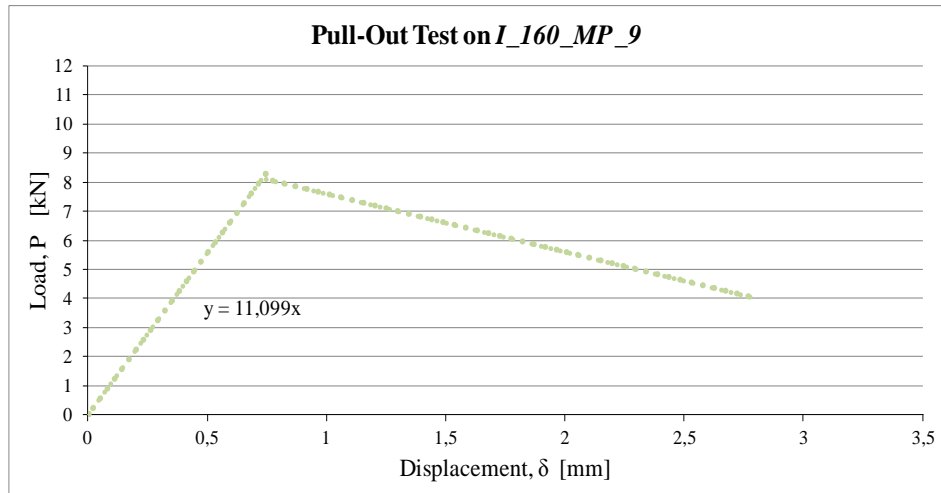


**Figure 3.36a.** Linearized Load-Displacement Curve for *I\_160\_MP\_9* specimen (200 mm) at loading-point.

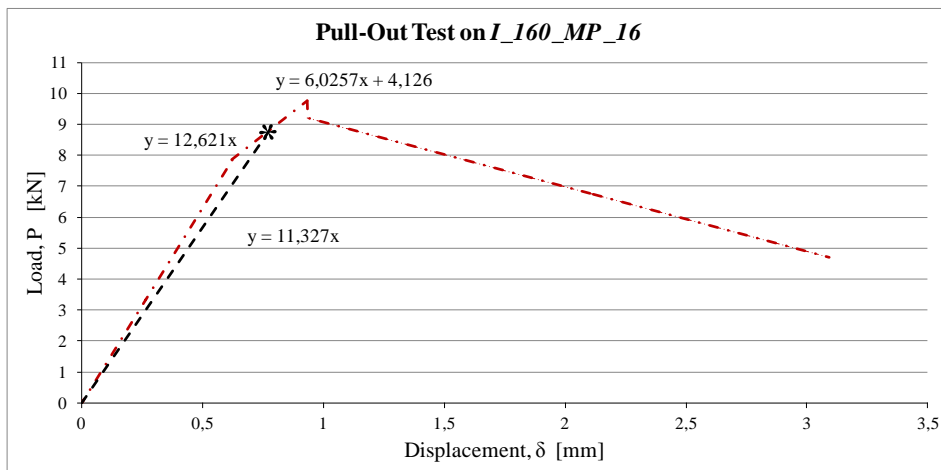


**Figure 3.36b.** Linearized Load-Displacement Curve for *I\_160\_MP\_16* specimen (200 mm) at loading-point.

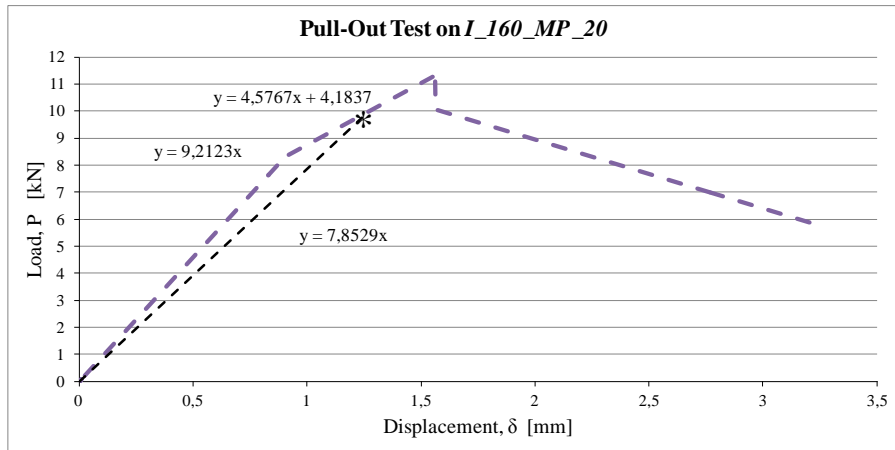


**Figure 3.36c.** Linearized Load-Displacement Curve for *I\_160\_MP\_20* specimen (200 mm) at loading-point.

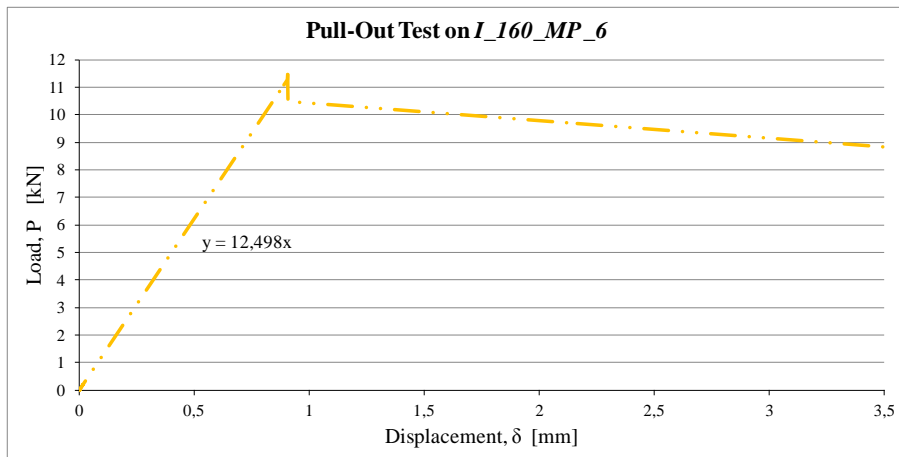


**Figure 3.36d.** Linearized Load-Displacement Curve for *I\_160\_MP\_6* specimen (300 mm) at loading-point.

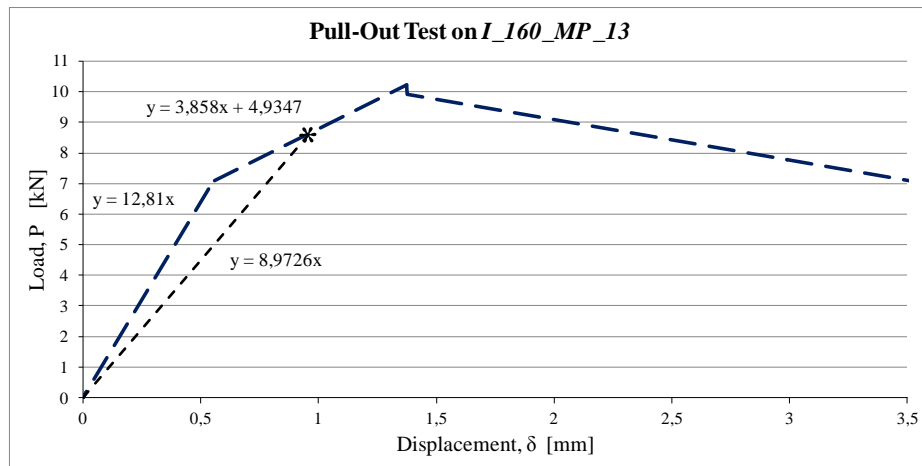


**Figure 3.36e.** Linearized Load-Displacement Curve for  $I_{160\_MP\_13}$  specimen (300 mm) at loading-point.

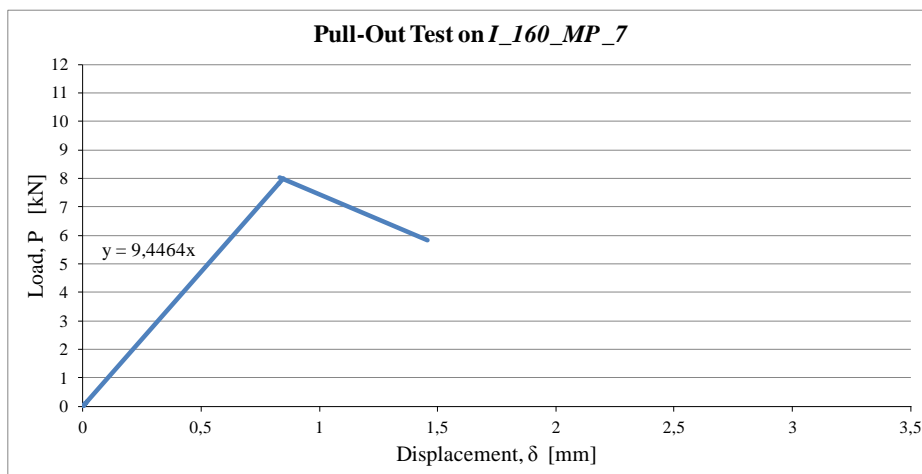


**Figure 3.36f.** Linearized Load-Displacement Curve for  $I_{160\_MP\_7}$  specimen (600 mm) at loading-point.

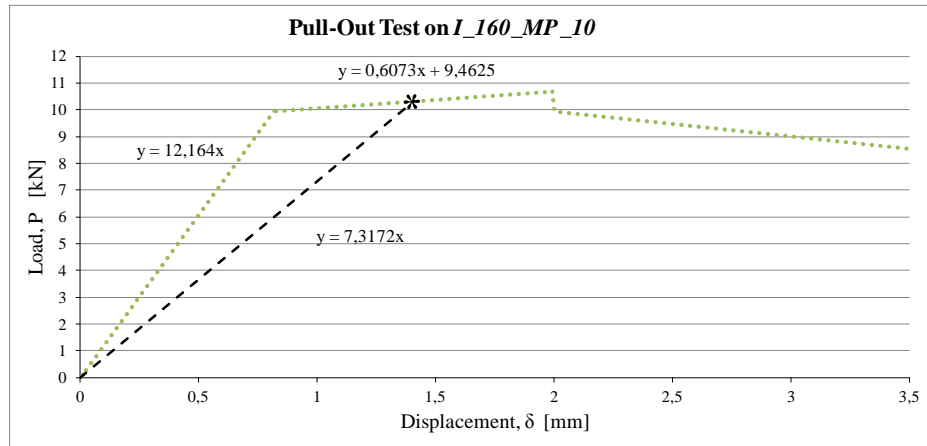


**Figure 3.36g.** Linearized Load-Displacement Curve for  $I_{160\_MP\_10}$  specimen (600 mm) at loading-point.

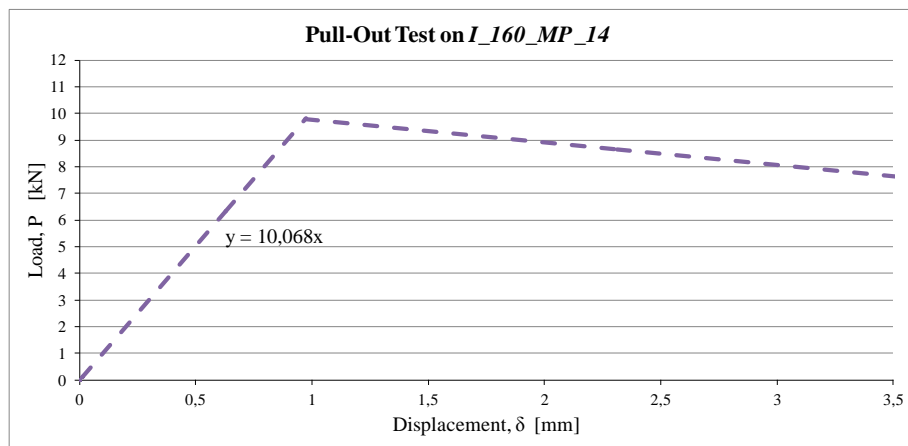


**Figure 3.36h.** Linearized Load-Displacement Curve for  $I_{160\_MP\_14}$  specimen (600 mm) at loading-point.



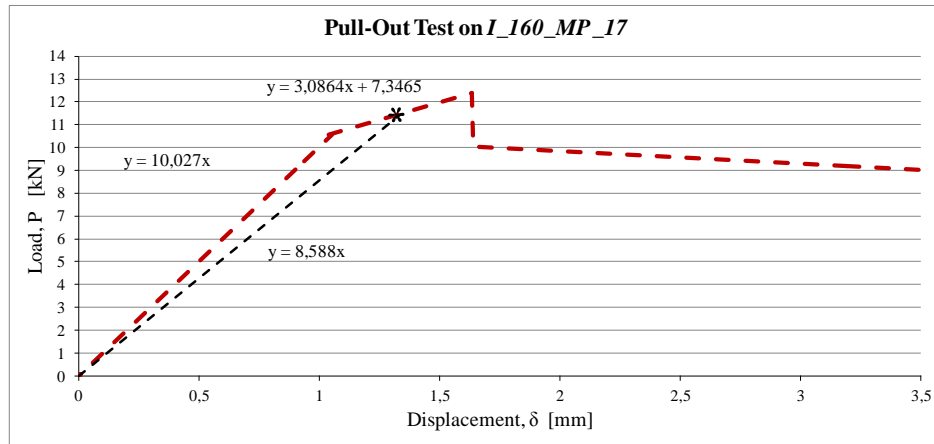


**Figure 3.36i.** Linearized Load-Displacement Curve for  $I_{160\_MP\_17}$  specimen (600 mm) at loading-point.

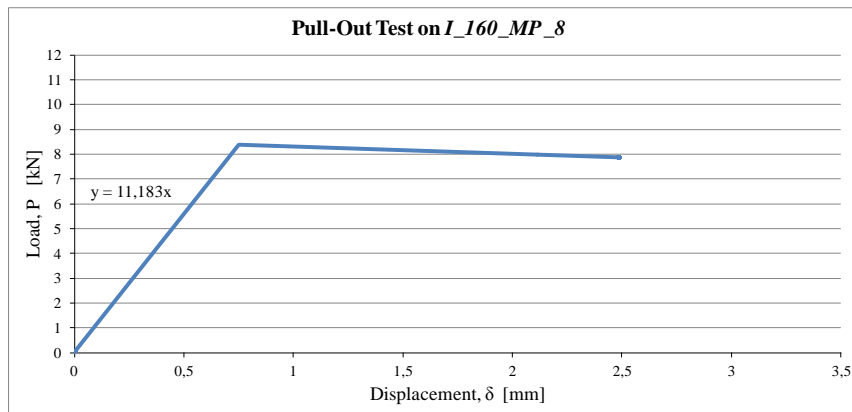


**Figure 3.36l.** Linearized Load-Displacement Curve for  $I_{160\_EP\_8}$  specimen (1200 mm) at loading-point.

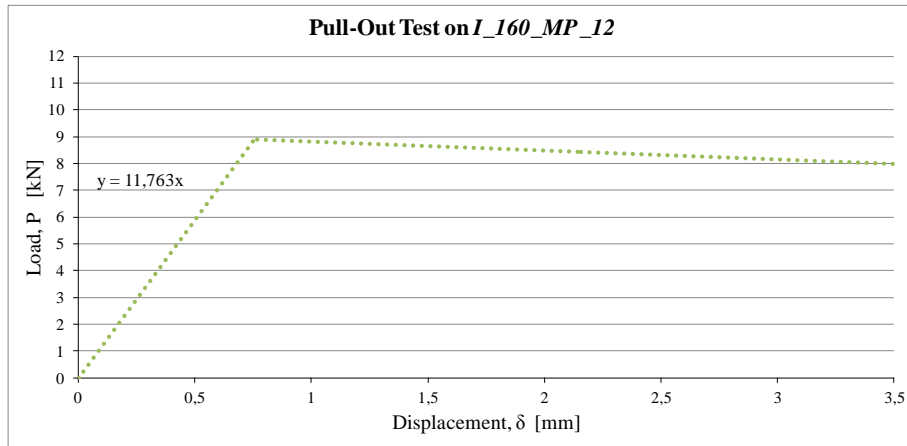


**Figure 3.36m.** Linearized Load-Displacement Curve for *I\_160\_EP\_12* specimen (1200 mm) at loading-point.

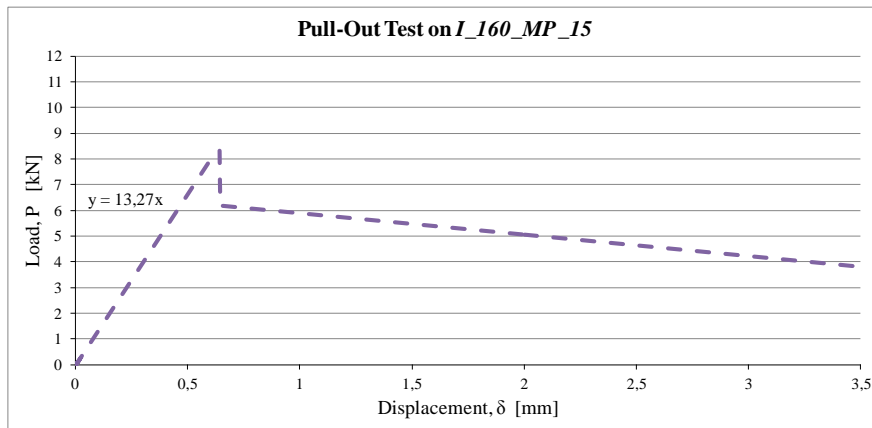


**Figure 3.36n.** Linearized Load-Displacement Curve for *I\_160\_EP\_15* specimen (1200 mm) at loading-point.

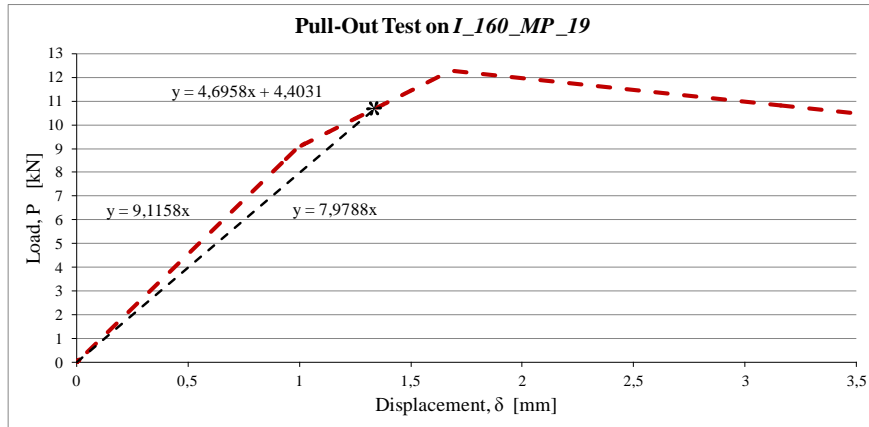


Figure 3.36. Linearized Load-Displacement Curve for *I\_160\_EP\_19* specimen (1200 mm) at loading-point.

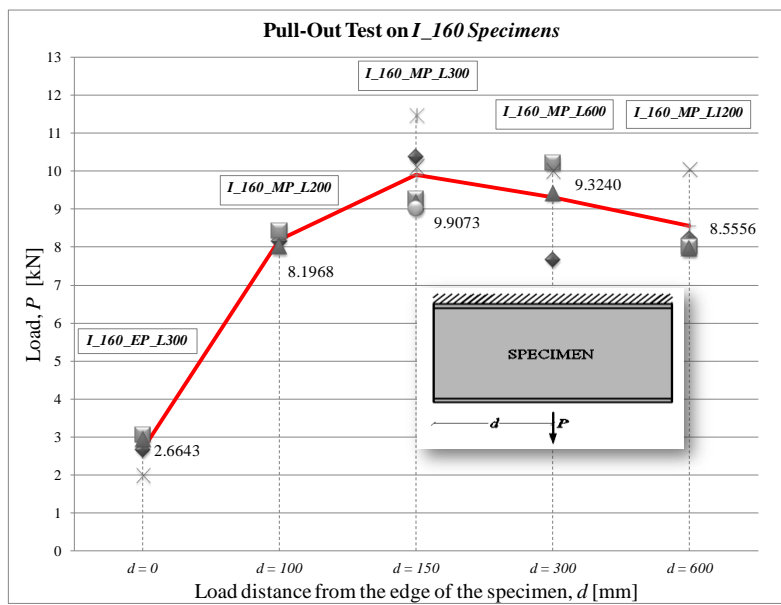


Figure 3.37. Influence of the load distance from the edge of the *I\_160* specimens on the failure strength of the web-flange junction.

**Table 3.8.** Mean values of failure loads, displacements and linear axial stiffnesses obtained from the experimental tests on all specimens.

#	Specimens	Length	Load ( $P_i$ ) (linear limit)	$\delta_i$	Failure Load ( $P_f$ )	$\delta_f$	Linear Axial stiffness $K_{jl}^A$	Average Lin. Axial stiffness $\bar{K}_{jl}^A$
		[mm]	[kN]	[mm]	[kN]	[mm]	[kN/mm]	[kN/mm]
1,2, 3, 4	I_160_EP	300	2.6643	0.4246	3.5863	0.8625	7.0978	5.2798
16,17,18	I_160_MP	200	8.1968	0.7911	9.4599	1.1543	10.9774	10.0929
5,6,7,8,19,20	I_160_MP	300	9.9073	0.9308	10.5270	1.3923	11.6881	10.4311
21,22,23,24	I_160_MP	600	9.3240	0.9212	10.1435	1.3988	10.4263	8.8549
25,26,27,28	I_160_MP	1200	8.5556	0.7744	9.3915	1.1055	11.3330	10.5487
9,10,11,12	I_200_EP	300	6.1450	0.6837	6.1450	0.6837	9.4334	9.4334
13,14,15	I_200_MP	300	15.5672	1.3925	15.5672	1.3925	11.3244	11.3244

### 3.3. FINITE ELEMENT ANALYSIS

In order to support and verify the experimental findings in the *Chapter 3*, a 3-D finite element analysis using a commercial finite-element software (*Straus 7* by G+D Computing) was employed in the linear elastic range. In the numerical analysis, the internal parts of the web and flanges of the pultruded profiles, composed of unidirectional fibres (*roving*), were modeled using eight-node orthotropic finite elements (*bricks*) of dimensions 1 mm ( $l_x$ ) x 1 mm ( $l_y$ ) x 5 mm ( $l_z$ ), while orthotropic surface elements (*plates*) of dimensions 1 mm x 5 mm ( $l_z$ ) were used to simulate the external layers composed of multi-directional fibres (*mat*). The values of the engineering properties of the materials (*bricks* and *plates*) used for the numerical analysis are reported in Table 3.9.

**Table 3.9.** Values of the engineering properties of bricks and plates used in the finite-elements analysis.

Engineering properties	Measurement	Value	Values
	Unit	(Bricks)	(Plates)
Longitudinal elastic modulus, $E_z$	MPa	23,000	-
Transversal elastic moduli, $E_x = E_y$	MPa	8,500	16,048.6
Transversal shear modulus, $G_{xy}$	MPa	3,000	7,164.3
Shear Moduli, $G_{zx} = G_{zy}$	MPa	3,455	-
Longitudinal Poisson's ratio, $\nu_{xy}$		0.23	0.12
Transversal Poisson's ratios, $\nu_{zx} = \nu_{zy}$		0.09	-

Figures 3.38a and 3.38b show the typical three-dimensional finite-element meshes of specimens *L\_160\_EP (L\_200\_EP)* and *L\_160\_MP (L\_200\_MP)*, respectively. In both cases, the nodes of the upper flange were constrained against all movements, while the uniform pull load, acting on the lower flange of the PFRP I-profile, was applied by modeling the steel device fixed to the testing machine.

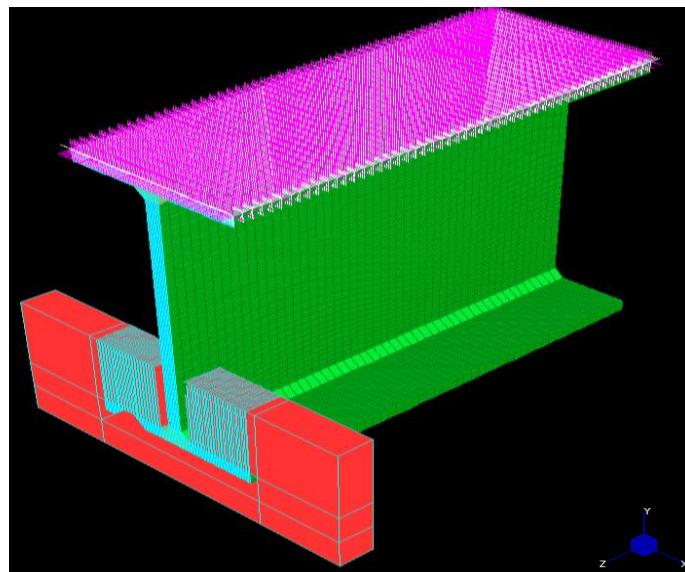


**Figure 3.38a.** Typical finite-element mesh of *I*<sub>160</sub>*\_EP* (*I*<sub>200</sub>*\_EP*) specimens.

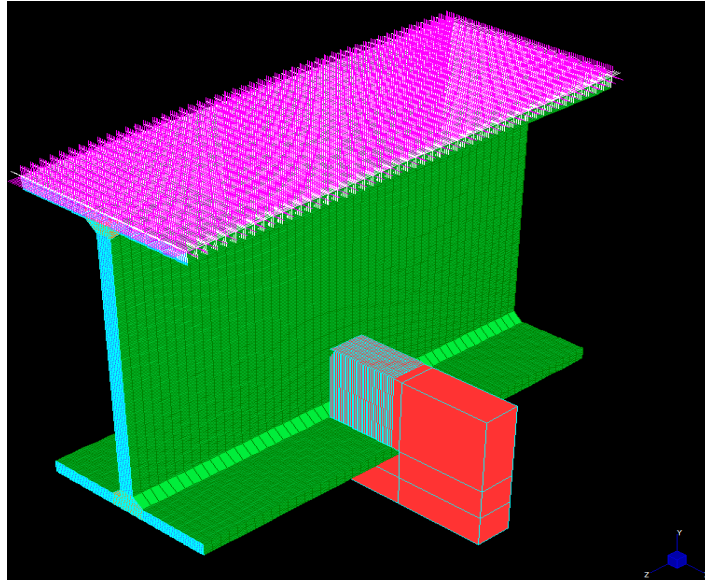


**Figure 3.38b.** Typical finite-element mesh of *I*<sub>160</sub>*\_MP* (*I*<sub>200</sub>*\_MP*) specimens.

Figures 3.39a-h show the brick and the plate stresses ( $\sigma_{yy}$ ) obtained from the finite element analysis of *I*<sub>160</sub>*\_EP*<sub>4</sub>, *I*<sub>160</sub>*\_MP*<sub>4</sub>, *I*<sub>200</sub>*\_EP*<sub>2</sub> and *I*<sub>200</sub>*\_MP*<sub>1</sub> specimens.

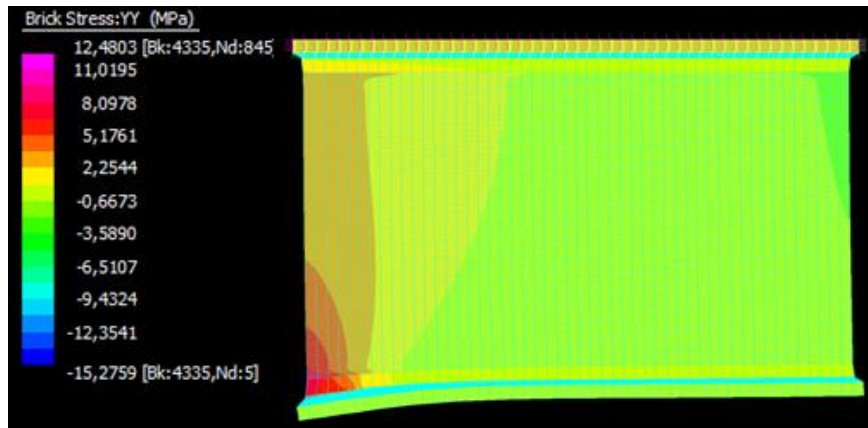


**Figure 3.39a.** Brick numerical stresses ( $\sigma_{yy}$ ) in the deformed configuration of L\_160\_EP\_4 specimen (P=1.5 kN).

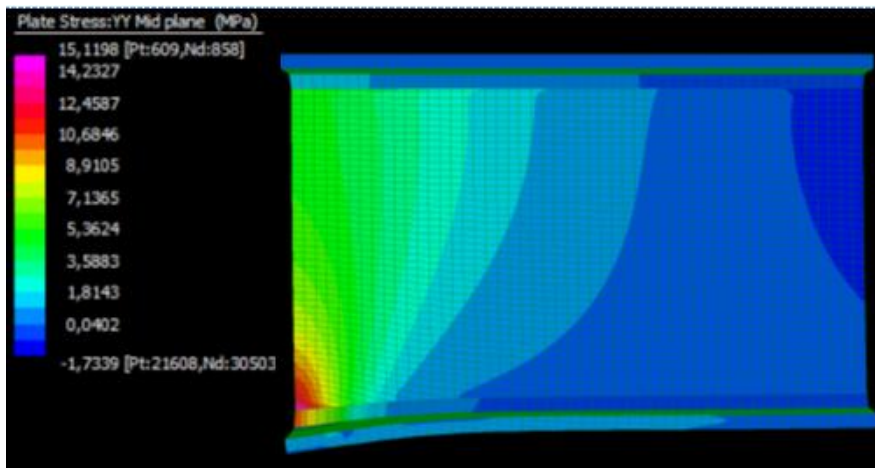


**Figure 3.39b.** Plate numerical stresses ( $\sigma_{yy}$ ) in the deformed configuration of L\_160\_EP\_4 specimen (P=1.5 kN).

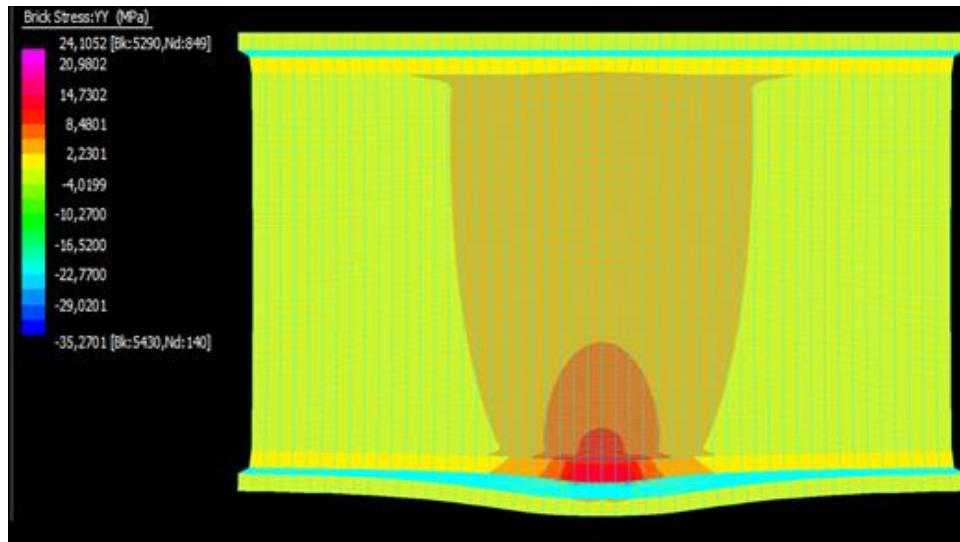


**Figure 3.39c.** Brick numerical stresses ( $\sigma_{yy}$ ) in the deformed configuration of I\_160\_MP\_4 specimen (P=5.0 kN).

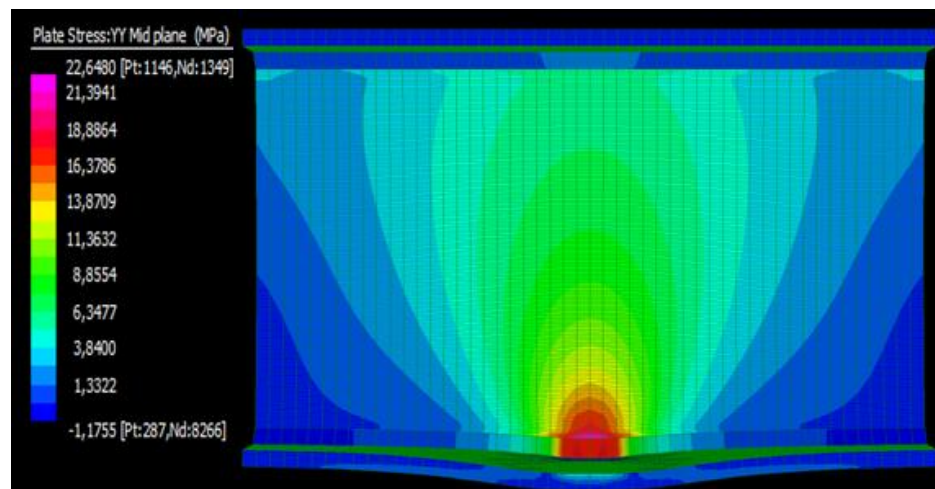


**Figure 3.39d.** Plate numerical stresses ( $\sigma_{yy}$ ) in the deformed configuration of I\_160\_MP\_4 specimen (P=5.0 kN).



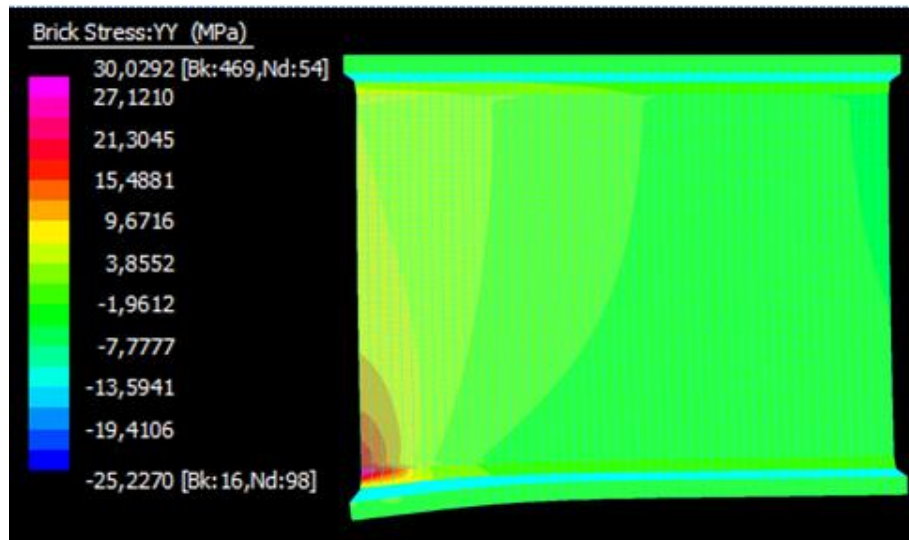


**Figure 3.39e.** Brick numerical stresses ( $\sigma_{yy}$ ) in the deformed configuration of *I\_200\_EP\_2* specimen ( $P=5.0063\text{kN}$ ).

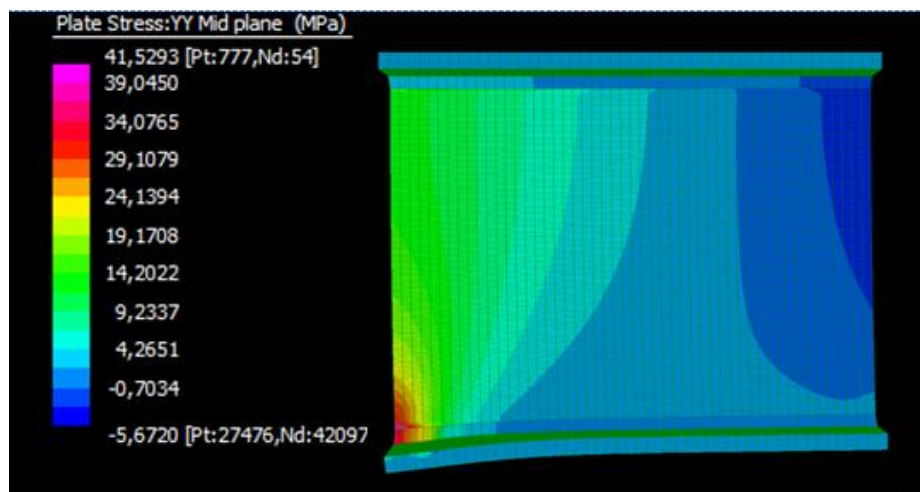


**Figure 3.39f.** Plate numerical stresses ( $\sigma_{yy}$ ) in the deformed configuration of *I\_200\_EP\_2* specimen ( $P=5.0063\text{kN}$ ).

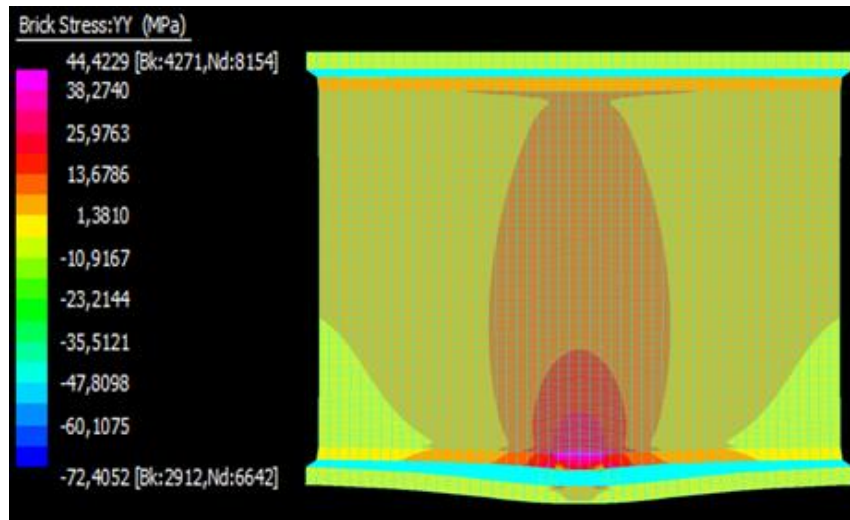


**Figure 3.39g.** Brick numerical stresses ( $\sigma_{yy}$ ) in the deformed configuration of I\_200\_MP\_1 specimen ( $P=17.90$  kN).

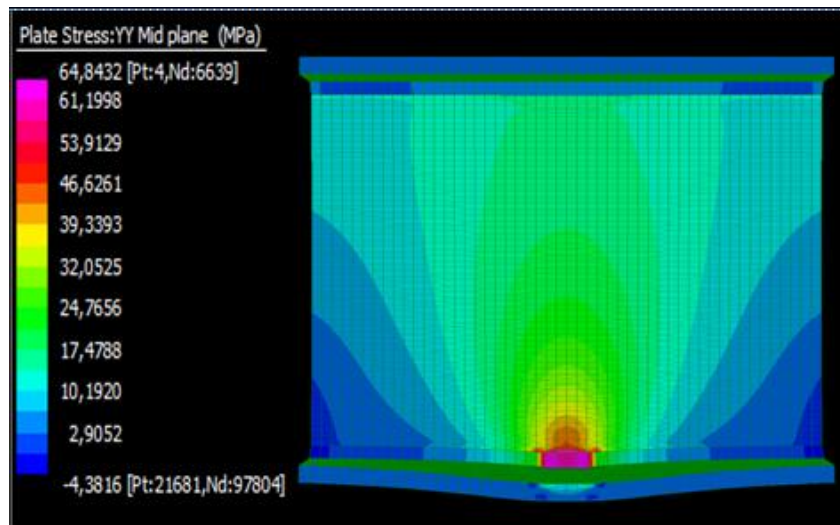


**Figure 3.39h.** Plate numerical stresses ( $\sigma_{yy}$ ) in the deformed configuration of I\_200\_MP\_1 specimen ( $P=17.90$  kN).

The stress distributions ( $\sigma_{yy}$ ) in the web-flange junction at the loading point of I\_160\_EP\_4, I\_160\_MP\_4, I\_200\_EP\_2 and I\_200\_MP\_1 specimens are shown in Figures 3.40a-d. From these figures, it is worth noticing the different numerically simulated stress distributions that contributed the different failure modes observed in the experimental program. Also, one can notice the growth of the “influence zone” with relation to the distance  $d$  confirming the experimental results described earlier.

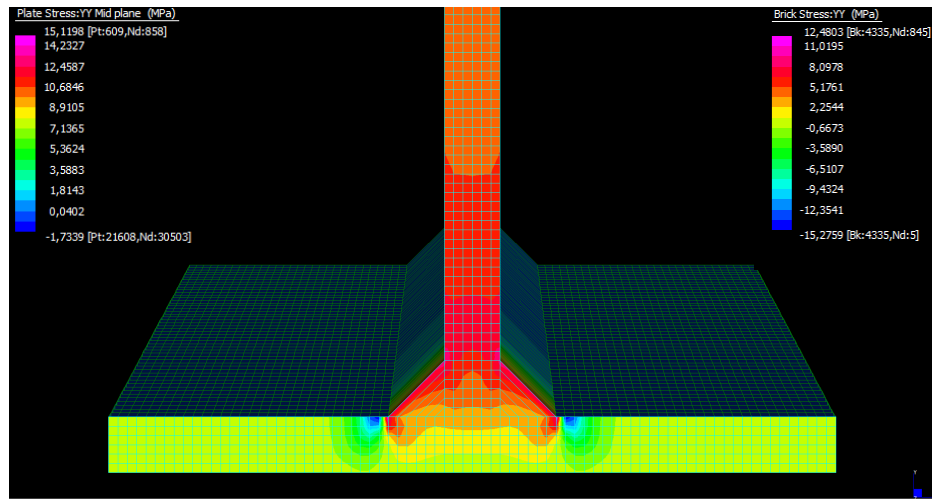


**Figure 3.40a.** Stress distributions ( $\sigma_{yy}$ ) at the web-flange junction of the end point of I\_160\_EP\_4 specimen (loading point at  $z=0$  mm;  $P=1.5$  kN).

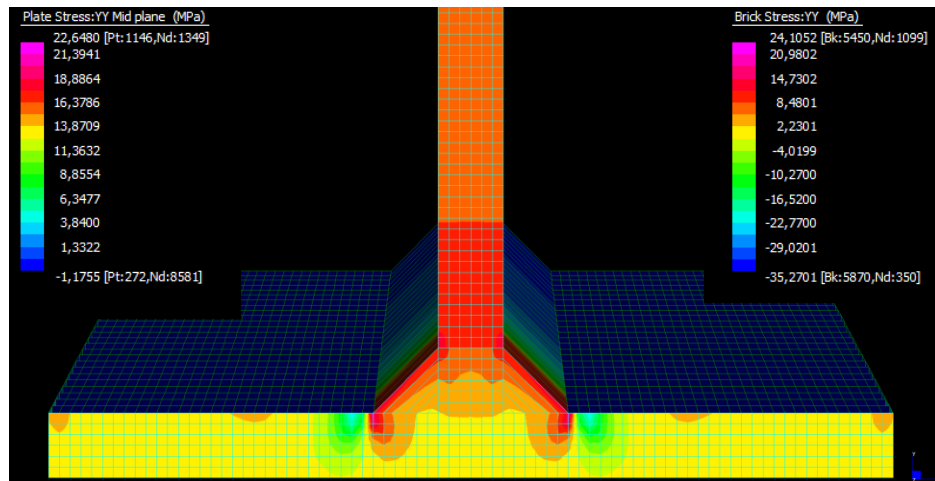


**Figure 3.40b.** Stress distributions ( $\sigma_{yy}$ ) at the web-flange junction of the end point of *I\_160\_MP\_4* specimen (loading point at  $z=150$  mm;  $P=5.0$  kN).

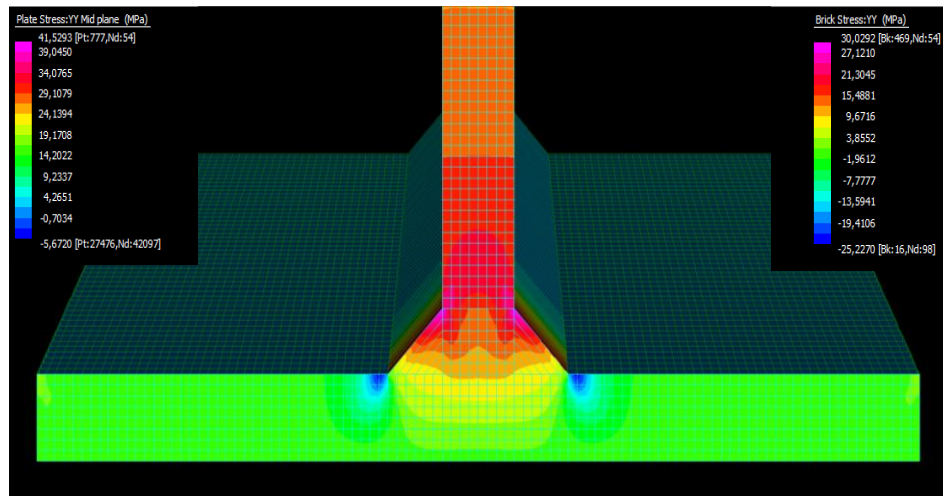


**Figure 3.40c.** Stress distributions ( $\sigma_{yy}$ ) at the web-flange junction of the end point of *I\_200\_EP\_2* specimen (loading point at  $z=0$  mm;  $P=5.0063$  kN).

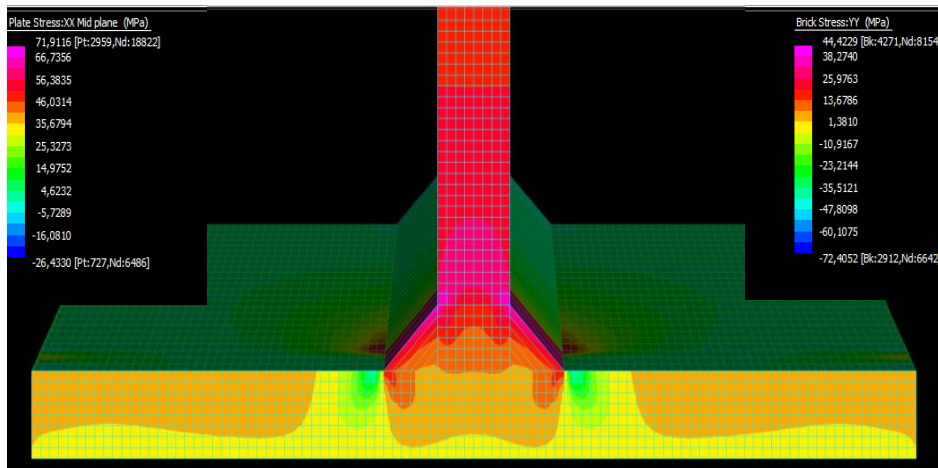
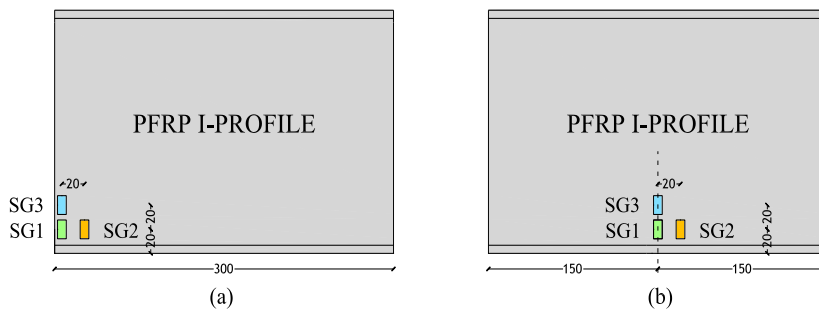


**Figure 3.40d.** Stress distributions ( $\sigma_{yy}$ ) at the web-flange junction of the mid point of *I\_200\_MP\_1* specimen (loading point at  $z=150$  mm;  $P=17.900$  kN).

Finally, the simulation strain results along the  $y$ -axis ( $\epsilon_{yy}$ ) for *I\_160\_EP\_4*, *I\_160\_MP\_4*, *I\_200\_EP\_2* and *I\_200\_MP\_1* specimens have been compared with the corresponding experimental data measured at the points SG1, SG2 and SG3 (Figs. 3.41a-b) where three rectangular self-temperature-compensated strain gages (Vishay MM C2A-06-125LW-120) were placed.



**Figures 3.41a,b.** Typical strain gages locations for (a) End Point Pull-Out, and (b) Mid-Point Pull-Out Test (dimensions in mm).

In all cases, a good agreement between the simulation and the experimental results is achieved (Figs. 3.42a-d).

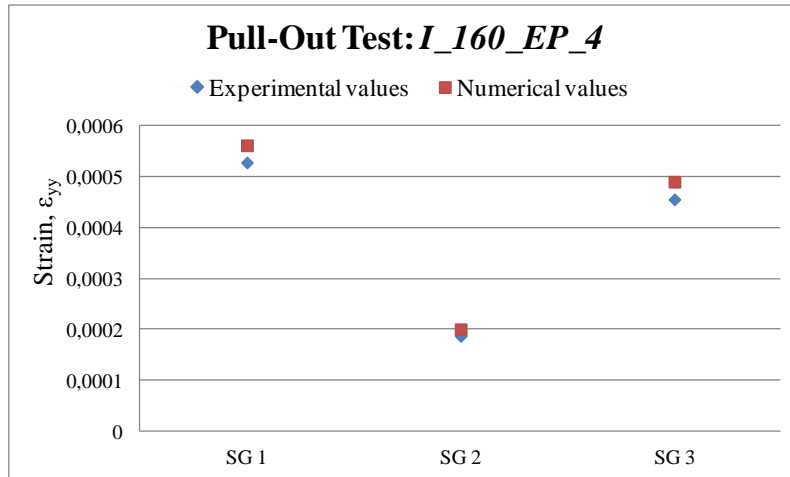


**Figure 3.42a.** Comparisons between experimental and numerical results of  $\epsilon_{yy}$  in the pull-out test of *I\_160\_EP\_4* specimen ( $P= 1.5$  kN).

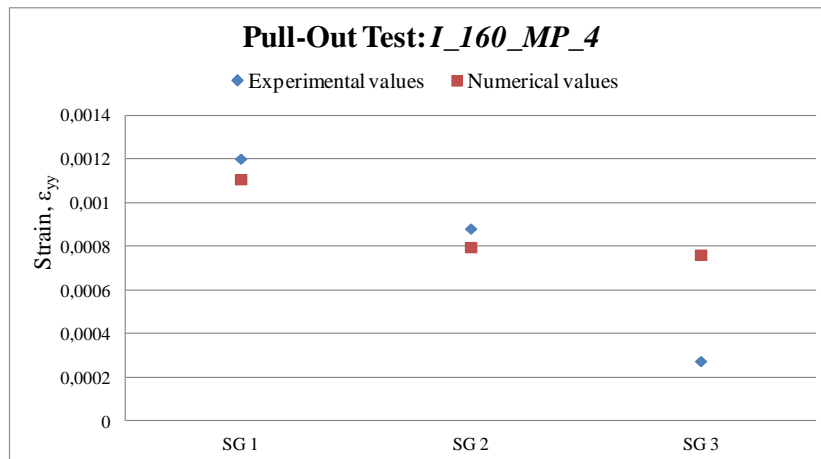


**Figure 3.42b.** Comparisons between experimental and numerical results of  $\epsilon_{yy}$  in the pull-out test of *I\_160\_MP\_4* specimen ( $P= 5.0$  kN).

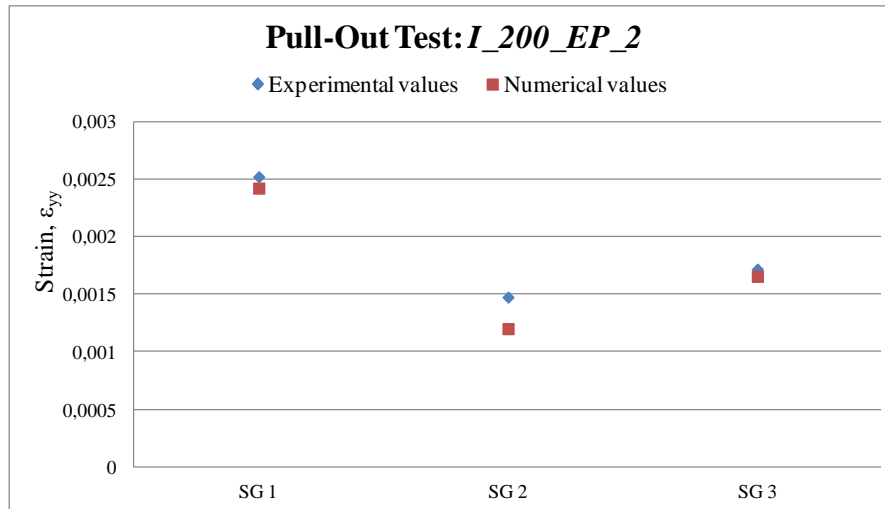


**Figure 3.42c.** Comparisons between experimental and numerical results of  $\epsilon_{yy}$  in the pull-out test of *I\_200\_EP\_2* specimen ( $P=P_{failure}=5.0063$  kN).

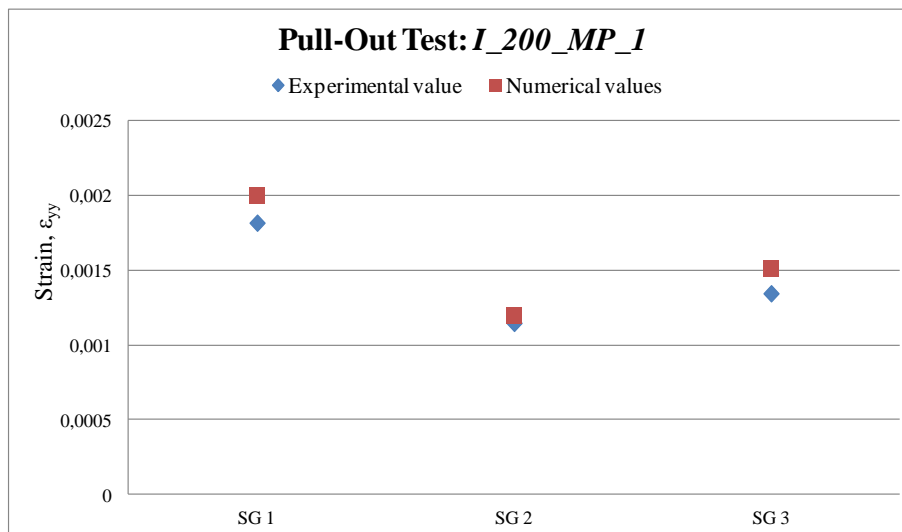


**Figure 3.42d.** Comparisons between experimental and numerical results of  $\epsilon_{yy}$  in the pull-out test of *I\_200\_MP\_1* specimen ( $P=12.3199$  kN).

### 3.4. RESULTS OF THE FIRST PHASE OF THE RESEARCH

The results gathered from the first phase of the research program provided important information on one of the major structural deficiencies and limitations related to the inherent weakness of the web/flange junctions of the majority of commercially produced, off-the-shelf unidirectional pultruded composites.

First of all, full-scale experimental results on PFRP I-profiles have indicated that their junction strength depends on the location of the applied pull force. In particular, the values of the failure load obtained from the end-point pull out tests were about one-third smaller than those obtained from the mid-point tests for all the specimens evaluated in this phase. In addition, experimental results also showed that the load–displacement ( $P-\delta$ ) curves of WFJ are influenced by the size of the PFRP profiles; for the I\_160\_EP and I\_160\_MP specimens the load–displacement curves present a linear behavior until the elastic limit after which a non-linear behavior and a stiffness degradation is observed up to the failure load. Whereas, for the I\_200\_EP and I\_200\_MP specimens an increasing linear displacement was observed until ultimate failure. Moreover, the influence of the pull-out load distance ( $d$ ) from the edge of the specimens on the failure strength of the web–flange junction has been investigated and a new definition for an “influence zone” has been proposed that is found to be dependent on the loaded length, with a maximum value equal to approximately the PFRP member’s depth.



This proposed zone was observed in all laboratory tests and its existence was confirmed by the results of FEM numerical analysis. The study also identified different failure modes of such junctions. For example, in the case of I\_160\_EP specimens, it has been observed that the crack generally initiated in the form of an inverted “v” shape at the center of the web-flange junction leading to a complete separation of the flange from the web. For the I\_200\_EP specimens, failure was sudden and occurred in the web portion of the I-profile. Finally, for all the mid-point pull-out tests, failure was initiated at the location where the load was applied and propagated along the junction length, resulting in a complete flange delamination.

3-D finite element models were also developed to predict the behavior of these specimens. The results from the numerical models were compared to those obtained from the experimental program and found to be satisfactory.



## **CHAPTER 4 – ON THE AXIAL AND ROTATIONAL BEHAVIOR OF WEB-FLANGE JUNCTIONS OF PFRP H- AND L-PROFILES**

### **4. INTRODUCTION**

This chapter presents the results of the second phase of the research program on the web-flange junction characterization of thin-walled pultruded profiles.

The test program was conducted at the Structural Engineering Testing Hall (SETH) of the University of California Irvine (UCI) and consisted of two parts: [64,65] the first one was an evaluation of the axial behavior for web-flange junctions of PFRP E-glass/polyester H-profiles (pull-out tests), while the second

part was an evaluation of the relative rotational behavior of the web-flange junctions of PFRP E-glass/polyester H- and L-profiles (relative rotation tests).

Unlike the majority of published research in the field of PFRP frame connections, this dissertation has examined several critical parameters that are commonly ignored. These parameters include axial and rotational flexibility of the web-flange junction of open-web thin-walled profile which play a major role on buckling and post-buckling behavior of such frames and, also, limit both the strength and stiffness of PFRP structural members. To date, the majority of published work focused in analyzing and experimentally evaluating PFRP frame structures with deficient “steel-like” connection details resulting in premature failure and offering minimum benefit to the engineering knowledge.

Moreover, the efficiency of beam-column connections are one of primary concern to structural engineers. These connections are designed to transfer moments, shear, axial forces and any other loads.

Figure 4.1 shows a typical failure of a bolted FRP beam-column connection in which angle sections are used to join the flanges of a beam and a column. The FRP angle fails by the formation of hinges, due to opening (top) or closing (bottom) moments. Other likely locations of failure are under the bolts going through the column (crushing) and at the junction of web and flange of FRP I-beams, which is an area that is relatively rich in resin and poor in fibers (matrix-dominated), as shown in Figure 4.2.

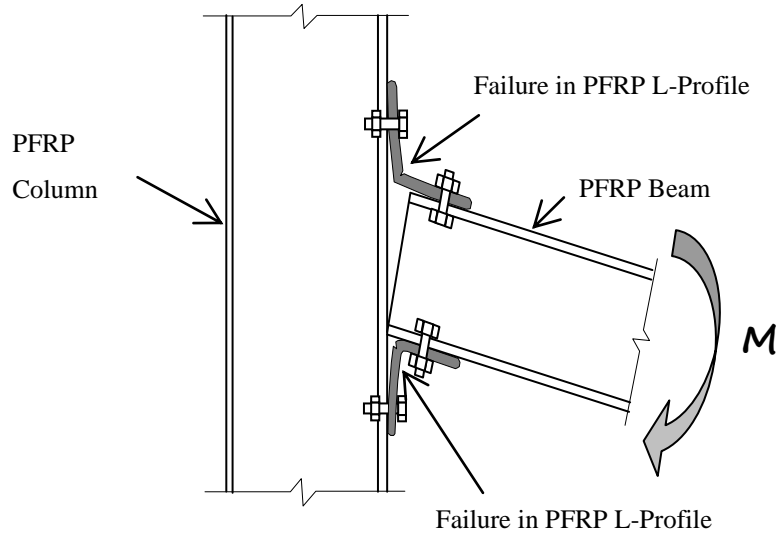


**Figure 4.1.** Typical failure of composite cleat connections.

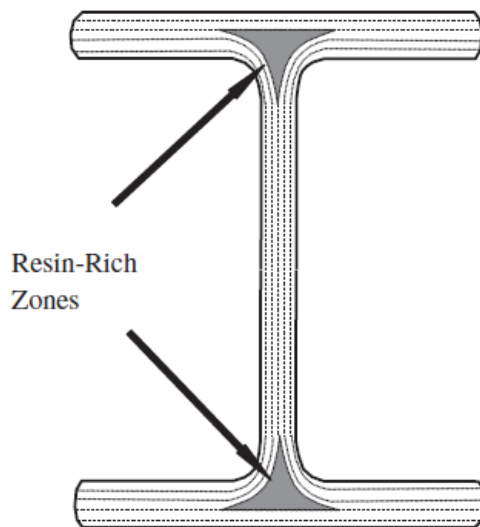


**Figure 4.2.** Resin (matrix)-rich zones at web-flange junction of unidirectional pultruded profiles.

#### 4.1. EXPERIMENTAL INVESTIGATION (@UCI)

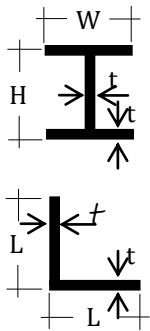
The geometrical characteristics of the PFRP profiles evaluated at University of California - Irvine are presented in Table 4.1. The nominal values of the main mechanical properties for the pultruded shapes, recommended by the manufacture (Bedford Reinforced Plastics), are summarized in Table 4.2.

##### 4.1.1. Pull-out test setup and instrumentation

For pull-out tests, a total of six specimens, cut from commercially-produced structural PFRP H- profiles and characterized by three different sizes, i.e.  $10'' \times 10'' \times \frac{1}{2}''$  ( $254 \times 254 \times 12.7$  mm),  $8'' \times 8'' \times \frac{3}{8}''$  ( $203.2 \times 203.2 \times 9.53$  mm) and  $6'' \times 6'' \times \frac{3}{8}''$  ( $152.4 \times 152.4 \times 9.53$  mm), were evaluated. The length ( $l$ ) of the specimens was equal to 24 inch (609.6 mm).

In particular, two different test setups were carried out, varying the location of the pull-out force: in the first setup (*Group 1* of specimens), the load was applied at the mid-point (*MP*) of the specimens, i.e. at a distance of  $l/2$  from the edge of the specimen as shown in Figure 4.3(a), while in the second test setup (*Group 2* of specimens), the load was eccentrically applied (*EP*) at a distance of  $l/4$  from the edge of the specimen as shown in Figure 4.3(b).

**Table 4.1.** Geometry of the pultruded profiles.

	Specimen type	Web length	Flange Length	Web & Flange Thickness
		H	W	t
		inch [mm]	inch [mm]	inch [mm]
	H_10" × 10" × ½"	10 [254.0]	10 [254.0]	½ [12.7]
	H_8" × 8" × ⅜"	8 [203.2]	8 [203.2]	⅜ [9.53]
	H_6" × 6" × ⅜"	6 [152.4]	6 [152.4]	⅜ [9.53]
	L_6" × 6" × ½"	6 [152.4]	6 [152.4]	½ [12.7]
	L_4" × 4" × ⅜"	4 [101.6]	4 [101.6]	⅜ [9.53]

**Table 4.2.** Mechanical properties for pultruded structural shapes (nominal values).

Property	Measurement unit	Value
<i>Tensile Strength</i>		
Lengthwise	psi (MPa)	30,000 (206.80)
Crosswise	psi (MPa)	6,500 (44.80)
<i>Tensile Modulus</i>		
Lengthwise	psi x10 <sup>6</sup> (GPa)	2.3 (15.85)
Crosswise	psi x10 <sup>6</sup> (GPa)	0.8 (5.51)
<i>Flexural Strength</i>		
Lengthwise	psi (MPa)	30,000 (206.80)
Crosswise	psi (MPa)	10,000 (68.94)
<i>Flexural Modulus</i>		
Lengthwise	psi x10 <sup>6</sup> (GPa)	1.5 (10.30)
Crosswise	psi x10 <sup>6</sup> (GPa)	0.7 (4.80)
<i>Compressive Strength</i>		
Lengthwise	psi (MPa)	30,000 (206.80)
Crosswise	psi (MPa)	10,000 (68.90)

Mechanical behavior of web-flange junctions of thin-walled pultruded fiber-reinforced polymer profiles: an experimental and numerical evaluation.

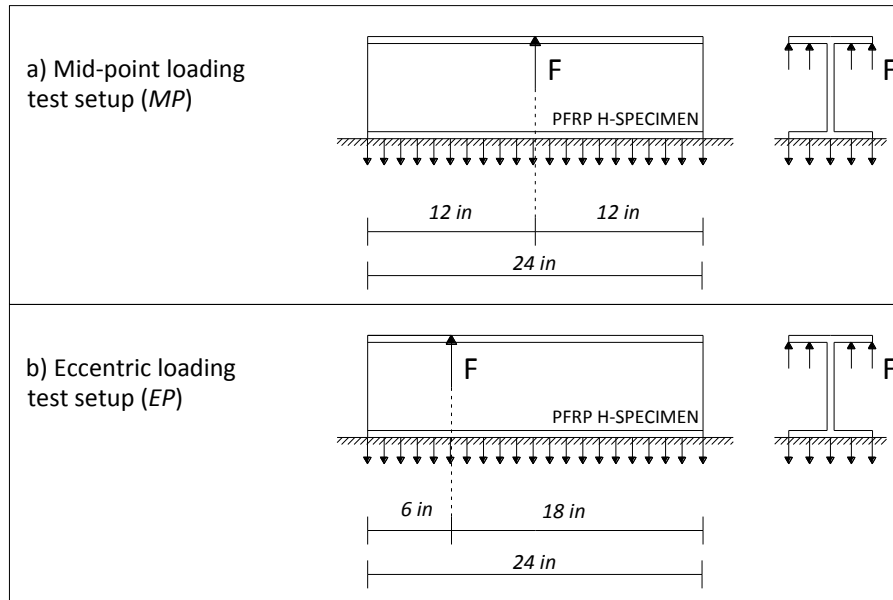


**Figure 4.3.** Schematic Setup of Web-Flange Junction Pullout Test: a) Mid-point loading test setup; b) Eccentric loading test setup.

For all specimens, the pull axial load was applied using a calibrated MTS 55-kip servo-hydraulic actuator. Two thick steel angles were used to provide fixity to the lower flange and web of PFRP H-profiles. A force-controlled loading protocol was adopted in all tests. Figures 4.4 and 4.5 show schematic diagram and photos of the pullout test setup, respectively.



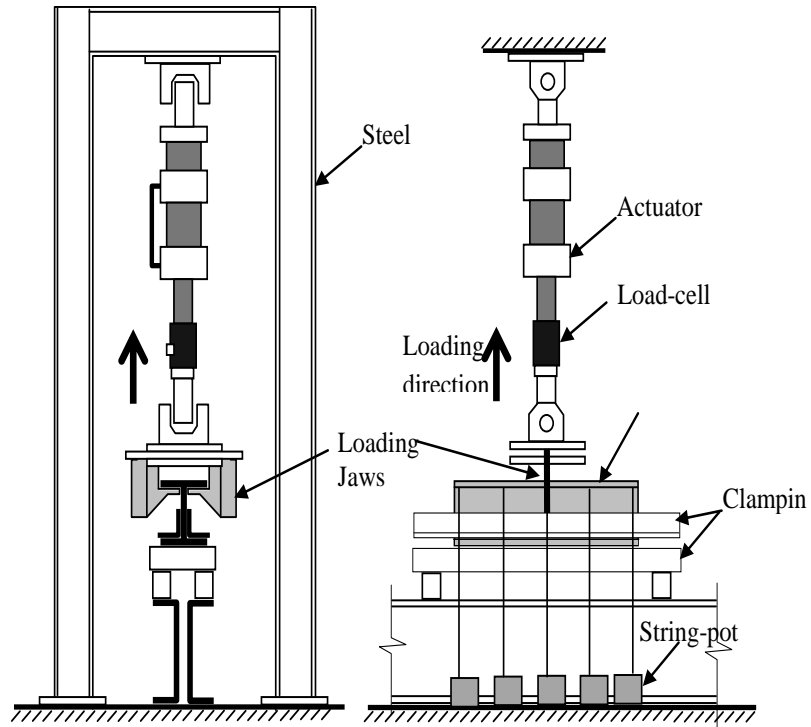
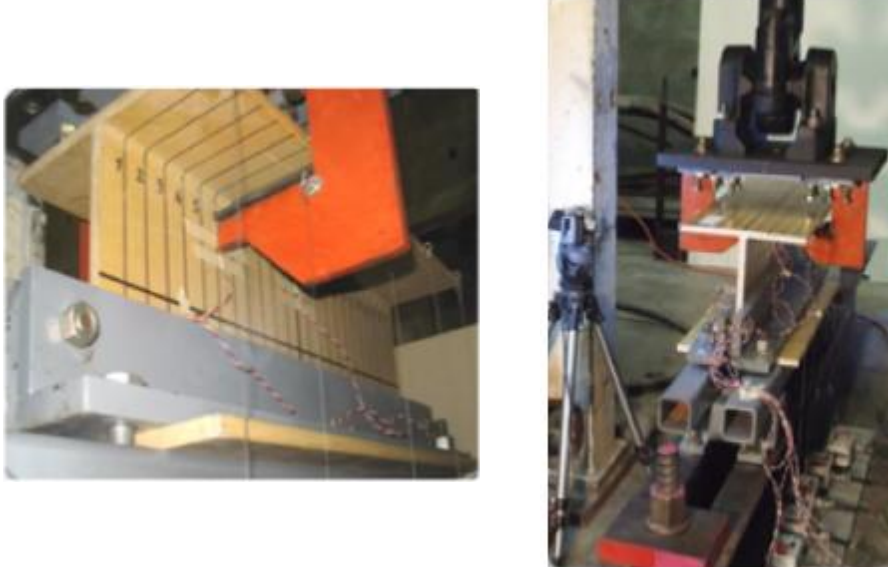


Figure 4.4. Schematic views of pull-out test setup.



**Figures 4.5a,b.** Pull-out test setup.

In order to capture the web displacements, five string potentiometers were used and placed at each side of specimen, at 6 inch (152.4 mm) relative distances as shown in Figure 4.6. Moreover, two strain gauges were used to measure the strain at the web-flange junction as shown in Figure 4.6. A calibrated data-acquisition system was used to continuously collect all information including load, displacement, and strain.

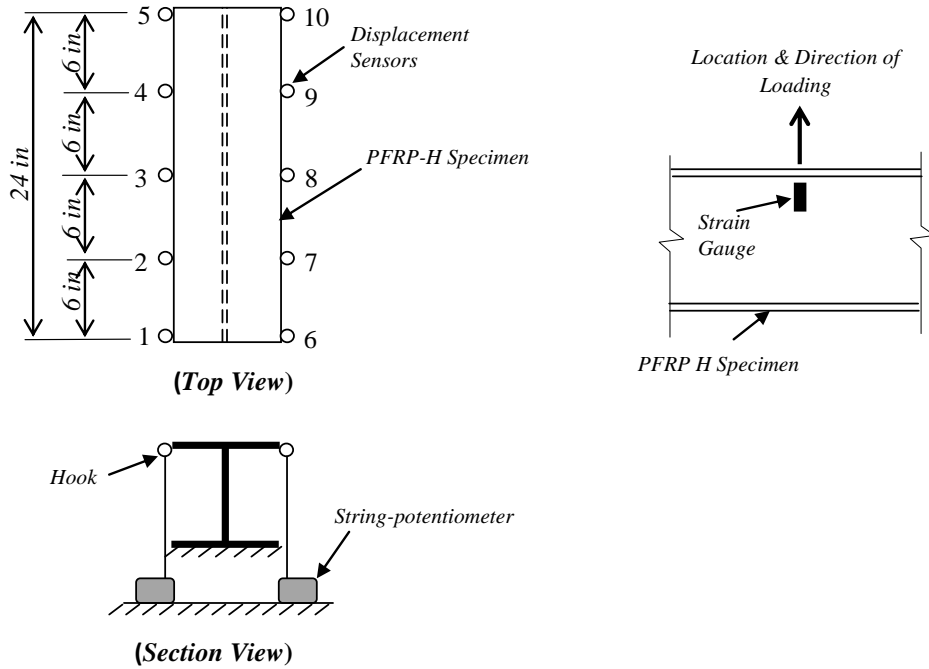
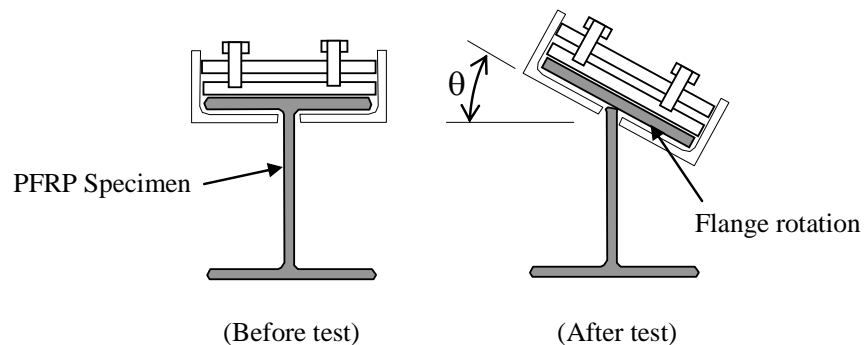


Figure 4.6. Locations of string-potentiometers and strain gauge.

#### 4.1.2. Relative rotation test setup and instrumentation

For relative rotation test, three sizes of PFRP H-profiles, i.e.  $10'' \times 10'' \times \frac{1}{2}''$  ( $254 \times 254 \times 12.7$  mm),  $8'' \times 8'' \times \frac{3}{8}''$  ( $203.2 \times 203.2 \times 9.53$  mm),  $6'' \times 6'' \times \frac{3}{8}''$  ( $152.4 \times 152.4 \times 9.53$  mm) and two sizes of PFRP L-profiles, i.e.  $6'' \times 6'' \times \frac{1}{2}''$  ( $152.4 \times 152.4 \times 12.7$  mm) and  $4'' \times 4'' \times \frac{3}{8}''$  ( $101.6 \times 101.6 \times 9.53$  mm), were used (Table 4.1). In this case, the length ( $l$ ) of the specimens was equal to 6 inch (152.4 mm). To generate the desired behavior, specimens were securely held at the lower flange and web, while rotation was applied on the upper flange. Figure 4.7 shows a schematic view of flange rotation test.



**Figure 4.7.** Schematic view of flange rotation.

For all specimens, the moment was obtained applying an eccentric axial load through a calibrated MTS 55-kip servo-hydraulic actuator. Two thick steel angles were used to provide fixity to the lower flange and web of the PFRP H-profiles.

The displacement-controlled protocol was adopted in all tests. Figure 4.8 shows a schematic diagram of rotation test setup and a view from the setup is shown in Figures 4.9(a-d).

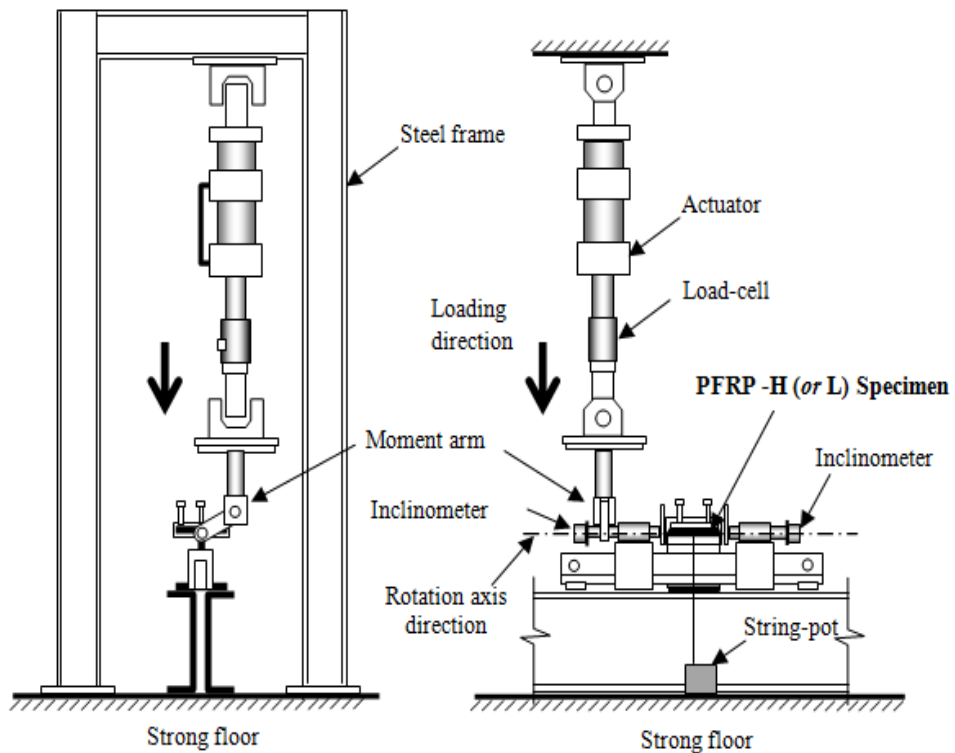


**Figure 4.8.** Schematic views of rotation test setup.



**Figure 4.9a.** View #1 from rotation test setup.



**Figure 4.9b.** View #2 from rotation test setup.



**Figure 4.9c.** View #3 from rotation test setup.



**Figure 4.9d.** View #4 from rotation test setup.

Two measurement methods were used to capture the web-flange relative rotation characteristics. In the first method, two calibrated string potentiometers were used and placed at each side of specimen as shown in Figure 4.8 to capture the relative displacement between the two edges of the upper flange in order to calculate the rotation angle. While, in the second method, two calibrated inclinometers were used to capture the rotation angle. In addition, two strain gauges were used to measure strain at the web-flange junction as shown. Also in this case, a calibrated data-acquisition system was used to continuously collect all information including load, displacement, rotation angle and strain.

## **4.2 EXPERIMENTAL RESULTS**

### **4.2.1. Pull-out test results**

The two sets of pullout tests were employed to simulate the following potential loading scenarios:

- i)* case of buckling and post-buckling at maximum compressive zone of a beam or a column that is simulated by a mid-point pull loading;
- ii)* case of beam/column connections that is simulated by an edge or eccentric loading.



The main experimental results obtained from the pullout tests are summarized in Tables 4.3 and 4.4. In the last two columns of these tables, two proposed values for junction's linear stiffness are presented and namely, the linear axial stiffness  $K_{jl}^A$ , and the average linear axial stiffness  $\bar{K}_{jl}^A$  (Fig. 4.10). Figures 4.11 and 4.12 present the load versus displacement curves for the H-specimens in mid-point loading and for the H-profiles in eccentric-point loading, respectively.

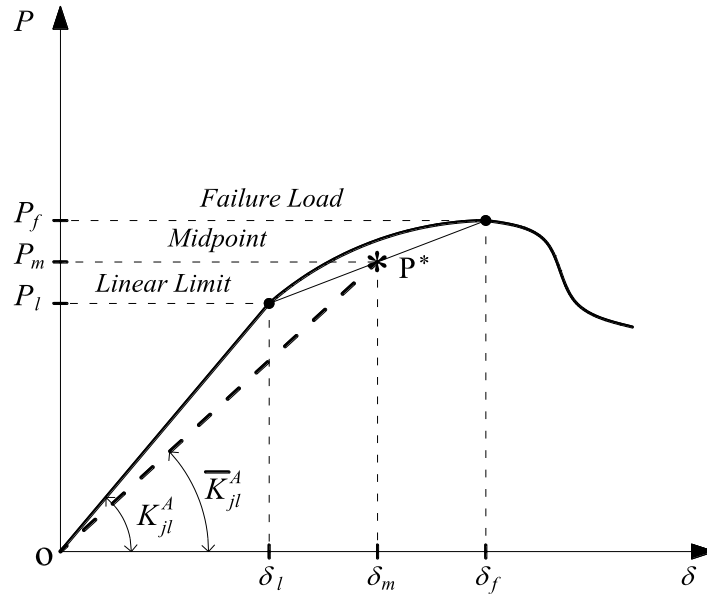


**Figure 4.10.** Linear axial stiffness,  $K_{jl}^A$ , and average linear axial stiffness,  $\bar{K}_{jl}^A$ .

**Table 4.3a.** Experimental results for specimens of *Group 1* (H-specimens in mid-point loading): failure loads, displacements and linear axial stiffnesses (Values in kips, inch).

#	Specimens	Length	Load (linear limit)	$\delta_i$	Failure Load	$\delta_f$	Linear Axial stiffness	Average Lin. Axial stiffness
			(P)		(P)		$K_{jl}^A$	$\bar{K}_{jl}^A$
		[inch]	[kips]	[inch]	[kips]	[inch]	[kip/in]	[kip/in]
1	H_10"×10"×1/2"_ <i>MP</i>	24	4.25	0.26	5.43	0.56	16.40	12.40
2	H_8"×8"×3/8"_ <i>MP</i>	24	3.58	0.20	3.58	0.20	19.16	-
3	H_6"×6"×3/8"_ <i>MP</i>	24	2.46	0.13	3.14	0.20	20.42	17.66

**Table 4.3b.** Experimental results for specimens of Group 1 (H-specimens in mid-point loading): failure loads, displacements and linear axial stiffnesses (Values in kN, mm).

#	Specimens	Length	Load (linear limit)	$\delta_i$	Failure Load	$\delta_f$	Linear Axial stiffness	Average Lin. Axial stiffness
			(P)		(P)		$K_{jl}^A$	$\bar{K}_{jl}^A$
		[mm]	[kN]	[mm]	[kN]	[mm]	[kN/mm]	[kN/mm]
1	H_10"×10"×1/2"_ <i>MP</i>	609.6	18.93	6.60	24.15	14.22	2.87	2.17
2	H_8"×8"×3/8"_ <i>MP</i>	609.6	15.93	5.08	15.93	5.08	3.36	-
3	H_6"×6"×3/8"_ <i>MP</i>	609.6	10.96	3.18	13.96	5.08	3.58	3.09

**Table 4.4a.** Experimental results for specimens of Group 2 (H-specimens in eccentric-point loading): failure loads, displacements and linear axial stiffnesses (Values in kips, inch).

#	Specimens	Length	Load (linear limit)	$\delta_i$	Failure Load	$\delta_f$	Linear Axial stiffness	Average Lin. Axial stiffness
			(P)		(P)		$K_{jl}^A$	$\bar{K}_{jl}^A$
		[inch]	[kips]	[inch]	[kips]	[inch]	[kip/in]	[kip/in]
4	H_10"×10"×1/2"_ <i>EP</i>	24	5.73	0.44	5.73	0.44	14.38	-
5	H_8"×8"×3/8"_ <i>EP</i>	24	3.54	0.36	3.54	0.36	9.99	-
6	H_6"×6"×3/8"_ <i>EP</i>	24	1.89	0.15	2.85	0.30	12.29	10.87

Mechanical behavior of web-flange junctions of thin-walled pultruded fiber-reinforced polymer profiles: an experimental and numerical evaluation.

**Table 4.4b.** Experimental results for specimens of *Group 2* (H-specimens in eccentric-point loading): Failure loads, displacements and linear axial stiffnesses (Values in kN, mm).

#	Specimens	Length	Load (linear limit)	$\delta_i$	Failure Load	$\delta_f$	Linear Axial stiffness	Average Lin. Axial stiffness
			( $P_l$ )		( $P_f$ )		$K_{jl}^A$	$\bar{K}_{jl}^A$
		[mm]	[kN]	[mm]	[kN]	[mm]	[kN/mm]	[kN/mm]
4	H_10"×10"× 1/2"_ <i>EP</i>	609.6	25.51	11.10	25.51	11.10	2.52	-
5	H_8"×8"×3/8"_ <i>EP</i>	609.6	15.74	9.19	15.74	9.19	1.75	-
6	H_6"×6"×3/8"_ <i>EP</i>	609.6	8.40	3.81	12.69	7.62	2.15	1.90

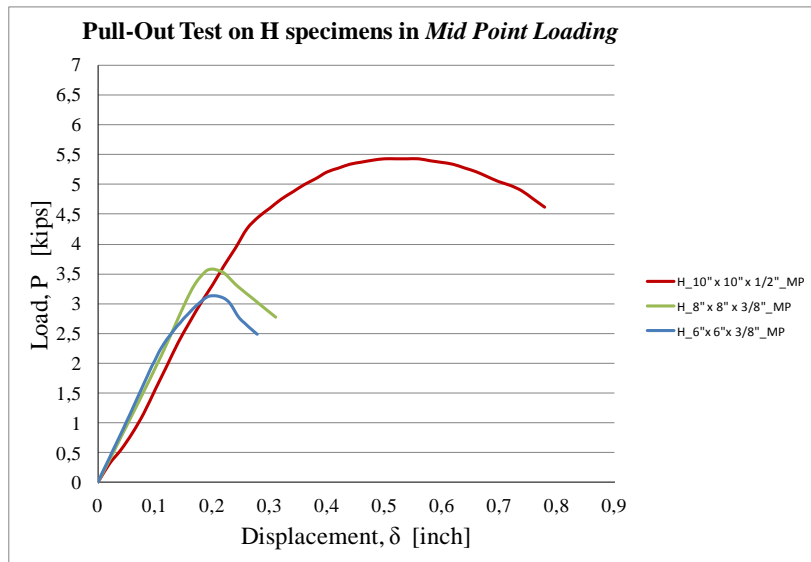


**Figure 4.11.** Load (P) versus displacement ( $\delta$ ) curve for H-specimens in mid-point loading (Group 1).

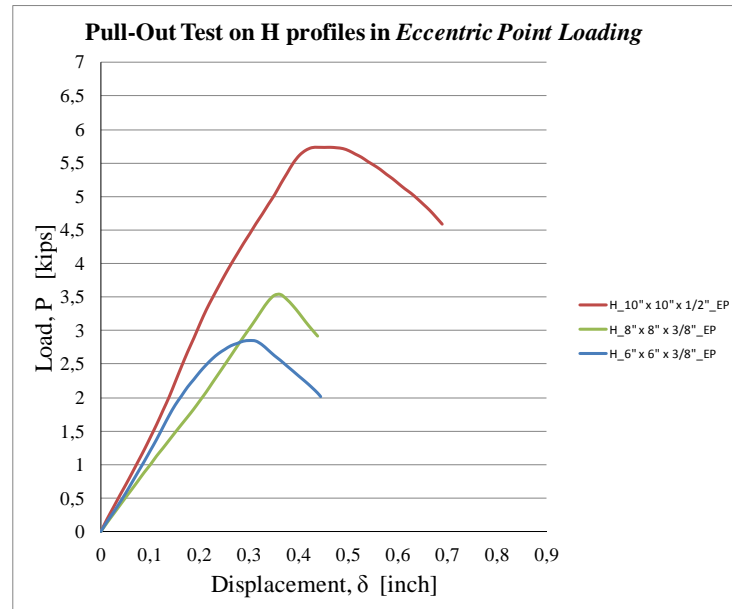


**Figure 4.12.** Load ( $P$ ) versus displacement ( $\delta$ ) curve for eccentric-point loading (Group 2).

In the following paragraphs, load-displacement curves at loading-point and the corresponding equivalent linearized relations  $P$ - $\delta$  for all the specimens are presented.

#### 4.2.1.1. Group 1: Mid-point loading tests results

- *Specimen #1: H\_10" x 10" x 1/2" (254 mm x 254 mm x 12.7 mm)\_MP*

For this specimen, the displacement increased linearly with increasing load up to an axial displacement of 0.26 inch (6.60 mm) that corresponds to a load level of 4.25 kips (18.93kN). After which, a stiffness degradation was observed and the

load-displacement ( $P$ - $\delta$ ) behavior followed a near-linear behavior until a 0.56 inch (14.22 mm) displacement level was reached corresponding to a 5.43 kips (24.15 kN) axial load. After that, signs of failure started to occur. Figure 4.13 shows the load-displacement curve at mid-point. Equivalent linearized load-displacement relation measured at specimen's mid-point is shown in Figure 4.14. Figure 4.15 shows the displacement pattern along the upper flange length at 1.0 kip (4.45 kN) loading steps.

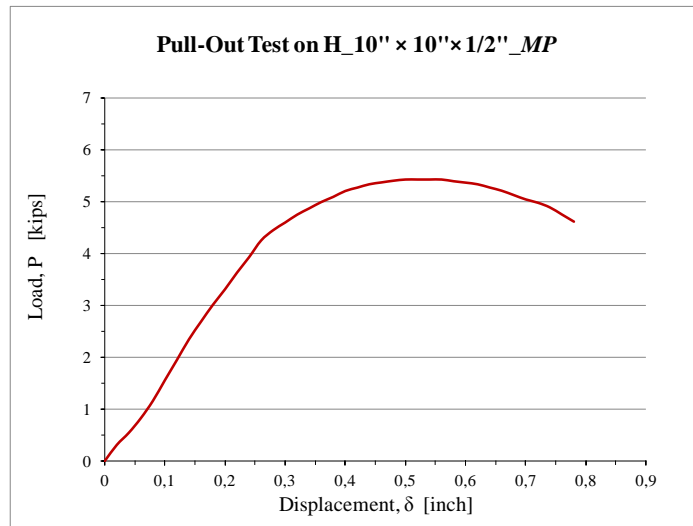


**Figure 4.13.** Load-Displacement Curve for H<sub>10''</sub> × 10'' × 1/2'' (254 mm × 254 mm × 12.7 mm)<sub>MP</sub> specimen at loading-point.

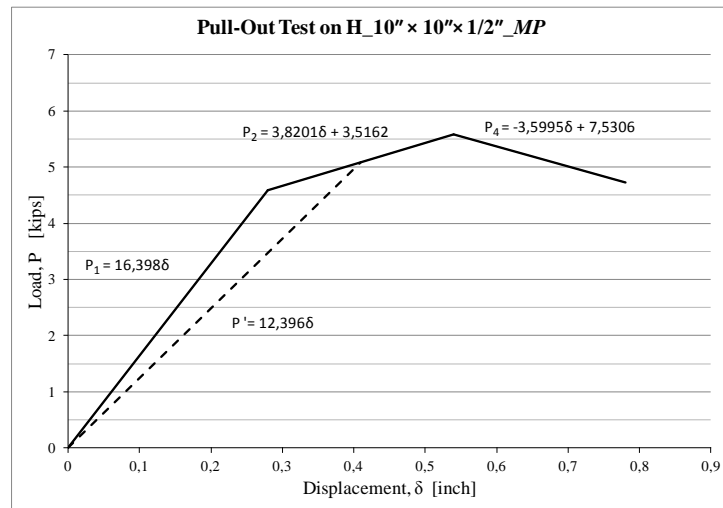


**Figure 4.14.** Linearized Load-Displacement Curve for H<sub>10</sub>'' × 10'' × 1/2'' (254 mm × 254 mm × 12.7 mm)<sub>MP</sub> specimen at loading-point.

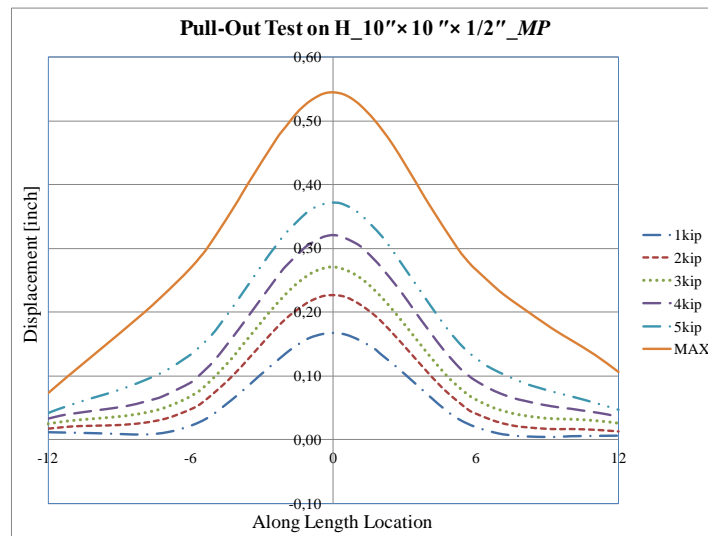


**Figure 4.15.** Displacement Pattern along Upper Flange Length for H<sub>10</sub>'' × 10'' × 1/2'' (254 mm × 254 mm × 12.7 mm)<sub>MP</sub> specimen at loading-point.

- Specimen #2: H<sub>8"</sub> × 8" × 3/8" (203.2 mm × 203.2 mm × 9.53 mm)<sub>MP</sub>

For this specimen, the  $P$ - $\delta$  behavior was similar to the previous one where linearity continued up to a displacement of 0.20 inch (5.08 mm) corresponding to a pull load level of 3.58 kips (15.93 kN). Beyond this load level, signs of failure were observed leading to a complete total separation of the flange from the web that was initiated at the location of the pull load line and propagated to the rest of the junction length. Figure 4.16 shows the load-displacement curve at the specimen's mid-point. Equivalent linearized  $P$ - $\delta$  relation at mid-point of this specimen is presented in Figure 4.17. Figure 4.18 shows the displacement pattern along the upper flange length drawn at 1.0 kip (4.45 kN) loading steps.

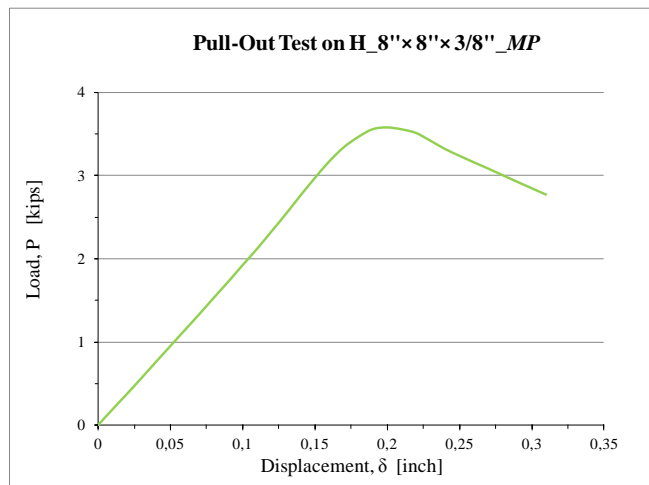


**Figure 4.16.** Load-Displacement Curve for H<sub>8"</sub> × 8" × 3/8" (203.2 mm × 203.2 mm × 9.53 mm)<sub>MP</sub> specimen at loading-point.

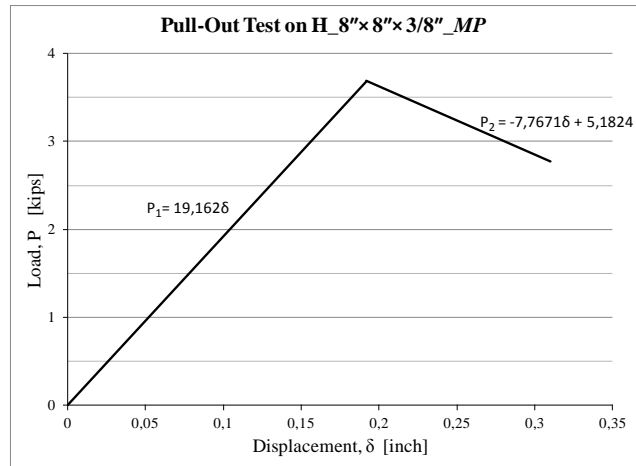


**Figure 4.17.** Linearized Load-Displacement Curve for H\_8'' x 8'' x 3/8'' (203.2 mm x 203.2 mm x 9.53 mm)\_MP specimen at loading-point.

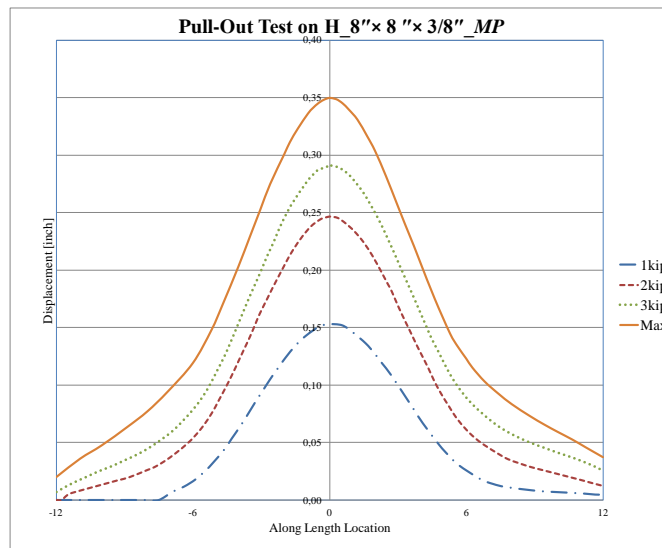


**Figure 4.18.** Displacement pattern along upper flange Length for H\_8'' x 8'' x 3/8'' (203.2 mm x 203.2 mm x 9.53 mm)\_MP specimen at loading-point.



- Specimen #3: H<sub>6"</sub> × 6" × 3/8" 6" × 6" × 3/8" (152.4 mm × 152.4 mm × 9.53 mm)<sub>MP</sub>

Also for this specimen, the  $P$ - $\delta$  behavior was similar to other two specimens where linearity was observed up to an axial displacement level of 0.125 inch (3.18 mm) corresponding to a load equal to 2.46 kips (10.96 kN). After that, the stiffness decreased while the relation between load and displacement remained linear up to 0.20 inch (5.08 mm) displacement and 3.14 kips (13.96 kN) load. Beyond this point, failure started to occur. The load-displacement curve at mid-point is shown in Figure 4.19, and the equivalent linearized curve is shown in Figure 4.20. Figure 4.21 shows the displacement pattern along the upper flange length at 1.0 kip (4.45 kN) loading steps.

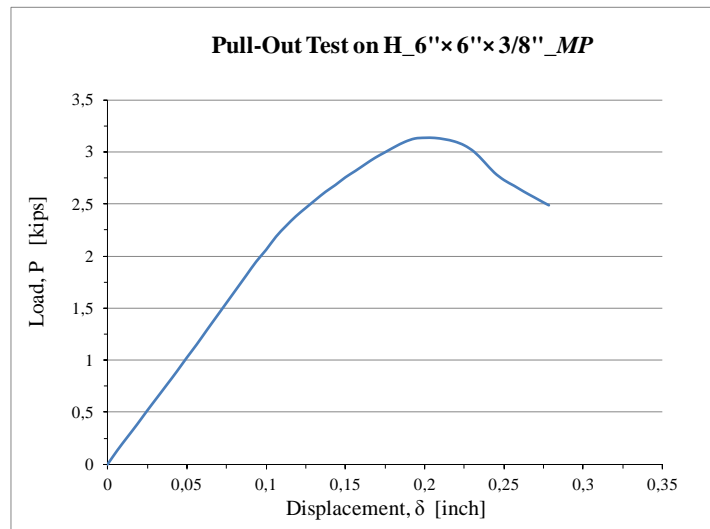


**Figure 4.19.** Load-Displacement Curve for H<sub>6"</sub> × 6" × 3/8" (152.4 mm × 152.4 mm × 9.53

mm)*MP* specimen at loading-point.

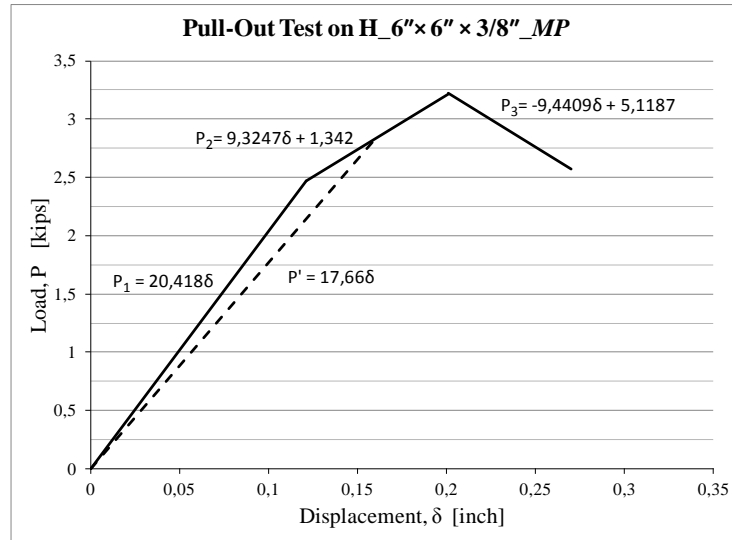


**Figure 4.20.** Linearized Load-Displacement Curve for H\_6'' x 6'' x 3/8'' (152.4 mm x 152.4 mm x 9.53 mm)*MP* specimen at loading-point.

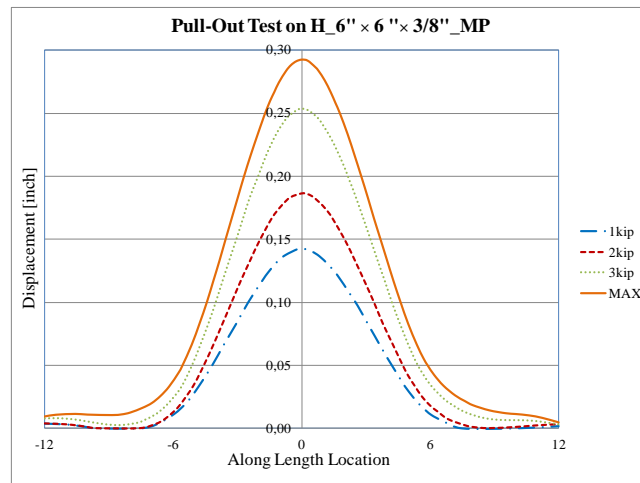


**Figure 4.21.** Displacement Pattern along Upper Flange Length for H\_6'' x 6'' x 3/8'' (152.4 mm x 152.4 mm x 9.53 mm)*MP* specimen at loading-point.

#### 4.2.1.2. Group 2: Eccentric-point loading tests results

- Specimen #4: H<sub>10"</sub> × 10" × 1/2" (254 mm × 254 mm × 12.7 mm)<sub>EP</sub>

For this specimen, the displacement was increased linearly with increasing load up to 0.44 inch (11.09 mm) displacement and 5.73 kips (25.51 kN) axial load. After which, failure started to occur. Figure 4.22 shows the load-displacement curve at loading-point. Equivalent linearized load-displacement at loading-point is shown in Figure 4.23. Figure 4.24 shows the displacement pattern along the upper flange length at 1.0 kip (4.45 kN) loading steps.

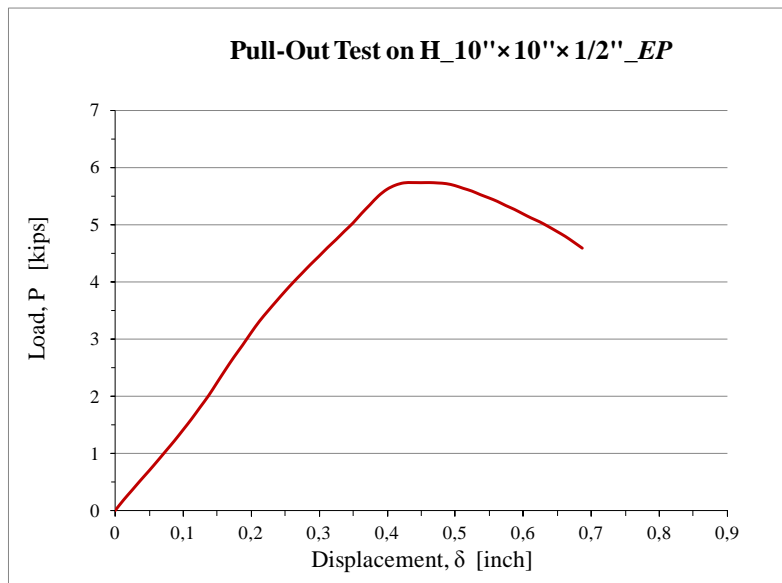


**Figure 4.22.** Load-Displacement Curve for H<sub>10"</sub> × 10" × 1/2" (254 mm × 254 mm × 12.7 mm)<sub>EP</sub> specimen at loading-point.

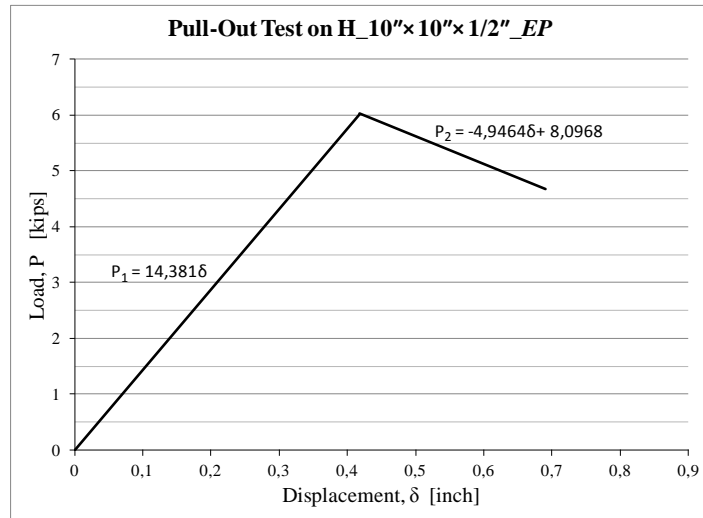


**Figure 4.23.** Linearized Load-Displacement Curve for H<sub>10</sub>'' × 10'' × 1/2''<sub>EP</sub> (254 mm × 254 mm × 12.7 mm)<sub>EP</sub> specimen at loading-point.

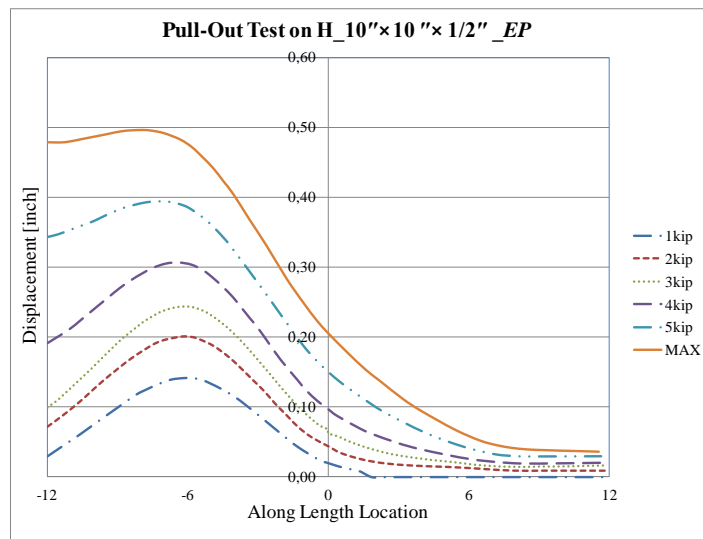


**Figure 4.24.** Displacement Pattern along Upper Flange Length for H<sub>10</sub>'' × 10'' × 1/2''<sub>EP</sub> (254 mm × 254 mm × 12.7 mm)<sub>EP</sub> specimen at loading-point.

- Specimen #5: H\_8" × 8" × 3/8" (203.2 mm × 203.2 mm × 9.53 mm)\_EP

For this specimen, the displacement was observed increasing linearly with load until achieving a displacement equal to 0.36 inch (9.19 mm) and load equal to 3.54 kips (15.74 kN). Beyond this level, failure started to occur. Figure 4.25 shows the load–displacement curve at loading-point while Figure 4.26 shows the equivalent linearized load-displacement at loading-point. Displacement pattern along the upper flange length at 1.0 kip (4.45 kN) loading steps is shown in Figure 4.27.

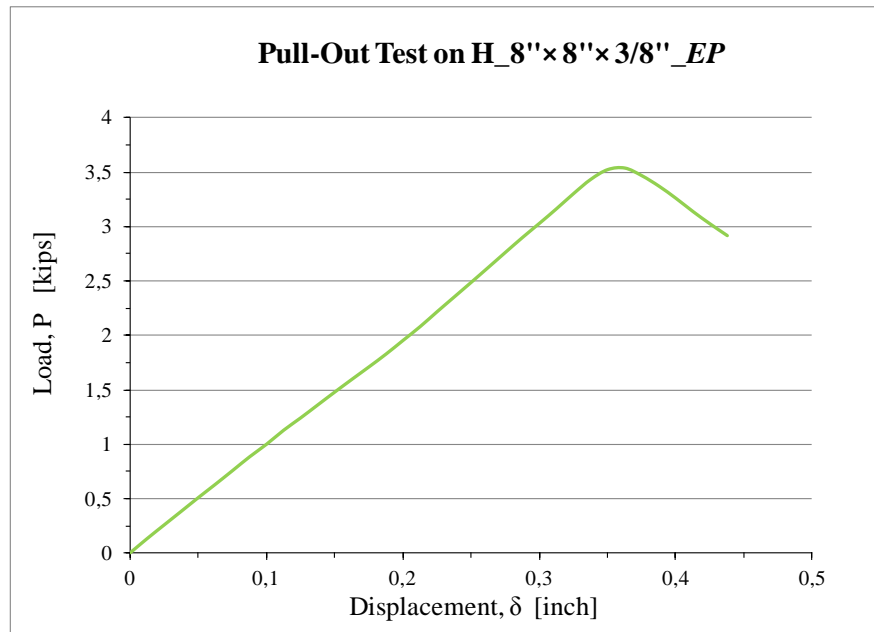


**Figure 4.25.** Load-Displacement Curve for H\_8" × 8" × 3/8" (203.2 mm × 203.2 mm × 9.53 mm)\_EP specimen at loading-point.

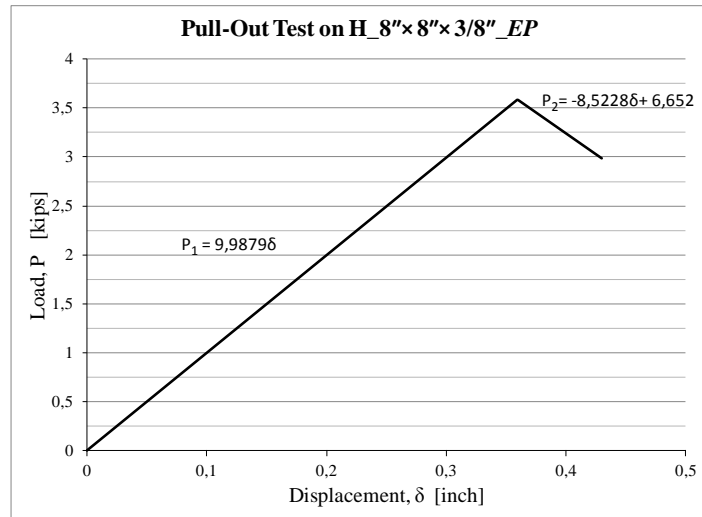


**Figure 4.26.** Linearized Load-Displacement Curve for H\_8'' x 8'' x 3/8'' (203.2 mm x 203.2 mm x 9.53 mm)\_EP specimen at loading-point.

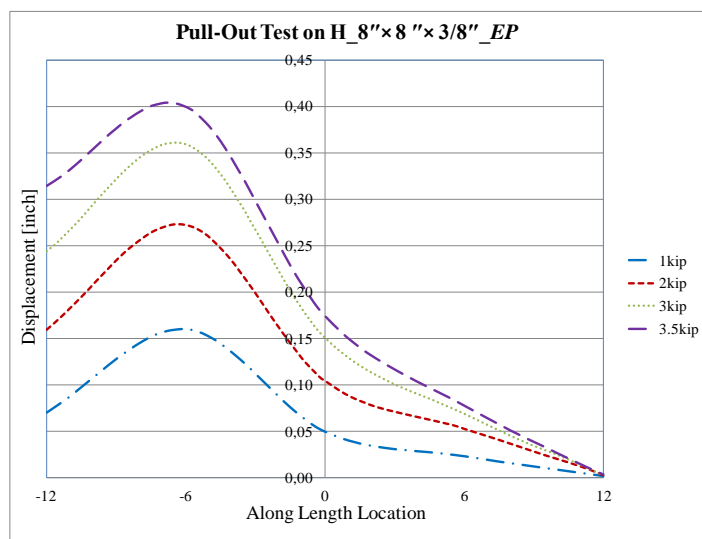


**Figure 4.27.** Displacement Pattern along Upper Flange Length for H\_8'' x 8'' x 3/8'' (203.2 mm x 203.2 mm x 9.53 mm)\_EP specimen at loading-point.

- Specimen #6: H\_6" × 6" × 3/8" (152.4 mm × 152.4 mm × 9.53 mm)\_EP

For this specimen, the displacement and the load was linearly proportional up to a displacement equal to 0.15 inch (3.81 mm) and load equal to 1.88 kips (8.40 kN). Beyond this point, stiffness decreased even though the relation between load and displacement remained linear up to 0.3 inch (7.62 mm) displacement and 2.85 kips (12.69 kN) load. After this point, failure started to occur. The load-displacement curve at loading-point is shown in Figure 4.28, and the equivalent linearized curve is shown in Figure 4.29. Figure 4.30 shows the displacement pattern along the upper flange length at 1.0 kip (4.45 kN) loading steps.

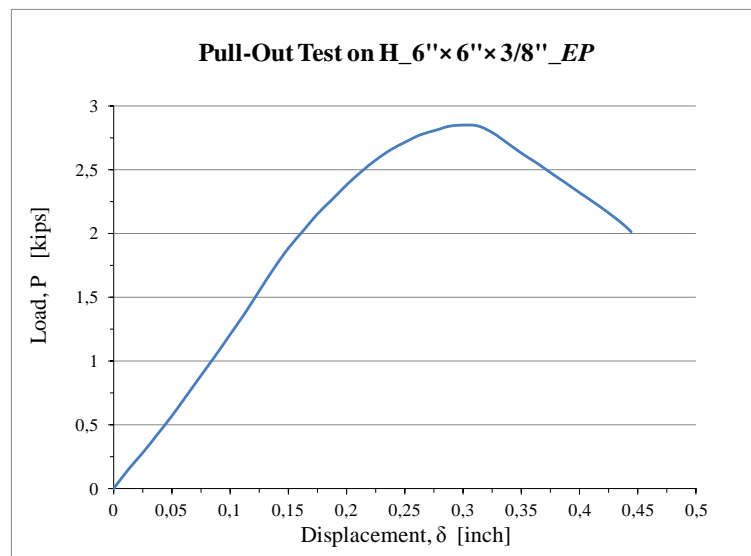


**Figure 4.28.** Load-Displacement Curve for H\_6" × 6" × 3/8" (152.4 mm × 152.4 mm × 9.53 mm)\_EP specimen at loading-point.

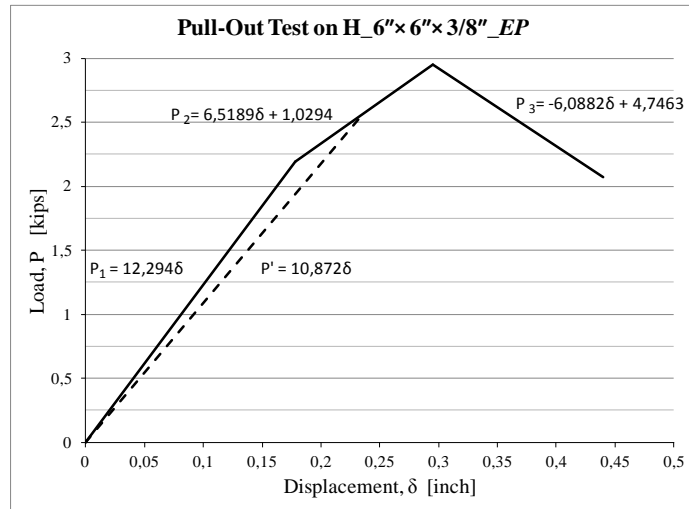


**Figure 4.29.** Linearized Load-Displacement Curve for H<sub>6''</sub> × 6'' × 3/8'' (152.4 mm × 152.4 mm × 9.53 mm)<sub>EP</sub> specimen at loading-point.

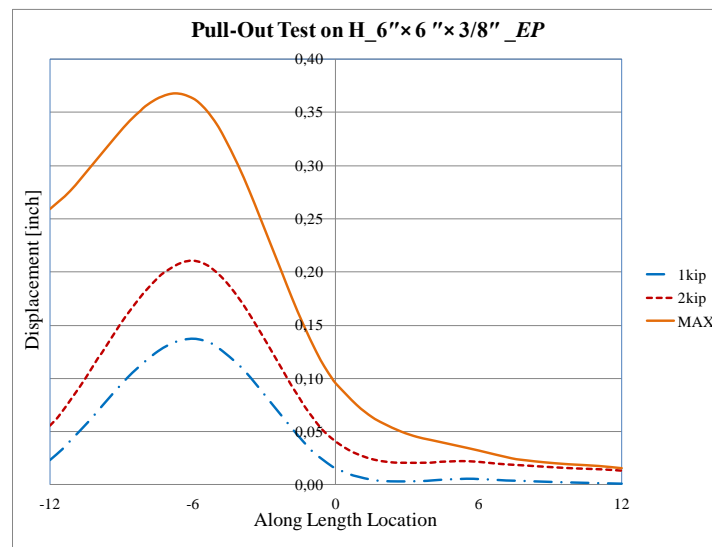


**Figure 4.30.** Displacement Pattern along Upper Flange Length for H<sub>6''</sub> × 6'' × 3/8'' (152.4 mm × 152.4 mm × 9.53 mm)<sub>EP</sub> specimen at loading-point.



In the following paragraphs, moment-rotation curves and the corresponding equivalent linearized relations  $M-\theta$  for all specimens are presented.

#### 4.2.2. Relative rotation test results

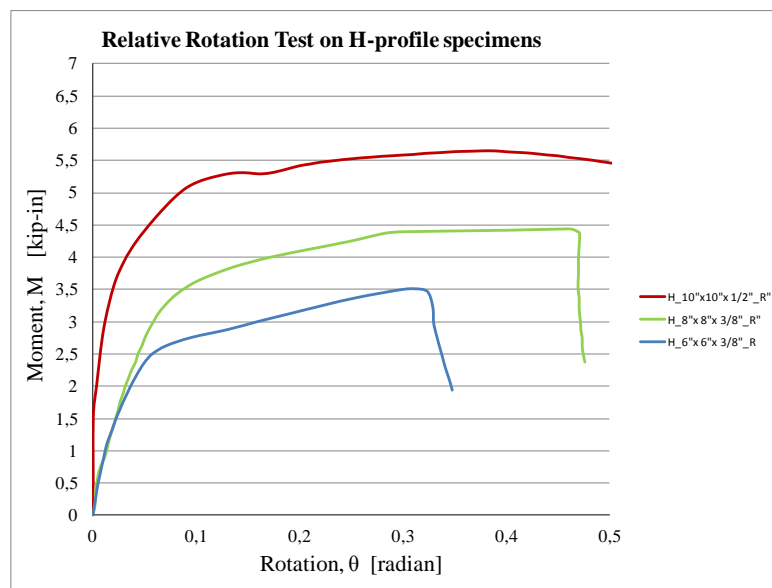
The main experimental results obtained from the relative rotations tests are summarized in Tables 4.5a,b. Figure 4.31 presents the moment-rotation ( $M-\theta$ ) curves for the H-profile (*Group 3*) specimens while Figures 4.32 and 4.33 show the  $M-\theta$  curves for L-profile specimens (*Group 4*) in both open-mode ( $R_{OM}$ ) and close-mode ( $R_{CM}$ ), respectively. It should be noted, in a typical semi-rigid framing connection such that shown in Figure 4.1, both opening mode (top clip angle) and closing mode (bottom clip seat angle) will potentially suffer local damages even when gravity loads are applied. This local damage will be amplified when the connection is exposed to cyclic loadings.

**Table 4.5a.** Relative Rotation Test Experimental results for H profile specimens (*Group III*).

#	Specimens	Length		Moment (linear limit) ( $M$ )		$\theta_l$ [rad]	Failure Moment ( $M_f$ )		$\theta_f$ [rad]	$\theta_u$ [rad]
		[mm] ]	[inch] ]	[kNmm] ]	[kip.in] ]		[kNmm] ]	[kip.in] ]		
7	H_10"× 10"× 1/2"_R	152.4	6.00	402.65	3.56	0.02	589.79	5.22	0.11	0.4
8	H_8"× 8"× 3/8"_R	152.4	6.00	409.73	3.63	0.10	497.09	4.40	0.30	0.46
9	H_6"× 6"× 3/8"_R	152.4	6.00	296.70	2.63	0.07	395.62	3.50	0.30	-

**Table 4.5b.** Relative Rotation Test Experimental results for L-profile specimens (*Group IV*).

#	Specimens	Length		Moment (linear limit) (M)		$\theta_l$ [rad]	Failure Moment (M <sub>f</sub> )		$\theta_f$ [rad]	$\theta_u$ [rad]
		[mm ]	[inch ]	[kNmm ]	[kip.in ]		[kNmm ]	[kip.in ]		
10	L_6"×6"×1/2" _R_OM	152.4	6.00	209.16	1.85	0.02	209.16	1.85	0.02	0.40
11	L_6"×6"×1/2" _R_CM	152.4	6.00	985.46	8.72	0.14	985.46	8.72	0.14	-
12	L_4"×4"×3/8" _R_OM	152.4	6.00	147.47	1.30	0.05	147.47	1.30	0.05	0.13
13	L_4"×4"×3/8" _R_CM	152.4	6.00	482.21	4.27	0.15	482.21	4.27	0.15	-

**Figure 4.31.** Moment-rotation ( $M-\theta$ ) curves for H-profile specimens in Relative Rotation Test.

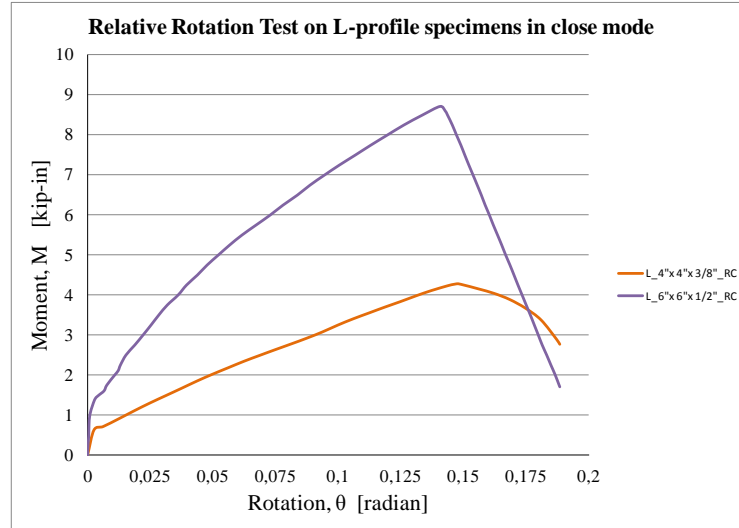


**Figure 4.32.** Moment-rotation ( $M-\theta$ ) curves for close mode L-profile specimens in Relative Rotation Test.

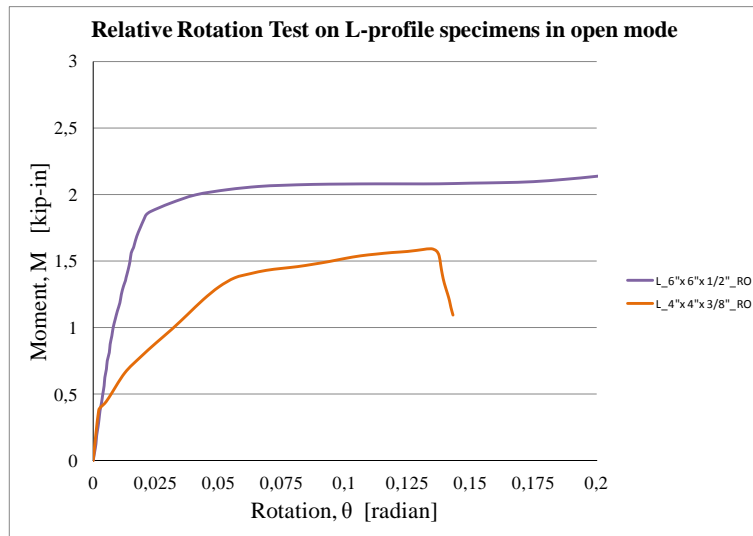


**Figure 4.33.** Moment-rotation ( $M-\theta$ ) curves for open mode L-profile specimens in Relative Rotation Test.

- *Specimen #7: H<sub>10</sub>" × 10" × 1/2"* (254 mm × 254 mm × 12.7 mm)*\_R* specimen

For this specimen, it was observed that the rotation was very small up to moment less or equal to 1.5 kip.in (169.5 kNm). The relation between moment and rotation angle remained linear up to 3.56 kip.in (402.65 kNm) moment and 0.02 radian rotation angle. After that level degradation in the stiffness started to occur, even though the relation between moment and rotation stayed linear up to 5.22 kip.in (589.79 kNm) moment and 0.11 radian rotation angle. From here, large increases in rotation angle were observed with very small changes in moment up to 0.4 radian rotation angle. After this point, failure started to occur (refer to Figure 4.34). Figure 4.35 shows the moment–rotation curve for the H-profile, while the linearized curve is shown in Figure 4.36.



**Figure 4.34.** Failure of H<sub>10</sub>" × 10" × 1/2" (254 mm × 254 mm × 12.7 mm)*\_R* specimen.

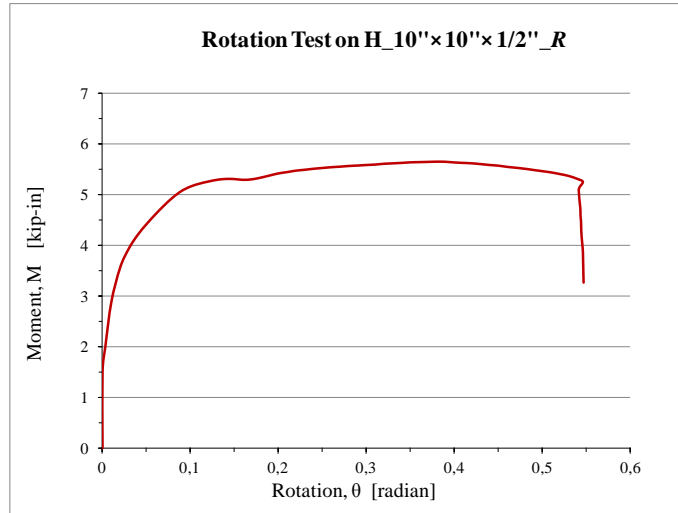


**Figure 4.35.** Moment-rotation curve for H<sub>10''</sub> × 10'' × ½'' (254 mm × 254 mm × 12.7 mm)<sub>R</sub> specimen.

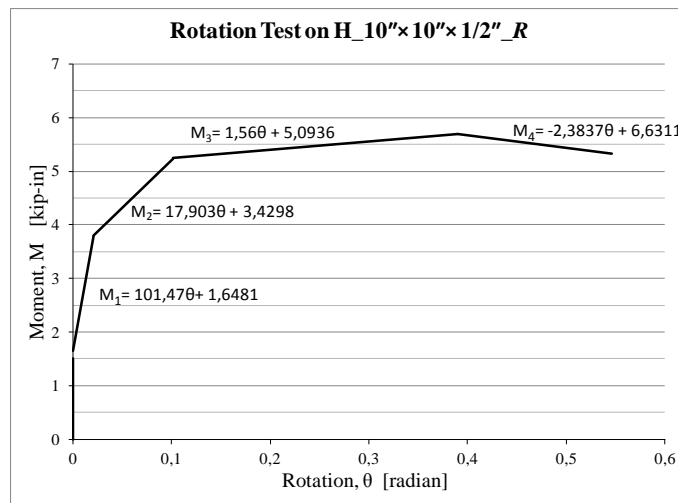


**Figure 4.36.** Linearized Moment-Rotation Curve for H<sub>10''</sub> × 10'' × ½'' (254 mm × 254 mm × 12.7 mm)<sub>R</sub> specimen.

- *Specimen #8*: H\_8" × 8" × 3/8" (203.2 mm × 203.2 mm × 9.53 mm)\_R specimen

For this specimen, it was observed that the rotation was very small up to moment equal to 0.7 kip.in (79.1 kNmm). Beyond this point, the relation between moment and rotation angle remained linear up to 3.62 kip.in (409.73 kNmm) moment and 0.10 radian rotation angle. After this point, stiffness degradation was observed; however, the relation between moment and rotation (M-θ) remained linear up to 4.40 kip.in (497.09 kNmm) moment and 0.3 radian rotation angle. In the final leg, increasing in rotation angle was observed without any change in moment up to 0.46 radian rotation angle, after that the failure suddenly occurred (Fig. 4.37). Figure 4.38 shows the M-θ curve for 8" × 8" × 3/8" H-profile, while the linearized curve is shown in Figure 4.39.



**Figure 4.37.** Failure of H\_8" × 8" × 3/8" (203.2 mm × 203.2 mm × 9.53 mm)\_R specimen.

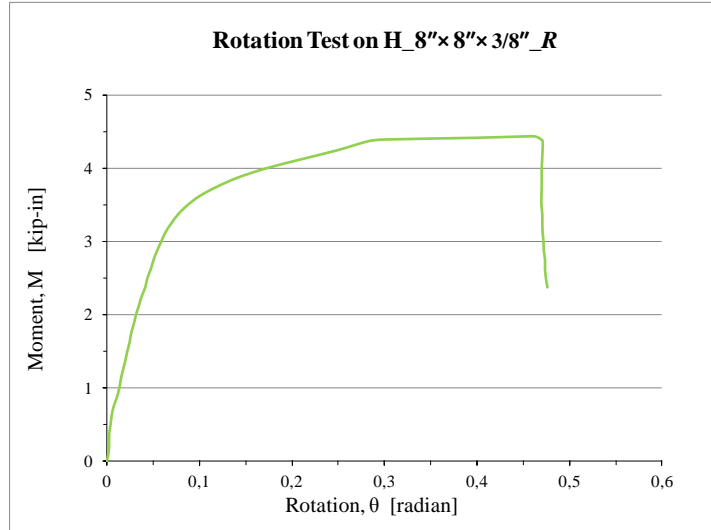


**Figure 4.38.** Moment-rotation curve for H<sub>8'' × 8'' × 3/8''</sub> (203.2 mm × 203.2 mm × 9.53 mm)<sub>R</sub> specimen.

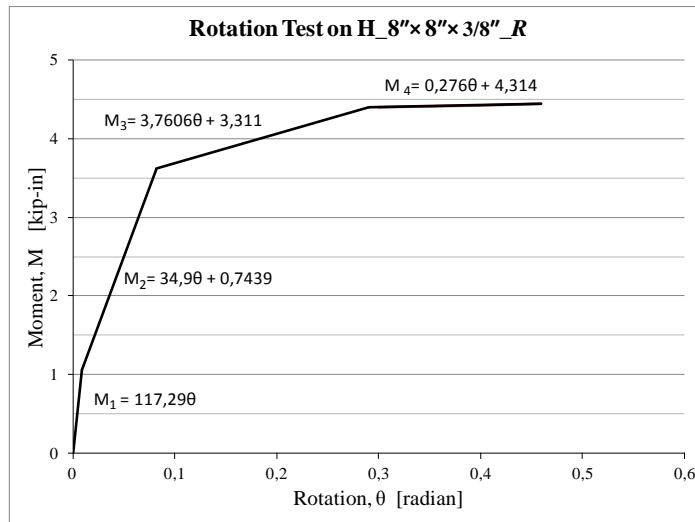


**Figure 4.39.** Linearized Moment-Rotation Curve for H<sub>8'' × 8'' × 3/8''</sub> (203.2 mm × 203.2 mm × 9.53 mm)<sub>R</sub> specimen.

- *Specimen #9: H<sub>6" × 6" × 3/8"</sub> (152.4 mm × 152.4 mm × 9.53 mm)<sub>R</sub>*

For this specimen, identical behavior was noticed. The rotation was very small up to moment equal to 0.7 kip.in (79.1 kNmm); after which, the relation between moment and rotation angle was linear up to 2.63 kip.in (296.70 kNmm) moment and 0.07 radian rotation angle. Beyond this point degradation in the stiffness started to occur but the relation between moment and rotation remained linear up to 3.50 kip.in (395.62 kNmm) moment and 0.30 radian rotation angle, at which time failure occurred (Fig. 4.40). Figure 4.41 shows the Moment–Rotation curve for the 6" × 6" × 3/8" H-profile, while the linearized curve is shown in Figure 4.42.



**Figure 4.40.** Failure of H<sub>6" × 6" × 3/8"</sub> (152.4 mm × 152.4 mm × 9.53 mm)<sub>R</sub> specimen.



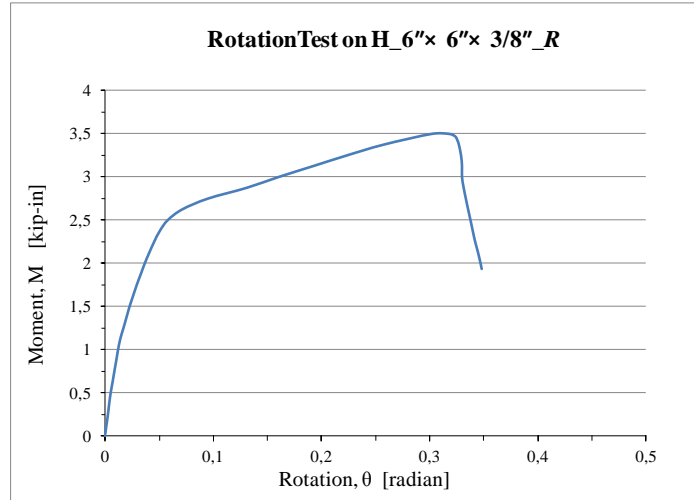


**Figure 4.41.** Moment-rotation curve for H<sub>6''</sub> × 6'' × 3/8'' (152.4 mm × 152.4 mm × 9.53 mm)<sub>R</sub> specimen.

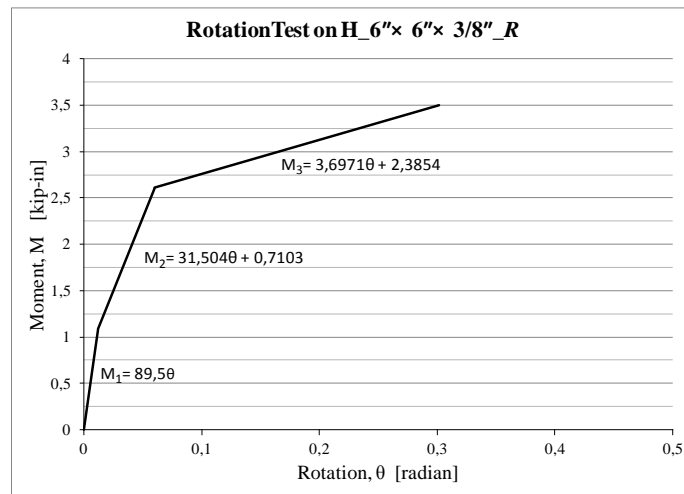


**Figure 4.42.** Linearized moment-rotation for H<sub>6''</sub> × 6'' × 3/8'' (152.4 mm × 152.4 mm × 9.53 mm)<sub>R</sub> specimen.

- Specimen #10: L\_6" × 6" × ½" (152.4 mm × 152.4 mm × 12.7 mm)\_R\_OM

For the L-specimen in open mode, it was observed that the rotation was very small up to a moment equal to 1.0 kip.in (113.03 kNmm); after that the relation between moment and rotation angle was linear up to 1.85 kip.in (209.16 kNmm) moment and 0.02 radian rotation angle. Increases in rotation angle were observed with small increases in moment till 0.40 radian rotation angle. After that the failure suddenly occurred (Fig. 4.43). Figure 4.44 shows the Moment-Rotation curve for open mode of 6" × 6" × ½" L-profile, while the linearized curve is shown in Figure 4.45.



**Figure 4.43.** Failure of L-profile specimens, *opening and closing mode*.

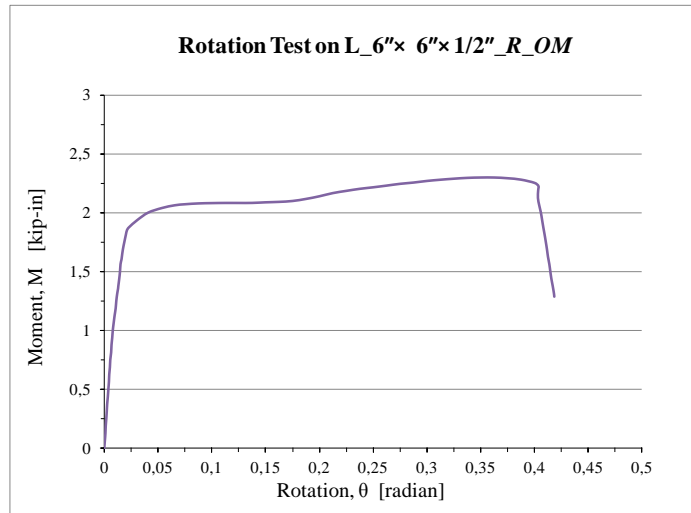


**Figure 4.44.** Moment-rotation curve for L<sub>6'' × 6'' × 1/2''</sub> (152.4 mm × 152.4 mm × 12.7 mm)<sub>R\_OM</sub> specimen.

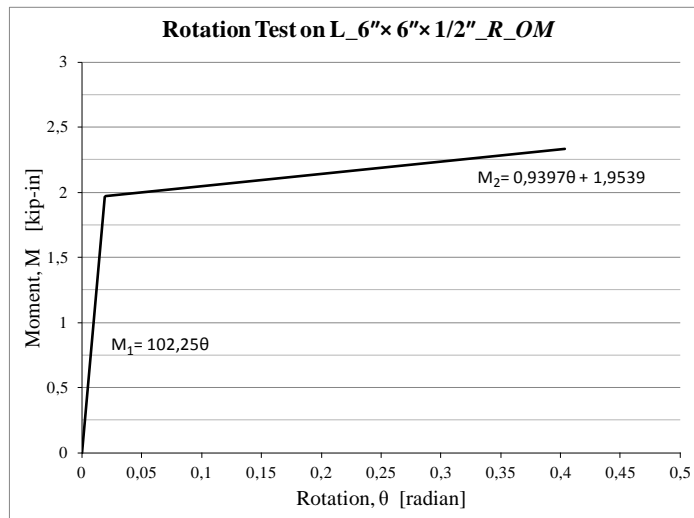


**Figure 4.45.** Linearized Moment-Rotation Curve for L<sub>6'' × 6'' × 1/2''</sub> (152.4 mm × 152.4 mm × 12.7 mm)<sub>R\_OM</sub> specimen.

- Specimen #11: L\_6" × 6" × ½" (152.4 mm × 152.4 mm × 12.7 mm)\_R\_CM

For the L-specimen in close mode, it was observed that the rotation was very small up to moment equal to 1.00 kip.in (113.03 kNmm), after that the relation between moment and rotation angle was linear up to 8.72 kip.in (985.46 kNmm) moment and 0.14 radian rotation angle. After that the failure started to occur (Fig. 4.43). Figure 4.46 shows the Moment–Rotation curve for close mode of 6" × 6" × ½" L-profile, while the linearized curve is shown in Figure 4.47.

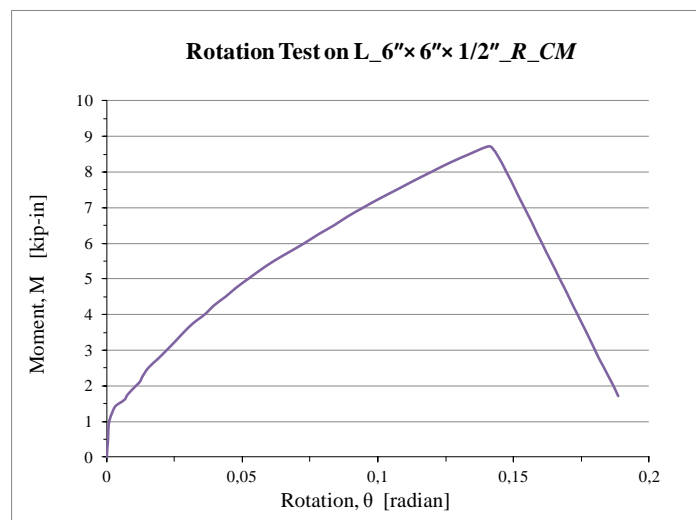


**Figure 4.46.** Moment-Rotation Curve for L\_6" × 6" × ½" (152.4 mm × 152.4 mm × 12.7 mm)\_R\_CM specimen.

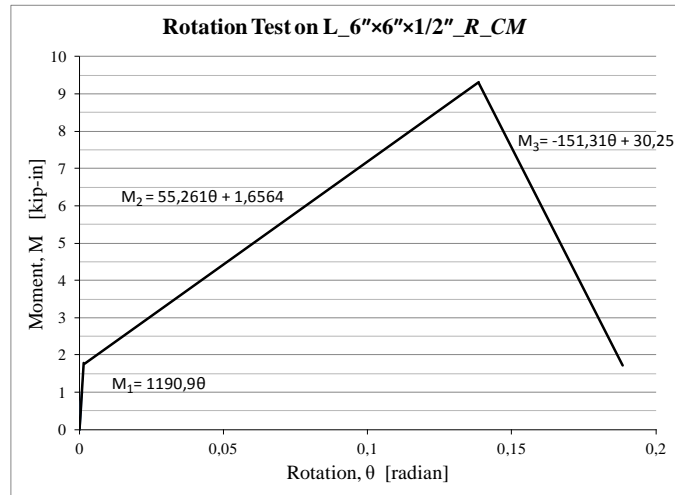


**Figure 4.47.** Linearized moment-rotation curve for  $L_6'' \times 6'' \times \frac{1}{2}''$  (152.4 mm  $\times$  152.4 mm  $\times$  12.7 mm) $_R_{CM}$  specimen.

- Specimen #12:  $L_4'' \times 4'' \times \frac{3}{8}''$  (101.6  $\times$  101.6  $\times$  9.53 mm) $_R_{OM}$

For this specimen in open mode, it was observed that the rotation was very small up to a moment equal to 0.4 kip.in (45.21 kNm). The relation between moment and rotation angle was linear up to 1.30 kip.in (147.47 kNm) moment and 0.05 radian rotation angle. After that, increases in rotation angle were observed with small increases in moment till 0.13 radian rotation angle. After this point, the failure suddenly occurred (refer to Figure 4.43). Figure 4.48 shows the Moment–Rotation curve for open mode of  $4'' \times 4'' \times \frac{3}{8}''$  L-profile, while the linearized curve is shown in Figure 4.49.

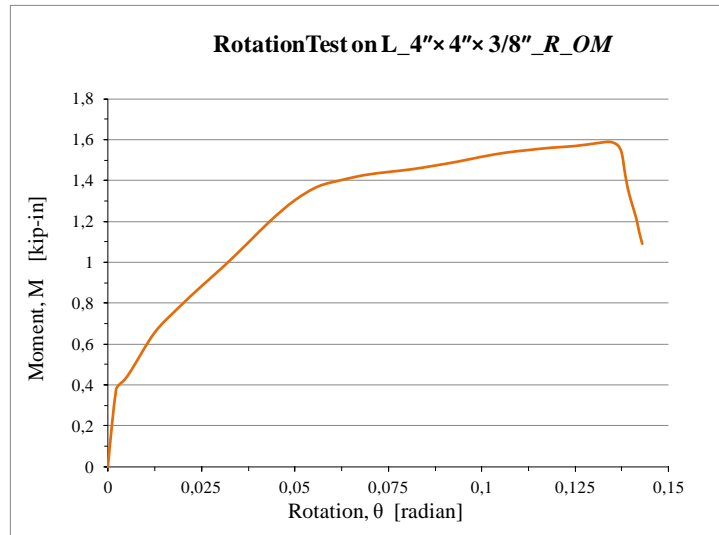


**Figure 4.48.** Moment-rotation curve for L<sub>4''</sub> × 4'' × 3/8'' (101.6 mm × 101.6 mm × 9.53 mm)<sub>R\_OM</sub> specimen.

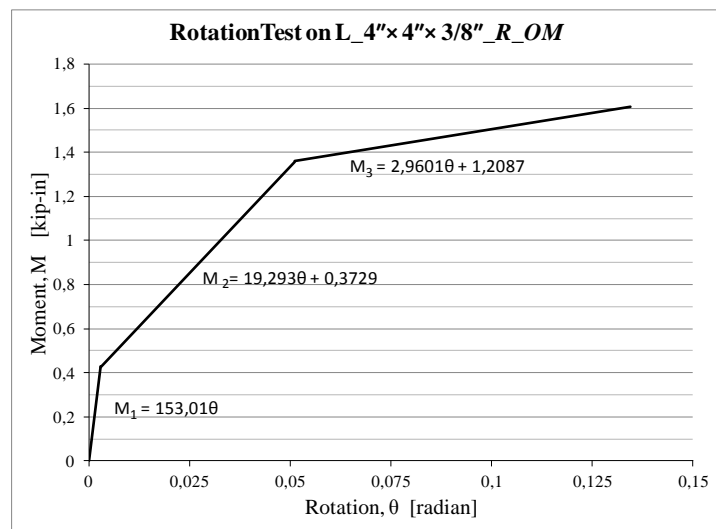


**Figure 4.49.** Linearized moment-rotation curve for L<sub>4''</sub> × 4'' × 3/8'' (101.6 mm × 101.6 mm × 9.53 mm)<sub>R\_OM</sub> specimen.

- Specimen #13: L<sub>4"</sub> × 4" × 3/8" (101.6 mm × 101.6 mm × 9.53 mm)<sub>R\_CM</sub> specimen

For this specimen in close mode, it was observed that the rotation was very small up to a moment equal to 0.71 kip.in (80.5 kNm). The relation between moment and rotation angle remained linear up to 4.27 kip.in (482.21 kNm) moment and 0.15 radian rotation angle. After that the failure started to occur (Fig. 4.43). Figure 4.50 shows the moment-rotation curve for close mode of 4" × 4" × 3/8" L-profile, while the linearized curve is shown in Figure 4.51.

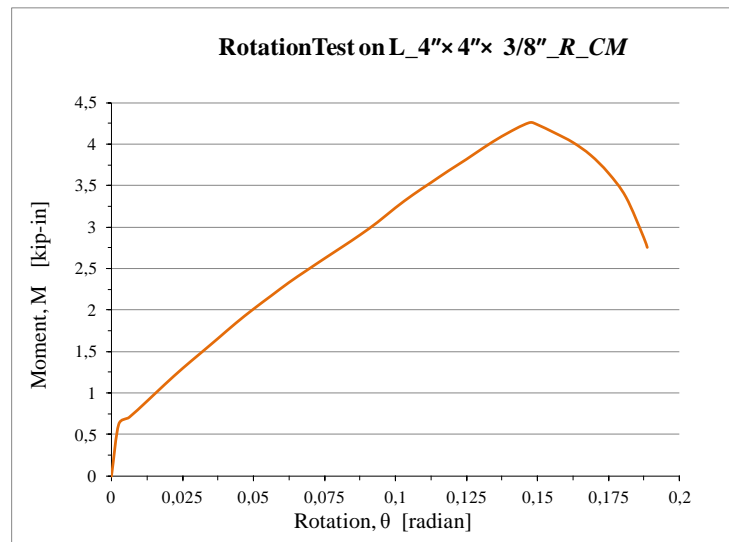


**Figure 4.50.** Moment-rotation curve for L<sub>4"</sub> × 4" × 3/8" (101.6 mm × 101.6 mm × 9.53 mm)<sub>R\_CM</sub> specimen.

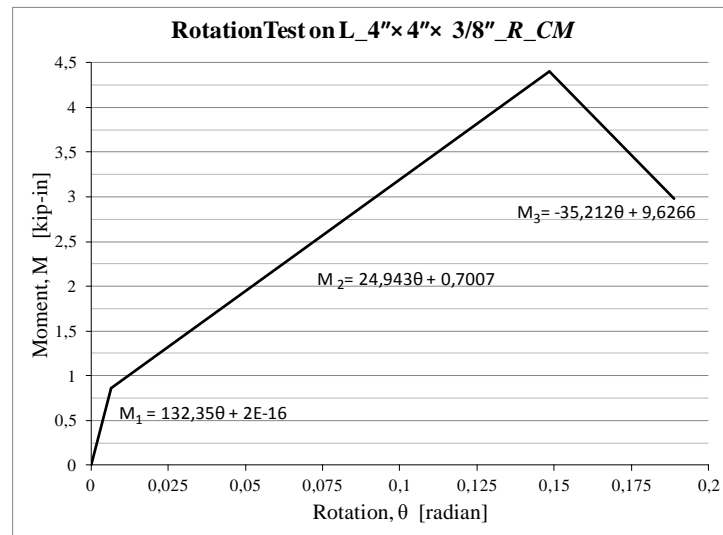


**Figure 4.51.** Linearized moment-rotation curve for L\_4'' x 4'' x 3/8'' (101.6 mm x 101.6 mm x 9.53 mm)\_R\_CM specimen.

### 4.3 FINITE ELEMENT ANALYSIS

In order to support and verify the results of the experimental investigation carried out at the Structural Engineering Testing Hall (SETH) of the University of California Irvine, a 3-D finite element was employed in the linear elastic range by using the Straus software.

As already done in the numerical analysis of thin walled pultruded I-profiles presented in chapter 3, the roving of the web and flanges was modeled using eight-node orthotropic finite elements (*bricks*), while orthotropic surface elements (*plates*) were used to simulate the external layers (*mat*) of the profiles.



The dimensions of the finite elements (*bricks* and *plates*) are summarized in Table 4.6 for each size of the profiles investigated in the 3-D FEM analysis.

**Table 4.6.** Dimensions of bricks and plates used in the 3-D finite-elements analysis.

Size profile	Brick dimensions $l_x(mm) \times l_y(mm) \times l_z(mm)$			Plate dimensions $l_x(mm) \times l_z(mm)$		
	Type I	Type II	Type III	Type I	Type II	Type II
H_10"×10"×1/2" (254 mm × 254 mm × 12.7 mm)	2.54×2.54×25.4	1.27×2.54×25.4	-	2.54×25.4 4	1.27 ×25.4 4	-
H_8"×8"×3/8" (203 mm × 203 mm × 9.53 mm)	2.54×2.54×25.4 4	0.3175×2.54×25.4 4	0.635×2.54×25.4 4	2.54×25.4 4	0.31 7×25 .4	0.635× 25.4
H_6"×6"×3/8" (152.4 mm × 152.4 mm × 9.53 mm)	2.54×2.54×25.4 4	0.3175×2.54×25.4 4	0.635×2.54×25.4 4	2.54×25.4 4	0.31 7×25 .4	0.635× 25.4
L_4"×4"×3/8" (101.6 mm × 101.6 mm × 9.53 mm)	2.54×2.54×25.4 4	0.3175×2.54×25.4 4	0.635×2.54×25.4 4	2.54×25.4 4	0.31 7×25 .4	0.635× 25.4
L_6"×6"×1/2" (152.4 mm × 152.4 mm × 12.7 mm)	2.54×2.54×25.4 4	-	-	2.54×25.4 4	-	-

The values of the material properties (*roving* and *mat*) are summarized in Table 4.7 and coincide with those by Bank et al. in [66].

**Table 4.7** Values of the engineering properties of roving and mat used in the 3-D finite-elements analysis (Bedford Reinforced Plastics).

Engineering properties	Measurement	Value	Values
	Unit	(Bricks)	(Plates)
Longitudinal elastic modulus, $E_z$	MPa	17,200	-
Transversal elastic moduli, $E_x = E_y$	MPa	6,900	11,719
Transversal shear modulus, $G_{xy}$	MPa	3,100	3,100
Shear Moduli, $G_{zx} = G_{zy}$	MPa	3,100	-
Longitudinal Poisson's ratio, $\nu_{xy}$		0.33	0.19
Transversal Poisson's ratios, $\nu_{zx} = \nu_{zy}$		0.09	-

Figures 4.52a-d show the typical three-dimensional finite-element mesh of the specimens. As it can be seen from these figures, in the finite element model of the specimens of groups 1 and 2 (Figs. 4.52a,b), the nodes of the lower flange were constrained against all movements, while the uniform pull load, acting on the upper flange of the PFRP H-profile, was simulated by modeling the steel device fixed to the testing machine.

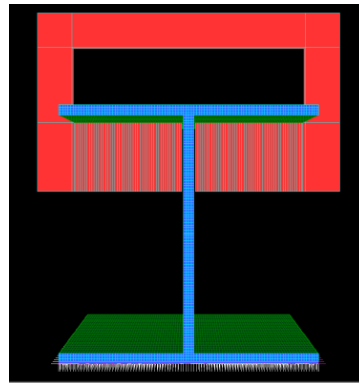
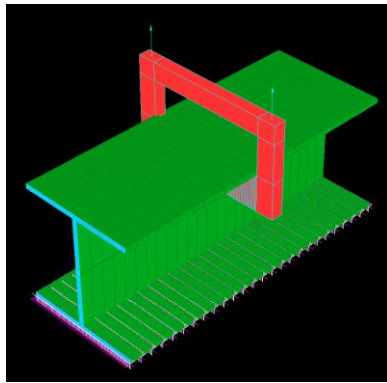


**Figure 4.52a.** Typical finite-element mesh of *Group 1* of specimens.

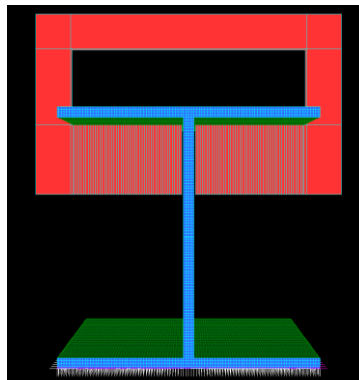
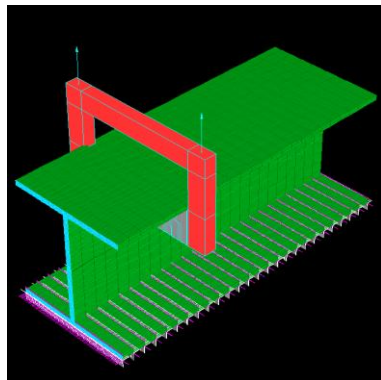


**Figure 4.52b.** Typical finite-element mesh of *Group 2* of specimens.

In the 3-D FEM model developed for the numerical analysis of groups 3 and 4 of specimens, the constrains were applied in correspondence of the nodes of the web at a distance equal to 1 inch (25,4 mm) from the web-flange junction of the PFRP profile (Figs. 4.52c,d). This model simulate the device used for the relative rotation test of the above mentioned profiles (Figs. 4.9a-d),

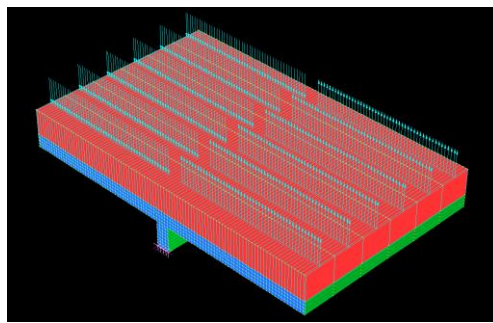


**Figure 4.52c.** Typical finite-element mesh of *Group 3* of specimens.

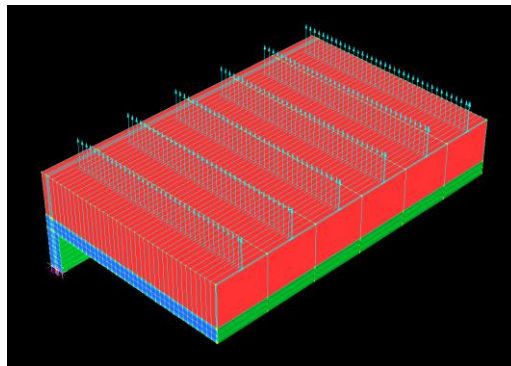
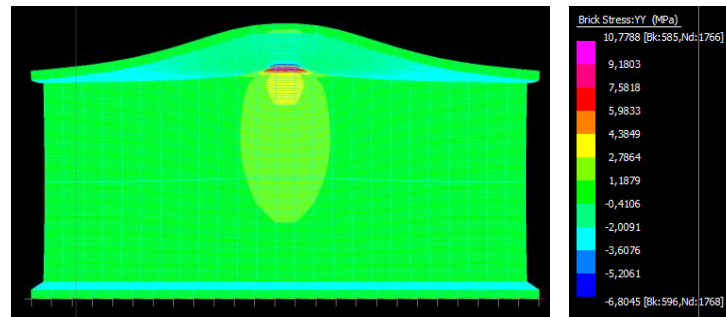


**Figure 4.52d.** Typical finite-element mesh of *Group 4* of specimens.

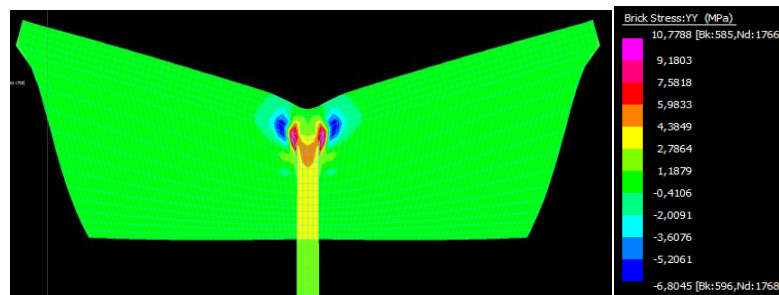
In the following paragraphs the numerical results obtained from the FEM analysis are presented and discussed.

### 4.3.1. Numerical results for specimen H\_10"×10"×1/2" (254 mm × 254 mm × 12.7 mm)\_MP of Group 1: Mid-point Loading Test

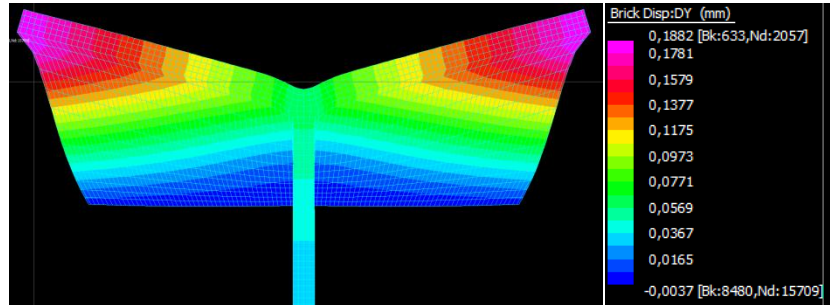
Figure 4.53 shows the numerical stresses ( $\sigma_{yy}$ ) distribution in the web of H\_10"×10"×1/2" (254 mm × 254 mm × 12.7 mm)\_MP specimen in the deformed configuration at a load level of 4.448 kN (1kip). The brick stresses ( $\sigma_{yy}$ ) and the displacement (DY) distributions at the web-flange junction of the loading point of the specimen are shown in Figures 4.54a and b, respectively.



**Figure 4.53.** Brick numerical stresses ( $\sigma_{yy}$ ) in the web of H\_10"×10"×1/2" (254 mm × 254 mm × 12.7 mm)\_MP specimen (P=4.448kN, P=1kip).



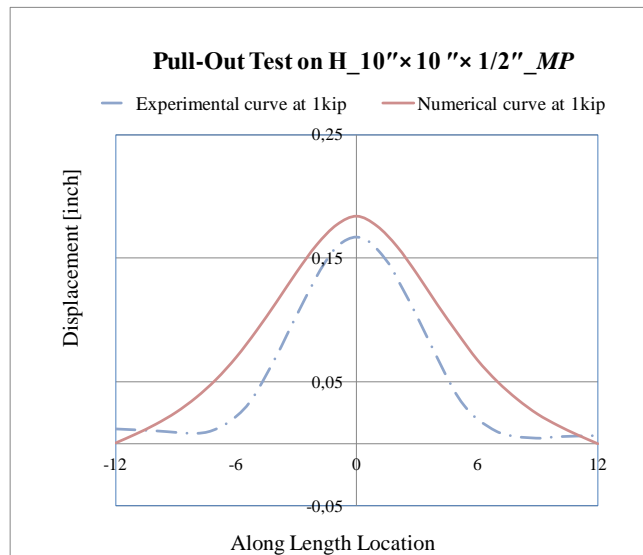
**Figure 4.54a.** Brick numerical stresses distributions ( $\sigma_{yy}$ ) at the web-flange junction of the loading point of H\_10"×10"×1/2" (254 mm × 254 mm × 12.7 mm)\_MP specimen (P=4.448kN, P=1kip.).



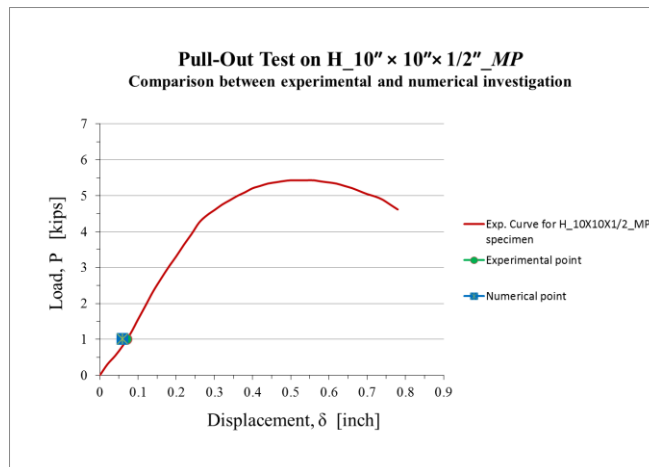
**Figure 4.54b.** Displacement distributions (DY) at the web-flange junction of the loading point of H<sub>10"</sub>×10"×1/2" (254 mm × 254 mm × 12.7mm)<sub>MP</sub> specimen (P=4.448kN, P=1kip).

Figure 4.55a shows the numerical and the experimental displacement patterns along the upper flange length of the specimen at a load level of 4.448 kN (1 kip).

A comparison between numerical and experimental displacement at the web-flange junction of the loading point is also presented in Figure 4.55b for the same value of the applied load.



**Figure 4.55a.** Comparison between numerical and experimental displacement patterns along upper flange Length for H<sub>10''</sub> × 10'' × 1/2'' (254 mm × 254 mm × 12.7mm)<sub>MP</sub> specimen (P=4.448kN, P=1kip.).



**Figure 4.55b.** Numerical and experimental displacement at the web-flange junction of the loading point of H<sub>10''</sub> × 10'' × 1/2'' (254 mm × 254 mm × 12.7mm)<sub>MP</sub> specimen (P=4.448kN, P=1kip.).

From Figures 4.55a-b, one can notice a good agreement between the numerical and the experimental results. Moreover, the numerical and the experimental results obtained for all specimens evaluated in the mid-point loading configuration of the second phase of the present research have confirmed that the “*Load influence zone*”, as defined in Chapter 3 for the PFRP I-profiles, depends on the depth of the PFRP member with a maximum value equal to approximately the PFRP member’s depth.

#### **4.3.2. Numerical results for H<sub>10</sub>”×10”×1/2” (254 mm × 254 mm ×12.7 mm)<sub>EP</sub> specimen of Group 2: End-point Loading Test**

Figure 4.56 shows the brick numerical stresses ( $\sigma_{yy}$ ) distribution in the web of H<sub>10</sub>”×10”×1/2” (254 mm × 254 mm × 12.7 mm)<sub>EP</sub> specimen in the deformed configuration at load level of 4.448 kN (1kip). The brick stresses ( $\sigma_{yy}$ ) and the displacement (DY) distributions at the web-flange junction of the loading point of the specimen are shown in Figures 4.57a and b, respectively.

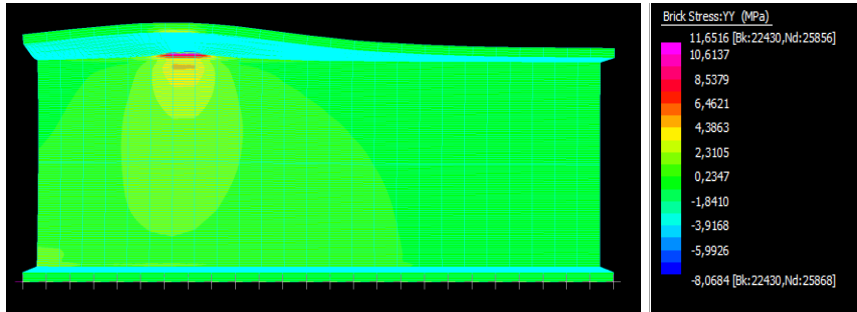


**Figure 4.56.** Brick numerical stresses ( $\sigma_{yy}$ ) in the web of H<sub>10</sub>''×10''×1/2'' (254 mm × 254 mm × 12.7 mm)<sub>EP</sub> specimen (P=4.448kN, P=1kip).

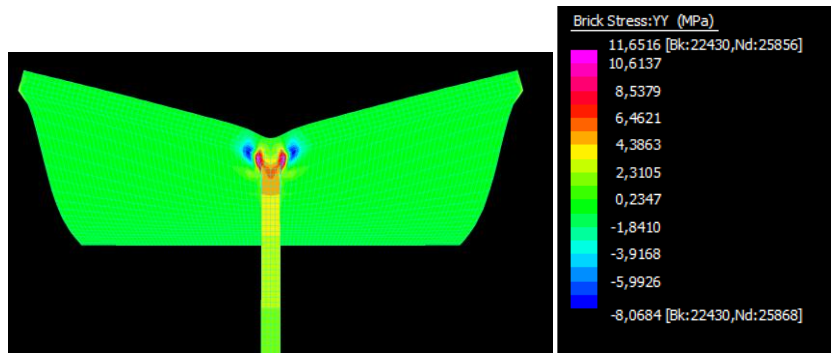


**Figure 4.57a.** Brick numerical stresses distributions ( $\sigma_{yy}$ ) at the web-flange junction of H<sub>10</sub>''×10''×1/2'' (254 mm × 254 mm×12.7 mm)<sub>EP</sub> specimen (P=4.448kN, P=1kip.).



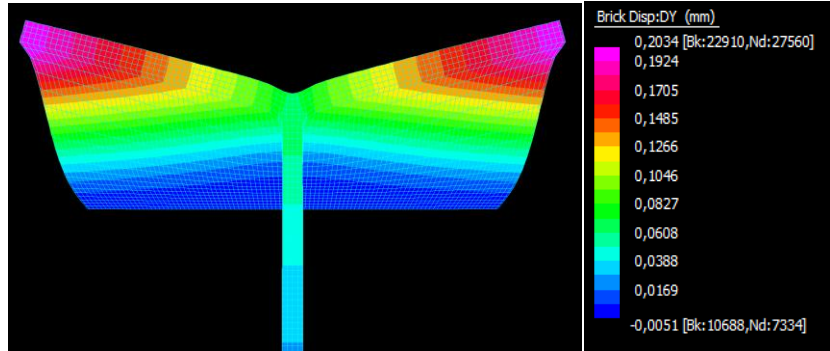


**Figure 4.57b.** Displacement distributions (DY) at the web-flange junction of the loading point of H<sub>10</sub>''x10''x1/2'' (254 mm × 254 mm × 12.7 mm)<sub>EP</sub> specimen (P=4.448kN, P=1kip).

Figure 4.58 shows a comparison between numerical and experimental displacement at the web-flange junction of the loading point for the same load value.

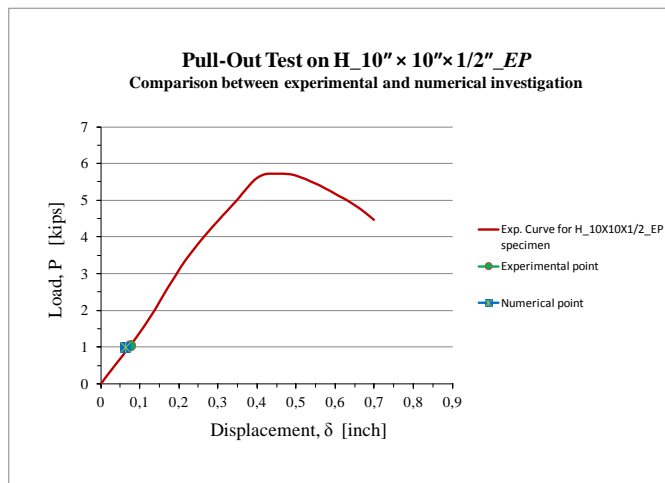


**Figure 4.58.** Comparison between numerical and experimental displacement at the web-flange junction of the loading point of H<sub>10</sub>''x10''x1/2'' (254 mm × 254 mm × 12.7 mm)<sub>EP</sub> specimen (P=4.448kN, P=1kip).

Also in this case, one can notice a good agreement between the numerical and the experimental results which have confirmed the definition of the “*Load influence zone*”, as defined in Chapter 3.

#### 4.3.3. Numerical results for *Group 3 of specimens: Relative rotation Test (H profile) on H\_10"×10"×1/2" (254 mm × 254 mm × 12.7 mm)\_R specimen*

Figures 4.59a and b show the brick numerical stresses ( $\sigma_{yy}$ ) and the displacement (DY) distributions at the web-flange junction of the loading point of the specimen in the deformed configuration for a value of the applied twisting moment equal to 402.65 kNmm (3.56 kip.in).

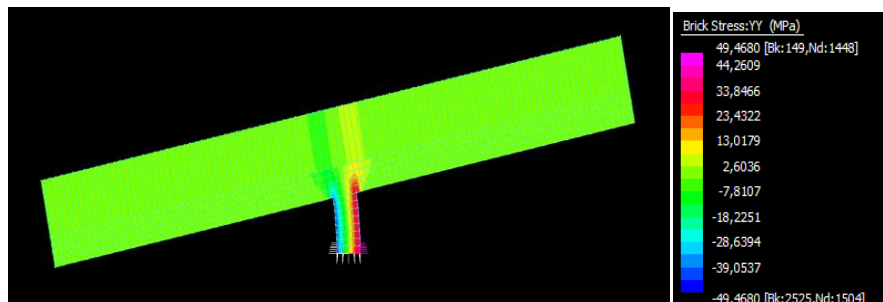


**Figure 4.59a.** Brick numerical stresses distributions ( $\sigma_{yy}$ ) at the web-flange junction of the loading point of H\_10"×10"×1/2" (254 mm × 254 mm × 12.7mm)\_R specimen (M=402.65 kNmm, M=3.56 kip.in).

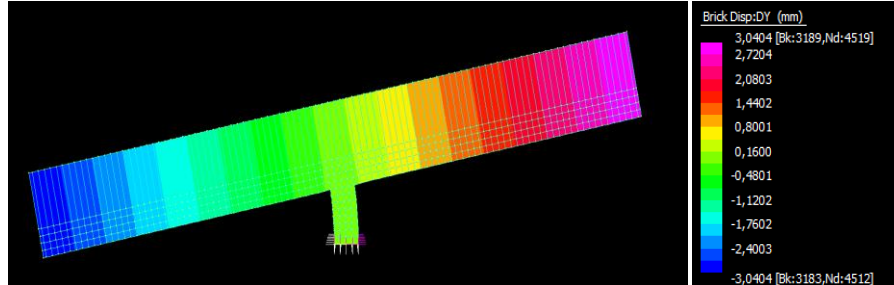


**Figure 4.59b.** Displacement distributions (DY) at the web-flange junction of the loading point of H<sub>10''</sub>×10''×1/2'' (254 mm × 254 mm × 12.7mm)<sub>R</sub> specimen (M=402.65 kNmm, M=3.56 kip.in).

Figure 4.60 shows the comparison between numerical and experimental displacement at the web-flange junction of the loading point for the same value of the twisting moment.

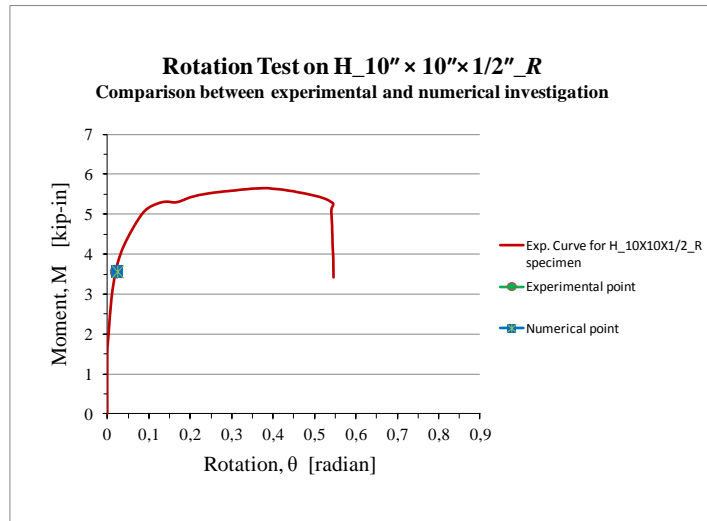


**Figure 4.60.** Numerical and experimental rotations of the web-flange junction of the loading point of H<sub>10''</sub>×10''×1/2'' (254 mm × 254 mm × 12.7mm)<sub>R</sub> specimen (M=402.65 kNmm, M=3.56 kip.in).

#### 4.3.4. Numerical results for L<sub>4"×4"×3/8"</sub> (101.6 mm × 101.6 mm × 9.53mm)<sub>R\_OM</sub> of Group 4: *Relative rotation Test (L profile) in open mode*

Figure 4.61a and b show the brick numerical stresses ( $\sigma_{yy}$ ) and the displacement (DY) distributions at the web-flange junction of the loading point of the specimen in the deformed open mode configuration for a value of the twisting moment equal to 123.9 kNmm (1.096 kip.in).

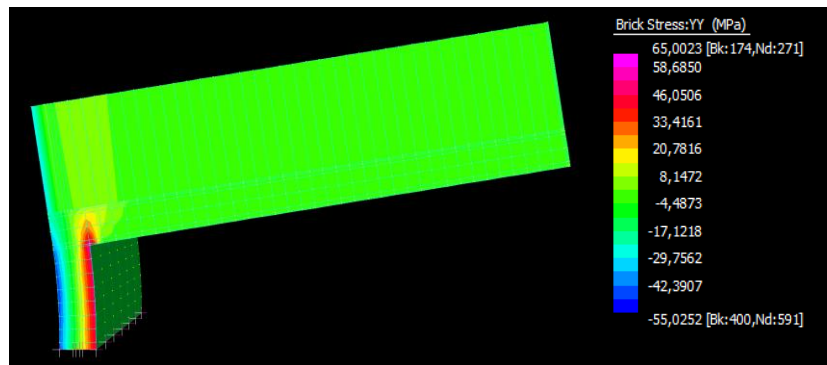


**Figure 4.61a.** Brick numerical stress distributions ( $\sigma_{yy}$ ) at the web-flange junction of the loading point of L<sub>4"×4"×3/8"</sub> (101.6 mm × 101.6 mm × 9.53 mm)<sub>R\_OM</sub> specimen (M=123.9 kNmm, M=1.096 kip.in).

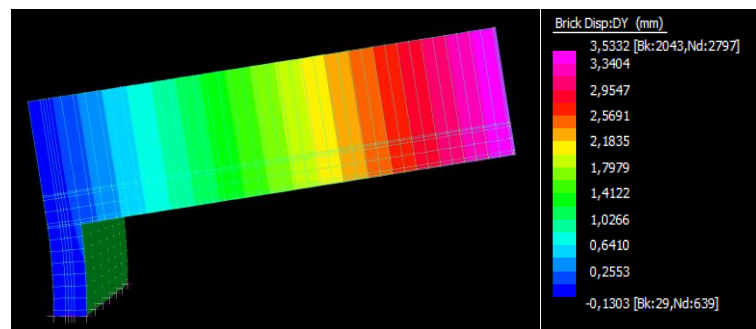


**Figure 4.61b.** Displacement distributions (DY) at the web-flange junction of the loading point of L<sub>4"×4"×3/8"</sub> (101.6 mm × 101.6 mm × 9.53 mm)<sub>R\_OM</sub> specimen (M=123.9 kNmm, M=1.096 kip.in).

Figure 4.62 shows the comparison between numerical and experimental displacement at the web-flange junction of the loading point for the same value of the applied moment.

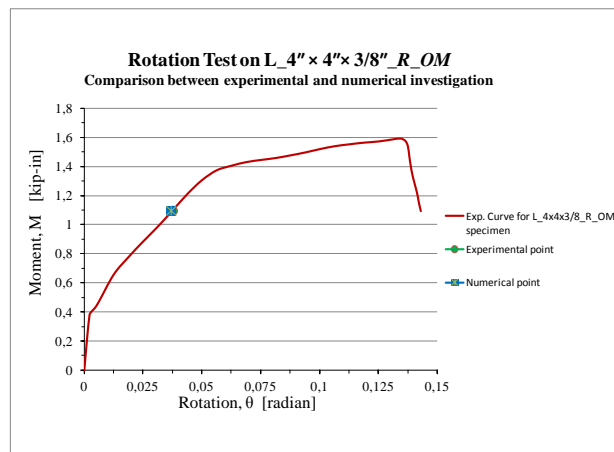


**Figure 4.62.** Numerical and experimental displacement at the web-flange junction of the loading point of  $L_4'' \times 4'' \times 3/8''$  (101.6 mm  $\times$  101.6 mm  $\times$  9.53 mm)<sub>R\_OM</sub> specimen ( $M=123.9$  kNmm,  $M=1.096$  kip.in).

From all these figures one can notice the good agreement between the numerical and the experimental results.

In conclusion, the finite element analysis developed in this study was able to predict the linear axial and rotational behavior of the web-flange junctions of the PFRP shapes. In a future step of the present research, the numerical analysis will be expanded in the nonlinear field in order to capture the nonlinear structural response of the PFRP web-flange junctions.

#### 4.4 RESULTS

The following observations and conclusions were made based on the second phase of this experimental study:

- i) the orthotropic and viscoelastic behavior of the PFRP sections must be taken into consideration when designing PFRP structural members;
- ii) local failure of web-flange junction of unidirectional pultruded profiles influences both stiffness and strength limit-states of pultruded structures. For this reason, web-flange junction strength should be included in all design equations, codes, specifications and standards to ensure reliability and serviceability of pultruded composite structures. Until this weakness is mitigated by the pultrusion industry, stiffened and strengthening details must be adopted in all design of PFRP structures;
- iii) due to the inherent flexibility of the junction between web and flanges of open-web pultruded profiles, this junction should be modeled as an axial spring or rotational spring depending on the nature of applied loads. For example, unlike steel open-web profiles, a rotational spring replacing the WFJ, should be used for accurate effective stiffness characterization used in analyzing buckling, post-buckling and torsional behavior of pultruded beams and columns. For realistic modeling, experimental non-linear or linearized rotational/axial

stiffness expressions should be used for simulating the behavior of PFRP members.

iv) experimental results indicated that PFRP L-profiles exhibit different behaviors in open- and close-modes. For example, the close-mode strength of the angle size is 3 to 4 times the open-mode strength of the pultruded angle profile. It should be noted that the damage in the open mode is due to the development of interlaminar cracks that are initiated by the action of the radial stress components due to the negligible through-the-thickness strength of pultruded composites. However, in the close-mode, the strength of the pultruded angle is controlled by both local buckling at the inner side of the angle corner and the matrix tensile rupture at the exterior side of the angle corner. In both modes, the fibers are running in orthogonal direction (wrong direction) to the applied load that is resisted mainly by the weak polymeric matrix. This L-profile is commonly used as a connecting element for different connection details, including: beam-column, beam-girder and column-base connections for PFRP structures. This difference in both stiffness and strength should be considered in designing such connections under both static and dynamic loads;

v) the numerical and the experimental results have highlighted the importance of the junction strength and stiffness and its influence on overall structural behavior of pultruded composite structures. For this reason, it is necessary to develop a set of ASTM or/and ISO standard tests to provide the

designers with the necessary strength and stiffness information that will establish the design limit states for pultruded composites structures. In this phase of the multi-phase research study, a simple, yet effective test fixtures were designed, fabricated and implemented. These fixture can be a foundation for tests standards for WFJ of pultruded composite open-web profiles.





## **CHAPTER 5 – CONCLUSIONS**

### **5. INTRODUCTION**

This chapter reviews the primary research objectives from each of the previous sections and draws conclusions based on the experimental and numerical results.

As said in the introduction, this dissertation has been developed within a multi-phase comprehensive joint research program between University of Salerno, Italy, and the University of California, Irvine, USA, on investigating one of the major structural issues that defines the strength limit-state of pultruded fibre-reinforced polymer (PFRP) profiles. Specifically, the axial and rotational strength and stiffness of the web-flange junction (WFJ) of the majority of commercially-produced pultruded composite profiles. The main experimental findings are reported in the following.

### 5.1. EXPERIMENTAL RESULTS (@UNISA)

A total of 28 tests were performed on the web-flange junctions of two different sizes of PFRP pultruded I-profile: H=160 mm (*I\_160*) and H=200 mm (*I\_200*).

All specimens were subjected to tensile loading both at the *End-Point (EP)* and at the *Mid-Point (MP)*. In particular, two groups of tests were carried out. The first group of 15 specimens, having the same length of 300 mm, was subdivided into four series in order to investigate the influence of the profile size and of the pull force location on the mechanical behavior of the web-flange junctions. The second group of 13 specimens, obtained from the same pultruded beam (*I\_160*) with different lengths (200 mm, 300 mm, 600 mm and 1200 mm), were tested with the aim to evaluate the influence of the location of the pull-out load on the stiffness and strength of the junctions.

Full-scale experimental results obtained at the University of Salerno indicated that the junction strength depends on the location of the applied pull force. In particular, the values of the failure load obtained from the end-point pull out tests were about one-third smaller than those obtained from the mid-point tests for all the specimens evaluated in this phase. In addition, experimental results also showed that the load-displacement ( $P-\delta$ ) curves of WFJ are influenced by the size of the PFRP profiles; for the *I\_160\_EP* and *I\_160\_MP* specimens the load-displacement curves present a linear behavior until the elastic limit after which a

non-linear behavior and a stiffness degradation is observed up to the failure load. Whereas, for the *I\_200\_EP* and *I\_200\_MP* specimens an increasing linear displacement was observed until ultimate failure.

Moreover, the influence of the pull-out load distance ( $d$ ) from the edge of the specimens on the failure strength of the web-flange junction has been investigated and a new definition for an “*influence zone*” is proposed that is found to be dependent on the loaded length, with a maximum value equal to approximately the PFRP member’s depth. This proposed zone was observed in all laboratory tests and its existence was confirmed by the results of FEM numerical analysis.

The study also identified different failure modes of such junctions. For example, in the case of *I\_160\_EP* specimens, it has been observed that the crack generally initiated in the form of an inverted “V” shape at the center of the web-flange junction leading to a complete separation of the flange from the web. For the *I\_200\_EP* specimens, failure was sudden and occurred in the web portion of the I-profile. Finally, for all the mid-point pull-out tests, failure was initiated at the location where the load was applied and propagated along the junction length, resulting in a complete flange delamination.

3-D finite element models were also developed to predict the behavior of these specimens.

The results from the numerical models were compared to those obtained from the experimental program and found to be satisfactory, as shown in *Chapter 5*.

## 5.2. EXPERIMENTAL RESULTS (@UCI)

Six pull-out tests and seven relative rotation tests were performed on the web-flange junctions of three different sizes of PFRP pultruded H-profiles and two different sizes of L-profiles in order to evaluate both the axial and the rotational stiffness and strength of such junctions.

For pull-out tests the specimens, were cut from commercially-produced structural PFRP H- profiles and characterized by three different sizes, i.e. 10"×10" × ½" (254 × 254 × 12.7 mm), 8"× 8" × ⅜" (203.2 × 203.2 × 9.53 mm) and 6" × 6" × ⅜" (152.4 × 152.4 × 9.53 mm), were evaluated. In particular, two different test setups were carried out, varying the location of the pull-out force: in the first test setup (*Group 1* of specimens), the load was applied at the mid-point (*MP*) of the specimens, i.e. at a distance of  $l/2$  from the edge of the specimen, while in the second test setup (*Group 2* of specimens), the load was eccentrically applied (*EP*) at a distance of  $l/4$  from the edge of the specimen.

For relative rotation test, three sizes of PFRP H-profiles, i.e. 10" × 10" × ½" (254 × 254 × 12.7 mm), 8" × 8" × ⅜" (203.2 × 203.2 × 9.53 mm), 6" × 6" × ⅜" (152.4 × 152.4 × 9.53 mm) and two sizes of PFRP L-profiles, i.e. 6" × 6" × ½" (152.4 × 152.4 × 12.7 mm) and 4" × 4" × ⅜" (101.6 × 101.6 × 9.53 mm), were used. The length ( $l$ ) of all specimens was equal to 24 inch (609.6 mm).

The following observations and conclusions were made based on this phase of the experimental study:

- i) the orthotropic and viscoelastic behavior of the PFRP sections must be taken into consideration when designing PFRP structural members;
- ii) local failure of web/flange junction of unidirectional pultruded profiles influences both stiffness and strength limit-states of pultruded structures. For this reason, web/flange junction strength should be included in all design equations, codes, specifications and standards to ensure reliability and serviceability of pultruded composite structures. Until this weakness is mitigated by the pultrusion industry, stiffened and strengthening details must be adopted in all design of PFRP structures. Chapter 7 of the American Society of Civil Engineers (ASCE) Design Manual MOP 102 [40] provides a variety of strengthening details for open and close-web pultruded composite profiles as well as different connection details,
- iii) due to the inherent flexibility of the junction between web and flanges of open-web pultruded profiles, this junction should be modeled as an axial spring or rotational spring depending on the nature of applied loads. For example, unlike steel open-web profiles, a rotational spring, replacing the WFJ should be used for accurate effective stiffness characterization used in analyzing buckling, post-buckling and torsional behavior of pultruded beams and columns. For realistic modeling, experimental non-linear or linearized rotational/axial stiffness expressions should be used for simulating the behavior of PFRP members,

iv) experimental results indicated that PFRP L-profiles exhibit different behaviors in open- and close-modes. For example, the close-mode strength of the angle size is 3 to 4 times the open-mode strength of the pultruded angle profile. It should be noted that the damage in the open mode is due to the development of interlaminar cracks that are initiated by the action of the radial stress components due to the negligible through-the-thickness strength of pultruded composites. However, in the close-mode, the strength of the pultruded angle is controlled by both local buckling at the inner side of the angle corner and the matrix tensile rupture at the exterior side of the angle corner as illustrated in Figure 46. In both modes, the fibers are running in orthogonal direction (wrong direction) to the applied load that is resisted mainly by the weak polymeric matrix. This L-profile is commonly used as a connecting element for different connection details, including: beam-column, beam-girder and column-base connections for PFRP structures. This difference in both stiffness and strength should be considered in designing such connections under both static and dynamic loads;

v) this study has highlighted the importance of the junction strength and stiffness and its influence on overall structural behavior of pultruded composite structures. For this reason, it is necessary to develop a set of ASTM or/and ISO standard tests to provide the designers with the necessary strength and stiffness information that will establish the design limit states for pultruded composites structures. In this phase of the multi-phase research study, a simple, yet effective

test fixtures were designed, fabricated and implemented. These fixture can be a foundation for tests standards for WFJ of pultruded composite open-web profiles.

It is hoped that the results of this dissertation research will contribute to fill the existing gaps and provide structural engineers with essential engineering data to assist to secure optimum designs and obtain the maximum benefit of PFRP materials.





## REFERENCES

- [1] Bank, L.C., Mosallam, A.S. (1990). "Performance of Pultruded FRP Beam to Column Connections," Proceedings, Structure Congress'91, Edt. T. Williamson, The 9th ASCE Structures Congress, ASCE, Indianapolis, Indiana, April 29-May 1, 389-392.
- [2] Bank, L. C. and Mosallam, A. S. (1992). "Creep and Failure of a Full-Size Fiber Reinforced Plastic Pultruded Frame," Composites Engineering, Vol. 2, No. 3, pp. 213-227.
- [3] Bedford Reinforced Plastics Design Guide (1998). Bedford Reinforced Plastics, Bedford, Pennsylvania, USA.
- [4] Creative Pultrusions (CP) Design Guide (1988), Creative Pultrusions Inc., Alum Bank, Pennsylvania, U.S.A.
- [5] EXTREN Design Manual, (1997), Strongwell Company (formerly MMFG), Bristol, Virginia, U.S.A.
- [6] Fiberline Design Manual (1995), Fiberline Composites A/S, Denmark.
- [7] Bank, L. C., Mosallam, A. S., and Gonsior, H.E. (1990). "Beam-to-Column Connections for Pultruded FRP Structures," Proceedings, ASCE Materials Congress, Denver, Colorado, August 13-15, 804-813.
- [8] Bank, L.C. and Mosallam, A.S. (1991). "Linear and Non-linear Response of Pultruded FRP Frames Subjected to Static Loads," in *Plastics and Plastic Composites: Material Properties, Part Performance, and Process Simulation*, ASME, N.Y., N.Y., pp. 371-386.
- [9] Bank, L.C., and Mosallam, A.S. (1991) "Performance of Pultruded FRP Beam-to-Column Connections," Proceedings, 49th ASCE Structures Congress, Indianapolis, Indiana, April 29- May 1, pp 389-392.
- [10] Bank, L.C. and Mosallam, A.S. (1991). "Linear and Non-linear Response of Pultruded FRP Frames Subjected to Static Loads," in *Plastics and Plastic Composites: Material Properties, Part Performance, and Process Simulation*, ASME, N.Y., N.Y., pp. 371-386.
- [11] Bank, L. C. and Mosallam, A.S., and McCoy, G.T. (1992). "Make Connections Part of Pultruded Frame Design," *Modern Plastics Magazine*, McGraw-Hill, 65-67. Reprinted in *Modern Plastics International*, August, pp. 34-36.

- [12] Mosallam, A. S., (1993), "Stiffness and Strength Characteristics of PFRP UC/Beam- to-Column Connections," Composite Material Technology, PD-Vol. 53, Proceedings, ASME Energy- Sources Technology Conference and Expo, Texas, January 31- February 4, pp 275-283.
- [13] Mosallam, A.S., Bedewi, N.E., and Goldstein, E. (1994) "Design Optimization of FRP Universal Connectors," Polymer & Polymer Composites, Vol. 2, No. 2, pp. 115A-123A.
- [14] Mosallam, A. S. (1994) "Connections for Pultruded Composites: A Review and Evaluation," in Infrastructures: New Materials and Methods of Repair, Editor: K.D. Basham, ASCE, N.Y., pp. 1001-1017.
- [15] Bank, L.C., Mosallam A.S. and McCoy, G.T. (1994). "Design and Performance of Connections for Pultruded Frame Structures," Journal of Reinforced Plastics and Composites, Vol. 13, March, pp. 199-211.
- [16] Mosallam, A.S. (1995) "Cyclic and Creep Behavior of UC Composite Frame Connections," Proceedings, The Second International Conference for Composites Engineering (ICCE/2), New Orleans, Louisiana, 521-522.
- [17] Mosallam, A.S., and Schmitz, H.G. (1996) "Experimental Investigation on the Behavior of UC Beam-to-Column Composite Connections Under Cyclic and Sustained Loads," Proceedings of the First International Conference on Composites in Infrastructures (ICCI'96), University of Arizona, Tucson, Arizona, January 15-17, pp. 638-650.
- [18] Mosallam, A.S. (1995) "Behavior of Pultruded Composites Frame Structures and Connections" in Research Transformed into Practice, Editors: J. Colville, and A. Amde, ASCE Press, N.Y., N.Y., pp. 96-107.
- [19] Mosallam, A.S. (1995) "Semi-Rigid Behavior of Beam-to-Column Connections For Polymer Composite Frame Structures," Proceedings, Fourth Pan American Congress of Applied Mechanics (PACAM IV), January 3-6, Universidad del Salvador, Buenos Aires, Argentina.
- [20] Mosallam, A.S. (1996) "Viscoelastic Behavior of Semi-rigid Composites Frame Connections" Proceedings of the Third International Conference on Composites Engineering (ICCE/3), New Orleans, Louisiana, July 21-26.

- 
- [21] Mosallam, A.S. (1997) "Structural Evaluation of Polymer Composite Connections for Civil Engineering Structures," Proceedings of SAMPE Conference, April 1997, Anaheim, California, pp. 269-280
- [22] Mosallam, A.S. (1998). "State-of-the-Art Review on Connections for Pultruded Composites," Proceeding, European Pultrusion Technology Association (EPTA) Annual Conference, Vienna, Austria, April.
- [23] Mosallam, A.S. (1999). "Cyclic Behavior of FRP Interior Frame Connections For Pultruded Structures" Proceedings, ASCE 5th Materials Congress, Cincinnati, Ohio, May 10-12, pp. 84-91.
- [24] Gerstle, K.H. (1985). "Flexibly Connected Steel Frames," Chapter 7 in Steel Framed Structures: Stability and Strength, Edt. R. Narayanan, Elsevier Applied Science, Essex, U.K., pp. 205-239.
- [25] Zahr, S., Hill, S., Morgan, H., (1993), "Semi-Rigid Behavior of PFRP/UC Beam-To-Column Connections," Proceedings, The ANTEC'93 Conference, Society of Plastic Engineers, New Orleans, Louisiana, May 9-13, pp. 1496-1502.
- [26] Bass, A.J., and Mottram, J.T. (1994) "Behavior of Connections in Frame Reinforced Polymer Composite Section" The Structural Engineer, Vol. 72 No. 17, pp. 280-285.
- [27] Mottram, J.T., and Zheng, Y., (1996). "State-of-the-art review on the design of beam- to-column connections for pultruded frames", Composite Structures, pp. 354, 387- 401.
- [28] Sanders, D.H., Gordaninejad, F., and Murdi, S. (1996) "FRP Beam-to-Column Connections Using Adhesives" Proceedings, ICCI'96, Tucson, AZ., January 15-17, pp. 596-607.
- [29] Smith, S.J., Parsons, I.D., and Hjelmstad, K.D. (1996) "A Study of the Behavior of Joints in GFRP Pultruded Rectangular Tubes and I-beams" Proceedings, ICCI'96, Tucson, AZ., January 15-17, pp. 583-595.
- [30] Smith, S.J., Parsons, I.D., and Hjelmstad, K.D. (1999). "Design Models of GFRP Connections," Proceedings, The 5th ASCE Materials Engineering Congress, Cincinnati, Ohio, May 10-12, pp. 100-107.
- [31] Turvey, G.J., and Cooper, C. (1998). "Semi-rigid Connections and their Effects on the Sway Response of Pultruded GRP Columns in Low-Rise Frame Structures," Proceedings, ICCI'98, Tucson, AZ., January, Vol. II, pp. 221-235.

- [32] Turvey, G.J. (1998). "Recent Developments in Testing, Design, Analysis and Modeling of Bolted Connections in Pultruded GRP Frames Made of Open-Section Profiles," Proceedings, 4th EPTA Pultrusion Conference, Vienna, Austria, April 9-11, Paper 4.
- [33] Turvey GJ, Zhang Y. Tearing failure of web-flange junctions in pultruded GRP profiles. *Compos Part A: Appl Sci Manuf* 2005;36:309-17.
- [34] Turvey GJ, Zhang Y. Shear failure strength of web-flange junctions in pultruded GRP WF profiles. *Constr Build Mater* 2006;20:81-9.
- [35] Turvey GJ, Zhang Y. Characterisation of the rotational stiffness and strength of web-flange junctions of pultruded GRP WF-sections via web bending tests. *Compos Part A: Appl Sci Manuf* 2006;37:152-64.
- [36] Borowicz DT, Bank LC. Behavior of pultruded fiber-reinforced polymer beams subjected to concentrated loads in the plane of the web. *J Compos Construct* 2011;15:229-38.
- [37] Eurocomp Design Code and Handbook, Structural design of polymer composites. The European Structural Polymeric Composites Group; 1996. (ISBN 0419194509).
- [38] European Committee for Standardization (CEN). EN 13706: Reinforced plastics composites - Specifications for pultruded profiles. Part 1: Designation; Part 2: Methods of test and general requirements; Part 3: Specific requirements, Brussels: CEN; 2002.
- [39] Technical Document CNR-DT 205/2007. Guide for the design and construction of structures made of FRP pultruded elements. Italian National Research Council (CNR) Rome; 2008.
- [40] Mosallam A. S., Design guide for FRP composite connections. Manuals of Practice (MOP) 102. American Society of Civil Engineers (ASCE); 2011. ISBN9780784406120: 624.
- [41] CEN/TC 250/2014 FIBRE REINFORCED POLYMER STRUCTURES: Scientific and Technical Report", drawn up by the Working Group No. 4 (2014), in press.
- [42] Lekhnitskii S.G., Anisotropic plates, Translated from Russian by S.W. Tsai and T. Cheron, Gordon and Breach, Newark, New Jersey, 1968.

- 
- [43] Calcote L.R., *The Analysis of laminated composite structures*, Von Nostrand Reinhold Company, New York, 1998.
- [44] Jones R.M., *Mechanics of composite materials*, Scripta Book Co., Washington, D. C., 1975.
- [45] Christensen R.M., *Mechanics of composite materials*, John Wiley & Sons, New York, 1979.
- [46] Agarwal B.D. and Broutman L. J., *Analysis and performance of fiber composites*, John Wiley & Sons, New York, 1980.
- [47] Tsai S.W. and Hahn H.T., *Introduction to composite materials*, Technomic, Lancaster, Pennsylvania, 1980.
- [48] Lekhnitskii S.G., *Theory of elasticity of an anisotropic body*, Mir Publishers, Moscow (Translated from the revised 1977 Russian Edition), 1981.
- [49] Vinson J.R. and Sierakowski R. L., *The behavior of structures composed of composite materials*, Kluwer, Netherlands, 1986.
- [50] Mallick P.K., *Fiber-reinforced composites, Materials, Manufacturing, and Design*, Marcel Dekker, New York, 1988.
- [51] Vasiliev V.V., *Mechanics of composite structures*, Taylor & Francis, Washington, D.C., 1988.
- [52] Gibson R.F., *Principles of composite material mechanics*, McGraw-Hill, New York, 1994.
- [53] Reddy J.N., *Mechanics of laminated composite plates*, CRC Press, Boca Raton, 1997.
- [54] Barbero E.J., *Introduction to composite material design*, Taylor & Francis, Philadelphia, 1998.
- [55] Kollár L. P., Springer G. S., *Mechanics of composites structures*. Cambridge University Press; 2003.
- [56] Ascione L., Feo L., *Mechanical behavior of composites for construction*. In "Wiley Encyclopedia of Composites", 2<sup>nd</sup> Edition, John Wiley & Sons, 2, pp.1625-1649; 2012.
- [57] Feo L., Mosallam A. S., Penna R., *Preliminary results of an experimental and computational analysis of the behaviour of web-flange junctions of GFRP pultruded profiles subjected to concentrated loads*. In *Proceeding of the 15<sup>th</sup> European Conference on Composites Materials (ECCM15)*, Venice; 2012.

- [58] Feo L., Mosallam A. S., Penna R., An Experimental Investigation on the Behavior of Web-Flange Junctions of GRP Pultruded Profiles in Proceeding of the ICCE-20 (20<sup>th</sup> Annual International Conference on Composites/Nano Engineering), Beijing; 2012.
- [59] Feo L., Penna R., Analisi delle tensioni nei nodi "ala-anima" di profili pultrusi fibrorinforzati in Proceeding of the Italian Association for Stress Analysis (AIAS) Conference, Padova (Italy); 2012.
- [60] Feo L., Penna R., On the behavior of web-flange junctions of GRP pultruded profiles. In Proceedings of Riga Technical University 53<sup>rd</sup> International Scientific Conference dedicated to the 150th anniversary and 1<sup>st</sup> Congress of World Engineers and Riga Polytechnical Institute / RTU Alumni. Riga (Latvija); 2012.
- [61] Elsadek A., Mosallam A., Pul S., Feo L., Penna R., Experimental Evaluation of Axial Flexibility of Web-Flange Junctions of Thin-Walled Pultruded H-Profiles, Composites Structures, In press; 2012.
- [62] Feo L., Mosallam A. S., Penna R., Experimental and numerical results on the failure strength of web-flange junctions of thin walled pultruded composites profiles, in Proceeding of the Italian Association for Stress Analysis (AIAS) Conference, Salerno (Italy); 2013.
- [63] Feo L., Mosallam A. S., Penna R., Mechanical behavior of web-flange junctions of Thin-walled pultruded I-profiles: An experimental and numerical evaluation. Composites Part B: Engineering, Volume 48, Pages 18-39, May 2013.
- [64] Mosallam A. S., Elsadek A. A., Pul S., Semi-rigid behavior of web-flange junctions of open-web pultruded composites. In Proceeding of the International Conference on FRP Composites, San Francisco, California; 2009.
- [65] Feo L., Mosallam A. S., Elsadek A., Pul S., Penna R., Structural evaluation of axial and rotational flexibility and strength of web-flange junctions of open-web pultruded. Composites Part B. (2014), Volume 66, Pages 311-327, October 2014.
- [66] Vanevenhoven L.M, Shield C.K., Bank L.C., LRFDFactors for Pultruded Wide-Flange Columns. Journal of Structural Engineering, Pages 554-564, May 2010.